

THE ROLE OF DISSOLVED ORGANIC MATTER FOR WATER MASS
CHARACTERIZATION AND TRACE METAL TRANSPORT IN THE ARCTIC OCEAN

A Dissertation

by

TATIANA WILLIFORD

Submitted to the Graduate and Professional School of
Texas A&M University
in partial fulfillment of the requirements for the degree of

DOCTOR OF PHILOSOPHY

Chair of Committee,	Rainer Amon
Committee Members,	Kaiser Karl
	Jessica Fitzsimmons
	Alejandro Orsi
Head of Department,	Shari Yvon-Lewis

August 2021

Major Subject: Oceanography

Copyright 2021 Tatiana Williford

ABSTRACT

The Arctic Ocean is an ideal place for dissolved organic matter (DOM) research and studies of metal-organic interactions because it has limited exchange with the other oceans and has abundant sources of organics and trace metals in the upper water column like fluvial discharge and shelf input. In this dissertation, the value of DOM, and specifically the chromophoric and terrigenous portions of it (CDOM and tDOM, respectively), as natural tracers directly linked to the carbon cycle and giving insight on key processes like sea-ice freezing and thawing, halocline formation, and water masses circulation, are explored. Another purpose of this body of work is to improve understanding of the role of CDOM and tDOM for trace metals distribution, as trace element availability to phytoplankton plays a significant role in primary production.

Foremost, this dissertation research traces DOM from various sources in the Arctic Ocean by combining hydrographic characterization of water masses, water fraction analyses, and the optical and chemical characterization of DOM. The first part of this research examined the distributions of lignin phenols, CDOM, and optical properties in waters of the eastern Arctic, and their relationship to dissolved iron (dFe) distributions to elucidate the sources, molecular characteristics and distributions of iron-binding ligands in the Arctic Ocean. The primary sources of iron-binding ligands appear to be the riverine discharge of terrigenous DOM, marine organic matter produced on the shelves, and degradation products of plankton-derived organic matter in the shelf sediments. The observed dFe distributions in the Arctic Ocean could not be explained by the presence of a single ligand type, but rather by a potpourri of ligand molecules of varying concentrations and binding strengths. In the second part, data from the International Arctic GEOTRACES project allowed us to expand the research into the western Arctic and examine the

DOM distribution in the Chukchi sea shelf, Canada, Makarov, Amundsen and Nansen basins more closely. The Geotraces data set also allowed examining more dissolved trace metals in relation to DOM. Besides dFe, we were able to include manganese (dMn), nickel (dNi), copper (dCu), zinc (dZn), and cadmium (dCd). The DOM and trace metals correlations were investigated *modus operandi* to elucidate the sources, molecular characteristics and distributions of metal-binding ligands in the Arctic Ocean. In the last part, we compiled and merged some of the existing regional datasets of the *in situ* measurements of optical properties in an attempt to fill in the gaps in our knowledge of Arctic water mass circulation on a pan-Arctic scale. Based on absorbance and fluorescence measurements, we computed the widely-known indices including absorption coefficients a_{254} , a_{350} , spectral slopes $S_{275-295}$, $S_{350-400}$, $S_{300-600}$, and fluorophores deciphered by the Parallel Factor Analysis (PARAFAC). These indices were proven to be helpful in tracing specific processes or chemical signatures in the Arctic Ocean on the regional level. We demonstrated that the optical properties of CDOM can be very beneficial on a pan-Arctic scale, e.g., for localization and constraining the geographical extent of major oceanographic features like the Beaufort Gyre, the Transpolar drift and the halocline layers.

DEDICATION

I would like to dedicate this dissertation to my family: my parents, Svetlana and Sergey Sarminy; my grandparents, Lubov and Ernest Sarminy, Amina and Khalil Kamaletdinovy, my aunts and uncles, Gulnara Ponomareva, Nelly Vinogradova, Victor and Alexei Sarminy. They instilled a love of nature in me, always encouraged curiosity, and helped strengthen my character. I would also like to dedicate it to my school Geography teacher, Galina Anatolievna Gorlova.

ACKNOWLEDGEMENTS

First and foremost, I would like to acknowledge my scientific advisor, Dr. Rainer Amon. He has always been a great professional example for me and an inspiring leader. I would like to say special thanks to Dr. Karl Kaiser, who spent hours with me in the lab and has always been patient with his students and passionate about the research. I would like to thank Dr. Jessica Fitzsimmons and Dr. Alejandro Orsi for their mentorship and great advice on the way to my graduation.

A huge thank you to my lab mates and colleagues: Dr. Sergey Molodtsov and Stephanie Mohan. They were always ready to help and always available for moral support.

Finally, a special thank you to my previous scientific advisors: Dr. Nikolai Dronin, Dr. Andrei Kirilenko, and Dr. Xiaodong Zhang, for believing in me and encouraging me on my way.

CONTRIBUTORS AND FUNDING SOURCES

Contributors

This work was supervised by a dissertation committee consisting of Drs. Rainer Amon, Karl Kaiser, Jessica Fitzsimmons and Alejandro Orsi that hold appointments in the Department of Oceanography (Texas A&M College Station) and/or the Department of Marine and Coastal Environmental Science (Texas A&M Galveston).

Funding Sources

This work was funded by the Arctic Natural Science Program at the US National Science Foundation (NSF) under Grants Number PLR-0425582 and PLR-0713991, awarded to Drs. Rainer Amon and Karl Kaiser. Its contents are solely the responsibility of the authors and do not necessarily represent the official views of the NSF.

The graduate study was additionally supported by:

- M.T. Halbouty '30/AAPG Foundation Endowed Fellowship, College of Geosciences, 2019
- James Sharp Graduate Fellowship, Department of Oceanography, Texas A&M University, 2015, 2017, 2018
- Travel Grants: Texas A&M 2015, 2016, 2017, 2018.

NOMENCLATURE

a_{254}	Absorption coefficient of CDOM at 254 nm
a_{350}	Absorption coefficient of CDOM at 350 nm
AB	Amundsen Basin
AG	Amundsen Gulf
AW	Atlantic Water
BS	Beaufort Sea
CA	Central Arctic
CB	Canada Basin
Cd	Cadmium
CDOM	Chromophoric Dissolved Organic Matter
CRAM	Carboxyl-rich alicyclic molecules
CS	Chukchi Shelf
CTD	Conductivity, temperature, depth
Cu	Copper
DIC	Dissolved Inorganic Carbon
dMe	Dissolved Metal
DOC	Dissolved Organic Carbon
DOM	Dissolved Organic Matter
EEM	Excitation-emission matrix
ESS	East Siberian Sea
f_{AW}	Fraction of Atlantic Water
Fe	Iron

f_{met}	Fraction of meteoric water
f_{PW}	Fraction of Pacific Water
f_{sim}	Fraction of sea-ice melt
LHC	Lower Halocline
LS	Laptev Sea
MB	Makarov Basin
Mn	Manganese
NB	Nansen Basin
Ni	Nickel
ODV	Ocean Data View
P/V	p-hydroxyl to Vanillyl phenol ratio
PARAFAC	Parallel Factor Analysis
PCA	Principal component analysis
PML	Polar Mixed Layer
S/V	Syringyl to Vanillyl phenol ratio
$S_{275-295}$	Spectral slope coefficient of CDOM absorption spectra between 275 nm and 295 nm
$S_{300-600}$	Spectral slope coefficient of CDOM absorption spectra between 300 nm and 600 nm
$S_{350-400}$	Spectral slope coefficient of CDOM absorption spectra between 350 nm and 400 nm
Sc	Scandium
Si	Silicate

Sr	Slope ratio
SUVA	Specific UV absorbance at 254 nm
TDLP	Total Dissolved Lignin Phenols
tDOM	Terrigenous Dissolved Organic Matter
TPD	Transpolar Drift
UHC	Upper Halocline
UV	Ultraviolet
Zn	Zinc

TABLE OF CONTENTS

	Page
ABSTRACT.....	ii
DEDICATION.....	iv
ACKNOWLEDGEMENTS.....	v
CONTRIBUTORS AND FUNDING SOURCES	vi
NOMENCLATURE	vii
TABLE OF CONTENTS.....	x
LIST OF FIGURES	xiii
LIST OF TABLES.....	xviii
1. INTRODUCTION	1
1.1 Overview.....	1
1.2 Dissolved trace metals in the Arctic Ocean	2
1.3 Methods for DOM assessment.....	3
1.4 Summary	5
1.5 References.....	6
2. INSIGHTS INTO THE ORIGINS, MOLECULAR CHARACTERISTICS AND DISTRIBUTION OF IRON-BINDING LIGANDS IN THE ARCTIC OCEAN	14
2.1 Overview.....	14
2.2 Introduction.....	15
2.3 Methods and data	17
2.3.1 Sampling	17
2.3.2 Dissolved organic carbon and optical properties	18
2.3.3 Lignin phenol analysis	22
2.3.4 Additional data.....	23
2.4 Results.....	23
2.5 Discussion	32
2.5.1 Origin of PARAFAC components.....	32
2.5.2 Distribution of biomarkers, optical properties and dissolved iron.....	35
2.5.3 DOM and dissolved iron in relation to hydrographic features	41

2.6	References.....	47
3.	RELATIONSHIPS BETWEEN DISSOLVED ORGANIC MATTER, HYDROGRAPHY AND TRACE ELEMENTS IN THE ARCTIC OCEAN	61
3.1	Introduction.....	61
3.2	Methods.....	65
3.2.1	Sampling	65
3.2.2.	Dissolved inorganic and organic carbon.....	68
3.2.3.	Optical properties of DOM	68
3.2.4.	Lignin phenols analysis.....	72
3.2.5.	Trace metal data	72
3.2.6.	Linear mixing model.....	73
3.3	Results.....	74
3.3.1.	Hydrographic setting.....	74
3.3.2.	<i>In situ</i> CDOM fluorescence	75
3.3.3.	Dissolved organic carbon.....	77
3.3.4.	Dissolved inorganic carbon.....	77
3.3.5.	Lignin phenols	80
3.3.6.	Optical properties.....	80
3.3.7.	Water fractions.....	83
3.3.8.	Trace metals	86
3.4.	Discussion	87
3.4.1.	Indicators of tDOM.....	87
3.4.2.	DOM and trace metals in relation to DOM and hydrographic features.....	88
3.4.2.1.	The TPD.....	89
3.4.2.2.	The haloclines	94
3.4.2.3.	The PML within the Beaufort Gyre	97
3.4.3.	Processes affecting the distribution of DOM and trace metals in the Arctic Ocean	99
3.5.	Acknowledgements.....	103
3.6.	References.....	104
4.	TRACING ARCTIC OCEAN WATER MASSES WITH OPTICAL INDICES	127
4.1	Introduction.....	127
4.2	Methods and data	129
4.2.1	Cruises and data sources	129
4.2.1.1	Beringia - Arctic Ocean Section (AOS 2005).....	129
4.2.1.2.	ARK-XXII/2 or PS70 (2007).....	103
4.2.1.3	NABOS (2008)	103
4.2.1.4.	CFL (2008).....	103
4.2.1.5	Malina (2009).....	131
4.2.1.6.	ICESCAPE (2010).....	131
4.2.1.7	HLY1502 (2015).....	131

4.2.1.8. PS94 (2015)	132
4.2.2 Hydrographical setting	132
4.2.3 The CDOM data.....	135
4.3 Results.....	138
4.3.1 PARAFAC components.....	138
4.3.2 Regional distributions of DOM	140
4.3.2.1 The Amundsen Gulf (CFL-2008, Malina-2009).....	140
4.3.2.2 The Beaufort Sea slope (CFL-2008, Malina-2009)	140
4.3.2.3 The Chukchi Sea (ICESCAPE-2010)	141
4.3.2.4 The East Siberian Sea and the Laptev Sea (ARK-XXII/2-2007; NABOS-2008)	142
4.3.2.5 The Canada Basin (AOS-2005, HLY1502)	146
4.3.2.6. The Nansen Basin (ARK-XXII/2-2007; NABOS-2008).....	151
4.3.2.7 The Central Arctic Ocean (ARK-XXII/2-2007; AOS-2005, HLY1502)	151
4.4. Discussion	151
4.4.1 Trends in DOM	151
4.4.2 The principal components based on the optical properties	157
4.5 References.....	161
 5. SUMMARY	 170

LIST OF FIGURES

FIGURE	Page
<p>2.1 The Ark-XXII/2 cruise track and sampling stations. The positions of sections A, B, and C are shown with arrows. <i>In situ</i> fluorescence (Dr. Haardt sensor) in surface waters is shown in color.</p>	18
<p>2.2 The fluorescence properties of five fluorescent components identified by PARAFAC modeling. The white square on the second EEM (C_{482}) shows the range of Haardt fluorometer measurements. Note: The secondary emission peak of component 5 (C_{302}) is a second-order peak (at twice the primary emission peak) and represents an artifact of the instrument design.</p>	21
<p>2.3 The <i>in situ</i> CDOM fluorescence (a, b, c, d), a_{254} absorption (e, f, g, h), a_{350} absorption (i, j, k, l), $S_{274-295}$ (m, n, o, p), dissolved iron (dFe) concentrations (q, r, s, t), TDLP9 concentrations (u, v), and dissolved organic carbon (DOC) concentrations (w, x) for the Ark-XXII/2 transects. White contours in the top panels represent isopycnals.....</p>	25
<p>2.4 The five fluorescent components identified by the PARAFAC model for the Ark-XXII/2 transects (left to right, West to East) B (a, c, e, g, i), and C (b, d, f, h, j) in the upper 400m of the water column. White contours in the top panels represent isopycnals.</p>	27
<p>2.5 Top to bottom panels: top 150 m of the p-hydroxy (P) and vanillyls (V) phenols ratio (P/V), syringyls (S), and V ratio (S/V) for the Ark-XXII/2 transect B (left to right, North to South, left column) and C (right column).</p>	29
<p>2.6 Possible iron-binding sites on molecules of various origins in natural waters. These types of molecules are found in humic substances extracted from freshwater and marine environments. Tannins, lignins, siderophore (catechol type), black carbon likely contribute to CDOM. CRAM- Carboxyl-rich alicyclic molecules</p>	44
<p>3.1 The U.S. GEOTRACES Arctic GN01 transect cruise track (triangles) and the TransARCII PS94 cruise track (circles) with relevant stations. Section A is presented as white color symbols; section B is presented as black color symbols. The approximate locations of major upper ocean circulation features are shown in grey, red (Transpolar Drift), and magenta (Beaufort Gyre). <i>In situ</i> CDOM fluorescence (excitation 350–460 nm/emission 550 nm HW 40 nm; Dr. Haardt, Optik Mikroelektronik, Germany) in surface waters is shown in color (in volts, V). This figure and section plots in the manuscript were generated using Ocean Data View (Schlitzer, 2020).</p>	67
<p>3.2 The fluorescence properties of fluorescent components identified by PARAFAC modeling in the Canada Basin (a) and the Nansen, Makarov, and Amundsen Basins (b).</p>	71
<p>3.3 <i>In situ</i> CDOM fluorescence for sections A (a) and B (b) in the upper 400 m. The white dashed line represents the border of the PML. Black dotted isohaline of $S = 34$ represents</p>	

the lower bound of the UHC. The LHC is bordered at the bottom by the isotherm of $\Theta = 0^{\circ}\text{C}$ (black solid line). Isopycnal of $\sigma=27.8 \text{ kg/m}^3$ (black dashed line) closely follows the lower border of the CDOM trace in the Canada basin. The silicate maximum marks the core of the UHC according to Anderson et al. (2013) 76

3.4 The dissolved organic carbon (DOC, a), dissolved inorganic carbon (DIC, b) and lignin phenols (TDLP9, c) concentrations for section A in the upper 400 m. The white dashed line represents the border of the PML. Black dotted isohaline of $S = 34$ represents the lower bound of the UHC. The LHC is bordered at the bottom by the isotherm of $\Theta = 0^{\circ}\text{C}$ (black solid line). The silicate maximum marks the core of the UHC according to Anderson et al. (2013) 78

3.5 The dissolved organic carbon (DOC, a), dissolved inorganic carbon (DIC, b) and lignin phenols (TDLP9, c) concentrations for section B in the upper 400 m. The white dashed line represents the border of the PML. Black dotted isohaline of $S = 34$ represents the lower bound of the UHC. The LHC is bordered at the bottom by the isotherm of $\Theta = 0^{\circ}\text{C}$ (black solid line). The silicate maximum marks the core of the UHC according to Anderson et al. (2013) 79

3.6 Calculated fractions of f_{Atl} , (a, e), f_{Pac} (b, f), f_{SIM} (c, g) and f_{Met} (d, h) for sections A and B. The white dashed line represents the border of the PML. Black dotted isohaline of $S = 34$ represents the lower bound of the UHC. The LHC is bordered at the bottom by the isotherm of $\Theta = 0^{\circ}\text{C}$ (black solid line). 85

3.7 Scatterplots between the lignin phenols concentrations and C1 PARAFAC components (a), C2 PARAFAC components (b), dissolved organic carbon (DOC, c) and absorption coefficients a_{254} and a_{350} (d) in the top 300 meters of the Arctic Ocean. Only significant correlations ($p < 0.001$) are shown). 88

3.8 Scatterplots between the dMn (top panels), dFe (bottom panels) and C1 PARAFAC components and *in situ* CDOM fluorescence (CDOMF; a, b), lignin phenols (TDLP9) and dissolved organic carbon (DOC; b, d), in the top 300 meters of the Makarov and Amundsen Basins. Only significant correlations ($p < 0.001$) are shown) 90

3.9 S Scatterplots between the dNi (top panels), dCu (bottom panels) and C1 PARAFAC components and *in situ* CDOM fluorescence (CDOMF; a, b), lignin phenols (TDLP9) and dissolved organic carbon (DOC; b, d), in the top 300 meters of the Amundsen and Makarov basins. Only significant correlations ($p < 0.001$) are shown). 93

3.10 Scatterplots between the trace metals and *in situ* CDOM fluorescence (a), DIC (b), DOC (c), terrigenous humic-like C1₄₈₂ (d), marine humic-like C1₄₃₄ (e), marine humic-like with sediment signature C1₄₀₂ (f), in the top 300 meters of the Arctic Ocean. Only significant correlations ($p < 0.001$) are shown). 96

3.11 Relationship (Pearson correlation) of the CDOM *in situ* fluorescence, with f_{SIM} (a) and f_{Met} (b) in the Chukchi Sea, Canada, Makarov, Amundsen, and Nansen Basins. Only significant ($p < 0.001$) correlations are shown. The *in situ* CDOM fluorescence for sections A (c)

and B (d) in the upper 400 m. The light gray dotted lines represent the fMet isolines, and the solid black lines represent f_{SIM} isolines. 101

S3.1 The calibration between the two fluorometers with the deep water measurements (<1000 m) 121

S3.2 The Nansen Basin (PS94 station 58) top 70 m profile of C2 PARAFAC components' intensities (top left panel), absorbance-based optical properties (bottom panels) and trace metals concentrations (top right panel). 122

S3.3 The Makarov Basin top 300 m. (PS94 station 87) profile of C2 PARAFAC components' intensities (top left panel), absorbance-based optical properties (bottom panels) and trace metals concentrations (top right panel). The grey shaded regions represent PML, the upper and the lower haloclines..... 123

S3.4 The Canada Basin (GN01 station 48) top 300 m profile of C1 PARAFAC components' intensities (top left panel), absorbance-based optical properties (bottom panels) and trace metals concentrations (top right panel). The grey shaded regions represent PML, the upper and the lower haloclines. 124

S3.5 Relationship (Pearson correlation) of lignin phenol (TDLP9) concentrations, f_{SIM} and fMet in the Chukchi Sea, Canada, Makarov, Amundsen and Nansen Basins. Only significant ($p < 0.001$) correlations are shown 125

4.1 General map of Arctic Ocean showing stations occupied during the cruises: AOS 2005 (dark blue circles), ARK-XXII/2 (green triangles), NABOS-2008 (red diamonds), CFL-2008 (yellow triangle), Malina-2009 (purple reversed triangles), ICESCAPE-2010 (orange squares), PS94-2015 (semi-transparent yellow squares) and Healy-2015 (light blue diamonds); and study areas in black boxes: the Nansen Basin (NB), the East Siberian and the Laptev Seas (ESS and LS), the Central Arctic (CA), the Amerasian Basin (AB), the Chukchi Sea (CS), the Beaufort Sea (BS) and the Amundsen Gulf (AG). The approximate locations of major upper ocean circulation features are shown with white, red (Transpolar Drift), and light purple (Beaufort Gyre)..... 134

4.2 The fluorescence properties of the fluorescent components identified by PARAFAC modeling 135

4.3 Surface distribution of five PARAFAC components identified in the study..... 139

4.4 The representative section showing a_{254} , a_{350} , $S_{275-295}$, $S_{350-400}$, $S_{300-600}$, Sr and PARAFAC components C_{484} , C_{336} , C_{418} , C_{303} , C_{404} in the upper 400 m in the Amundsen Gulf (AG). Black solid contour lines represent isohalines that bound water masses: PML ($S=32$), UHC ($S=32$, $S=33.9$), LHC ($S>33.9$). The LHC layer is overlaid by the black dot pattern and the UHC- by the light gray dot pattern. 143

4.5 The representative section showing a_{254} , a_{350} , $S_{275-295}$, $S_{350-400}$, $S_{300-600}$, Sr and PARAFAC components C_{484} , C_{336} , C_{418} , C_{303} , C_{404} in the upper 300 m in the Beaufort Sea slope

regions (BS). Black solid contour lines represent isohalines that bound water masses: PML (S=28), LPML (S=28, S=30.7), PSW (S=32.3, S=33.9). The LHC layer is overlaid by the black dot pattern and the UHC- by the light gray dot pattern. The PSW is emphasized by the striped pattern.144

4.6 The representative section showing a_{254} , a_{350} , $S_{275-295}$, $S_{350-400}$, $S_{300-600}$, S_r and PARAFAC components C_{484} , C_{336} , C_{418} , C_{303} , C_{404} in the upper 300 m in the Chuckchi Sea (CS). The following water masses are shown: PSW (S<33, $\theta > 0^\circ\text{C}$), the PWW separated into colder ($\theta < -1.6^\circ\text{C}$) newly-ventilated PSW and warmer ($\theta > -1.6^\circ\text{C}$) remnant PWW. 145

4.7 The representative section showing a_{254} , a_{350} , $S_{275-295}$, $S_{350-400}$, $S_{300-600}$, S_r and PARAFAC components C_{484} , C_{336} , C_{418} , C_{303} , C_{404} , and in situ CDOM fluorescence in the upper 120 m in the East Siberian and Laptev Sea shelves. Black dashes contour line represents the isohalines of S=33 and S=34, marking the upper and the lowers limit of the Laptev shelf bottom water.147

4.8 The representative section showing a_{254} , a_{350} , $S_{275-295}$, $S_{350-400}$, $S_{300-600}$, S_r and PARAFAC components C_{484} , C_{336} , C_{418} , C_{303} , C_{404} , and in situ CDOM fluorescence in the upper 300 m in the Canada Basin (CB). Only AOS 2005 data is used for the plot. Black dotted contour line represents the isohaline of S=31, which marks the base of the PML. White solid contour line of [Si] = 25 $\mu\text{mol/L}$ represents the bounds of the UHC, overlaid by the white dot pattern. The LHC layer is overlaid by the black dot pattern, bordered at the bottom by the isopycnals (black dash line) of $\sigma = 27.4 \text{ kg/m}^3$ 148

4.9 The representative section showing a_{254} , a_{350} , $S_{275-295}$, $S_{350-400}$, $S_{300-600}$, S_r and PARAFAC components C_{484} , C_{336} , C_{418} , C_{303} , C_{404} in the upper 400 m in the Nansen Basin (NB). PML is characterized by $\theta < 0^\circ\text{C}$ and S<34.5. AAW is marked by the $\theta > 0^\circ\text{C}$., with the layer core located around $\theta \text{ max}$ 149

4.10 The representative section showing a_{254} , a_{350} , $S_{275-295}$, $S_{350-400}$, $S_{300-600}$, S_r and PARAFAC components C_{484} , C_{336} , C_{418} , C_{303} , C_{404} in the upper 400 m in the Central Arctic region (CA). The top 100 m is occupied by the TPD in the Amundsen and the Northern Makarov Basins. The PML of the southern Makarov Basin contains up to 60% of fPac (Williford et al. 2021). The LHC is bordered at the bottom by the isopycnal of $\sigma = 27.4 \text{ kg/m}^3$. (black dashed line; Bertosio et al. 2020)..... 150

4.11 PARAFAC components fluorescence intensity by region and water mass..... 152

4.12 Scatter plot of a_{350} vs. a_{254} (left panel). Different regions are shown with different markers. The linear regression trend is shown as a dashed line. The lower absorbance region is zoomed in the right panel..... 153

4.13 Spectral slopes by region and water mass 154

4.14 S_r by region and water mass..... 155

4.15 Scatter plot of FDOM (sum of all PARAFAC components) vs. in situ CDOM fluorescence (top panel). The linear regression trend is shown as a dashed line. The bottom panel shows the scatter plot of the sum of the PARAFAC components except for C336 and in situ CDOM fluorescence.	156
4.16 Scatter plot of FDOM vs. in situ CDOM fluorescence. Different regions are shown with different markers. The linear regression trend is shown as a dashed line.....	157
4.17 Loadings and scores for the PCA. The length of the vector associated with optical indices represents the overall strength of that variable on PC1, PC2.....	158
4.18 The surface distribution (top two panels) of the PC1 (left) and PC2 (right), overlaid by the main surface circulation patterns shown in arrows. The distribution of PC1 and PC2 at the salinity surface of S=34.7 is shown in the bottom panels.....	159
4.19 The PC1 (top) and PC2 (bottom) cross-section from the Beaufort Sea slope through the central Arctic into the Laptev Sea shelf.....	160

LIST OF TABLES

TABLE	Page
2.1 The optical and chemical parameters reported in this study.....	22
2.2 Pearson correlation matrix of TDLP9 concentrations and the parameters salinity, DOC, in situ CDOM fluorescence, absorption coefficients a_{254} and a_{350} , SUVA, $S_{275-295}$, and PARAFAC components.....	28
2.3 Pearson correlation matrix between dFe and salinity, CDOM, absorption coefficients a_{254} and a_{350} , spectral slopes, SUVA, DOC, TDLP9, and PARAFAC components.....	31
2.4 Spectral characteristics of the five components identified by PARAFAC and their comparison to previously identified components.	32
2.5 Examples of published data on organic iron-binding ligands in the ocean, measured with the voltammetry techniques.....	46
2.6 Water mass characteristics along with optical properties and biomarker distribution across the Arctic basins. (CB- Canada Basin, MB- Makarov Basin, AB- Amundsen Basin, NB- Nansen Basin).....	47
3.1 End-member values used in mass balance calculations.....	74
3.S1 Spectral characteristics of the six fluorescence components identified by PARAFAC in the Eurasian Basin and the TPD region and comparisons to previously identified components.	125
3.S2 Spectral characteristics of the four components identified by PARAFAC in the Canada Basin and the Chukchi Sea and their comparison to previously identified components.	126
4.1 Data compiled for this study.....	137
4.2 Spectral characteristics of the five components identified by PARAFAC and their comparison to previously identified components, sorted by loadings.....	138

1. INTRODUCTION

1.1. Overview

The Arctic Ocean plays a special role in forming the Earth's climate. First, changes in the Arctic Ocean freshwater budget are directly linked to thermohaline circulation strength, as the Arctic Ocean is a source of freshwater to the North Atlantic (Broecker, 1997). The studies show that the decline in thermohaline circulation can partly be explained by increased fluvial discharge into the Arctic Ocean (Rennermalm et al. 2006), and sea ice loss (Holland et al. 2001). Secondly, the Arctic Ocean has been widely thought of as a sink of anthropogenic CO₂ (Bates and Mathis, 2009; MacGilchrist et al. 2014; Ulfsbo et al. 2018). Some studies foresee future increases in carbon sequestration resulting from the extensive sea ice melt that enhances the ocean-atmosphere gas exchange (Bates et al. 2006) and potential increases in biological production due to improved light availability (Anderson and Kaitin 2001; Tremblay et al. 2015). Other studies show that the Arctic Ocean freshening, lowering of total alkalinity, and enhanced stratification of the water column can reduce the capability of the Arctic Ocean to take up and store CO₂. (Cai et al. 2010; Grebmeier et al. 2010; Woosley and Millero, 2020). Because many processes that can affect the carbon cycle in the Arctic Ocean occur at the same time, the net impact remains uncertain.

Marine organic chemistry provides tools to study complex processes linked to climate change in the Arctic Ocean. The dissolved organic matter (DOM) encompasses a wide range of compounds (e.g., amino acids, carbohydrates, lipids, carboxyl-rich alicyclic molecules (CRAM), pigments, lignins, tannins, etc.), whose relative abundance varies in different water masses, depending on their origin and prevailing biochemical and physical processes. For example, the biomarker lignin and the optical properties of DOM were shown to be useful tracers of the fluvial discharge (Opsahl et al. 1999; Amon et al. 2003; Amon 2004; Benner et al. 2004; Walker et al.

2009; Fichot et al. 2013; Kaiser et al. 2017; Williford et al. 2021). Combined with the stable oxygen isotope measurements, the optical properties of DOM can also be used to estimate the freshwater contribution from glacial melt and precipitation (Stedmon et al. 2015). The amino acids, chlorophyll, and protein-like fluorescence measurements have been used to trace primary productivity in the Arctic Ocean (Dittmar et al. 2001; Walker et al. 2009; Arrigo et al. 2011; Chen et al. 2018). The main objective of this dissertation is to encapsulate some major aspects of DOM distribution in relation to water masses and biochemical and physical processes in the Arctic Ocean by presenting pan-Arctic field observations from 8 oceanographic cruises from 2005 to 2015 years.

1.2. Dissolved trace metals in the Arctic Ocean

The collateral effects of climate change in the Arctic (e.g., permafrost thaw, tundra greening, and coastal erosion) enhance mobilization of carbon from the terrestrial Arctic ecosystems (Fritz et al. 2017; Berner et al. 2020), which could have a cascading effect on the supply of trace elements and their cycling in the Arctic Ocean (Pokrovsky et al. 2012; Berner et al. 2020). The biogeochemistry of DOM and trace metals is intrinsically linked due to organic ligands as they often share the same sources, can retain metals in solution, facilitate transport and influence their bioavailability to biota. The second objective of this dissertation is to enhance understanding of the complex relationships among organic ligands and some of the dissolved trace metals (Fe, Mn, Cd, Ni, Cu, Zn, Sc) in Arctic seawater.

Many trace metals are essential components of important environmental processes such as primary production (Morel et al. 2003), carbon and nitrogen fixation (Raven et al. 1990; Schulz et al. 2004; Walve et al. 2014). The low concentrations of bioactive metals can be a limiting factor for primary productivity. For example, the Fe limitation potentially prevented up to 54% of the

available nitrate and nitrite from being used for primary production in the Nansen Basin (Rijkenberg et al. 2018). Trace metals may also be toxic to phytoplankton and inhibit metabolism when they bind to the wrong metabolic sites like those normally occupied by other essential metal ions (Sunda et al. 1989). For example, Cu and Cd were shown to reduce the marine phytoplankton reproduction rates (Brand et al. 1986). Some organisms (e.g., prokaryote) can produce strong organic ligands, presumably to detoxify Cu (Semeniuk et al. 2015). The effects of trace metals on marine biota are reciprocal, and the phytoplankton itself has a profound effect on the distribution of trace metals in seawater.

The biogeochemical cycling of trace metals in the Arctic appears unique (Jensen et al. 2019, Zhang et al. 2019; Jensen et al. 2020; Jensen 2020). The studies showed that the conventional “nutrient”, “scavenged”, “hybrid”-type trace metal profiles characteristic for the global ocean were absent in the Arctic Ocean. Some of the highlights include the lack of biological uptake in the photic zone, high fluvial discharge that keeps metals elevated on the surface, and strong shelf-derived signal for Fe, Zn, and Mn carried into the central basin by a subsurface water mass (Jensen et al. 2019, Zhang et al. 2019; Charette et al. 2020; Jensen et al. 2020; Jensen 2020). In this dissertation, we use the unique opportunity to combine the measured trace metals with the DOM data on a pan-Arctic scale.

1.3. Methods for DOM assessment

The Arctic Ocean is a semi-circular, semi-enclosed basin, centered over the North Pole. The Arctic Ocean is relatively shallow and small (1.3% of the global ocean volume) and receives a disproportionate fraction (~11%) of global river discharge (Kalinin and Shiklomanov, 1974). The major inflows into the Arctic Ocean are from the Atlantic and Pacific oceans and the North

American and Eurasian rivers. Its stratification of the water column in the Arctic Ocean is predominantly controlled by salinity, and the sea ice formation/thawing processes play a major role in the freshwater cycle and currents moderation by mediating the surface wind stress (Carmack et al. 2015).

The chemical composition of seawater and organic compounds concentrations integrate environmental processes in the water column. The biogeochemical and physical processes in the ocean leave specific signatures on the chromophoric portion of dissolved organic matter (CDOM) detectable by a number of indices developed by the scientific community. The DOM spectroscopy is a cost-effective tool onboard and in the laboratory. Autonomous devices such as *in situ* fluorimeters can instantly deliver high resolution CDOM measurements. For example, such measurements, along with hydrographic parameters were efficiently used to describe the biochemical exchanges between the Nordic Seas, the Arctic Ocean, and the North Atlantic (Amon et al. 2003).

The absorption coefficients at 254 (a_{254}) and 350 nm (a_{350}) were previously used as conventional tracers of the meteoric water (river portion) in the ocean (Walker et al. 2013; Griffin 2016; Chen et al. 2018). A number of spectral slopes ($S_{xxx-xxx}$, where subscripts denote wavelength range) for different absorbance spectra regions (e.g., 275-295 nm, 350-400 nm, and 300-600 nm) were developed simply by applying an exponential function to the UV-VIS spectral range. The choice of each spectral range for the assessment of the spectral slope varies among different studies and sampling regions. $S_{275-295}$ and $S_{350-400}$ serve as indicators of photochemical alterations, and Spectral Ratio (S_R ; $S_{275-295}/S_{350-400}$) correlates well with CDOM molecular weight (Helms et al., 2008). $S_{275-295}$ is also used as an effective tracer of tDOM in river-influenced ocean margins (Fichot and Benner, 2012). $S_{300-600}$ was shown to have potential as DOC concentration proxy

(Makarewicz et al. 2018). Specific UV absorbance at 254 nm (SUVA), determined by dividing the absorbance at 254 nm by the dissolved organic carbon (DOC) concentration, is known to be directly linked to DOM aromaticity (Helms et al. 2013).

The Parallel Factor Analysis (PARAFAC) allows further differentiation of fluorescent components in CDOM (Stedmon et al., 2003; Stedmon and Bro, 2008). Recent studies empirically link specific groups of organic molecules and the PARAFAC-derived fluorophores (Stubbins et al., 2014; Kellerman et al., 2015), or compare the discovered components to the ones accumulated and described in the OpenFluor database (Murphy et al., 2014), such as fulvic and humic acids, tyrosine and tryptophan (Wünsch et al., 2015).

The separate indices were proven to be effective for different applications in the Arctic Ocean, but an accurate baseline in ocean optics is needed to observe environmental changes in the Arctic Ocean. In this study, we bring together a large amount of data on optical properties collected in the field above the polar circle from 2005 to 2015. The third goal of the dissertation is to highlight the most efficient ways to use optical properties to increase our understanding of water masses and their variability in a rapidly changing the Arctic Ocean.

1.4 Summary

This dissertation strives to enhance the existing knowledge of the changing Arctic using a large suite of biogeochemistry tools, including biomarker applications, ocean optics, and trace metals measurements. I endeavored to maximize the scientific outcomes from a unique pan-Arctic dataset, which are rare, due to access difficulties arising from ice cover, and icebreakers' cost.

The first chapter (Section 2) presents results from the expedition conducted in the Nansen, Amundsen, Makarov basin, and the Laptev Sea from July to October 2007, published in the journal

Marine Chemistry (Williford et al. 2021). Dissolved lignin phenols, *in situ* fluorescence, and optical properties of CDOM were determined in waters of the major Arctic basins, and they were compared with dissolved iron (dFe) distributions to elucidate the sources, molecular characteristics, and distributions of iron-binding ligands in the Arctic Ocean. The second chapter (Section 3) continues the story of metal-organic ligands relationships in the Arctic Ocean. This study involves tracing DOM from various sources in the Canada, Makarov, Amundsen, and Nansen Basins by combining hydrographic characterization of water masses, water fraction analyses, and the optical and chemical characterization of DOM. Using optical properties of sea water, we explore the potential links between the diverse groups of molecules in CDOM and several dissolved trace metals, including dFe, dMn, dNi, dCu, dZn, dPb, dCd, and dSc. Section 4 consists of a study bringing together data from 8 expeditions in the Arctic Ocean collected from 2005 to 2015. This study investigates the most efficient ways to use optical properties to increase our understanding of water masses and their variability in a rapidly changing the Arctic Ocean.

1.5. References

- Amon, R. M. W., G. Budeus, and B. Meon, Dissolved organic carbon distribution and origin in the Nordic Seas: Exchanges with the Arctic Ocean and the North Atlantic, *J. Geophys. Res.*, 108(C7), 3221, doi:10.1029/2002JC001594, 2003.
- Amon, R.M.W., 2004. The role of dissolved organic matter for the Arctic Ocean carbon cycle. In: Stein, R., Macdonald, R.W. (Eds.), *The Arctic Ocean Organic Carbon Cycle: Present and Past*. Springer, pp. 83–99.
- Anderson, L. G., & Kaltin, S. (2001). Carbon fluxes in the Arctic Ocean—potential impact by climate change. *Polar Research*, 20(2), 225-232.

Arrigo, K. R., Matrai, P. A., & Van Dijken, G. L. (2011). Primary productivity in the Arctic Ocean: Impacts of complex optical properties and subsurface chlorophyll maxima on large-scale estimates. *Journal of Geophysical Research: Oceans*, 116(C11).

Bates, N. R., & Mathis, J. T. (2009). The Arctic Ocean marine carbon cycle: evaluation of air-sea CO₂ exchanges, ocean acidification impacts and potential feedbacks. *Biogeosciences*, 6(11), 2433-2459.

Bates, N. R., Moran, S. B., Hansell, D. A., & Mathis, J. T. (2006). An increasing CO₂ sink in the Arctic Ocean due to sea-ice loss. *Geophysical Research Letters*, 33(23).

Benner, R., Benitez-Nelson, B., Kaiser, K., & Amon, R. M. (2004). Export of young terrigenous dissolved organic carbon from rivers to the Arctic Ocean. *Geophysical Research Letters*, 31(5).

Berner, L. T., Massey, R., Jantz, P., Forbes, B. C., Macias-Fauria, M., Myers-Smith, I., ... & Goetz, S. J. (2020). Summer warming explains widespread but not uniform greening in the Arctic tundra biome. *Nature communications*, 11(1), 1-12.

Brand, L. E., Sunda, W. G., & Guillard, R. R. (1986). Reduction of marine phytoplankton reproduction rates by copper and cadmium. *Journal of experimental marine biology and ecology*, 96(3), 225-250.

Broecker, W. S. (1997). Thermohaline circulation, the Achilles heel of our climate system: Will man-made CO₂ upset the current balance? *Science*, 278, 1582–1588.

Cai, W. J., Chen, L., Chen, B., Gao, Z., Lee, S. H., Chen, J., ... & Zhang, H. (2010). Decrease in the CO₂ uptake capacity in an ice-free Arctic Ocean basin. *Science*, 329(5991), 556-559.

Carmack, E. C., et al. (2016), Freshwater and its role in the Arctic Marine System: Sources, disposition, storage, export, and physical and biogeochemical consequences in the Arctic and global oceans, *J. Geophys. Res. Biogeosci.*, 121, 675–717, doi:10.1002/2015JG003140.

Charette, M. A., Kipp, L. E., Jensen, L. T., Dabrowski, J. S., Whitmore, L. M., Fitzsimmons, J. N., ... & Zhang, R. (2020). The Transpolar Drift as a Source of Riverine and Shelf-Derived Trace Elements to the Central Arctic Ocean. *Journal of Geophysical Research: Oceans*, 125(5), e2019JC015920.

Chen, M., Jung, J., Lee, Y. K., & Hur, J. (2018). Surface accumulation of low molecular weight dissolved organic matter in surface waters and horizontal off-shelf spreading of nutrients and humic-like fluorescence in the Chukchi Sea of the Arctic Ocean. *Science of the Total Environment*, 639, 624-632.

Dittmar, T., Fitznar, H. P., & Kattner, G. (2001). Origin and biogeochemical cycling of organic nitrogen in the eastern Arctic Ocean as evident from D- and L-amino acids. *Geochimica et Cosmochimica Acta*, 65(22), 4103-4114.

Stedmon, C. A., Granskog, M. A., & Dodd, P. A. (2015). An approach to estimate the freshwater contribution from glacial melt and precipitation in East Greenland shelf waters using colored dissolved organic matter (CDOM). *Journal of Geophysical Research: Oceans*, 120(2), 1107-1117.

Fritz, M., Vonk, J. E., & Lantuit, H. (2017). Collapsing arctic coastlines. *Nature Climate Change*, 7(1), 6-7.

Front. Mar. Sci., 2:98, 1–15, doi:10.3389/fmars.2015.00098.

Grebmeier, J. M., Cai, W. J., Hu, X., Lee, S. H., Murata, A., Sullivan, K., ... & Jones, E. P. (2010). Decrease in the CO₂ uptake capacity in an ice-free Arctic Ocean Basin.

Griffin, C. G. (2016). Dissolved organic matter in major rivers across the Pan-Arctic from remote sensing (Doctoral dissertation).

Helms, J. R., Stubbins, A., Ritchie, J. D., Minor, E. C., Kieber, D. J., & Mopper, K. (2008). Absorption spectral slopes and slope ratios as indicators of molecular weight, source, and

photobleaching of chromophoric dissolved organic matter. *Limnology and oceanography*, 53(3), 955-969.

Holland, M. M., Bitz, C. M., Eby, M., & Weaver, A. J. (2001). The role of ice–ocean interactions in the variability of the North Atlantic thermohaline circulation. *Journal of Climate*, 14(5), 656-675.

Jensen, L. T. (2020). THE BIOGEOCHEMICAL CYCLING OF DISSOLVED AND COLLOIDAL TRACE METALS IN THE WESTERN ARCTIC OCEAN (Doctoral dissertation).

Jensen, L. T., Morton, P., Twining, B. S., Heller, M. I., Hatta, M., Measures, C. I., ... & Fitzsimmons, J. N. (2020). A comparison of marine Fe and Mn cycling: US GEOTRACES GN01 Western Arctic case study. *Geochimica et Cosmochimica Acta*.

Jensen, L. T., Wyatt, N. J., Twining, B. S., Rauschenberg, S., Landing, W. M., Sherrell, R. M., & Fitzsimmons, J. N. (2019). Biogeochemical cycling of dissolved zinc in the Western Arctic (Arctic GEOTRACES GN01). *Global Biogeochemical Cycles*, 33(3), 343-369.

Kaiser, K., R. Benner, and R. M. W. Amon (2017), The fate of terrigenous dissolved organic carbon on the Eurasian shelves and export to the North Atlantic, *J. Geophys. Res. Oceans*, 122, 4–22, doi:10.1002/2016JC012380

Kalinin, G.P., and I.A. Shiklomanov, (1974) Exploitation of the Earth's water resources, in *World Water Balance and Water Resources of the Earth* (in Russian), pp. 575-606, Gidrometeoizdat, St. Petersburg, Russia.

Kellerman, A. M., D. N. Kothawala, T. Dittmar, and L. J. Tranvik (2015), Persistence of dissolved organic matter in lakes related to its molecular characteristics, *Nat. Geosci.*, 8(6), 454–457, doi:10.1038/ngeo2440.

MacGilchrist, G. A., Garabato, A. N., Tsubouchi, T., Bacon, S., Torres-Valdés, S., & Azetsu-Scott, K. (2014). The Arctic Ocean carbon sink. *Deep Sea Research Part I: Oceanographic Research Papers*, 86, 39-55.

Makarewicz, A., Kowalczyk, P., Sagan, S., Granskog, M. A., Pavlov, A. K., Zdun, A., ... & Zabłocka, M. (2018). Characteristics of chromophoric and fluorescent dissolved organic matter in the Nordic Seas. *Ocean Science*, 14(3), 543-562.

Morel, F. M. M. (2008), The co-evolution of phytoplankton and trace element cycles in the oceans, *Geobiology*, 6(3), 318-324. Newton,

Morel, F. M., Milligan, A. J., & Saito, M. A. (2003). Marine bioinorganic chemistry: the role of trace metals in the oceanic cycles of major nutrients. *Treatise on geochemistry*, 6, 625.

Murphy, K. R., C. A. Stedmon, P. Wenig, and R. Bro (2014), OpenFluor– an online spectral library of auto-fluorescence by organic compounds in the environment, *Anal. Methods*, 6(3), 658–661, doi:10.1039/C3AY41935E.

Pokrovsky, O. S., Viers, J., Dupre, B., Chabaux, F., Gaillardet, J., Audry, S., ... & Shevchenko, V. P. (2012). Biogeochemistry of carbon, major and trace elements in watersheds of northern Eurasia drained to the Arctic Ocean: the change of fluxes, sources and mechanisms under the climate warming prospective. *Comptes Rendus Geoscience*, 344(11-12), 663-677.

Raven, J. A. (1990). Predictions of Mn and Fe use efficiencies of phototrophic growth as a function of light availability for growth and of C assimilation pathway. *New Phytologist*, 116(1), 1-18.

Rennermalm, A. K., Wood, E. F., Déry, S. J., Weaver, A. J., & Eby, M. (2006). Sensitivity of the thermohaline circulation to Arctic Ocean runoff. *Geophysical research letters*, 33(12).

Rijkenberg, Micha J A; Slagter, Hans A; Rutgers van der Loeff, Michiel M; van Ooijen, Jan C; Gerringa, Loes J A (2018): Dissolved Fe in the Deep and Upper Arctic Ocean With a Focus on Fe

Limitation in the Nansen Basin. *Frontiers in Marine Science*, 5, <https://doi.org/10.3389/fmars.2018.00088>

Schulz, K. G., Zondervan, I., Gerringa, L. J. A., Timmermans, K. R., Veldhuis, M. J. W., & Riebesell, U. (2004). Effect of trace metal availability on coccolithophorid calcification. *Nature*, 430(7000), 673-676.

Semeniuk, D. M., Bundy, R. M., Payne, C. D., Barbeau, K. A., & Maldonado, M. T. (2015). Acquisition of organically complexed copper by marine phytoplankton and bacteria in the northeast subarctic Pacific Ocean. *Marine Chemistry*, 173, 222-233.

Stedmon,

Stedmon, C. A., and R. Bro (2008), Characterizing dissolved organic matter fluorescence with parallel factor analysis: a tutorial, *Limnol. Oceanogr. Methods*, 6, 1–6.

Stedmon, C. A., S. Markager, and R. Bro (2003), Tracing dissolved organic matter in aquatic environments using a new approach to fluorescence spectroscopy, *Mar. Chem.*, 82, 239–254, doi:10.1016/S0304-4203(03)00072-0.

Stubbins, A., J.-F. Lapierre, M. Berggren, Y. T. Prairie, T. Dittmar, and P. A. del Giorgio (2014), What's in an EEM? Molecular Signatures Associated with Dissolved Organic Fluorescence in Boreal Canada, *Environ. Sci. Technol.*, 48(18), 10598–10606, doi:10.1021/es502086e.

Sugimura,

Sunda, W. G. (1989). Trace metal interactions with marine phytoplankton. *Biological Oceanography*, 6(5-6), 411-442.

Tremblay, J. É., Anderson, L. G., Matrai, P., Coupel, P., Bélanger, S., Michel, C., & Reigstad, M. (2015). Global and regional drivers of nutrient supply, primary production and CO₂ drawdown in the changing Arctic Ocean. *Progress in Oceanography*, 139, 171-196.

- Ulfso, A., Jones, E. M., Casacuberta, N., Korhonen, M., Rabe, B., Karcher, M., & van Heuven, S. M. A. C. (2018). Rapid changes in anthropogenic carbon storage and ocean acidification in the intermediate layers of the Eurasian Arctic Ocean: 1996–2015. *Global Biogeochemical Cycles*, 32, 1254–1275. <https://doi.org/10.1029/2017GB005738>
- Walker, S. A., Amon, R. M. W., Stedmon, C., Duan, S., & Louchouart, P. (2009). The use of PARAFAC modeling to trace terrestrial dissolved organic matter and fingerprint water masses in coastal Canadian Arctic surface waters. *Journal of Geophysical Research: Biogeosciences*, 114(G4).
- Walve, J., Gelting, J., & Ingri, J. (2014). Trace metals and nutrients in Baltic Sea cyanobacteria: Internal and external fractions and potential use in nitrogen fixation. *Marine Chemistry*, 158, 27-38.
- Williford, T., Amon, R. M. W., Benner, R., Kaiser, K., Bauch, D., Stedmon, C., ... & Klunder, M. B. (2021). Insights into the origins, molecular characteristics and distribution of iron-binding ligands in the Arctic Ocean. *Marine Chemistry*, 103936.
- Woosley, R. J., & Millero, F. J. (2020). Freshening of the western Arctic negates anthropogenic carbon uptake potential. *Limnology and Oceanography*, 65(8), 1834-1846.
- Wünsch, U. J., K. R. Murphy, and C. A. Stedmon (2015), Fluorescence Quantum Yields of Natural Organic Matter and Organic Compounds: Implications for the Fluorescence-based Interpretation of Organic Matter Composition,
- Wünsch, U. J., Murphy, K. R., & Stedmon, C. A. (2015). Fluorescence quantum yields of natural organic matter and organic compounds: Implications for the fluorescence-based interpretation of organic matter composition. *Frontiers in Marine Science*, 2, 98.

Zhang, R., Jensen, L. T., Fitzsimmons, J. N., Sherrell, R. M., & John, S. (2019). Dissolved cadmium and cadmium stable isotopes in the western Arctic Ocean. *Geochimica et Cosmochimica Acta*, 258, 258-273.

2. INSIGHTS INTO THE ORIGINS, MOLECULAR CHARACTERISTICS AND DISTRIBUTION OF IRON-BINDING LIGANDS IN THE ARCTIC OCEAN*1

2.1. Overview

Dissolved lignin phenols, chromophoric dissolved organic matter (DOM), and *in situ* fluorescence were determined in waters of the Laptev Sea and major Arctic basins, and they were compared with dissolved iron (dFe) distributions to elucidate the sources, molecular characteristics, and distributions of iron-binding ligands in the Arctic Ocean. In the Transpolar Drift region (TPD), concentrations of dFe were positively correlated with concentrations of lignin phenols and multiple optical proxies of DOM composition and source. Strong relationships between dFe and visible and ultraviolet wavelength fluorescent DOM indicated that vascular plant and algal-derived DOM contributed to the dFe-ligand pool. These observations are consistent with previous studies suggesting the association of dFe with humic terrigenous and marine organic ligands. The primary sources of iron-binding ligands appear to be the riverine discharge of terrigenous DOM, marine organic matter produced on the shelves, and degradation products of plankton-derived organic matter in the shelf sediments. A stronger relationship between dFe and visible wavelength CDOM fluorescence than with lignin phenols suggested the presence of multiple terrigenous ligands, such as aromatic tannins. The aromatic nature of these terrigenous ligands was indicated by a strong relationship between dFe and the absorption coefficient at 254 nm. A strong negative correlation between the p-hydroxyl to vanillyl lignin phenols ratio and dissolved iron concentrations indicated recently-discharged terrigenous DOM

* Manuscript published in Marine Chemistry (2021) 103936. Copyright © 2021 Elsevier B.V. or its licensors or contributors.
<https://doi.org/10.1016/j.marchem.2021.103936>

(tDOM) was an important source of iron-binding ligands. Given the strong relationships of marine and terrigenous DOM with dissolved iron, iron-binding functional groups appear to occur in diverse molecules of multiple sources. Examples of such iron-binding functional groups included catechols and carboxylates found in lignins and tannins of terrigenous origins and carboxyl-rich alicyclic molecules (CRAM) of terrigenous and marine origins. The observed dFe distributions in the Arctic Ocean could not be explained by the presence of a single ligand type, but rather by a potpourri of ligand molecules of varying concentrations and binding strengths. This molecular diversity of ligands and associated binding strengths ultimately controls the distribution and transport of dFe in the Arctic Ocean and beyond.

2.2. Introduction

As a relatively small basin (1.3% of the global ocean volume), the Arctic Ocean receives a disproportionately high fraction (11%) of global river discharge, giving dissolved organic matter (DOM) in the Arctic Ocean a strong terrigenous signal (Opsahl et al., 1999, Amon, 2004, Benner et al., 2005, Anderson and Amon, 2015; Kaiser et al., 2017a, 2017b). Fluvial discharge is an important source of both DOM and trace metals to the Arctic Ocean (Batchelli et al., 2010; Klunder et al., 2012a; Krachler et al., 2012; Whitby et al., 2020). Recent studies demonstrate that peat-derived, lignin-containing humic substances are not only efficient in mobilizing iron from the soils due to the functional groups reacting with ferrous oxides, but they are also carriers of riverine iron to the open ocean (Krachler et al., 2012). This is consistent with elevated concentrations of iron and humic substances serving as iron-binding ligands, as recently reported for the Transpolar Drift (TPD) region (Slagter et al., 2017). A prominent role for humic substances as iron-binding ligands has also been suggested for the halocline layer in the Canada Basin, where Nakayama et al. (2011) detected elevated dissolved iron concentrations along with

the optical fingerprints of humic substances. Some Arctic shelf seas, like the Barents and the Kara Seas, were characterized by lower dissolved iron concentrations, but elevated iron concentrations were found in the Laptev Sea, particularly in bottom waters (Klunder et al., 2011).

Iron is an essential nutrient for marine organisms, but it has poor solubility in seawater, and acquiring iron in oxic waters is challenging for most marine microorganisms. The biogeochemistry of DOM and trace metals is intrinsically linked due to organic ligands that retain metals such as iron in solution, thereby facilitating transport by pre-venting iron scavenging and influencing iron bioavailability (Rijkenberg et al., 2018; Hassler et al., 2011; Laglera et al., 2019). Siderophores, carbohydrates, and humic substances are viewed as potential iron-binding ligands in the ocean (Benner, 2011a, 2011b; Hassler et al., 2011; Laglera et al., 2019). Siderophores are strong ligands synthesized by marine bacteria to specifically bind iron, but they are found in very low concentrations in natural waters (Mawji et al., 2008). Other organic molecules contain functional groups similar to those found in siderophores. Examples of such functional groups are catechols and carboxylates that are present in naturally occurring biochemicals found in dissolved humic substances, and they can form iron-binding complexes of varying binding strengths and varying resistance to photodegradation (Barbeau et al., 2003). Catecholates are prone to photooxidation in the free form, but are more resistant when complexed to iron, while α -hydroxy carboxylate groups are stable as the free acid, but prone to photooxidation when coordinated to iron (Barbeau et al., 2001, 2003). Carboxyl-rich alicyclic molecules (CRAM) are another naturally occurring group of molecules that are potentially important ligands in the ocean iron cycle (Hertkorn et al., 2006; Hassler et al., 2020; Whitby et al., 2020).

In this paper, we explore how a diverse group of molecules in DOM can serve as binding sites for iron complexation in different water masses of the Arctic Ocean, and how they affect dissolved iron distributions and transport. Lignin phenols are well-established biomarkers for tracing terrigenous DOM in the ocean (Opsahl and Benner, 1997; Opsahl et al., 1999; Benner et al., 2005; Kaiser et al., 2017a, 2017b), and we use these biomarkers along with the measurements of the optical properties of DOM to investigate the relationships among potential organic ligands and dissolved iron concentrations in specific water masses. Studying the Arctic Ocean, which is heavily influenced by river discharge and shelf-basin interactions, can provide insights into the origins, binding strengths, and distributions of organic ligands from various sources.

2.3. Methods and data

2.3.1. Sampling

Samples were collected during the Ark-XXII/2 expedition on board the research ice breaker Polarstern (July-October 2007). *In situ* CDOM fluorescence, water samples, and hydrographic data (conductivity, temperature, and depth measured using two SeaBird CTDs (Wisotzki, 2008; Schauer, 2008) were collected from several sections across the Nansen Basin, Amundsen Basin, and Makarov Basin (Fig. 2.1). The western portion of section A (A1) starts on the Barents Sea shelf (stations 227–260) and the eastern portion (A2) starts in the St. Anna Trough (stations 261–276), both crossing the Nansen Basin. This section is dominated by the inflowing Atlantic water. Section B stretches from the Kara Sea shelf break across the Nansen Basin, the Amundsen Basin, and the Lomonosov Ridge into the Makarov Basin and the northern Canada Basin (stations 279–342). Section B provides observations of the TPD region. Section C

starts on the Laptev Sea shelf and follows the Gakkel Ridge which separates the Nansen and Amundsen Basins, providing an opportunity to investigate shelf processes (stations 346–411).

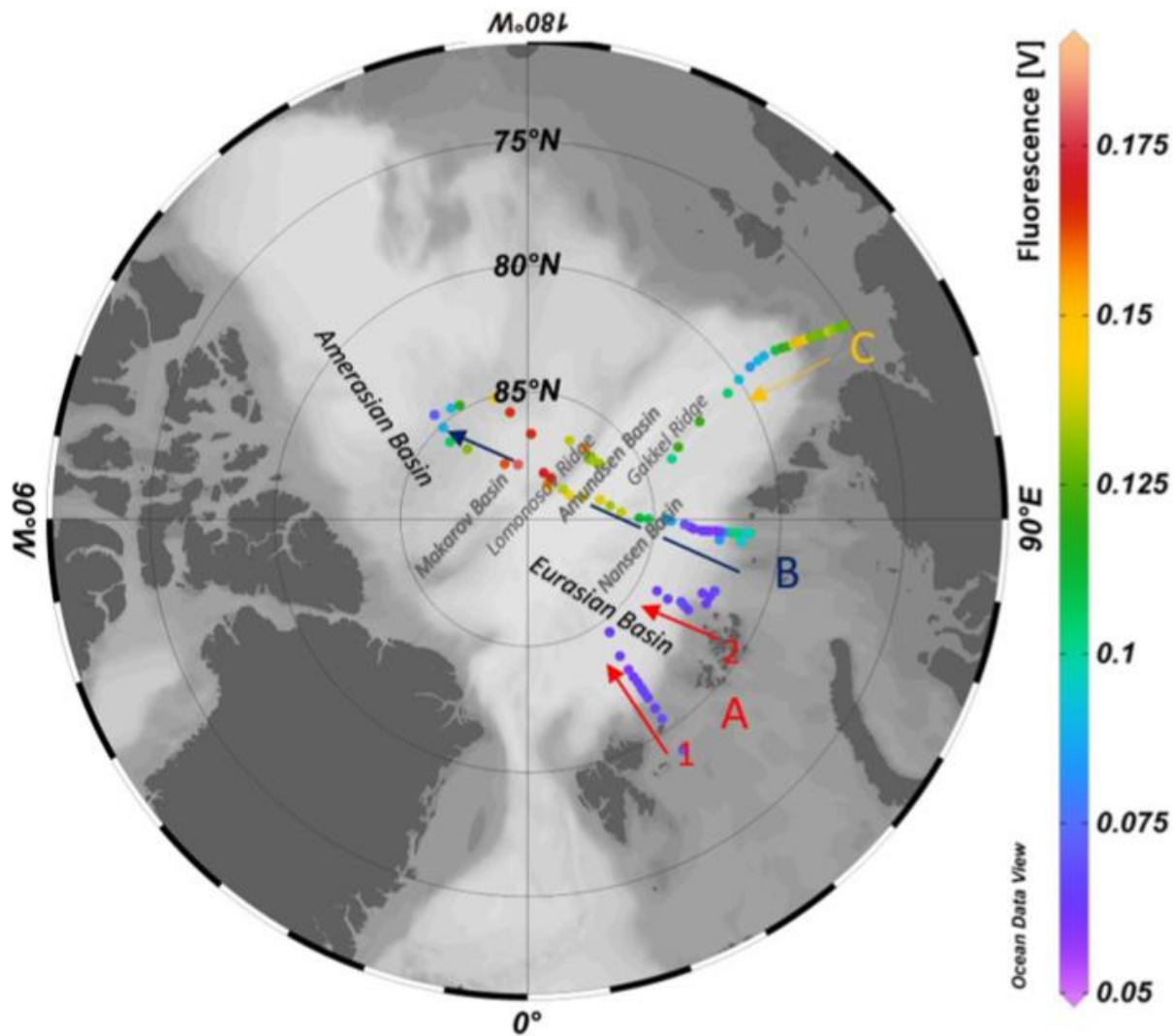


Fig. 2.1. The Ark-XXII/2 cruise track and sampling stations. The positions of sections A, B, and C are shown with arrows. In situ fluorescence (Dr. Haardt sensor) in surface waters is shown in color.

2.3.2. Dissolved organic carbon and optical properties

Samples for dissolved organic carbon (DOC) analysis and optical properties were filtered through pre-combusted 0.7 mm GF/F filters (Whatman) and sealed in pre-combusted glass ampoules on board. The samples for DOC and optics were analyzed within one year of

collection. For the DOC analysis, the samples were frozen at -20 °C in glass ampoules until analysis at the home laboratory. DOC concentrations were determined using a modified MQ-1001 TOC Analyzer or a Shimadzu TOC-V CSH/CSN. The calibration curve was created daily using potassium hydrogen phthalate, and the accuracy was ensured by measuring deep-sea standards (Hansell, 2005). DOC concentrations were calculated using the average of five replicate sample injections, followed by a Milli-Q blank subtraction.

In situ CDOM fluorescence was measured with a backscatter fluorometer (excitation 350–460 nm/emission 550 nm HW 40 nm; Dr. Haardt Optik Mikroelektronik). Absorbance was measured from 240 to 800 nm on a Shimadzu UV-1800 dual-beam ultraviolet-visible spectrophotometer using a 5 cm quartz cuvette and pure water as a blank. The raw absorbance was baseline corrected by subtracting an offset- exponential fit of the absorbance spectrum over the range from 300 nm to 650 nm (Stedmon et al., 2000). The corrected absorbance (A_λ) was converted to Napierian absorption coefficients (a_λ) for each wavelength, λ , with the following formula:

$$a_\lambda = \ln(10) \frac{A_\lambda}{L}, \quad (1)$$

where L is the length of the cuvette in meters. Here we use the absorption at 254 (a_{254}) and 350 nm (a_{350}) as a proxy for CDOM concentration.

The spectral slope between 275 nm and 295 nm ($S_{275-295}$) can be used as a tracer of the percent terrigenous dissolved organic carbon in river-influenced ocean margins (Fichot and Benner, 2012) and an indicator of photooxidation and photobleaching (Helms et al., 2008). $S_{275-295}$ was computed using a linear fit of the log-linearized a_λ spectrum over the spectral range between 275 and 295 nm and are reported here with units of nm^{-1} .

Spectral organic matter fluorescence was measured with a Photon Technologies International spectrofluorometer (Quanta Master-4 SE) using a 1 cm quartz cuvette with excitation and emission slit widths of 5 nm. Excitation-emission matrix scans (EEMs) for each sample covering emission from 300 to 600 nm (2 nm increment) and excitation wavelengths ranging from 240 to 450 nm (5 nm increment). Daily pure water (Milli-Q) blanks were obtained and subtracted to remove water scattering peaks. Measured data were spectrally corrected for instrument bias and subsequently, Raman calibrated using the pure water blanks. The fluorescence was characterized using Parallel Factor (PARAFAC) analysis on normalized EEMs using the drEEM toolbox (Murphy et al., 2013) and the normalization was reversed after the model fitting so that the fluorescence intensities of each component are in Raman Units.

Four outlier samples were identified to disproportionally bias the PARAFAC modeling and therefore removed. The final Ark-XXII/2 dataset consisted of 354 EEMs and a five-component model was found optimal based on spectral loadings, residual examination, and split-half validation using a convergence criterion of $1e^{-8}$ (Fig. 2.2). The components were labeled based on their emission maxima: C₄₂₈, C₄₈₂, C₄₀₈, C₃₁₅, and C₃₀₂.

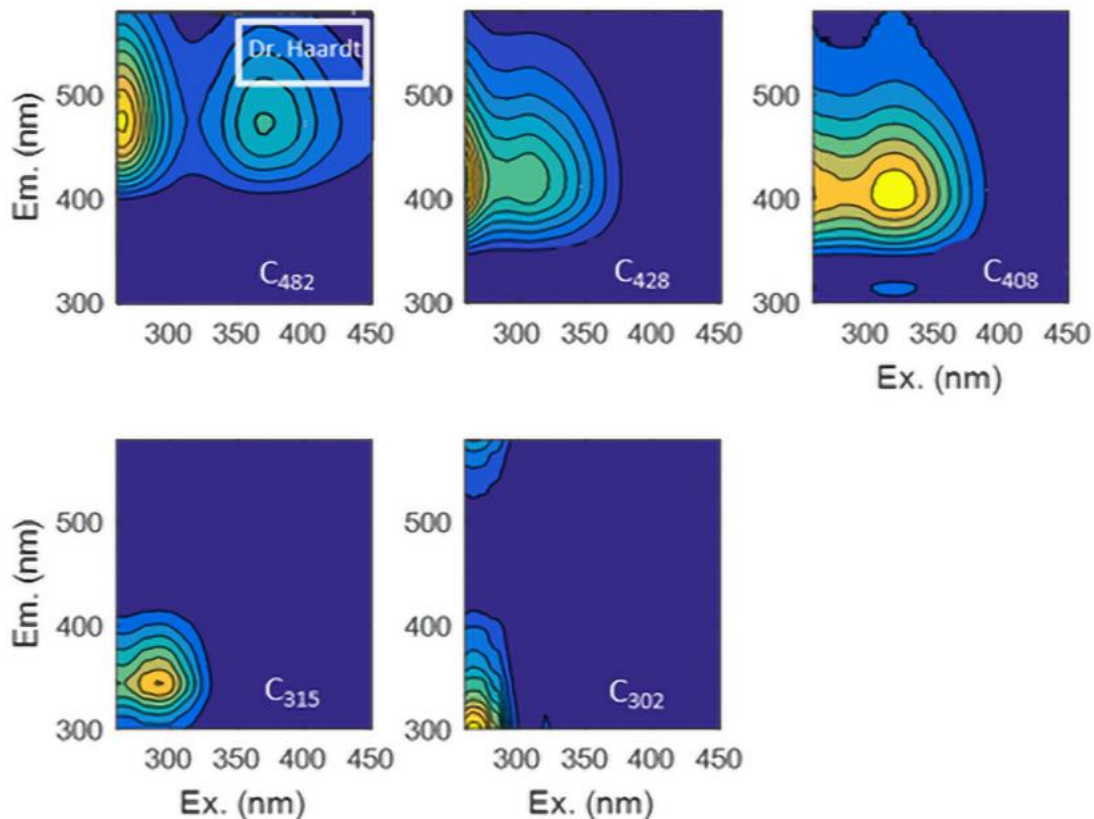


Fig. 2.2. The fluorescence properties of five fluorescent components identified by PARAFAC modeling. The white square on the second EEM (C₄₈₂) shows the range of Haardt fluorometer measurements. Note: The secondary emission peak of component 5 (C₃₀₂) is a second-order peak (at twice the primary emission peak) and represents an artifact of the instrument design.

Table 2.1. The optical and chemical parameters reported in this study.

Parameter	Description
CDOM	In situ fluorescence from Dr. Haardt fluorometer. Units: volts
a_{254}, a_{350}	Absorption coefficients at 254 and 350 nm are commonly used proxies for CDOM abundance and origin. Units: m^{-1}
TDLP9	Sum concentration of 9 lignin phenols based on LC/MS. Units: nmol/L
$S_{275-295}$	Exponential spectral absorption slope. Proxies for CDOM character (origin and photooxidation). Units nm^{-1}
SUVA	The specific UV absorbance at 254 nm. Decadic absorption at 254 normalized to the DOC concentration. Surrogate for aromaticity Units: $m^2 g^{-1}C$
S/V	Proxy for taxonomic source: high S/V - angiosperm, low S/V – gymnosperms. No units
P/V	Increase with DOM age, increase with sun exposure, an indicator for bryophyte vegetation in peatlands, Ob river estuary, sensitive to changes in river flow. No units
dFe	Dissolved iron concentration (Klunder et al., 2012a, 2012b). Units: nmol/L

2.3.3. Lignin phenol analysis

For lignin analysis 10–15 L seawater samples were filtered using a 0.2 mm pore size NuclePore filter cartridge, acidified to pH 2.5 using concentrated HCl (reagent grade), followed by solid-phase extraction using C18 cartridges (Varian MegaBond 10 g, 60 mL, Louchouart et al., 2000). Cartridges were stored at -20 °C until extracted with 30 mL of methanol at 4 mL min⁻¹ in the lab. The extracts were preserved at -20 °C until lignin analysis in the home laboratory. Lignin phenol analysis was performed following the method of Yan and Kaiser (2018a, 2018b). It allows the quantification of dissolved lignin phenols in small volumes of seawater using alkaline CuSO₄ at 150 °C at 5–100 µg of sample organic carbon content. Ultra-high performance liquid chromatography with mass spectrometry detection in dynamic Multiple Reaction Monitoring mode and isotopically-labeled surrogate standards were used for the detection and quantification of monomeric lignin phenols.

The sum of concentrations of nine lignin phenols (TDLP9) is reported in this study: p-hydroxybenzaldehyde (PAL), p-hydroxyacetophenone (PON), p-hydroxybenzoic acid (PAD), vanillin (VAL), acetovanillone (VON), vanillic acid (VAD), syringaldehyde (SAL), acetosyringone (SON), syringic acid (SAD). The ratios of syringyl (SAD, SAL, SON) to vanillyl (VAL +VAD +VON) phenols (S/V) and p-hydroxyl (PAL +PAD +PON) to vanillyl phenols (P/V), are commonly used as a source or diagenetic indicators (Amon et al., 2012). In Arctic rivers, these lignin monomer ratios exhibit spatial and seasonal variability, but in general S/V ratios are higher in the Yukon, Ob, and Kolyma (0.4–0.6), relative to the Mackenzie, Lena, and Yenisei (<0.3) (Amon et al., 2012). The ratio of P/V is also used as diagenetic indicators, as they increase with increasing DOC-age (Amon et al., 2012). In this study, we use the new method for lignin phenols analysis (Yan and Kaiser, 2018a, 2018b). The phenols concentrations for the marine samples are comparable between the new and the old methods, although the new method results in lower acid/aldehyde ratios (Yan and Kaiser, 2018b). The limit of detection ranges from 10 to 87 femtomoles for individual lignin phenols (Yan and Kaiser, 2018b).

2.3.4. Additional data

The dissolved iron (dFe) data used in this study were obtained from (Klunder et al., 2012a, 2012b; also available in Schlitzer et al., 2018), we limited it to the upper 500 m. The samples for iron analysis were collected from the GO-FLO bottles in a class 100 clean room environment and filtered through a 0.2 mm filter cartridge (Sartrobran-300, Sartorius) under nitrogen pressure (1.5 atm.) (Klunder et al., 2012a, 2012b; the GEOTRACES intermediate data product 2017) (Table 2.1).

2.4. Results

Surface water *in situ* CDOM fluorescence reflects the general horizontal circulation patterns in the Arctic Ocean (Fig. 2.1). The Nansen Basin is influenced by AW inflow and has the lowest *in situ* fluorescence, which can be observed in sections A and B. The CDOM-enriched fluvial discharge is partially observed on the Laptev Sea shelf (section C), as the river influenced coastal waters travel towards the east, contained on the shelves by the Atlantic water boundary current. These high CDOM coastal waters are entrained into the TPD east of section C, in the East Siberian Sea or the Chukchi Sea (Alkire et al., 2017) and flow across the Central Arctic Ocean as part of the TPD. The TPD is characterized by highly elevated *in situ* CDOM fluorescence in the central Arctic Ocean (higher CDOM than Laptev Sea surface waters), covering most of the Makarov Basin (Fig. 2.1). This circulation pattern is seen in the oceanographic cross sections (Fig. 2.3). The high salinity (>34.7), low CDOM, North Atlantic inflow to the Eurasian Basin consists of two main branches entering the Arctic Ocean through the eastern Fram Strait and the Barents Sea (e.g. Rudels, 2001). Waters coming from the Atlantic are characterized by low levels of CDOM absorbance and fluorescence and low terrigenous biomarker concentrations (TDLP9; Fig. 2.3). DOC concentrations were also lowest in these Atlantic influenced sections, particularly in the Nansen Basin (~50 $\mu\text{mol/L}$). Dissolved iron concentrations are slightly elevated near the bottom of the Franz Josef Victoria Trough seen in section A1 (~3 nmol/L , Fig. 2.3s), but were generally lower than in sections B and C which are influenced by river discharge. The locally elevated dFe concentrations near the bottom of section A1 likely originate from sediments since low TDLP9 concentrations exclude a riverine source (Fig. 2.3). These elevated dFe levels were concurrent with high concentrations of dissolved manganese which were attributed to benthic efflux in a previous study (Middag et al., 2011) and confirms sediment influence.

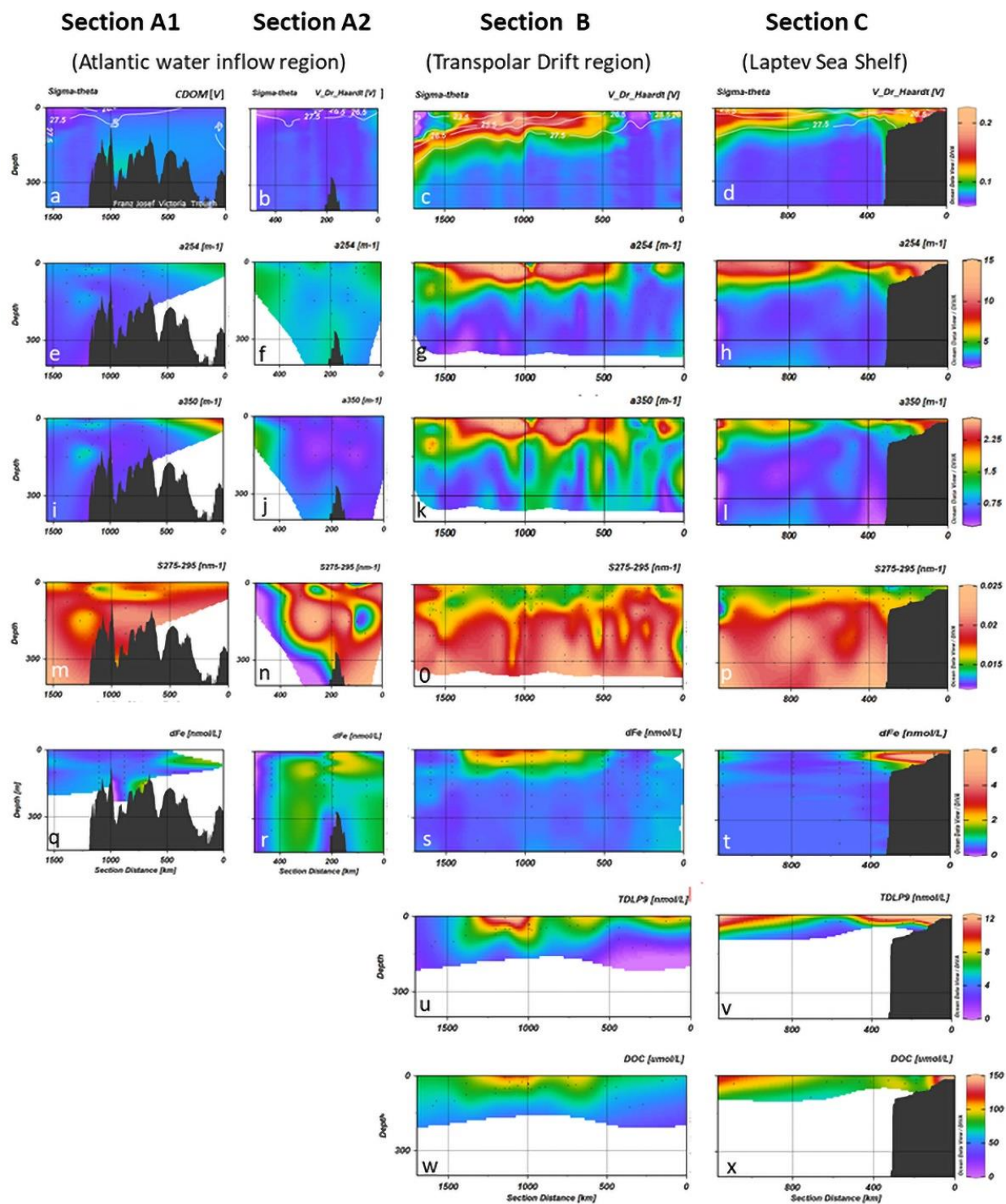


Fig. 2.3. The in situ CDOM fluorescence (a, b, c, d), a₂₅₄ absorption (e, f, g, h), a₃₅₀ absorption (i, j, k, l), S₂₇₅₋₂₉₅ (m, n, o, p), dissolved iron (dFe) concentrations (q, r, s, t), TDLP9 concentrations (u, v), and dissolved organic carbon (DOC) concentrations (w, x) for the Ark-XXII/2 transects. White contours in the top panels represent isopycnals.

Section B, which stretches from the Kara Sea shelf break (82°N), crosses the Nansen and Amundsen Basins, the Lomonosov Ridge and Makarov Basin and ends over the Alpha Ridge in the Canada Basin (Fig. 2.1), is fundamentally different from section A. Section B can be characterized by slightly elevated *in situ* CDOM fluorescence in surface waters along the Kara Sea shelf break, low CDOM in the Nansen Basin, but very high CDOM concentrations within the TPD (Fig. 2.3). The high CDOM fluorescence in the TPD is mirrored by elevated concentrations of several tDOM indicators, including TDLP9 concentrations (Fig. 2.3u), absorption coefficients a_{254} and a_{350} (Fig. 2.3g, k), lower $S_{275-295}$ (Fig. 2.3o), elevated PARAFAC component C₄₈₂ (Fig. 2.4), and DOC concentrations (Fig. 2.3w). The TPD feature is about 1000 km wide, spanning from the Gakkel Ridge to the Alpha Ridge based on *in situ* CDOM fluorescence. The dissolved iron concentrations in section B are also highly elevated in surface waters of the TPD (Fig. 2.3s) and closely resemble the distribution of CDOM and TDLP9 in the central Arctic Ocean.

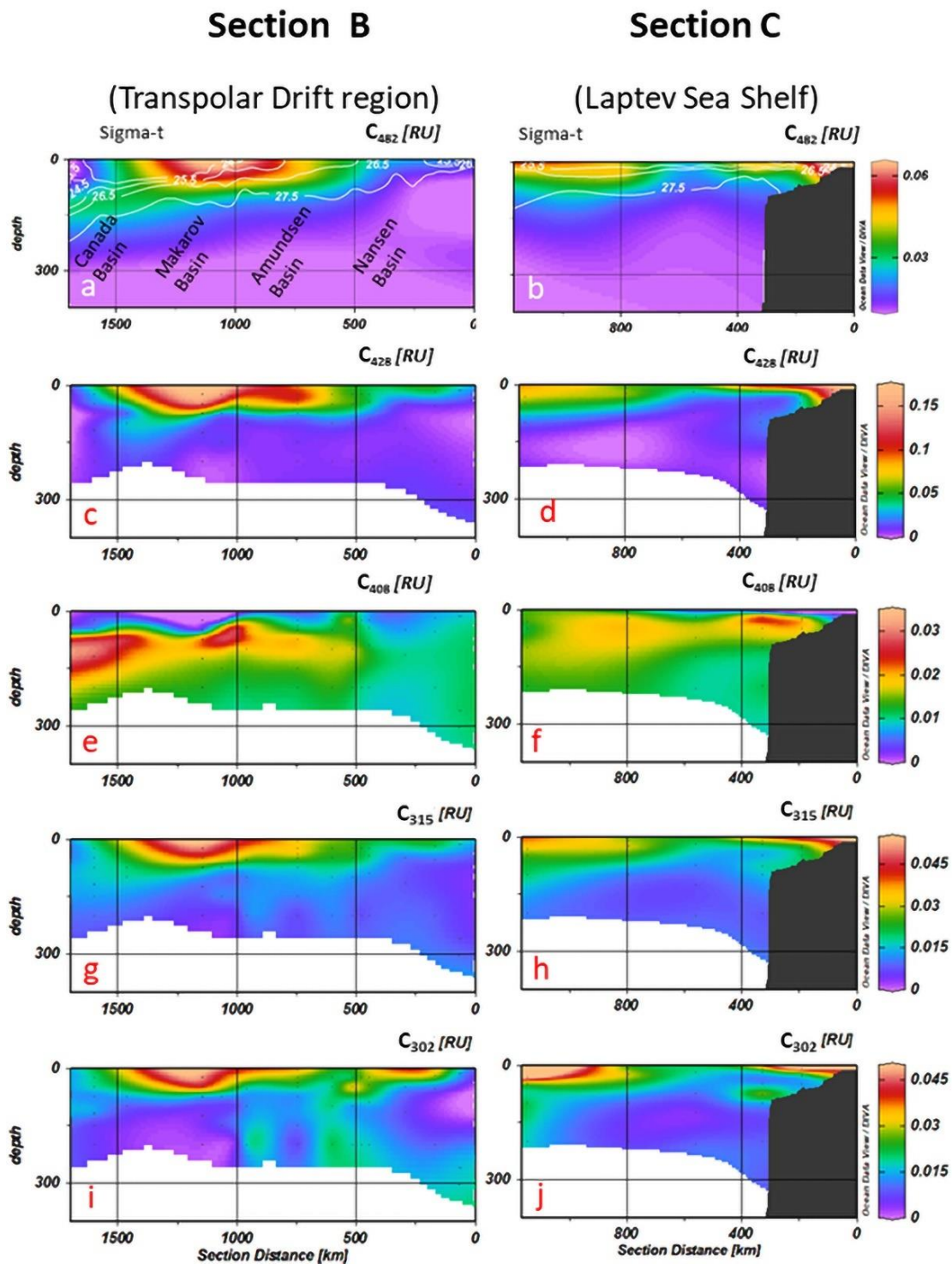


Fig. 2.4. The five fluorescent components identified by the PARAFAC model for the Ark-XXII/2 transects (left to right, West to East) B (a, c, e, g, i), and C (b, d, f, h, j) in the upper 400 m of the water column. White contours in the top panels represent isopycnals.

The coastal section C begins on the Laptev Sea shelf (75°N) and follows the Gakkel Ridge into the Amundsen Basin (Fig. 2.1). CDOM is elevated in shelf station surface waters but not as much as in the TPD (Fig. 2.1). However, subsurface waters on the inner shelf have elevated levels of *in situ* CDOM fluorescence relative to surface waters (Stations 409–411), and they exceed concentrations seen in the TPD. The elevated CDOM fluorescence close to the bottom of the Laptev Sea shelf, at relatively high potential density comparing to the surface water, represents a unique CDOM feature in this data set (Fig. 2.3d). This feature was also reflected in high a_{254} and a_{350} values (Fig. 2.3h and i), low $S_{275-295}$ values (Fig. 2.3p), elevated PARAFAC components C_{482} , C_{428} , C_{315} , C_{302} (Fig. 2.4), and high TDLP9 concentrations (Fig. 2.3v). The concentration of dFe on the bottom of the Laptev Sea shelf exceeds 10 nmol/L, however, the peak does not extend to the shelf break (Fig. 2.3t). Shelf water concentrations of dFe were higher than in the TPD and generally coincided with *in situ* CDOM fluorescence and UV absorption at 254 nm (Fig. 2.3).

Table 2.2. Pearson correlation matrix of TDLP9 concentrations and the parameters salinity, DOC, *in situ* CDOM fluorescence, absorption coefficients a_{254} and a_{350} , SUVA, $S_{275-295}$, and PARAFAC components.

	Pearson correlation
Salinity	-0.75*
DOC	0.76*
CDOM	0.77*
a_{254}	0.82*
a_{350}	0.81*
SUVA	0.69*
$S_{275-295}$	-0.41
C_{482}	0.82*
C_{428}	0.77*
C_{408}	-0.07
C_{315}	0.5*
C_{302}	0.46*

* $p < <0.01$.

The PARAFAC component C_{482} was found in several studies, and it is usually described as a terrigenous fluorophore in the Arctic Ocean (Walker et al., 2009; Chen et al., 2018; Gonçalves-Araujo et al., 2015, 2016). As such, the C_{482} component had the strongest correlation with *in situ* CDOM fluorescence and with TDLP9 concentrations. The maximum C_{482} fluorescence was observed in the TPD region, shown in section B (Fig. 2.4a), and in the Laptev Sea shelf bottom waters (Fig. 2.4b). Most of the PARAFAC components, except C_{408} , have a negative relationship with salinity. The distribution of C_{408} in the TPD region is different from all other components, showing a pronounced fluorescence signal in the upper halocline (isopycnals between 25.7 and 26.8 kg/m^3 ; Fig. 2.4, top panel), at the depth of about 80 m on the Canadian side of section B (Fig. 2.4e). Relative to C_{482} and C_{428} , protein-like components C_{315} and C_{302} are more evenly distributed through the euphotic zone of section B (Fig. 2.4a, c), however, they also show elevated levels on the shallow Laptev shelf and within the surface of the TPD region (Fig. 2.4b, d).

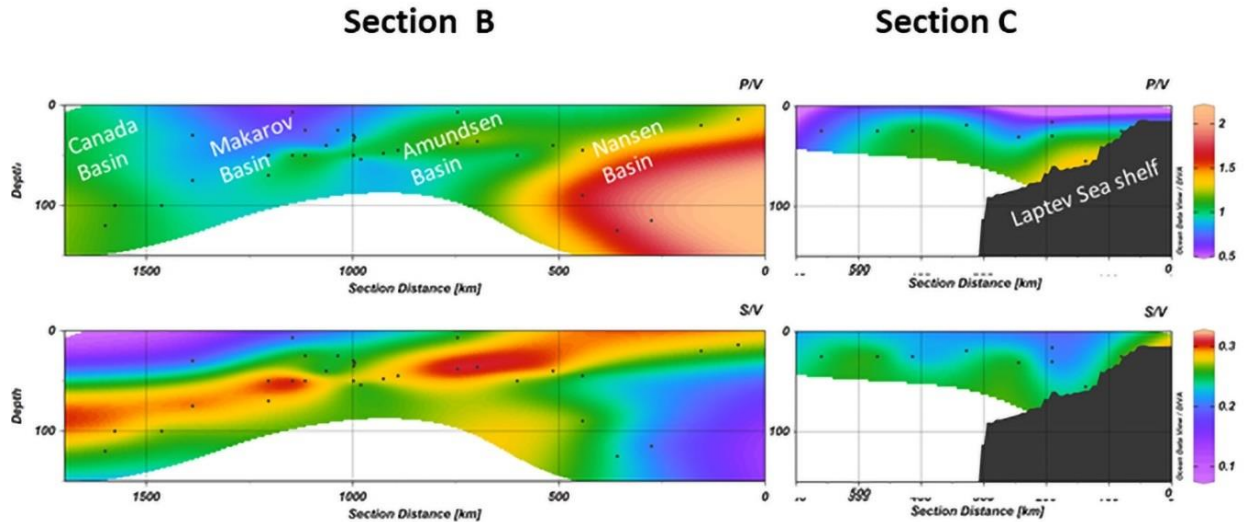


Fig. 2.5. Top to bottom panels: top 150 m of the p-hydroxy (P) and vanillyls (V) phenols ratio (P/V), syringyls (S) and V ratio (S/V) for the Ark-XXII/2 transect B (left to right, North to South, left column) and C (right column).

The distribution of TDLP9 is generally similar to *in situ* CDOM fluorescence (Fig. 2.3) and DOC concentrations, with the highest values in the TPD region and in Laptev shelf bottom waters (inner shelf in section C). Elevated concentrations of TDLP9 were also observed in the halocline of the Makarov and Amundsen basins and in continental shelf waters. However, the statistical relationship between lignin and *in situ* CDOM fluorescence was not as strong as for other proxies ($R = 0.77$, $p < 0.00001$; Table 2.2) or as previously observed in the East Greenland Current ($R = 0.95$; Amon et al., 2003). Among all the tDOM proxies, the strongest correlation to TDLP9 was found with PARAFAC component C_{482} , demonstrating the usefulness of C_{482} for indicating a terrigenous signal in the Arctic Ocean ($R = 0.82$, $p < 0.00001$; Table 2.2). Another, equally useful, optical proxy for tDOM was the absorption coefficient a_{254} , which is commonly used as a tracer of aromaticity and humic substances in freshwater systems (Weishaar et al., 2003).

In terms of TDLP9 composition, the Nansen Basin has the highest p- hydroxyl to vanillyl phenol (P/V) ratios (>1.5) due to the major influence of AW, which has the highest P/V ratio (~ 1.9) among Arctic water masses (Kaiser et al., 2017a, 2017b). The P/V values are slightly elevated in deeper water on the Laptev Sea shelf (>50 m, $P/V = 1.35$), which likely indicates the efflux of degraded terrigenous DOM from sediments (Fig. 2.5). In contrast, the Makarov Basin surface layer has the lowest P/V and syringyl to vanillyl phenol (S/V) ratios (<1), most likely due to the influence of river discharge originating mostly from the Yenisei and Lena rivers, which have low P/V and S/V ratios (Amon et al., 2012; Kaiser et al., 2017a, 2017b). The S/V ratios are also elevated in the upper halocline (0.27–0.31) and the Laptev Sea shelf (<20 m), which could indicate the influence of sea ice formation or a mix of tDOM from different Siberian rivers with varying S/V ratios (Amon et al., 2012).

The strongest correlations to the distribution of dFe were found for a_{254} ($R = 0.87$, $p < 0.00001$) and a_{350} ($R = 0.86$, $p < 0.00001$; Table 2.3). Strong positive correlations of dFe were also found to TDLP9 ($R = 0.74$, $p < 0.00001$), all indicating that tDOM likely plays an important role in delivering dissolved iron to the central Arctic Ocean. All CDOM fluorescence components but one (C_{408}), were positively correlated with dissolved iron (Table 2.3).

Table 2.3. Pearson correlation matrix between dFe and salinity, CDOM, absorption coefficients a_{254} and a_{350} , spectral slopes, SUVA, DOC, TDLP9, and PARAFAC components.

	Pearson correlation
Salinity	-0.72*
DOC	0.57*
TDLP9	0.74*
S/V	-0.49*
P/V	-0.61*
CDOM	0.76*
a_{254}	0.87*
a_{350}	0.86*
$S_{275-295}$	-0.27
SUVA	0.81*
C_{482}	0.78*
C_{428}	0.82*
C_{408}	-0.23
C_{315}	0.82*
C_{302}	0.56*

* $p < 0.01$.

Table 2.4. Spectral characteristics of the five components identified by PARAFAC and their comparison to previously identified components.

Ark-XXII/ 22007	Description	Excitation max/ Emission max, nm	Similar components found in OpenFluor database	References
C ₄₈₂	Humic-like, terrigenous	<240, 385/ 482	BERC3, Arctic Seawater C4, Arctic outflow C1, Lena2013 C2, Partners C2-4	Walker et al., 2009; Chen et al., 2018; Gonçalves- Araujo et al., 2015 Walker et al., 2013
C ₄₂₈	Humic-like	320(250)/ 428	BERC1, Lena2013 C1, Partners C1	Walker et al., 2009; Gonçalves- Araujo et al., 2015 Walker et al., 2013
C ₄₀₈	Humic-like	<240, 315/ 408	Arctic Seawater C2	Chen et al., 2018
C ₃₁₅	Tryptophan- like	295/315	Arctic Seawater C1, Partners C5	Chen et al., 2018; Walker et al., 2013
C ₃₀₂	Tyrosine-like, marine	<240, 275/ 302	BERC5, Arctic outflow C3	Walker et al., 2009 Gonçalves- Araujo et al., 2016

2.5. Discussion

2.5.1. Origin of PARAFAC components

The five fluorescence components identified by the PARAFAC model (C_{482} , C_{428} , C_{408} , C_{315} , C_{302}) have been described in previous studies (Table 2.4). The broad spectra of the visible wavelength (>400 nm) fluorescent components are often referred to as humic-like due to the dominance of this signal in hydrophobic organic matter extracts. The broad character is likely indicative of its complex chemical structure (Wünsch et al., 2015). The composition of visible wavelength fluorescence varies depending on DOM source (e.g. terrestrial vs aquatic) and exposure to degradation, with longer wavelength fluorescence being removed fastest (Murphy et al., 2018). The narrow UV wavelength fluorescence of C_{315} and C_{302} is similar to that of simple aromatic compounds such as the amino acids tryptophan and tyrosine (free and combined in proteins), and benzoic acid derivatives (Wünsch et al., 2016). This is traditionally referred to as protein-like fluorescence and is present in the hydrophobic and hydrophilic fractions of DOM. These signals represent bioavailable DOM that is often absent in deep waters and far from DOM sources.

Using the OpenFluor database (Murphy et al., 2014), the spectral characteristics of each component can be matched with those from several previous Arctic studies (Table 2.4). The distributions of the components identified can be largely explained by the major hydrographic features of the Arctic Ocean.

Of all PARAFAC components, C_{482} was correlated strongest with lignin phenol concentrations (TDLP9) indicating a terrigenous source. Its spectral characteristics were equivalent to that found in river water and plumes of several major Arctic rivers (Table 2.4; Walker et al., 2009; Gonçalves-Araujo et al., 2015; Walker et al., 2013). C_{482} was prevalent in the upper 60 m of the TPD, indicating a major contribution of river discharge to this current system crossing the Arctic Ocean, as suggested previously (Opsahl et al., 1999; Benner et al.,

2005; Charette et al., 2020). Another visible wavelength peak, C₄₂₈, had the highest fluorescence intensity of all components, accounting for half of the total fluorescence signal in the present as well as previous studies. It has a weaker correlation with lignin phenols than C₄₈₂ but was more strongly correlated with dissolved iron concentrations than the other fluorescent components. C₄₂₈ has also been identified in Arctic rivers (Table 2.4; Walker et al., 2009; Gonçalves-Araujo et al., 2015; Walker et al., 2013).

The C₄₀₈ component is most pronounced in the upper halocline extending into the Canada Basin, but it is also elevated near the Laptev Sea shelf break and below the terrigenous signal in the TPD (Fig. 2.4e, f). A similar fluorescence signal has been observed spreading from the Chukchi Sea shelf to the core of the upper halocline in the Canada Basin (Chen et al., 2018). This signal likely originates from organic matter decomposition in surface sediments on the shelf. The pronounced fluorescence signal far away from its apparent source on the Chukchi shelf indicates the intensity of the source (extensive productive shelf area) and its refractory nature. The fluorescence intensity of this component was the lowest among all PARAFAC components which likely also reflects its large distance from the source region.

C₃₁₅ is similar to the tryptophan-like component described in Chen et al. (2018) and shows elevated concentrations on the shelf as well as in the TPD. The primary sources of this component are thought to be marine organic matter, including the decomposition of plankton-derived organic matter in shelf sediments. However, tannins and lignins, common constituents of terrestrial plants, are known for their protein-binding capability and could contribute to the fluorescence signature with an emission maximum near 315 nm (Maie et al., 2008). This would be consistent with the observed pattern of C₃₁₅ on the shelf and within the TPD. Previous studies demonstrated that fluorescence at these wavelengths can be highly correlated with lignin (Hernes

et al., 2009; Osburn et al., 2016), but our data do not reflect such a relationship. A component with a similar fluorescence signature was found in Arctic rivers and appeared to be related to microbial activity (Walker et al., 2013). Similar to C₃₁₅, component C₃₀₂ is thought to be linked to phytoplankton-derived organic matter and is correlated with amino-acid concentrations (Gonçalves-Araujo et al., 2016; Yamashita et al., 2020). This component is analogous to BERC5 (Walker et al., 2009) and Arctic outflow C3 (Gonçalves-Araujo et al., 2016).

2.5.2. Distribution of biomarkers, optical properties and dissolved iron

The concentrations of dissolved iron are correlated with several indicators of organic matter sources based on optical properties and lignin phenols concentrations. The strongest relationships with dissolved iron concentrations were observed with absorption coefficients a_{254} and a_{350} , followed by the PARAFAC components C₄₂₈ and C₃₁₅, SUVA, C₄₈₂, and lignin phenols. The strong correlations of marine and terrigenous indicators (C₃₁₅, C₄₂₈, C₄₈₂, TDLP9) with dissolved iron concentrations indicates that marine and terrigenous humic substances contribute to iron complexation. These observations are consistent with previous studies suggesting the association of dissolved iron with humic-like terrigenous organic ligands, particularly in the TPD, and humic-like marine ligands (Nakayama et al., 2011; Slagter et al., 2017, 2019; Sukekava et al., 2018; Laglera et al., 2019; Charette et al., 2020). The correlation between dissolved iron concentrations and C₄₈₂ was stronger than that with lignin phenols, possibly indicating the presence of other fluorescent terrigenous ligands, such as tannins, in the Eurasian Basin. The strong negative correlation between P/V of lignin phenols and dissolved iron concentrations indicates recently discharged tDOM is an important source of iron-binding ligands in the study area. These observations are consistent with the strong correlation between

lignin phenol concentrations and the natural radiocarbon content of DOC in the Arctic Ocean, indicating terrigenous DOC is mostly young in polar surface waters (Benner et al., 2004).

The observed correlations between dissolved iron concentrations and optical proxies of terrigenous and marine organic matter suggest a ubiquitous distribution of specific types of binding sites in dissolved organic molecules across the land-ocean aquatic continuum. Iron is a biologically vital trace metal that has very low solubility in oxygenated seawater. Iron solubility depends on complexation with organic molecules referred to as ligands, but little is known about the origins and molecular properties of ligands in natural waters. Ligands are categorized by their binding strength using a competitive ligand exchange—adsorptive cathodic stripping voltammetry technique (Rue and Bruland, 1995; Gledhill and Buck, 2012; Slagter et al., 2019). The number of iron-binding sites and their spatial arrangement are important features determining the binding strength of ligands, and it can range from monodentate to hexadentate complexation. Molecular size is another important characteristic influencing the binding strength of ligands, with higher-molecular-weight molecules typically having a greater number of binding sites, more flexible molecular geometries, and greater binding strength. Typically, one or two ligand types are reported, L_1 ($\log K'_{Fe'L} > 11$) is the stronger ligand class, L_2 is weaker ligand class ($\log K'_{Fe'L} < 11$), and $L_{Total} = [L_1] + [L_2]$. Some studies (summarized by Gledhill and Buck, 2012), suggested to use a definition for ligand classes based on the range of $\log K'_{Fe'L}$ values reported in natural systems: “ L_1 ” for $\log K'_{Fe'L} > 12$, “ L_2 ” for $\log K'_{Fe'L}$ varying between 11 and 12, and “ L_3 ” $\log K'_{Fe'L} < 11$. However, the different ligand classes are often hard to distinguish based on this definition (Gledhill and Buck, 2012; Gerringa et al., 2014; Hassler et al., 2017).

Siderophores are examples of strong binding ligands synthesized by bacteria to facilitate the acquisition of iron. Several siderophores have been chemically characterized and structurally defined (Mawji et al., 2008; Boiteau et al., 2013; Bundy et al., 2018; Sanchez et al., 2019). Hydroxamates are the most common class produced by heterotrophic bacteria and fungi, but despite the resistance to photodegradation (Barbeau et al., 2003), its concentrations in the ocean is too low (3–20 pM) to be a major ligand group (Mawji et al., 2008; Xu et al., 2020). Other organic molecules, however, can contain functional groups similar to the ones found in siderophores and can serve as strong ligands by chance rather than by design. Examples of other functional groups are catechol type and carboxylate type, present in many naturally occurring biochemicals (Fig. 2.6). In addition, there are numerous other ligand types described in the literature (Crosa et al., 2004; Vraspir and Butler, 2009; Khan et al., 2018). For example, carbohydrates have carboxyl and hydroxyl groups that can have weak to strong affinities for iron, and carbohydrates are in much higher concentrations (nanomolar to micromolar) than carboxylate siderophores (Benner et al., 1992; Wang et al., 2006). Exopolysaccharides released from microorganisms can bind iron, thereby enhancing iron availability to eukaryotic phytoplankton that do not produce siderophores (Hassler et al., 2011; Hassler et al., 2017). Recent studies suggest that hydroxamate-like moieties are also present in particulate organic matter, but are a minor component of the particulate organic carbon (POC) pool (<1.5% of POC; Chuang et al., 2013). The POC pool of iron-binding molecules is dominated by aromatics, followed by black carbon-like and CRAM-like compounds, with minor contributions of aliphatics (Xu et al., 2020).

Humic substances are thought to include important iron-binding ligands in the ocean (Laglera and van den Berg, 2009; Hassler et al., 2020), but little is known about the origins and

molecular properties of these iron-binding humic ligands. Dissolved humic substances are an operationally-defined, diverse mixture of molecules that can be isolated from water using hydrophobic solid-phase extraction (Amador et al., 1990; Hedges et al., 1992). Nuclear magnetic resonance (NMR) spectroscopy of terrigenous humic substances isolated from the Amazon River system indicated high aromaticity and lignin-derived methoxyl carbon, as well as aliphatic and carboxyl carbon (Hedges et al., 1992). In contrast, NMR spectroscopic analyses of marine humic substances isolated from the Pacific Ocean indicated an abundance of carboxylated aliphatic molecules with a highly branched structure and low unsaturated carbon (Hedges et al., 1992). The elemental C:N ratio of the terrigenous humic substances was ~60 and that of the marine humic substances was ~36, indicating a relatively low nitrogen content in the molecules comprising humic substances (Hedges et al., 1992). Ultrahigh-resolution mass spectrometry (e.g. FT-ICR-MS) analyses of terrigenous and marine humic substances indicate a tremendous diversity of molecules, and in combination with NMR spectroscopy revealed an abundance of CRAM that could function as iron chelators (Hertkorn et al., 2006; Lam et al., 2007; Hertkorn et al., 2013; Lechtenfeld et al., 2014; Bundy et al., 2015). It was estimated that CRAM accounts for ~25% of the DOC in the ocean, making this an abundant and diverse class of molecules that are distributed throughout the ocean water column (Fig. 2.6; Hertkorn et al., 2013). It appears humic sub-stances and associated carboxyl-rich alicyclic molecules are very resistant to microbial degradation but can be susceptible to photodegradation (Shen and Benner, 2018), thereby potentially enhancing iron bioavailability in surface waters (Hassler et al., 2020).

The number of iron-binding sites in terrigenous humic-like ligands is variable (Krachler et al., 2015), but the aromaticity and iron-binding capacity of these humic substances seem positively related (Kikuchi et al., 2004). Arctic rivers are major sources of terrigenous humic

substances that are rich in aromatic molecules, such as lignins and tannins, which likely play a role in iron complexation in river and coastal waters, including the TPD (Laglera and van den Berg, 2009; Laglera et al., 2019; Slagter et al., 2019). Like catechol type siderophores, lignin molecules are also enriched in catechol-type binding sites (Fig. 2.6). CRAM are thought to be degraded and altered forms of terpenoid compounds, such as sterols, hopanoids, and carotenoids, that are produced by terrestrial and marine organisms (Hertkorn et al., 2006; Lam et al., 2007), so they are potentially important ligands in freshwater and marine humic substances (Fig. 2.6). Carboxyl and hydroxyl functional groups are particularly abundant in CRAM of terrigenous and marine humic substances, and they are iron-binding sites (Hertkorn et al., 2006; Bundy et al., 2015). In addition, dissolved black carbon also contains carboxyl and hydroxyl functional groups and has been estimated to comprise ~10% of the DOC in fluvial discharge (Jaffé et al., 2013), but they have a relatively weak iron-binding capacity (Fig. 2.6).

The conditional stability constants of isolated terrigenous (Laglera and van den Berg, 2009) and marine humic substances (Hassler et al., 2020) are similar and can be explained by similar functional groups that bind to iron (Table 2.5 and Fig. 2.6). The covariation of iron and humic substances in the coastal waters and estuaries suggest the further transport of terrigenous humic substances and dFe into the open ocean (Laglera and van den Berg, 2009; Gerringa et al., 2015). This is consistent with the more recent finding that the mean iron-binding capacity of the open ocean samples indicate a similar range to terrestrial standards (Laglera et al., 2019; Whitby et al., 2020). It has been suggested that marine humic substances could account for 41% of the iron-binding ligands in deep waters and 7% in surface waters (Hassler et al., 2020). The conditional stability constants and concentrations of isolated terrigenous and marine humic substances are similar to those of L₂ type ligands reported in other studies (Table 2.5). This

confirms that CRAM and other types of potential ligands are ubiquitous in natural waters and the data in Table 2.5 and Fig. 2.6 provide strong evidence indicating diverse groups of molecules in humic substances can serve as iron-binding ligands and play a major role in maintaining bioavailable iron in the global ocean.

Measurements of ligand concentrations and conditional stability constants reported in natural waters indicate a ubiquitous distribution of specific types of binding sites in dissolved organic molecules across the land-ocean aquatic continuum (Table 2.5). Even in the Arctic Ocean, which is strongly influenced by tDOM, the differences in the conditional stability constants among different water masses were minimal (Thuroczy et al., 2011; Slagter et al., 2017). Slagter et al. (2017) reported that L₁ ligand type has a stronger affinity and higher concentration inside the TDP than in surface waters outside the TPD and in deep waters, which is likely due to the contribution of terrigenous ligands in humic substances. The L₂ ligand type also has a stronger affinity inside TPD, but it has higher concentrations in surface waters outside the TPD, implying that it has a marine origin.

The conditional stability constants and concentrations of ligands in the Barents Sea (Slagter et al., 2019), which is representative of the Atlantic water inflow to the Arctic, are similar to those of L₂ type ligands identified in the Arctic (Slagter et al., 2017; Table 2.5). Bering Sea water is representative of Pacific water inflow to the Arctic, and a strong correlation was observed between dissolved iron concentrations and L₁ concentrations in surface and subsurface waters over the Bering Sea shelf in proximity to terrigenous sources of iron (Buck et al., 2007). These authors found that over 99% of the dissolved iron was complexed by L₁ ligands, and they did not find a significant correlation between dissolved iron and L₂ ligand concentrations. In the Bering Sea, dissolved iron was supplied to the surface waters of the Green Belt region from the

shelf waters as FeL_1 complexes. Within this productive region, dissolved iron is depleted by phytoplankton while L_1 type ligand concentrations remained high (Buck et al., 2007). Elevated concentrations of L_1 and L_2 ligands were also observed in the subsurface waters over the shelf, indicating sediments are an important source of these ligands. Among the marine and freshwater domains presented in Table 2.5, the conditional stability constants of iron-binding ligands are highest in the Arctic Ocean, especially in the TPD. This can not be explained by the presence of a single ligand type, but rather by the unique diversity of ligand molecules with weaker binding strength, which in combination have the best chance of binding to dissolved iron, as similar functional groups might be present in different organic compounds.

2.5.3. DOM and dissolved iron in relation to hydrographic features

It appears dissolved iron can bind to a large and diverse group of organic ligand molecules with terrigenous and marine origins. The distribution of DOM has been linked to water mass modification and circulation in the Arctic Ocean (Anderson and Amon, 2015). Optical properties, biomarker, and dFe concentrations presented in this study reflect 3 major hydrographic (T/S) features of the Arctic Ocean. The most prominent distribution pattern is the Trans Polar Drift, with very high concentrations of dissolved iron, distinct optical properties, and high lignin phenol concentrations over 1500 km from riverine and shelf sources. The second most prominent distribution pattern is found associated with Eurasian shelf waters, which also had high concentrations of dissolved iron, optical properties, and lignin phenol concentrations derived from river and sediment sources. Sediments have been shown to be important sources of dissolved iron independent of river contributions on the Chuckchi shelf (Jensen et al., 2020). The third, less obvious hydrographic feature explaining the distribution of DOM and dissolved iron is

the halocline layer, with slightly elevated concentrations of dissolved iron, distinct optical properties, and lower concentrations of lignin phenols.

The Arctic halocline separates the relatively warm Atlantic layer from the cold PML. The different halocline layers in the Arctic are complex and consist of many types of water masses coming from different sources and greatly vary in thickness (Rudels et al., 1996, Rudels, 2001; Supplemental Table 2.6). The halocline structure in the Canada Basin differs from the Eurasian Basin stratification as the upper halocline (UHC) found in the Canadian Basin is almost absent from the Eurasian Basin (Anderson et al., 1994). In the Canada Basin, the UHC overlies the Eurasian Basin derived lower halocline (LHC). The halocline layers can be easily traced by elevated in situ CDOM fluorescence seen in section B (in high vertical resolution; Fig. 2.3). CDOM fluorescence originates on the Arctic shelves (river discharge and sediment release) and links the halocline-formation process to the shelves as originally suggested by Aagaard et al. (1981). We observed elevated levels of certain optical properties and dissolved iron in Eurasian halocline layers (supplemental Table 2.6), and a previous study related dFe concentrations to elevated absorbance-based optical indicators of DOM in the UHC of the Canada Basin (Nakayama et al., 2011). While many DOM indicators used in this study were also found at elevated levels in the halocline, the only indicator unique to the halocline was PARAFAC component C₄₀₈. This component has a pronounced peak in the upper halocline of the Canada Basin, near the Laptev Sea shelf break and directly underneath the TPD. The fluorescence signal of C₄₀₈ was lower than that of the other fluorophores. The C₄₀₈ component is most likely of marine origin and could be generated during organic matter decomposition in surface sediments on the shelf. The cruise only covered the northernmost portion of the Canada Basin, so it is difficult to clarify the role of C₄₀₈ as a dissolved iron ligand indicator, but C₄₀₈ fluorescence

intensity increased along the Eurasian shelf-Canada Basin transect. The dissolved iron concentrations were much lower in the upper halocline compared to the TPD or the Laptev Sea shelf, indicating selective loss of dFe within the upper halocline, even though the optical properties indicate the ligands were probably present. The residence time of the halocline with respect to shelf inputs occurs on time scales of ≤ 19 –23 years (Kipp et al., 2019), so we don't see the halocline as an important vector for dissolved iron transport to neighboring ocean basins.

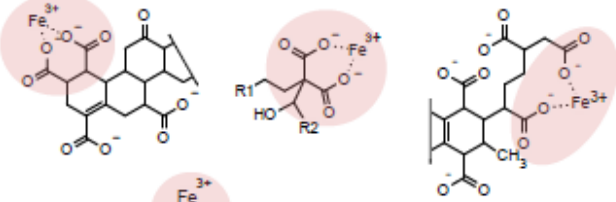
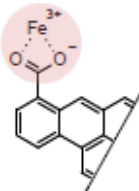
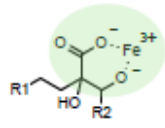
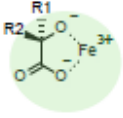
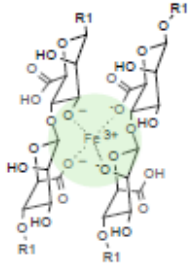
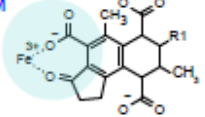
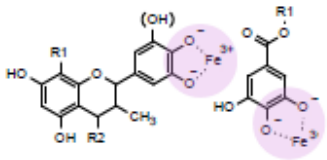
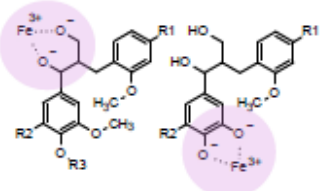
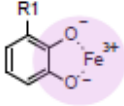
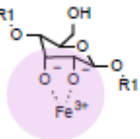
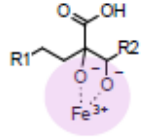
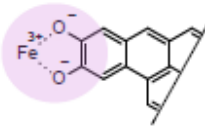
Functional groups for Fe(III) binding	Representative compound classes with structural examples	Origin	Bonding type and affinity
Carboxyl $R1-C(=O)OH$	CRAM  Dissolved black carbon 	marine and terrestrial	Bi- or multidentate weak to strong
Hydroxy/ carboxyl $R1-OH$ $HO-C(=O)R2$	CRAM  Siderophores (carboxylate type)  Carbohydrates 	marine and terrestrial	Multidentate weak to strong
Carbonyl/ carboxyl $R1-C(=O)R2$ $HO-C(=O)R2$	CRAM 	marine and terrestrial	Bi- or multidentate weak to strong
Hydroxyl $R1-OH$	Tannins (condensed/ hydrolyzable types)  Lignins  Siderophores (catechol type)  Carbohydrates  CRAM  Dissolved black carbon 	terrestrial marine	Bi- or multidentate weak to strong Bi- or multidentate weak to strong
		marine and terrestrial	Bi- or multidentate weak to strong

Fig. 2.6. Possible iron-binding sites on molecules of various origins in natural waters. These types of molecules are found in humic substances extracted from freshwater and marine environments. Tannins, lignins, siderophore (catechol type), black carbon likely contribute to CDOM. CRAM- Carboxyl-rich alicyclic molecules.

The second major hydrographic feature of the Arctic Ocean influencing the distribution of dFe is the broad and shallow shelves, which receive very large freshwater discharge from rivers with high concentrations of DOM (Raymond et al., 2007; Amon et al., 2012) and dFe. In addition, the Eurasian shelves represent a location of net sea ice formation and shelf water modification (Bauch et al., 2016). The shallow, river dominated, shelves produce a diverse cocktail of organic molecules introduced by rivers and sediment-water exchanges that are reflected in the distribution of optical properties, the terrigenous biomarker, and associated dFe. The low salinity surface waters carry dFe-enriched tDOM along the Eurasian shelf from the Kara Sea to the Laptev Sea and the East Siberian Sea where it eventually gets entrained into the TPD. Within the TPD the dFe-enriched tDOM crosses the Arctic Ocean and is exported to the North Atlantic (Bauch et al., 2011). Much of the dFe-enriched Chuckchi and coastal Beaufort Sea shelf waters are swept towards the Canadian Archipelago by the Alaskan coastal current and flow into the Baffin Bay and the Labrador Sea (Fichot et al., 2013). The brine-enriched shelf waters produced during winter sea ice formation enter subsurface layers in the open Arctic and the dFe entrained in these layers will meet the fate described above for the halocline.

Table 2.5. Examples of published data on organic iron-binding ligands in the ocean, measured with the voltammetry techniques.

Region	Ligand predominant origin	Salinity	$\log K'_{FeL_1}$	$\log K'_{FeL_2}$	$\log K_{FeL_3}$	$[L_1]$, nM	$[L_2]$, nM	$[L_3]$, nM	Reference
Suwannee River, GA, USA	Terrigenous (isolated humic acid)	0		11.1 ± 0.2					Laglera and van den Berg (2009)
	Terrigenous (isolated fulvic acid)	0			10.6 ± 0.2				
NW Atlantic Ocean (1000 m)	Marine (isolated humic substances)	35.5	12.26–12.4	11.64 ± 0.45		1,0.39–2.25	1.17		Hassler et al. (2020)
Mississippi River plume, LA, USA	Terrigenous	19.5–36.14	10.4–12.3			4.3–64.1			Powell and Wilson-Finelli (2003)
Transport from Peatland to Marine Waters (the Thurso river), Scotland	Terrigenous/ Marine mix	0–34.7		11.05 ± 0.24			96–21,125		Muller and Cuscov (2017)
NE Atlantic surface coastal water	Terrigenous/ Marine mix	28–35		10.23–11.97			46.5–573.2		Batchelli et al. (2010)
Arctic Ocean, Inside TPD (≤ 200 m)	Terrigenous/ Marine mix	34–34.2	13.3–13.6	11.6–11.76		1.58–2.29	1.26–2.76		Slagter et al. (2017)
Arctic Ocean, Outside TPD (≤ 200 m)	Terrigenous/ Marine mix	34.2–34.6	13.26 + 0.71	11.2 ± 0.17		0.69 + 0.27	1.34 + 0.56		
Arctic Ocean/ >200 m	Marine	34.6–35	13.14 ± 0.61	11.16 ± 0.17		0.62 ± 0.2	1.28 ± 0.49		
Barents Sea	Marine	28–33.5		11.2–12.1			1.26–2.14		Slagter et al. (2019)
Bering Sea (2–57 m)	Marine	31.6–31.9		11.1–12	9.7–10.8		0.43–18	1.2–15	Buck et al. (2007)
Arctic Ocean (0–4251 m)	Marine	29.5–35	11.5–12.57				0.31–4.5		Thuróczy et al. (2011)

The Trans Polar Drift carries iron-enriched tDOM and sediment derived DOM from Eurasian rivers and shelves across the Arctic Ocean and becomes the East Greenland Current exporting the high CDOM-high tDOM to the North Atlantic (Amon et al., 2003; Benner et al., 2005). The TPD had high concentrations of dissolved iron and DOM near the North Pole, so it is likely that most of the dissolved iron and DOM is trans-ported to the North Atlantic. Previous work has detected elevated concentrations of Arctic river CDOM and tDOM in surface waters of the Denmark Strait and the Irminger Sea (Amon et al., 2003, Benner et al., 2005) as well as in Denmark Strait Overflow Water, contributing to North Atlantic Deep Water (Benner et al., 2005). Elevated concentrations of dissolved iron were observed in the Western North Atlantic at depths between 800 and 2500 m, corresponding to Labrador Sea Water (Conway and John, 2014). Tonnard et al. (2020) also reported elevated iron concentrations within Denmark Strait Overflow Water, Iceland– Scotland-Ridge Overflow Water, and Upper Labrador Sea Water, and they attributed the elevated concentrations to iron-binding organic ligand complexes that were transported to the deep ocean by convection of water masses. This long-range transport of iron-

rich Arctic shelf DOM may have a significant effect on primary production and the bioavailability of dissolved iron in North Atlantic surface waters and the Southern Ocean through the upwelling of North Atlantic Deep Water in the Southern Ocean (Gerringa et al., 2015; Klunder et al., 2011).

Table 2.6. Water mass characteristics along with optical properties and biomarker distribution across the Arctic basins. (CB- Canada Basin, MB- Makarov Basin, AB- Amundsen Basin, NB- Nansen Basin)

Water mass	Salinity (psu)				Potential temperature (°C)				Depth (m)				Dissolved iron (nmol/L)				DOC (nmol/L)				<i>in situ</i> CDOM (V)				TDLP9 (nmol/L)			
	CB	MB	AB	NB	CB	MB	AB	NB	CB	MB	AB	NB	CB	MB	AB	NB	CB	MB	AB	NB	CB	MB	AB	NB	CB	MB	AB	NB
Polar Mixed Water	30-31	32-33	32-33	32-33	<0°	<-1.6°	<-1.6°	<-1.6°	<100	<80	<20	<50	0.26 ± 0.1	2.67 ± 0.3	2 ± 0.4	0.48 ± 0.1	90.9 ± 12	101.7 ± 7	99.3 ± 17	58.9 ± 9	0.06 ± 0.01	0.19 ± 0.1	0.15 ± 0.1	0.06 ± 0.1	NaN	11.92 ± 0.6	7.26 ± 0.2	5.5 ± 0.2
Upper Halocline Water	32-33.5	NA	NA	NA	<-1°	NA	NA	NA	100-145	80-110	20-80	NA	0.67 ± 0.2	1.53 ± 0.4	1.58 ± 0.4	NA	80.5 ± 10	84.2 ± 10	88.5 ± 10	NA	0.09 ± 0.01	0.17 ± 0.01	0.15 ± 0.01	NA	3.5 ± 0.2	6.1 ± 0.2	7 ± 0.2	NaN
Lower Halocline Water	34-34.7	34-34.7	34-34.7	34-34.7	<0°	<0°	<0°	<0°	170-300	100-250	90-190	50-150	0.64 ± 0.2	0.28 ± 0.1	0.3 ± 0.1	0.26 ± 0.1	70.7 ± 18	72.7 ± 12	74.2 ± 13	73.1 ± 13	0.11 ± 0.01	0.15 ± 0.01	0.15 ± 0.01	0.06 ± 0.01	NaN	NaN	NaN	NaN
Atlantic Water	>34.9	>34.9	>34.9	>34.9	>3°	>3°	>3°	>3°	>300	>250	>190	>150	0.34 ± 0.1	0.32 ± 0.1	0.48 ± 0.1	0.4 ± 0.1	55.1 ± 2	56.3 ± 2	54.8 ± 2	50.05 ± 2	0.06 ± 0.01	0.06 ± 0.01	0.06 ± 0.01	0.06 ± 0.01	NaN	NaN	NaN	NaN
Laptev Sea shelf surface waters	27-33				>0°				<40				2.96 ± 0.1				0.8 ± 0.05				0.12 ± 0.02				12 ± 0.3			
Laptev Sea shelf bottom waters	>33				0- -1.7°				40-90				10.4 ± 0.2				1.5 ± 0.05				0.18 ± 0.02				13.8 ± 0.3			

2.6 References

Aagaard, K., Coachman, L.K., Carmack, E., 1981. On the halocline of the Arctic Ocean. Deep Sea research part a. Oceanogr. Res. Pap. 28 (6), 529–545.

Alkire, M.B., Polyakov, I., Rember, R., Pnyushkov, A., Ivanov, V., Ashik, I., 2017. Combining physical and geochemical methods to investigate lower halocline water formation and modification along the Siberian continental slope. Ocean Sci. 13 (6), 983–995.

Amador, J., Milne, P.J., Moore, C.A., Zika, R.G., 1990. Extraction of chromophoric humic substances from seawater. Mar. Chem. 29, 1–17.

- Amon, R.M.W., 2004. The role of dissolved organic matter for the Arctic Ocean carbon cycle. In: Stein, R., Macdonald, R.W. (Eds.), *The Arctic Ocean Organic Carbon Cycle: Present and Past*. Springer, pp. 83–99.
- Amon, R.M.W., Budeus, G., Meon, B., 2003. Dissolved organic carbon, DOC distribution and origin in the Nordic Seas: Exchanges with the Arctic Ocean and the North Atlantic. *J. Geophys. Res.-Oceans* 108 (C7), 3221. <https://doi.org/10.1029/2002JC001594>.
- Amon, R.M.W., Rinehart, A.J., Duan, S., Louchouart, P., Prokushkin, A., Guggenberger, G., McClelland, J.W., 2012. Dissolved organic matter sources in large Arctic rivers. *Geochimica et Cosmochimica Acta* 94, 217–237.
- Anderson, L.G., Amon, R.M.W., 2015. DOM in the Arctic Ocean. In: *Biogeochemistry of Marine Dissolved Organic Matter*. Academic Press, pp. 609–633.
- Anderson, L.G., Björk, G., Holby, O., Jones, E.P., Kattner, G., Koltermann, K.P., Swift, J., 1994. Water masses and circulation in the Eurasian Basin: Results from the Oden 91 expedition. *J. Geophys. Res. Oceans* 99 (C2), 3273–3283.
- Barbeau, K., Rue, E.L., Bruland, K.W., Butler, A., 2001. Photochemical cycling of iron in the surface ocean mediated by microbial iron (III)-binding ligands. *Nature* 413 (6854), 409–413.
- Barbeau, K., Rue, E.L., Trick, C.G., Bruland, K.W., Butler, A., 2003. Photochemical reactivity of siderophores produced by marine heterotrophic bacteria and cyanobacteria based on characteristic Fe (III) binding groups. *Limnol. Oceanogr.* 48 (3), 1069–1078.
- Batchelli, S., Muller, F.L., Chang, K.-C., Lee, C.-L., 2010. Evidence for strong but dynamic iron-humic colloidal associations in humic-rich coastal waters. *Environ. Sci. Technol.* 44 (22), 8485–8490. <https://doi.org/10.1021/es101081c>.

- Bauch, D., Hölemann, J., Andersen, N., Dobrotina, E., Nikulina, A., Kassens, H., 2011. The Arctic shelf regions as a source of freshwater and brine-enriched waters as revealed from stable oxygen isotopes. *Polarforschung* 80 (3), 127–140.
- Bauch, D., Cherniavskaia, E., Timokhov, L., 2016. Shelf basin exchange along the Siberian continental margin: modification of Atlantic water and lower halocline water. *Deep-Sea Res. I Oceanogr. Res. Pap.* 115, 188–198.
- Benner, R., 2011a. Loose ligands and available iron in the ocean. *Proc. Natl. Acad. Sci.* 108 (3), 893–894.
- Benner, R., 2011b. Loose ligands and available iron in the ocean. *Proc. Natl. Acad. Sci.* 108 (3), 893–894.
- Benner, R., Pakulski, J.D., McCarthy, M., Hedges, J.I., Hatcher, P.G., 1992. Bulk chemical characteristics of dissolved organic matter in the ocean. *Science* 255 (5051), 1561–1564.
- Marine Chemistry* 231 (2021) 10393613
- Benner, R., Benitez-Nelson, B., Kaiser, K., Amon, R.M.W., 2004. Export of young terrigenous dissolved organic carbon from rivers to the Arctic Ocean. *Geophys. Res. Lett.* 31, L05305
<https://doi.org/10.1029/2003GL019251>.
- Benner, R., Louchouart, P., Amon, R.M.W., 2005. Terrigenous dissolved organic matter in the Arctic Ocean and its transport to surface and deep waters of the North Atlantic. *Glob. Biogeochem. Cycles* 19, 2.
- Boiteau, R.M., Fitzsimmons, J.N., Repeta, D.J., Boyle, E.A., 2013. Detection of iron ligands in seawater and marine cyanobacteria cultures by high-performance liquid chromatography-inductively coupled plasma-mass spectrometry. *Anal. Chem.* 85 (9), 4357–4362.

- Buck, K.N., Lohan, M.C., Berger, C.J., Bruland, K.W., 2007. Dissolved iron speciation in two distinct river plumes and an estuary: implications for riverine iron supply. *Limnol. Oceanogr.* 52 (2), 843–855.
- Bundy, R.M., Abdulla, H.A., Hatcher, P.G., Biller, D.V., Buck, K.N., Barbeau, K.A., 2015. Iron-binding ligands and humic substances in the San Francisco Bay estuary and estuarine-influenced shelf regions of coastal California. *Mar. Chem.* 173, 183–194.
- Bundy, R.M., Boiteau, R.M., McLean, C., Turk-Kubo, K.A., McIlvin, M.R., Saito, M.A., Repeta, D.J., 2018. Distinct siderophores contribute to iron cycling in the mesopelagic at station ALOHA. *Frontiers in Marine Science* 5, 61.
- Charette, M.A., Kipp, L.E., Jensen, L.T., Dabrowski, J.S., Whitmore, L.M., Fitzsimmons, J. N., et al., 2020. The Transpolar Drift as a source of riverine and shelf-derived trace elements to the central Arctic Ocean. *J. Geophys. Res. Oceans* 125. <https://doi.org/10.1029/2019JC015920> e2019JC015920.
- Chen, M., Jung, J., Lee, Y.K., Hur, J., 2018. Surface accumulation of low molecular weight dissolved organic matter in surface waters and horizontal off-shelf spreading of nutrients and humic-like fluorescence in the Chukchi Sea of the Arct.
- Chuang, C.Y., Santschi, P.H., Ho, Y.F., Conte, M.H., Guo, L., Schumann, D., Li, Y.H., 2013. Role of biopolymers as major carrier phases of Th, Pa, Pb, Po, and Be radionuclides in settling particles from the Atlantic Ocean. *Marine Chemistry*, 157, 131-143. *Science of the Total Environment* 639, 624–632.
- Conway, T.M., John, S.G., 2014. Quantification of dissolved iron sources to the North Atlantic Ocean. *Nature* 511 (7508), 212–215.

- Crosa, J.H., Mey, A.R., Payne, S.M. (Eds.), 2004. Iron Transport in Bacteria, vol. 410. ASM press, Washington, DC.
- Fichot, C.G., Benner, R., 2012. The spectral slope coefficient of chromophoric dissolved organic matter, S_{275–295} as a tracer of terrigenous dissolved organic carbon in river-influenced ocean margins. *Limnol. Oceanogr.* 57 (5), 1453–1466.
- Fichot, C.G., Kaiser, K., Hooker, S.B., Amon, R.M.W., Babin, M., Belanger, S., Benner, R., 2013. Pan-Arctic distributions of continental runoff in the Arctic Ocean. *Scientific reports* 3, 1053.
- Gerringa, L.J., Rijkenberg, M.J., Thuroczy, C.E., Maas, L.R., 2014. A critical look at the calculation of the binding characteristics and concentration of iron complexing ligands in seawater with suggested improvements. *Environ. Chem.* 11 (2), 114–136.
- Gerringa, L.J., Rijkenberg, M.J., Schoemann, V., Laan, P., De Baar, H.J., 2015. Organic complexation of iron in the West Atlantic Ocean. *Mar. Chem.* 177, 434–446.
- Gledhill, M., Buck, K.N., 2012. The organic complexation of iron in the marine environment: a review. *Front. Microbiol.* 3, 69.
- Gonçalves-Araujo, R., Stedmon, C., Kraberg, A., Bracher, A., 2015. Dynamics of Dom in the Lena Delta Region, Siberia Revealed by Parallel Factor Analysis.
- Gonçalves-Araujo, R., Granskog, M.A., Bracher, A., Azetsu-Scott, K., Dodd, P.A., Stedmon, C.A., 2016. Using fluorescent dissolved organic matter to trace and distinguish the origin of Arctic surface waters. *Sci. Rep.* 6, 33978.
- Hansell, D.A., 2005. Dissolved organic carbon reference material program. *Eos. Trans. Am. Geophys. Union* 86 (35), 318–318.

Hassler, C.S., Schoemann, V., Nichols, C.M., Butler, E.C., Boyd, P.W., 2011. Saccharides enhance iron bioavailability to Southern Ocean phytoplankton. *Proc. Natl. Acad. Sci.* 108 (3), 1076–1081.

Hassler, C.S., van den Berg, C.M., Boyd, P.W., 2017. Toward a regional classification to provide a more inclusive examination of the ocean biogeochemistry of iron-binding ligands. *Front. Mar. Sci.* 4, 19.

Hassler, C., Cabanes, D., Blanco-Ameijeiras, S., Sander, S.G., Benner, R., 2020. Importance of refractory ligands and their photodegradation for iron oceanic inventories and cycling. *Mar. Freshw. Res.* 71 (3), 311–320.

Hedges, J.I., Hatcher, P.G., Ertel, J.R., Meyers-Schulte, K.J., 1992. A comparison of dissolved humic substances from seawater with Amazon River counterparts by ¹³C- NMR spectrometry. *Geochim. Cosmochim. Acta* 56 (4), 1753–1757.

Helms, J.R., Stubbins, A., Ritchie, J.D., Minor, E.C., Kieber, D.J., Mopper, K., 2008. Absorption spectral slopes and slope ratios as indicators of molecular weight, source, and photobleaching of chromophoric dissolved organic matter. *Limnol. Oceanogr.* 53 (3), 955–969.

Hernes, P.J., Bergamaschi, B.A., Eckard, R.S., Spencer, R.G., 2009. Fluorescence-based proxies for lignin in freshwater dissolved organic matter. *J. Geophys. Res. Biogeosci.* 114, G4.

Hertkorn, N., Benner, R., Frommberger, M., Schmitt-Kopplin, P., Witt, M., Kaiser, K., Hedges, J.I., 2006. Characterization of a major refractory component of marine dissolved organic matter. *Geochimica et Cosmochimica Acta* 70 (12), 2990–3010.

Hertkorn, N., Harir, M., Koch, B., Michalke, B., Schmitt-Kopplin, P., 2013. High-field NMR spectroscopy and FTICR mass spectrometry: powerful discovery tools for the molecular level characterization of marine dissolved organic matter. *Biogeosciences* 10, 1583–1624.

Jaffe, R., Ding, Y., Niggemann, J., Vähätalo, A.V., Stubbins, A., Spencer, R.G., Dittmar, T., 2013. Global charcoal mobilization from soils via dissolution and riverine transport to the oceans. *Science* 340 (6130), 345–347.

Jensen, L.T., Morton, P., Twining, B.S., Heller, M.I., Hatta, M., Measures, C.I., John, S., Zhang, R., Pinedo-Gonzalez, P., Sherrell, R.M., Fitzsimmons, J.N., 2020. A comparison of marine Fe and Mn cycling: U.S. GEOTRACES GN01 Western Arctic case study. *Geochimica et Cosmochimica Acta* 288, 138–160.

Kaiser, K., Benner, R., Amon, R.M.W., 2017a. The fate of terrigenous dissolved organic carbon on the Eurasian shelves and export to the North Atlantic. *J. Geophys. Res. Oceans* 122, 4–22. <https://doi.org/10.1002/2016JC012380>.

Kaiser, K., Canedo-Oropeza, M., McMahon, R., Amon, R.M.W., 2017b. Origins and transformations of dissolved organic matter in large Arctic rivers. *Sci. Rep.* 7 (1), 13064.

Khan, A., Singh, P., Srivastava, A., 2018. Synthesis, nature and utility of universal iron chelator–Siderophore: a review. *Microbiol. Res.* 212, 103–111.

Kikuchi, T., Hatakeyama, K., Morison, J.H., 2004. Distribution of convective lower halocline water in the eastern Arctic Ocean. *J. Geophys. Res. Oceans* 109, C12.

Kipp, L.E., Kadko, D.C., Pickart, R.S., Henderson, P.B., Moore, W.S., Charette, M.A., 2019. Shelf-basin interactions and water mass residence times in the Western Arctic Ocean: insights provided by radium isotopes. *J. Geophys. Res. Oceans* 124 (5), 3279–3297.

Klunder, M.B., Laan, P., Middag, R., De Baar, H.J.W., Van Ooijen, J.C., 2011. Dissolved iron in the Southern Ocean , Atlantic sector. *Deep-Sea Res. II Top. Stud. Oceanogr.* 58 (25–26), 2678–2694.

Klunder, M.B., Bauch, Dorothea, Laan, Patrick, de Baar, Hein J.W., van Heuven, Steven, Ober, Sven, 2012a. Dissolved iron measurements from 44 stations in the shallow Arctic Ocean waters and Shelf Sea's during POLARSTERN cruise ARK-XXII/2. PANGAEA

https://urldefense.com/v3/__doi:10.1594/PANGAEA.780543__;!!

KwNVnqRv!TXJ3dnn7_nX_4ixhjFIGQ378Bgni_YsxqC14u2bOiXCdJhVcrCl1uzFKEh4RyQ\$. Supplement to: Klunder, MB et al., 2012a.

Klunder, M.B., Bauch, D., Laan, P., De Baar, H.J.W., van Heuven, S., Ober, S., 2012b.

Dissolved iron in the Arctic shelf seas and surface waters of the Central Arctic Ocean: impact of Arctic river water and ice-melt. *J. Geophys. Res. Oceans* 117. C01027,

https://urldefense.com/v3/__doi:10.1029/2011JC007133__;!!KwNVnqRv!

TXJ3dnn7_nX_4ixhjFIGQ378Bgni_YsxqC14u2bOiXCdJhVcrCl1uzFNe3zqgw\$.

Krachler, R., von der Kammer, F., Jirsa, F., Süphandag, A., Krachler, R.F., Plessl, C., Vogt, M., Keppler, B.K., Hofmann, T., 2012. Nanoscale lignin particles as sources of dissolved iron to the ocean. *Glob. Biogeochem. Cycles* 26. <https://doi.org/10.1029/2012GB004294>.

Krachler, R., Krachler, R.F., Wallner, G., Hann, S., Laux, M., Recalde, M.F.C., Keppler, B. K., 2015. River-derived humic substances as iron chelators in seawater. *Marine chemistry* 174, 85–93.

Laglera, L.M., van den Berg, C.M., 2009. Evidence for geochemical control of iron by humic substances in seawater. *Limnol. Oceanogr.* 54 (2), 610–619.

Laglera, L.M., Sukekava, C., Slagter, H.A., Downes, J., Aparicio-Gonzalez, A., Gerringa, L. J., 2019. First quantification of the controlling role of humic substances in the transport of iron across the surface of the Arctic Ocean. *Environ. Sci. Technol.* 53 (22), 13136–13145. Lam, B., Baer, A., Alae, M., Lefebvre, B., Moser, A., Williams, A., Simpson, A.J., 2007. Major

structural components in freshwater dissolved organic matter. *Environ. Sci. Technol.* 41 (24), 8240–8247.

Lechtenfeld, O.J., Kattner, G., Flerus, R., McCallister, S.L., Schmitt-Kopplin, P., Koch, B. P., 2014. Molecular transformation and degradation of refractory dissolved organic matter in the Atlantic and Southern Ocean. *Geochim. Cosmochim. Acta* 126, 321–337.

Louchouart, P., Opsahl, S., Benner, R., 2000. Isolation and quantification of dissolved lignin from natural waters using solid-phase extraction and GC/MS. *Anal. Chem.* 72 (13), 2780–2787.

Maie, N., Pisani, O., Jaffe, R., 2008. Mangrove tannins in aquatic ecosystems: their fate and possible influence on dissolved organic carbon and nitrogen cycling. *Limnol. Oceanogr.* 53 (1), 160–171.

Mawji, E., Gledhill, M., Milton, J.A., Tarran, G.A., Ussher, S., Thompson, A., Achterberg, E.P., 2008. Hydroxamate siderophores: occurrence and importance in the Atlantic Ocean. *Environ. Sci. Technol.* 42 (23), 8675–8680.

Middag, R., Laan, P., de Baar, H.J.W., Klunder, M.B., 2011. Fluvial and hydrothermal input of manganese into the Arctic Ocean. *Geochim. Cosmochim. Acta* 75, 2393–2408.

<https://doi.org/10.1016/j.gca.2011.02.011>.

Muller, F.L., Cuscov, M., 2017. Alteration of the copper-binding capacity of iron-rich humic colloids during transport from peatland to marine waters. *Environ. Sci. Technol.* 51 (6), 3214–3222.

Murphy, K.R., Stedmon, C.A., Graeber, D., Bro, R., 2013. Fluorescence spectroscopy and multi-way techniques. PARAFAC. *Anal. Methods*. <https://doi.org/10.1039/c3ay41160e>.

Murphy, K.R., Stedmon, C.A., Wenig, P., Bro, R., 2014. OpenFluor—an online spectral library of auto-fluorescence by organic compounds in the environment. *Anal. Methods* 6 (3), 658–661.

Murphy, K.R., Timko, S.A., Gonsior, M., Powers, L.C., Wunsch, U.J., Stedmon, C.A., 2018. Photochemistry illuminates ubiquitous organic matter fluorescence spectra. *Environ. Sci. Technol.* 52 (19), 11243–11250.

Nakayama, Y., Fujita, S., Kuma, K., Shimada, K., 2011. Iron and humic-type fluorescent dissolved organic matter in the Chukchi Sea and Canada Basin of the western Arctic Ocean. *J. Geophys. Res. Oceans* 116, C7.

Opsahl, S., Benner, R., 1997. Distribution and cycling of terrigenous dissolved organic matter in the ocean. *Nature* 386 (6624), 480.

Opsahl, S., Benner, R., Amon, R.M.W., 1999. Major flux of terrigenous dissolved organic matter through the Arctic Ocean. *Limnol. Oceanogr.* 44, 2017–2023.

Osburn, C.L., Boyd, T.J., Montgomery, M.T., Bianchi, T.S., Coffin, R.B., Paerl, H.W., 2016. Optical proxies for terrestrial dissolved organic matter in estuaries and coastal waters. *Front. Mar. Sci.* 2, 127.

Powell, R.T., Wilson-Finelli, A., 2003. Importance of organic Fe complexing ligands in the Mississippi River plume. *Estuar. Coast. Shelf Sci.* 58 (4), 757–763.

Raymond, P.A., McClelland, J.W., Holmes, R.M., Zhulidov, A.V., 2007. Flux and age of dissolved organic carbon exported to the Arctic Ocean: A carbon isotopic study of the five largest Arctic rivers. *Glob. Biogeochem. Cycles* 21, GB4011. <https://doi.org/10.1029/2007GB002934>.

Rijkenberg, M.J.A., Slagter, H.A., Rutgers van der Loeff, M., van Ooijen, J., Gerringa, L.J. A., 2018. Dissolved Fe in the deep and upper Arctic Ocean with a focus on Fe limitation in the Nansen Basin. *Front. Mar. Sci.* 5, 88. <https://doi.org/10.3389/fmars.2018.00088>.

- Rudels, B., 2001. Ocean Current: Arctic Basin Circulation. In: Steele, J., Thorpe, S., Turekian, K. (Eds.), *Encyclopedia of Ocean Sciences*, pp. 177–187.
- Rudels, B., Anderson, L.G., Jones, E.P., 1996. Formation and evolution of the surface mixed layer and halocline of the Arctic Ocean. *J. Geophys. Res.* 101, 8807–8821.
- Rue, E.L., Bruland, K.W., 1995. Complexation of iron, III by natural organic ligands in the Central North Pacific as determined by a new competitive ligand equilibration/ adsorptive cathodic stripping voltammetric method. *Mar. Chem.* 50 (1–4), 117–138.
- Sanchez, N., Peterson, C.K., Gonzalez, S.V., Vadstein, O., Olsen, Y., Ardelan, M.V., 2019. Effect of hydroxamate and catecholate siderophores on iron availability in the diatom *Skeletonema costatum*: implications of siderophore degradation by associated bacteria. *Mar. Chem.* 209, 107–119.
- Schauer, U., 2008. The expedition ARKTIS-XXII/2 of the Research Vessel “Polarstern”. In: 2007. *Berichte zur Polar- und Meeresforschung – Reports on Polar and Marine Research*, vol. 579, p. 271.
- Schlitzer, R., Anderson, R., Masferrer Dodas, E., Lohan, M.C., Geibert, W., et al., 2018. The GEOTRACES Intermediate Data Product 2017. *Chemical geology*, vol. 493. Elsevier, pp. 210–223. <https://doi.org/10.1016/j.chemgeo.2018.05.040>. hal- 01819333.
- Shen, Y., Benner, R., 2018. Mixing it up in the ocean carbon cycle and the removal of refractory dissolved organic carbon. *Sci. Rep.* 8 (1), 1–9.
- Slagter, H.A., Reader, H.E., Rijkenberg, M.J.A., Van Der Loeff, M.R., de Baar, H.J.W., Gerringa, L.J.A., 2017. Organic Fe speciation in the Eurasian basins of the Arctic Ocean and its relation to terrestrial DOM. *Mar. Chem.* 197, 11–25.

Slagter, H.A., Laglera, L.M., Sukekava, C., Gerringa, L.J., 2019. Fe-binding organic ligands in the humic-rich TransPolar drift in the surface Arctic Ocean using multiple voltammetric methods. *J. Geophys. Res. Oceans* 124 (3), 1491–1508.

Stedmon, C.A., Markager, S., Kaas, H., 2000. Optical properties and signatures of chromophoric dissolved organic matter, CDOM in Danish coastal waters. *Estuar. Coast. Shelf Sci.* 51 (2), 267–278.

Sukekava, C., Downes, J., Slagter, H.A., Gerringa, L.J., Laglera, L.M., 2018. Determination of the contribution of humic substances to iron complexation in seawater by catalytic cathodic stripping voltammetry. *Talanta* 189, 359–364.

Thuroczy, C.E., Gerringa, L.J.A., Klunder, M., Laan, P., Le Guitton, M., De Baar, H.J.W., 2011. Distinct trends in the speciation of iron between the shallow shelf seas and the deep basins of the Arctic Ocean. *J. Geophys. Res. Oceans* 116, C10.

Tonnard, M., Planquette, H., Bowie, A., Van Der Merwe, P., Gallinari, M., de Gesincourt, F.D., Treguer, P., 2020. Dissolved iron in the North Atlantic Ocean and Labrador Sea along the GEOVIDE section, GEOTRACES section GA01. *Biogeosciences* 17 (4), 917–943.

Vraspir, J.M., Butler, A., 2009. Chemistry of marine ligands and siderophores. *Annu Rev MarSci* 1, 43–63.

Walker, S.A., Amon, R.M.W., Stedmon, C., Duan, S.W., Louchouart, P., 2009. The use of PARAFAC modeling to trace terrestrial dissolved organic matter and fingerprint water masses in coastal Canadian Arctic surface waters. *J. Geophys. Res.* 114
<https://doi.org/10.1029/2009jg000990>.

- Walker, S.A., Amon, R.M.W., Stedmon, C.A., 2013. Variations in high-latitude riverine fluorescent dissolved organic matter: a comparison of large Arctic rivers. *J. Geophys. Res. Biogeosci.* 118 (4), 1689–1702.
- Wang, D., Henrichs, S.M., Guo, L., 2006. Distributions of nutrients, dissolved organic carbon and carbohydrates in the western Arctic Ocean. *Cont. Shelf Res.* 26 (14), 1654–1667.
- Weishaar, J.L., Aiken, G.R., Bergamaschi, B.A., Fram, M.S., Fujii, R., Mopper, K., 2003. Evaluation of specific ultraviolet absorbance as an indicator of the chemical composition and reactivity of dissolved organic carbon. *Environ. Sci. Technol.* 37 (20), 4702–4708.
- Whitby, H., Planquette, H., Cassar, N., Bucciarelli, E., Osburn, C.L., Janssen, D.J., Sarthou, G., 2020. A call for refining the role of humic-like substances in the oceanic iron cycle. *Scientific Reports* 10.
- Wisotzki, Andreas, 2008. Physical oceanography measured on water bottle samples during POLARSTERN cruise ARK-XXII/2. Alfred Wegener Institute, Helmholtz Centre for Polar and Marine Research, Bremerhaven, PANGAEA.
- Wünsch, U.J., Murphy, K.R., Stedmon, C.A., 2015. Fluorescence quantum yields of natural organic matter and organic compounds: implications for the fluorescence- based interpretation of organic matter composition. *Front. Mar. Sci.* 2, 98. [https:// doi.org/10.3389/fmars.2015.00098](https://doi.org/10.3389/fmars.2015.00098).
- Wünsch, U.J., Murphy, K.R., Stedmon, C.A., 2016. Corrigendum: fluorescence quantum yields of natural organic matter and organic compounds: implications for the fluorescence-based interpretation of organic matter composition. *Front. Mar. Sci.* 3, 9.
- Xu, C., Lin, P., Sun, L., Chen, H., Xing, W., Kamalanathan, M., Santschi, P.H., 2020. Molecular nature of marine particulate organic iron-carrying moieties revealed by electrospray ionization

Fourier-transform ion cyclotron resonance mass spectrometry, ESI-FTICRMS. *Frontiers in Earth Science* 8, 266.

Yamashita, Y., Nishioka, J., Obata, H., Ogawa, H., 2020. Shelf humic substances as carriers for basin-scale iron transport in the North Pacific. *Sci. Rep.* 10 (1), 1–10.

Yan, G., Kaiser, K., 2018a. A rapid and sensitive method for the analysis of lignin phenols in environmental samples using ultra-high performance liquid chromatography- electrospray ionization-tandem mass spectrometry with multiple reaction monitoring. *Anal. Chim. Acta* 1023, 74–80.

Yan, G., Kaiser, K., 2018b. Ultra-low sample volume cupric Sulfate oxidation method for the analysis of dissolved lignin. *Anal. Chem.* 68 (1–2), 59–70. <https://doi.org/10.1021/acs.analchem.8b01867>

3. *RELATIONSHIPS BETWEEN DISSOLVED ORGANIC MATTER, HYDROGRAPHY AND TRACE ELEMENTS IN THE ARCTIC OCEAN

Tatiana Williford^{1*}, Rainer M.W. Amon^{1,2*}, Ronald Benner³, Karl Kaiser², Colin Stedmon⁴, Dorothea Bauch^{5,6}, Jessica Fitzsimmons¹, Loes J.A. Gerringa⁷, Robert Newton⁸, Dennis Hansell⁹, Mats A. Granskog¹⁰, Laramie Jensen¹, Luis M. Laglera¹¹, Angelica Pasqualini⁸, Benjamin Rabe¹², Heather Reader¹³, Michiel Rutgers van der Loeff¹², Ge Yan^{2#}

¹Texas A&M University, USA, ²Texas A&M University Galveston Campus, USA, ³University of South Carolina, USA, ⁴Technical University of Denmark, Denmark, ⁵Leibniz-Laboratory, University of Kiel CAU, Germany, ⁶GEOMAR Helmholtz Centre for Ocean Research, Germany, ⁷Royal Netherlands Institute for Sea Research, Netherlands, ⁸Columbia University, City of New York, USA, ⁹Rosenstiel School of Marine and Atmospheric Sciences, Miami, Florida, ¹⁰Norwegian Polar Institute, Fram Centre, Tromsø, Norway, ¹¹Universidad de las Islas Baleares, Spain, ¹²Alfred-Wegener Institute for Polar- und Marine Research, Germany, ¹³Memorial University of Newfoundland, St. John's, Canada

Abstract

Dissolved lignin phenols and optical properties of chromophoric dissolved organic matter (DOM) were determined in the Arctic Ocean during the International Arctic GEOTRACES effort in 2015. The apparent terrigenous contribution to Arctic DOM was observed by high correlation between concentrations of DOC and the terrigenous biomarker lignin. The *in situ* chromophoric DOM (CDOM) fluorescence had lower correlation with lignin phenols concentrations, than dissolved organic carbon (DOC), meaning that marine fluorophores were also present in the study region.

The Nansen basin water column was characterized by low DOM, with minor spikes of CDOM close to the Svalbard shelf break and protein-like fluorescence near the surface. High concentrations of tDOM proxies including lignin phenols were found in the Transpolar Drift current. At the surface of the Canada Basin, lignin phenol concentrations and CDOM were low, while the DOC concentrations were high, indicating significant marine DOM production in the western Arctic Ocean. The halocline structure was also reflected in the distribution of optical properties and biomarker concentrations. The levels of the *in situ* CDOM fluorescence and DOC concentration were lower in lower halocline (LHC) than in upper halocline (UHC) but are high comparing to the Atlantic-derived water ranges. Elevated concentrations of the sediment-derived

fluorophores were observed in the UHC. The concentration of the marine humic-like fluorophore was higher in the UHC comparing to the LHC, but the concentration of the terrigenous humic-like fluorophore was higher in the LHC comparing to the UHC. Lignin phenols concentrations and *in situ* CDOM fluorescence peaked at the UHC/LHC border.

The *in situ* CDOM fluorescence exhibits a stronger correlation with the sea-ice melt fraction than with the meteoric water fraction, suggesting that the freezing and thawing of sea ice is important for controlling DOM distributions in the Arctic Ocean. In contrast to the TPD, surface waters of the Canada Basin with similar levels of meteoric water, had very low concentrations of terrigenous DOM.

The DOM data were compared with dissolved trace metals: iron (dFe), manganese (dMn), nickel (dNi), copper (dCu), zinc (dZn), and cadmium (dCd). The DOM and trace metal correlations were examined to elucidate the sources, molecular characteristics and distributions of metal-binding ligands in the Arctic Ocean.

3.1. Introduction

The Arctic Ocean is a semi-enclosed, relatively shallow and small basin (1.3% of the global ocean volume) receiving a disproportionate fraction (~11%) of global river discharge. Fluvial discharge is an important source of both DOM and dissolved trace metals on the shelves and in the central basins of the Arctic Ocean (Opsahl et al. 1999; Amon 2004; Benner et al. 2005; Krachler et al. 2012; Klunder et al. 2012; Jensen et al. 2020; Benner 2011, Charette et al. 2020; Williford et al. 2021). Increased sea ice melt and increased precipitation over Arctic watersheds (Richter-Menge et al. 2019) and the Arctic Ocean (Vihma et al. 2016) result in further surface freshening that provokes major changes in stratification, circulation, and productivity. At the same time, permafrost thaw, tundra greening, and coastal erosion enhance mobilization of carbon from terrestrial Arctic ecosystems (Fritz et al. 2017; Berner et al. 2020), likely with a cascading effect on the supply of trace elements (Pokrovsky et al. 2012; Berner et al. 2020).

Poor understanding of the complex relationships among organic ligands and dissolved trace metals in seawater has limited our ability to predict the magnitude of certain metal fluxes, the spatial extent of their transport away from their source, and the rate of metal scavenging to the particulate phase across a range of metals. The Arctic Ocean is an ideal place to study metal-organic interactions because it has limited exchange with the other oceans and has abundant sources of organics and trace metals in the upper water column like fluvial discharge and shelf input. The low biological influences in the deep Arctic basins help to keep the sources signatures generally undisturbed by vertical remineralization.

In this study, we divide the surface Arctic Ocean into three regions based on the distribution of DOM, its optical properties, and its binding potential for dissolved trace metals:

1. The Nansen basin– Atlantic Eurasian shelf region, heavily influenced by Atlantic water (AW; $S > 34.7$; Rudels et al. 2001) inflow and north-flowing Eurasian rivers carrying significant quantities of freshwater, DOM, nutrients, trace metals and sediments into the Arctic Ocean (Sholkovitz et al. 1981; Walker et al. 2013; Rudels 2015; Holmes et al., 2019). The buoyant, low-salinity fluvial discharge mixed with the Atlantic water creates a steric height gradient from the shelves to the central Arctic Ocean (Rennermalm et al. 2006). Then it is diverted by the Coriolis force to form a circumpolar anti-clockwise current complexed by coastal geometry resulting in multiple branches and confluences (Carmack et al., 2016; Horner-Devine et al., 2015). The lower halocline is believed to be formed in this region via several mechanisms described in literature: the convective formation implying salination of cold and fresh surface water and melting of sea ice as Atlantic water enters the ice-covered Arctic shelves, and the advective formation involving the cold and saline shelf water spreading into the deep Arctic basins (Metzner et al. 2020).

2. The central Arctic basins, consisting of Amundsen and Makarov basins. The organic matter and trace metals pools are influenced by the TPD current, connecting the Eurasian shelves to the Fram Strait through surface advection (Charette et al. 2020). The region is marked by the presence of a clear terrigenous signature in DOM (Slagter et al. 2019; Paffrath et al. 2021; Williford et al. 2021).
3. The Chukchi shelf-Canada basin region, influenced by the advection of the relatively fresh ($S < 33$) nutrient-rich waters from the Pacific (Woodgate et al. 2012), modified on the shallow Chukchi shelf by the contact with sediments (Nakayama et al. 2011; Nishimura et al. 2012; Kondo et al. 2016). The upper halocline (UHC) derived from the Pacific water (PW) inflow lays on top of the LHC, and its core is identified by its maximum in nutrient concentration (Jones and Anderson, 1986). Atmospheric forcing creates the anticyclonic Beaufort Gyre in the Canada Basin (Fig.3.1; Morison et al. 2021), deepening the nutricline and chlorophyll maximum in the Canada Basin interior (McLaughlin et al. 2010).

The study regions physics and biogeochemistry are dynamic and are heavily affected by climate change. The exact geographical location of the TPD depends on the prevailing Arctic Oscillation regime (AO; Proshutinsky and Johnson, 1997). Since the early 1990s, the average AO has increased by one standard deviation, and the Arctic Ocean surface circulation underwent a cyclonic shift with an increased eastward transport of Siberian shelf waters (Morison et al. 2021). Besides the shifts in TPD location, the cyclonic mode is marked by the increased spatially averaged vorticity, enhanced export of sea ice and freshwater, a freshened Beaufort Sea, and a weakened lower halocline (Morison et al. 2021). The AO is anticipated to remain predominantly in a positive mode with further climate change (Givati and Rosenfeld, 2013). Describing the

organic matter distribution, which is the first objective of this paper, can be useful for identification of surface circulation patterns, stratification, and sea-ice processes.

This study traces DOM from various sources in the Arctic Ocean by combining hydrographic characterization of water masses, water fraction analyses, and the optical and chemical characterization of DOM. The second objective of this study is to explore the potential links between the diverse groups of molecules in chromophoric dissolved organic matter (CDOM) and the dissolved trace metals, dFe, dMn, dNi, dCu, dZn, dCd. To differentiate the DOM and potential trace metals sources, we use the terrigenous biomarker lignin phenols and optical properties including Parallel Factor Analysis (PARAFAC) of the fluorescent CDOM (FDOM). Lignin phenols are unique biomarkers of terrigenous DOM (tDOM) in the ocean (Opsahl and Benner, 1997; Opsahl et al. 1999; Benner et al. 2005, Kaiser et al. 2017, Williford et al. 2021).

3.2.Methods

3.2.1. Sampling

Water samples, *in situ* fluorescence, and hydrographic data were collected in summer 2015 during the U.S. Arctic GEOTRACES (GN01) cruise aboard the USCGC Healy (HLY1502) and the GEOTRACES TransARC II cruise (PS94) on the German icebreaker RV Polarstern (Fig. 3.1; Rabe et al. 2016; Schauer, 2016). The GN01 cruise track (August 9th to October 12th 2015; Kadko and Landing, 2015) consisted of a “northbound” transect along ~170°W stretching through Bering Strait and across the Canada and Makarov Basin to the North Pole (GN01 stations 1–32), and the “southbound” transect returning southward along ~150°W across the Makarov and Canada Basins back into Chukchi shelf waters (GN01 stations 33–57). The PS94 cruise track (August 17th to October 15th; Schauer, 2016) consisted of 2 transects extending

from the Barents Sea and the Gakkel Ridge, respectively, into Makarov Basin. The hydrographic data can be found in Pangaea (<https://www.pangaea.de>, CTD data:

<https://doi.org/10.1594/PANGAEA.859558>), the British Oceanographic Data Centre

(<http://www.bodc.ac.uk/geotraces>), and Biological and Chemical Oceanography Data

Management Office (Landing et al., 2019a, 2019b). The dissolved metal sections from both

cruises have been published previously (Rijkenberg et al. 2018 for GN04 Fe, Jensen et al. 2019

for GN01 Zn, Zhang et al. 2020 for GN01 Cd, Jensen et al. 2020 for GN01 Fe and Mn, Gerringa

et al. 2021 for GN04 trace metals, and Jensen et al. this issue for GN01 Cu and Ni).

The U.S. GEOTRACES GN01 and the TransARCII PS94 missions included two inter-calibration stations. Data from the North Pole station were collected synchronously (PS94 station 87, corresponding to GN01 station 32), while those from the deep Makarov Basin at 87°30'N 180°E (PS94 station 101, corresponding to GN01 station 30) were collected by the two missions two weeks apart.

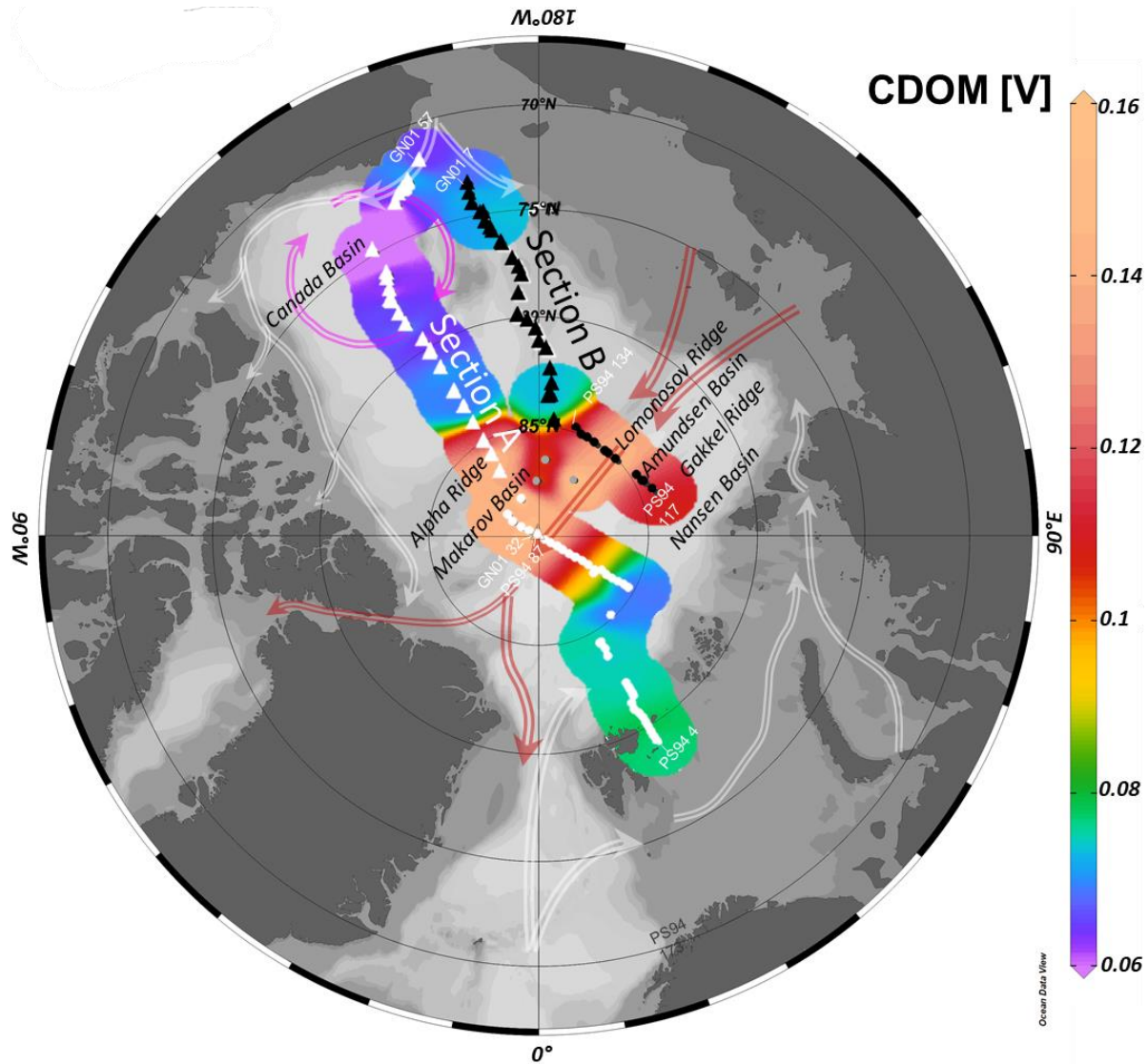


Figure 3.1. The U.S. GEOTRACES Arctic GN01 transect (triangles) and the TransARCII PS94 cruise track (circles) with relevant stations. Section A is presented as white color symbols; section B is presented as black color symbols. The approximate locations of major upper ocean circulation features are shown in grey, red (Transpolar Drift), and magenta (Beaufort Gyre). In situ CDOM fluorescence (excitation 350–460 nm/emission 550 nm HW 40 nm; Dr. Haardt, Optik Mikroelektronik, Germany) in surface waters is shown in color (in volts, V). This figure and section plots in the manuscript were generated using Ocean Data View (Schlitzer, 2020).

Here we define Section A (white symbols, Fig.1) as stretching from the Chukchi Sea shelf, across the North Pole (GN01 stations), and through the Amundsen and Nansen Basins to the Barents Sea (PS94 stations). Section B (black symbols, Fig. 1) is situated closer to the Asian continent and consists of the “northbound” leg of the GN01 cruise and the PS94 cruise transect between stations 117 and 134. Unfortunately, *in situ* fluorescence data was not collected along most of the Amerasian Basin portion of the section (Fig.3.1). Like section A, section B crossed the Amundsen and Makarov Basins, where the TPD was observed by the elevated surface *in situ* CDOM.

3.2.2 Dissolved inorganic and organic carbon

Dissolved inorganic carbon (DIC) concentrations were measured using the methods described in Woosley et al. (2017) and Ulfsbo et al. (2018). Details about the analysis during the two cruises and about uncertainty analyses were also discussed in Charette et al. (2020).

DOC concentrations were determined using a Shimadzu TOC-L, according to Halewood et al. (2010); all samples were filtered at the time of collection using 0.2 µm pore size. The data are available at Hansell (2017) and Hansell (2021). The accuracy was confirmed by measuring deep-water standards from the Consensus Reference Waters (Hansell, 2005). DOC measurements from both cruises (GN01 and PS94) were done at the Rosenstiel School of Marine & Atmospheric Sciences, University of Miami; they were consistent at the crossover stations.

3.2.3. Optical properties of DOM

CDOM fluorescence was measured *in situ* using two Dr. Haardt fluorometers with backscatter fluorescence sensors at 350-460 nm excitation and 550 nm HW 40 nm emission. The

light sources in the two instruments were slightly different on the GN01 and PS95 cruises, so the measurements were intercalibrated at the crossover stations, using a polynomial fit ($r^2=0.99$) of the data below 1000 m, where the fluorescence intensity is close to the detection limit (0.06 V) (Figure S3.1).

For the PS94 portion of the data, the details for the collected absorbance and fluorescence data are described in Stedmon et al. (2021). For the GN01 portion of the seawater optical data, 132 samples were collected. Absorbance was measured from 240 to 800 nm on a Shimadzu UV-1800 dual-beam spectrophotometer using a 5 cm quartz cuvette and pure water as a blank. DOM fluorescence was measured with a Photon Technologies International spectrofluorometer (Quanta Master-4 SE) using a 1 cm quartz cuvette. Excitation-emission matrix scans (EEMs) for each sample covering emission from 280 to 600 nm (2 nm increment) and excitation wavelengths ranging from 220 to 450 nm (5 nm increment). Daily pure water (Milli-Q®) blanks were obtained and subtracted to remove water scattering peaks. Data were spectrally corrected for instrument bias and subsequently, Raman calibrated (excitation 350 nm) using the pure water blanks using the drEEM toolbox (version 0.2.0, Murphy et al., 2013).

Studies show that not all the instrument bias is removed using the manufacturer's spectral correction procedures (Cory et al. 2010). This problem is particularly important when multivariate data analyses will be applied. To circumnavigate the potential minor spectral differences the datasets collected using different instruments were analyzed separately. The fluorescence was characterized using parallel factor analysis in MATLAB using the drEEM toolbox (version 0.2.0, Murphy et al., 2013). Excitation below 250 nm was not included due to excessive instrument noise resulting from poor lamp output.

Two PARAFAC models were developed for the EEMs data: a four-component model was developed for the Chukchi Sea-Canada Basin data set (C1) and a six-component model for the Nansen, the Amundsen, and the Makarov Basins data set (C2).

The Canada Basin EEMs were modeled separately from the TPD region EEMs to avoid the dominating effect of the terrigenous fluorescence signal overshadowing the more subtle fluorophores of the western Arctic. The four-component model (C1) was optimized based on spectral loadings, residual examination, and split-half validation using a convergence criterion of $1e^{-8}$ (Fig. 3.2a). The components were labeled based on their emission maxima: C1₄₈₂, C1₄₂₈, C1₄₀₂, C1₃₄₈. For the EEMs from the PS94 cruise, a six-component model (C2) was optimized based on spectral loadings, residual examination, and split-half validation using a convergence criterion of $1e^{-8}$ (Fig.3.2b). The components were labeled based on their emission maxima: C2₄₁₁, C2₄₅₆, C2₄₀₄, C2₄₉₂, C2₃₃₈, and C2₃₀₂.

The spectral characteristics of each component were matched those from several previous studies using the OpenFluor database (Murphy et al. 2014; Table S3.1, S3.2).

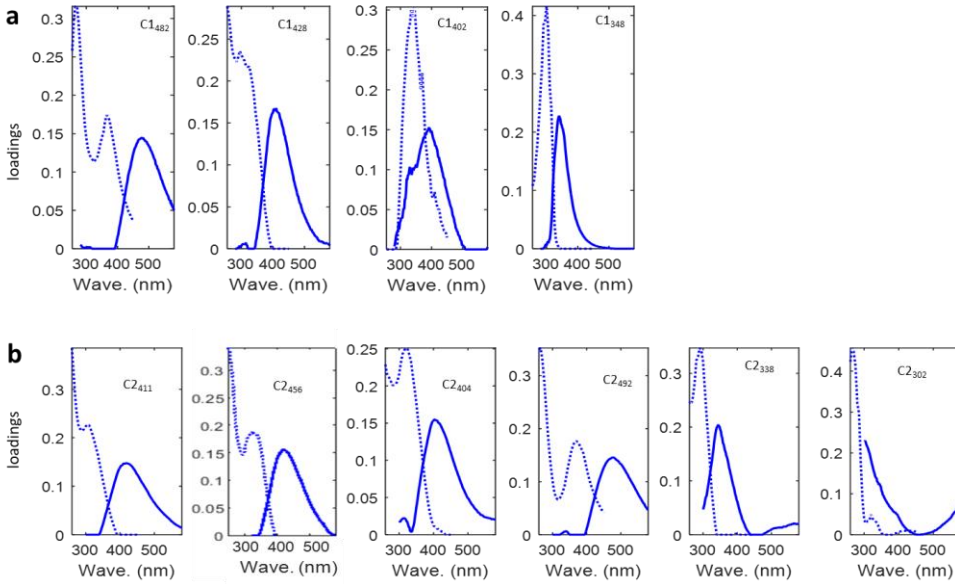


Figure 3.2. The fluorescence properties of fluorescent components identified by PARAFAC modeling in the Canada Basin (a) and the Nansen, Makarov, and Amundsen Basins (b).

The raw absorbance was baseline corrected by subtracting an offset-exponential fit of the absorbance spectrum over the range from 300 nm to 650 nm (Stedmon et al. 2000). The corrected absorbance (A_λ) was converted to Napierian absorption coefficients (a_λ) for each wavelength, λ , with the following formula:

$$a_\lambda = \ln(10) \frac{A_\lambda}{L}, \quad (5)$$

where L is the length of the cuvette in meters. Here we use the absorption at 254 (a_{254}) and 350 nm (a_{350}) as proxies for CDOM concentration and origin. Both absorbance coefficients were reported as good tracers for the terrigenous fluvial runoff in the Arctic Ocean (Walker et al. 2013; Griffin 2016; Chen et al. 2018).

Besides the absorption coefficients, the following optical indices were calculated: spectral slopes, the spectral slope ratio, and specific UV absorbance at 254 nm (SUVA; Helms et al. 2013; Fichot et al. 2013; Gonçalves-Araujo et al. 2020). The spectral slopes ($S_{xxx-xxx}$, where

subscripts denote wavelength range) for three absorbance spectra regions (275-295 nm, 350-400 nm, and 300-600 nm), and the Spectral Ratio (S_R ; $S_{275-295}/S_{350-400}$) were computed. Slopes $S_{275-295}$ and $S_{350-400}$ serve as indicators of photochemical alterations, and S_R correlates well with CDOM molecular weight (Helms et al., 2008; Granskog et al. 2012). $S_{275-295}$ is also an effective tracer of tDOM in river-influenced ocean margins (Fichot and Benner, 2012). The $S_{300-600}$ has the potential as a DOC concentration proxy (Makarewicz et al. 2018). SUVA is determined by dividing the absorbance at 254 nm by the DOC concentration and has been linked to DOM aromaticity (Helms et al. 2013).

3.2.4. Lignin phenols analysis

The sum of concentrations of nine lignin phenols (TDLP9) is reported in this study: p-hydroxyls (p-hydroxybenzaldehyde, p-hydroxy acetophenone, p-hydroxybenzoic acid), vanillyls (vanillin, acetovanillone, vanillic acid), and syringyls (syringaldehyde, acetosyringone, syringic acid). To measure the lignin phenols, 200 ml of unfiltered seawater samples were acidified to pH 2.5 using concentrated HCl (reagent grade) and extracted onto 1 g reversed-phase (C18) sorbent cartridges using a Dionex Autotrace 280 Solid-Phase Extraction instrument. Lignin phenol analysis was performed following the method of Yan and Kaiser (2018 a, b). It allows the quantification of dissolved lignin phenols in small volumes of seawater (<200 mL) using alkaline CuSO_4 at 150°C. Ultra-high performance liquid chromatography with mass spectrometry detection in dynamic Multiple Reaction Monitoring mode and isotopically labeled surrogate standards were used for the detection and quantification of monomeric lignin phenols.

3.2.5. Trace metal data

The dissolved iron and other trace metals data were obtained from Jensen et al. 2019 for GN01 Zn, Zhang et al. 2020 for GN01 Cd, Jensen et al. 2020 for GN01 Fe and Mn, Gerringa et al. this issue for GN04 trace metals, and Jensen et al. this issue for GN01 Cu and Ni. Sample collection and analyses followed GEOTRACES protocols (Cutter et al., 2010; Rijkenberg et al., 2018; Jensen et al., 2020).

3.2.6 Linear mixing model

In order to study the pathways of DOM and trace metals in the Arctic Ocean, the fractions of seawater with Pacific (f_{Pac}) and Atlantic (f_{Atl}) origin, sea ice melt (f_{SIM}), and meteoric water (f_{Met}) were determined based on the salinity (S), $\delta^{18}O$ -H₂O (stable oxygen isotope ratio (water)), and the Arctic N-P tracer (ANP, Newton et al., 2013). The mass balance for each sample was described by the system of the following equations:

$$f_{Pac} + f_{Atl} + f_{SIM} + f_{Met} = 1 \quad (1)$$

$$f_{Pac}[S_{Pac}] + f_{Atl}[S_{Atl}] + f_{SIM}[S_{SIM}] + f_{Met}[S_{Met}] = [S]_{measured}, \quad (2)$$

$$f_{Pac}[\delta^{18}O_{Pac}] + f_{Atl}[\delta^{18}O_{Atl}] + f_{SIM}[\delta^{18}O_{SIM}] + f_{Met}[\delta^{18}O_{Met}] = [\delta^{18}O]_{measured}, \quad (3)$$

$$f_{Pac}[ANP_{Pac}] + f_{Atl}[ANP_{Atl}] + f_{SIM}[ANP_{SIM}] + f_{Met}[ANP_{Met}] = [ANP]_{measured} \quad (4)$$

The end-member (water sources) values used in the calculations are presented in Table 3.1. The end-member definitions are also sources of error, due to the nonconservative behavior of nutrients across the Arctic Ocean, large variability, and potential drift of salinity and $\delta^{18}O$ in the source waters. The isotope data was previously presented by Pasqualini et al. (2017) and by Paffrath et al. (2021). Dissolved macronutrients were analyzed shipboard at room temperature on a Seal Analytical continuous-flow AutoAnalyzer 3, following the methods according to the

protocols (Hydes et al., 2010; Cutter et al., 2014). The limitations of the method are discussed in detail in Newton et al. (2013) and Charette et al. (2020).

Table 3.1. End-member values used in mass balance calculations

Water Mass	Salinity	d18O [permille]	Arctic N:P (ANP)
Atlantic	34.92	0.3	0
Pacific	32.5	-1.1	1
Meteoric	0	-19	0
SIM	4	surf +2.6	surf

3.3. Results

3.3.1. Hydrographic setting

The following hydrographic distinctions of water masses were assigned. The thickness of the relatively fresh Polar Mixed Layer (PML; $S < 31$) is conventionally defined by the temperature minimum (Rudels et al. 1996). However, in cases where the temperature minimum cannot be identified with certainty, the rapid change in magnitude of the salinity gradient may be used (Korhonen et al. 2013). For example, the Chuckchi Sea and southern Canada Basin, where both sections A and B depart from, are strongly influenced by the seasonal ice melt, resulting in the near-surface temperature maximum from radiative warming of surface waters during summer (Shimada et al. 2001). According to the climatology, the average depth of winter convection is about 45m in the northern Canada Basin and to 35m in the southern Canada Basin (Korhonen et al. 2013). In the Amundsen and Makarov basins, the average depth of the PML deepens to about

55 m, becomes shallower and occupies a depth of 40 to 50 m in the Nansen Basin (Korhonen et al. 2013).

In the Canada Basin, below the PML, lays the UHC, largely derived from the Pacific water. Because of its origin, the boundary between the upper and the lower haloclines is roughly defined by the isohaline of $S = 34$ (Korhonen et al. 2013). The Beaufort Gyre is a large anticyclonic system in the surface layer of the Canada Basin, marked by low salinity and low *in situ* CDOM fluorescence (Fig.3.1). Shelf-waters within the UHC and LHC are pushed downward by convergence associated with Ekman forcing in the surface Beaufort Gyre (Watanabe 2012). According to the climatology (Korhonen et al. 2013), the UHC is the thickest (180-200 m) in the southern Canada Basin. In the Makarov and Amundsen Basins the thickness decreases to 40m and 30 m, respectively, and in the Nansen Basin the UHC is generally absent (Korhonen et al. 2013). The LHC thickness in the Canada Basin varies between 60 and 70 m and increases towards the central Arctic Basins (~80 m in the Amundsen and Makarov Basins), and becomes thinner, < 50 m, in the Nansen Basin (Korhonen et al. 2013). The AW beneath the haloclines transitions into dense ($\sigma > 28 \text{ kg/m}^3$) deep water (DW) below 1000 m depth.

3.3.2 *In situ* CDOM fluorescence

In situ CDOM fluorescence was consistently low throughout the water column of the Nansen Basin (~0.07V; Fig.3.3). The hydrography of the surface central Arctic Ocean is governed by the TPD system: the upper 70 meters are characterized by high *in situ* CDOM fluorescence (up to 0.17 V). The fluorescence signal could be traced to the depth of 210 meters in the Makarov and Amundsen Basin, and to about 180 meters above the Lomonosov ridge dividing the basins.

In situ CDOM fluorescence was very low at the surface of the Canada Basin (close to the detection limit of 0.06V), and enriched in the UHC, consistent with previous studies (e.g. Shen et al. 2016; Gao and Guéguen 2018). The peak of CDOM fluorescence was detected at the UHC/LHC interface, about 50 meters below the UHC core as defined by the nutrient maximum depths (Figure 3.3). The LHC is also characterized by elevated *in situ* fluorescence intensity compared to underlying AW. The *in situ* CDOM fluorescence signal follows the density gradient in the water column, e.g., isopycnal of $\sigma\sim 27.8 \text{ kg/m}^3$ closely coincided with the lower border of the CDOM trace in the Canada basin.

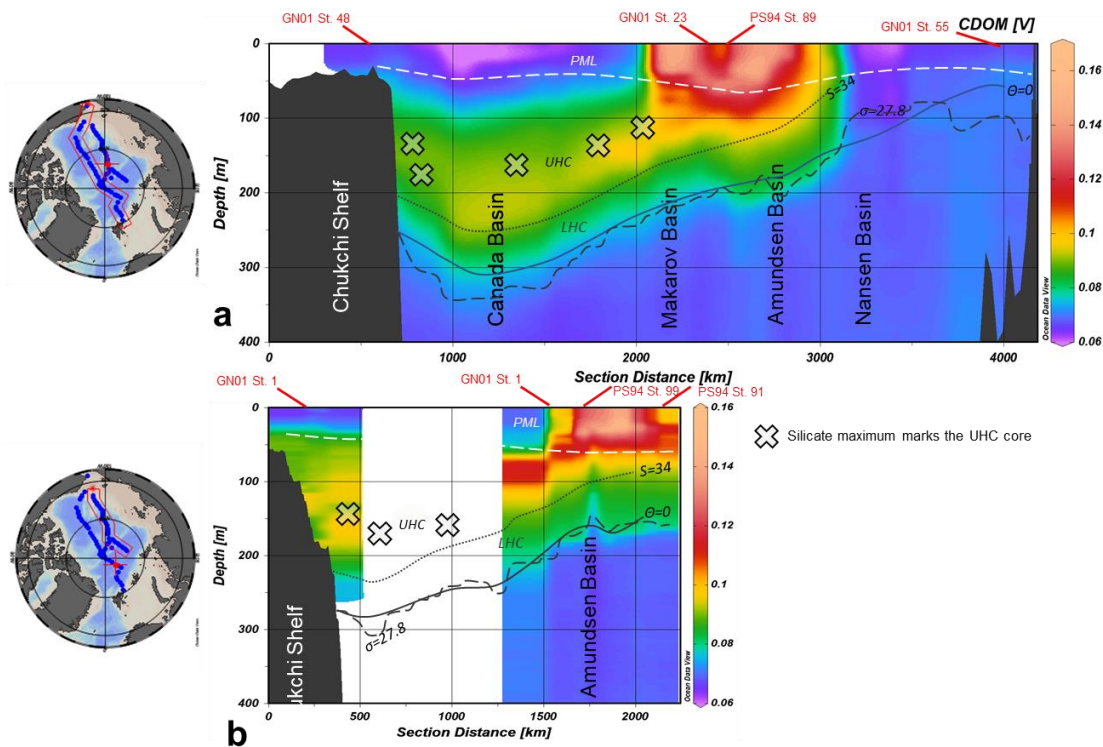


Figure 3.3. *In situ* CDOM fluorescence for sections A (a) and B (b) in the upper 400 m. The white dashed line represents the border of the PML. Black dotted isohaline of $S = 34$ represents the lower bound of the UHC. The LHC is bordered at the bottom by the isotherm of $\Theta = 0^\circ\text{C}$ (black solid line). Isopycnal of $\sigma=27.8 \text{ kg/m}^3$ (black dashed line) closely follows the lower

border of the CDOM trace in the Canada basin. The silicate maximum marks the core of the UHC according to Anderson et al. (2013)

3.3.3. Dissolved organic carbon

Similarly to the *in situ* CDOM fluorescence, the DOC concentrations were low throughout the water column ($\sim 60 \mu\text{mol/L}$) in the Nansen Basin (Figure 3.4a, 3.5a). Within the TPD region, the DOC concentrations were also high (up to $138 \mu\text{mol/L}$), but the signal was shallower than for CDOM (maximum depth was 170 meters in the Amundsen Basin).

The distribution of DOC concentration was the opposite to the CDOM in the Canada Basin. The former was enriched at the surface of the central Canada Basin and decreased with depth. DOC was near background levels ($\sim 50 \mu\text{M}$) within the LHC and AW. The surface of the Canada Basin around section B was enriched in DOC ($\sim 80 \mu\text{M}$) comparing to that around section A ($\sim 65 \mu\text{M}$), which is closer to the Eurasian shelves.

3.3.4. Dissolved inorganic carbon

Similar to the *in situ* CDOM fluorescence, the DIC in the Canada Basin was very low at the surface (Figure 3.4b, 3.5b), and enriched in the UHC. The maximum concentration of the DIC generally coincided with the nutrient maximum marking the core of the UHC. Within the TPD, the trend was the opposite to that of *in situ* CDOM fluorescence, as the surface of the Makarov and Amundsen basins was depleted in DIC. The Atlantic inflow in the eastern Arctic had higher DIC than the Pacific inflow at the Chuckchi shelf, which indicates the elevated DIC in the UHC is produced within the Arctic.

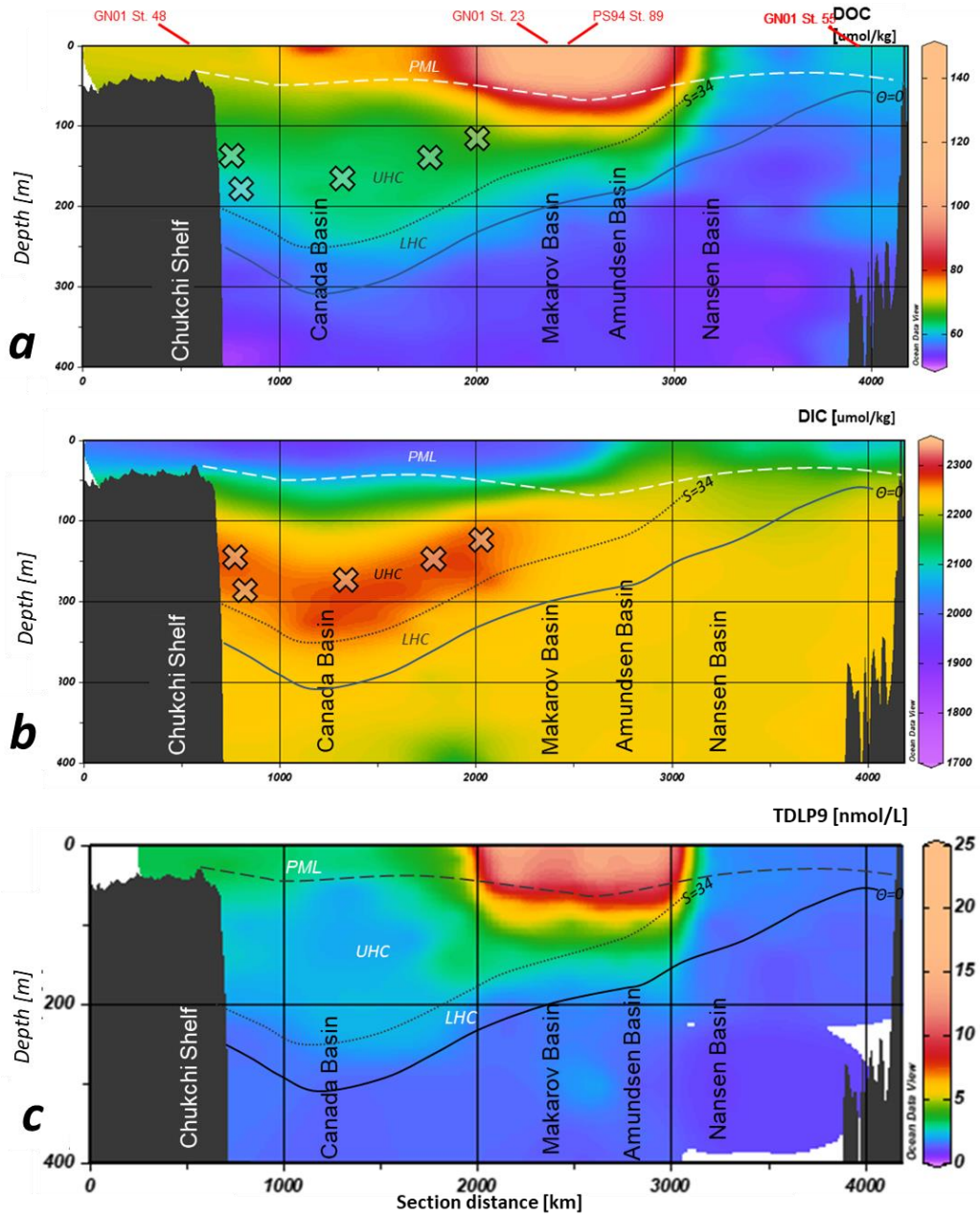


Figure 3.4. The dissolved organic carbon (DOC, a), dissolved inorganic carbon (DIC, b) and lignin phenols (TDLP9, c) concentrations for section A in the upper 400 m. The white dashed line represents the border of the PML. Black dotted isohaline of $S = 34$ represents the lower bound of the UHC. The LHC is bordered at the bottom by the isotherm of $\Theta = 0^\circ\text{C}$ (black solid line). The silicate maximum marks the core of the UHC according to Anderson et al. (2013)

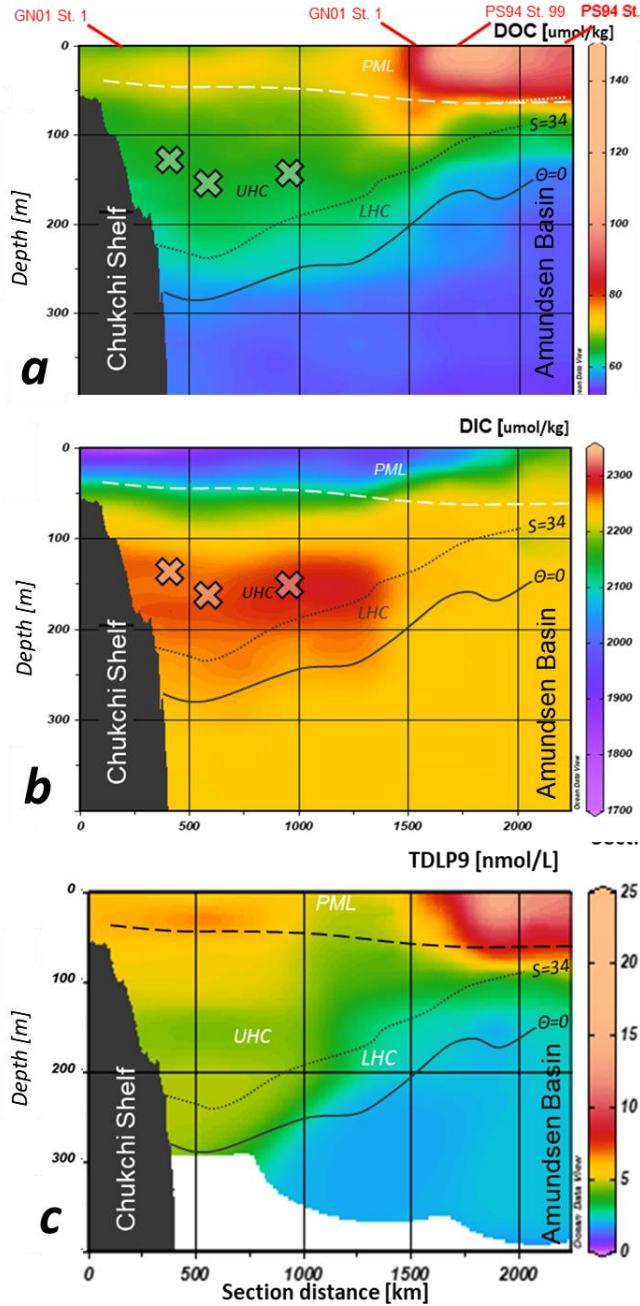


Figure 3.5. The dissolved organic carbon (DOC, a), dissolved inorganic carbon (DIC, b) and lignin phenols (TDLP9, c) concentrations for section B in the upper 400 m. The white dashed line represents the border of the PML. Black dotted isohaline of $S = 34$ represents the lower

bound of the UHC. The LHC is bordered at the bottom by the isotherm of $\Theta = 0^{\circ}\text{C}$ (black solid line). The silicate maximum marks the core of the UHC according to Anderson et al. (2013)

3.3.5. Lignin phenols

The high salinity (>34.7) waters of Atlantic origin dominating the Nansen Basin were characterized by low concentrations of lignin phenols (Fig.3.4a). The terrigenous origin of DOM within the TPD is confirmed by the high lignin phenol concentrations (up to 21 nmol/L). In the Canada Basin, the vertical gradient was different from CDOM or DOC distributions. Lignin phenols concentrations reached ~ 3 nM at the surface of the Canada Basin, decreased to ~ 1.9 nM within the UHC, and was slightly enriched (up to ~ 3 nM) in the UHC/LHC border. Regarding the differences between the sections A and B, the trend was the opposite to the DOC distribution: the lignin phenols had higher concentrations around section B.

3.3.6. Optical properties

The absorption coefficients a_{254} and a_{350} had the highest values ($\sim 8 \text{ m}^{-1}$; $\sim 1.5 \text{ m}^{-1}$, respectively) within the TPD region (Figure S.3.3). The a_{254} was also slightly enriched at the surface of the Nansen Basin ($\sim 2.6 \text{ m}^{-1}$), and a_{350} values were slightly enriched ($\sim 0.5 \text{ m}^{-1}$) within the UHC in the Canada Basin (Figures S3.2, S3.3, S3.4). The rest of the water masses were characterized with low absorption coefficients values. The distribution of SUVA was similar to that of the DOC: low values were reported for the water masses of the Nansen Basin ($\sim 2.5 \text{ m}^2 \text{ gC}^{-1}$), the highest values were related to the TPD system (up to $\sim 6 \text{ m}^2 \text{ gC}^{-1}$, and some enrichment in SUVA was discovered at the surface of the Canada Basin ($\sim 4 \text{ m}^2 \text{ gC}^{-1}$).

For the $S_{275-295}$, the highest values were reported in the Nansen Basin (up to 35 nm^{-1}), followed by the Chukchi shelf (up to 30 nm^{-1} ; Figures S3.2, S3.3, S3.4). Throughout the water column of the Nansen Basin and below the haloclines the values remained elevated ($>27 \text{ nm}^{-1}$). The low values ($20\text{-}25 \text{ nm}^{-1}$) were reported for the TPD region, the UHC and the surface of the Canada basin. The $S_{350-400}$ values generally varied between 15 and 18 nm^{-1} . The slightly higher values were reported for the PML, and below the haloclines. The $S_{300-600}$ distribution in the Arctic Ocean did not show any meaningful patterns in relation to the water masses. The S_r values were the highest (>35) for the Atlantic inflow in the Nansen basin and the Pacific inflow on the Chukchi shelf, and below the haloclines. The TPD region, the surface of the Canada Basin and the UHC had low levels of S_r (<25).

Of the different fluorophores observed in the Canada Basin in this study, component $C1_{482}$ was earlier described as a terrigenous fluorophore, e.g. in Arctic boreal lakes (Kothawala et al. 2014) and the Arctic Ocean (Walker et al. 2009; Williford et al. 2021). In the Canada Basin, the $C1_{482}$ component had the strongest correlation with *in situ* CDOM fluorescence and with lignin phenol concentrations ($r=0.72$ and $r=0.8$, respectively, $p<0.001$), indicating terrigenous origin. The $C1_{482}$ fluorescence intensity increased in the PML/UHC border and in the UHC/LHC border of the Canada Basin. Component $C1_{434}$ has lower aromaticity than $C1_{482}$ and appears to have a ubiquitous origin (Kothawala et al. 2014), as indicated by a higher correlation with DOC ($r=0.79$, $p<0.001$) and slightly lower correlation with lignin phenols ($r=0.75$, $p<0.001$).

$C1_{402}$ has been observed spreading from the Chukchi Sea shelf to the core of the UHC in the Canada Basin (Chen et al. 2018). This signal likely originates from marine organic matter decomposition in surface sediments on the shelf consistent with a significant correlation between

C1₄₀₂ fluorescence intensity and DIC concentration in the Canada Basin ($r=0.7$, $p<0.0001$). The distribution of the only protein-like component C1₃₄₈ in the Canada Basin was similar to that of C1₄₀₂, but with a more pronounced fluorescence signal closer to the Chukchi Sea shelf.

Among the fluorophores identified in the Nansen, Amundsen, and Makarov Basins, components C2₄₁₁, C2₄₅₆, C2₄₀₄, and C2₄₉₂ were humic-like while C2₃₃₈ and C2₃₀₂ had a protein-like signature. C2₄₁₁ had the highest fluorescence intensity and is usually suggested to be produced in the water column (Yamashita et al. 2013). The two fluorescent components, C2₄₅₆, and C2₄₉₂ are usually described to be of terrigenous origin (Yamashita et al. 2013; Kothawala et al. 2014, Williford et al. 2021) had the strongest correlations with lignin phenol concentrations ($r=0.88$ and $r=0.92$, respectively, $p<0.001$). C2₄₅₆ is commonly found in the Arctic Ocean and was reported in surface waters of the central Arctic, close to the Mackenzie River mouth and the Amundsen Gulf (How about Walker et al. 2009? Guéguen et al., 2015), and in the Lena River (Gonçalves-Araujo et al. 2015). C2₄₉₂ has a longer emission wavelength than C2₄₅₆, indicating molecules with higher molecular weight, and hydrophobicity. Relative to C2₄₅₆, C2₄₉₂ is prone to flocculation, and its fluorescence intensity in the TPD region and the lower halocline is lower but relatively higher on the shelf. C2₄₉₂ fluorescence co-varied with dFe in boreal lakes (Kothawala et al. 2014). Similar to C1₄₀₂, the fourth humic component (third by intensity) C2₄₀₄ resembled a fluorescence signal that had been observed near the Chukchi Sea shelf and in the core of the upper halocline in the Canada Basin (Chen et al. 2018; Williford et al. 2021). The tryptophan-like C2₃₃₈ and the tyrosine-like C2₃₀₂ components have been reported in marine surface waters (Stedmon et al. 2011b; Chen et al. 2018; Williford et al. 2021). Previously, the C2₃₃₈ was reported as related to sea-ice CDOM and brine accumulation (Stedmon et al. 2011b). The

tyrosine-like C2302 was reported to be derived partly from the shelf and slope sediments (Chen et al. 2018).

In the Amundsen and Makarov basins, among the PARAFAC components, C2411 and C2456 dominated the fluorescence signal in the PML and the upper and lower haloclines of the Makarov basin (Fig. S3.3). C2338 and C2492 were slightly elevated in the PML and the haloclines. C2411 and C2338 had the highest fluorescence intensity in the PML, while terrigenous C2456 and C2492 were most elevated at about 20 m depth at the upper boundary of the upper halocline.

The fluorescence intensity of all different PARAFAC components was low in the Nansen Basin (Fig.S3.2). The protein-like components were slightly elevated at the surface of the northern Nansen basin. The Svalbard slope was also characterized by an increase in the fluorescence intensity of all the components.

3.3.7. Water fractions

The four basic water fractions identified for the Arctic Ocean (Atlantic water or f_{Atl} , Pacific water or f_{Pac} , meteoric water or f_{Met} , and ice melt water or f_{SIM}), based on the salinity, $\delta^{18}O$, and the ANP (Newton et al. 2013) indicate that up to 100% of the water in the central Nansen Basin originated from the Atlantic Ocean (Fig.3.6). The f_{SIM} constituted 5% of the PML in the Nansen Basin. The Makarov and the Amundsen Basins were similar in terms of the water fraction contributions to the PML, UHC, and LHC, except that the major water masses had a shallower distribution in the Amundsen Basin than in the Makarov Basin. The PML and the UHC were dominated by the f_{Pac} (up to ~78%), with a significant (up to ~22%) contribution of the f_{Met} from the TPD. According to the computed fractions, the PML, UHC were also affected by brine formation in the upper 100m. Surface waters of the Amundsen and Makarov Basins are

heavily influenced by freshwater in the TPD originating from the Siberian shelves. These waters are not only affected by river discharge but also subject to ice melt, ice formation, and brine injection. The brine formation process is reflected in f_{SIM} differences between section A, crossing the Arctic Ocean through the North Pole, and section B, situated closer to the Eurasian shelves (Fig. 3.1). According to the water fraction analysis, the surface layer (50-100 m) in section B contained up to ~6% as brine, and section A (further downstream) up to ~10%, possibly implying the freezing process in the central Arctic and/or reflecting variability in shelf waters. Nevertheless, it is more likely due to the release of shelf water within the TPD system in pulses (Bauch et al. 2011; Karcher et al. 2012; Thibodeau et al., 2014; Thibodeau and Bauch, 2015).

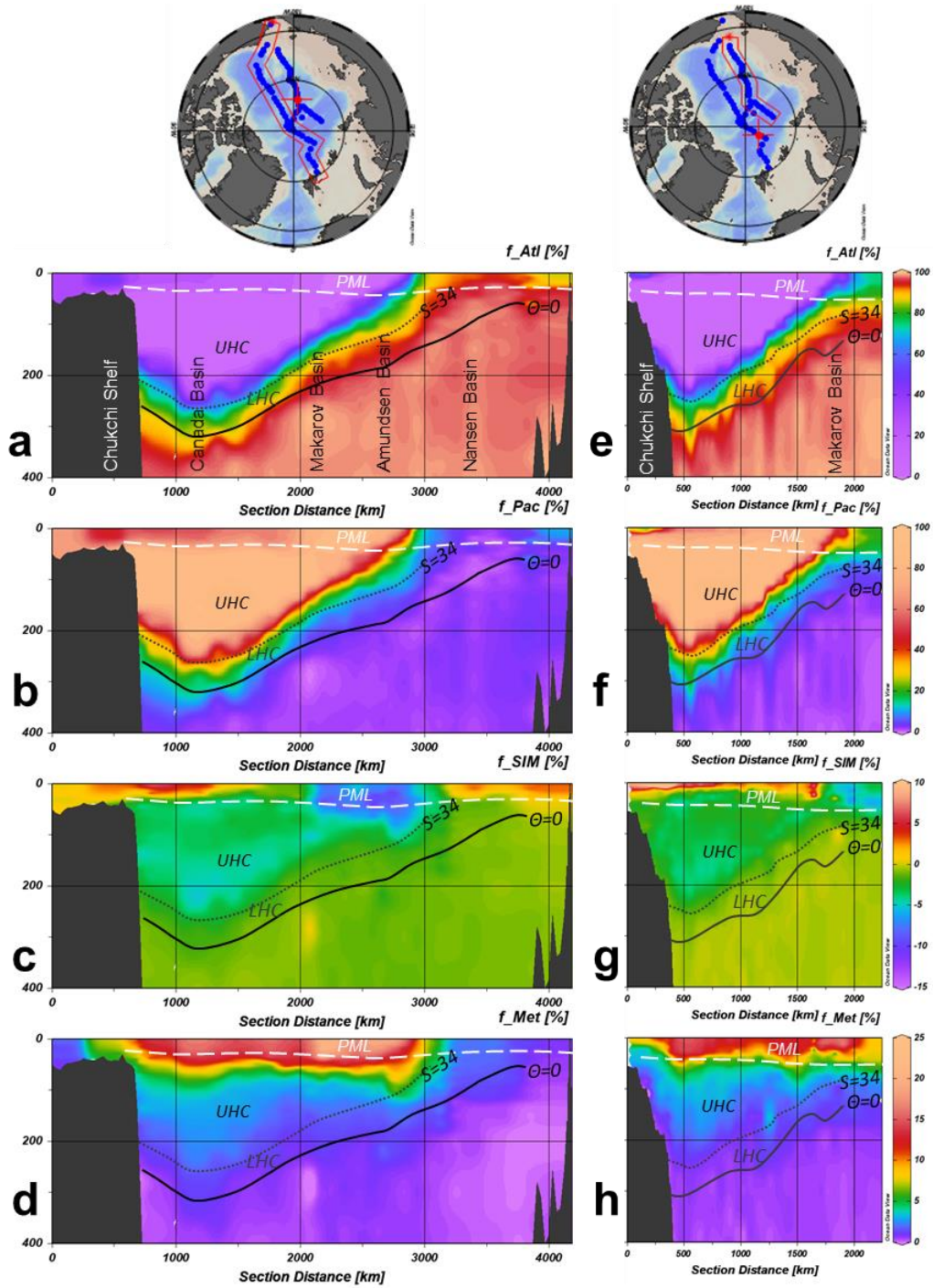


Figure 3.6. Calculated fractions of f_{Atl} , (a, e), f_{Pac} (b, f), f_{SIM} (c, g) and f_{Met} (d, h) for sections A and B. The white dashed line represents the border of the PML. Black dotted isohaline of $S = 34$ represents the lower bound of the UHC. The LHC is bordered at the bottom by the isotherm of $\Theta = 0^\circ\text{C}$ (black solid line).

3.7.8. Trace metals

Due to the TPD influence, the top 20 meters of the Makarov and Amundsen Basins showed a strong increase in concentrations of dFe, dNi, dCu and dMn, and a decrease below 50 meters (Charette et al. 2020; Figure S3.2). Below the PML, concentrations of dFe, dNi, dCu, and dMn exhibit patterns similar to the humic components profiles in the TPD region. In contrast, concentration of dZn and dCd peaked at ~200 m. The concentration of the dZn was low within the TPD and the concentration of dCd was slightly elevated at the surface comparing to the AW, but both trace metals were enriched in the UHC (Jensen et al. 2019; Zhang et al. 2019).

The dFe concentrations were elevated close on the Chukchi shelf, but the signal rapidly dissipated offshore (Jensen et al. 2020). The dMn concentrations were elevated within the PML in the Arctic Ocean, with the strong gradient from the high values at the Chukchi shelf and the lowest values in the Nansen Basin (Jensen et al. 2020). The dCu and dNi had similar distributions in the Arctic Ocean (Jensen et al 2021), both trace metals concentrations were elevated in the TPD, and slightly elevated in the PML and UHC of the Canada Basin (dNi has a more pronounced peak within the UHC than dCu). The distributions of dZn and dCd were also similar in the Arctic Ocean (Jensen et al. 2019, Zhang et al. 2019), with an apparent enrichment within the UHC, and a slight enrichment in the LHC. However, the surface of the Canada Basin was slightly enriched in dCd, but the concentration of dZn was low.

In the Nansen Basin, the concentrations of the trace metals were also low throughout the upper water column (top 300 meters), with an exception of dMn, elevated at the surface (Gerringa et al. 2021; Figure S3.4).

3.4. Discussion

3.4.1. Indicators of tDOM

The apparent terrigenous contribution to the DOM pool distinguishes the Arctic Ocean from the other oceans (Anderson and Amon 2015). This was observed with the high correlation between the DOC and terrigenous biomarker lignin concentrations in this study (Figure 3.7c). The *in situ* CDOM fluorescence had lower correlation with lignin phenols concentrations, than DOC, meaning that autochthonous fluorophores were also present in the study region (Figure 3.7b). For comparison, in the 2007 study in the eastern Arctic Ocean (Williford et al. 2021), lignin phenols concentration correlated equally with the DOC and *in situ* CDOM fluorescence ($r=0.76$, $r=0.77$, respectively; $p<0.01$), indicating significant marine DOM production in the western Arctic Ocean.

Among the optical properties calculated in this paper, the C_{2492} and C_{2456} were the strongest proxies of lignin phenols (Figure 3.7b). The correlations between the fluorophores in the Canada Basin were weaker between the biomarker concentrations and the PARAFAC components C1, than C2 components in the Amundsen, Makarov and Nansen Basins (Figure 3.7a, b), indicating the fluvial discharge leaves more apparent signal in the DOM pool on the Eurasian side and in the TPD. The absorption indices a_{254} and a_{350} had high agreement with lignin phenols concentration (Figure 3.7c). In general, the correlations between the lignin phenols and the optical properties were higher in 2015 study, than in the 2007 one (Williford et al. 2021). This could be explained by remarkable amount of ice melt in 2007 in the eastern Arctic Ocean.

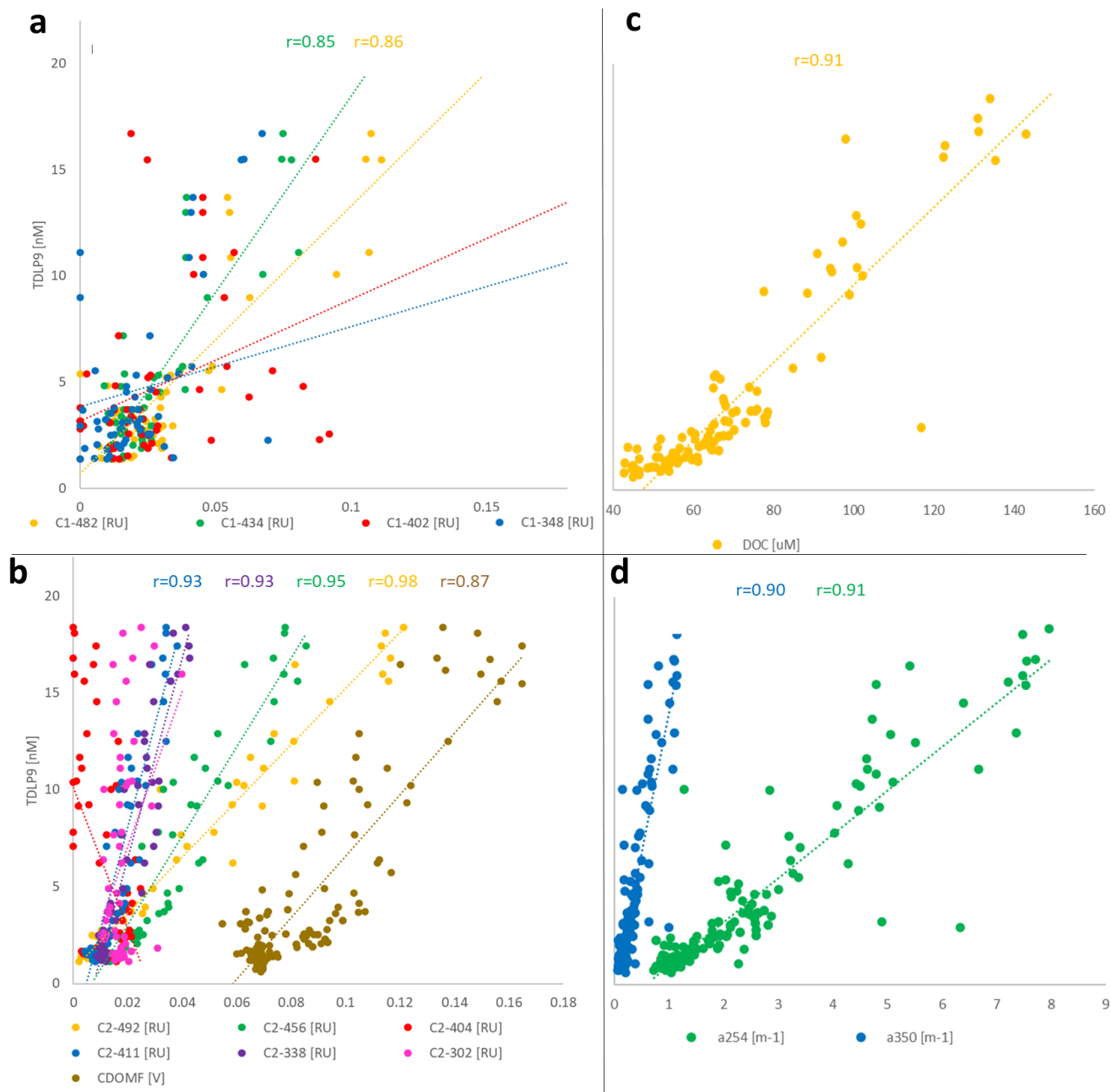


Figure 3.7. Scatterplots between the lignin phenols concentrations and C1 PARAFAC components (a), C2 PARAFAC components (b), dissolved organic carbon (DOC, c) and absorption coefficients a_{254} and a_{350} (d) in the top 300 meters of the Arctic Ocean. Only significant correlations ($p < 0.001$) are shown.

3.4.2. DOM and trace metals in relation to DOM and hydrographic features

3.4.2.1. The TPD

Fluvial discharge is an important source of DOM and trace metals in the Arctic Ocean (Sholkovitz et al. 1981; Walker et al. 2013; Holmes et al., 2019). In the Amundsen and Makarov Basins, the concentrations of tDOM indicators, dFe, dNi, dCu, and dMn were elevated in the upper 70 meters (Charette et al. 2020), the layer heavily influenced by the TPD current. The C₂₄₉₂ as the strongest indicator of tDOM shown by the highest correlation with lignin phenols concentration in top 300 meters of the Amundsen and Makarov basins ($r=0.99$, $p<0.0001$), followed by C₂₄₅₆ ($r=0.91$, $p<0.0001$). Besides the humic-like components of terrigenous and marine origin, the protein-like C₂₃₃₈ exhibited high correlation with the biomarker concentration ($r=0.90$, $p<0.0001$).

Among the metals elevated within the TPD, dFe is known for complexation with tDOM ligands (Slagter et al. 2017, 2019; Laglera et al. 2019; Williford et al. 2021), a process confirmed by high correlation with C₂₄₅₆ and C₂₄₉₂ in this study (0.96 and 0.92, respectively, Figure 3.8b). The former humic-like compounds composing C₂₄₅₆ are less prone to flocculation and are transported further offshore (it is more abundant in the TPD region and the lower halocline), which makes it a more important ligand in the central Arctic Ocean than C₂₄₉₂, despite lower molecular weight and aromaticity, both linked to the binding strength of ligands (Kikuchi et al. 2017). The dFe concentrations exhibited stronger correlations with DOC and optical indicators of tDOM than with lignin phenols in the central Arctic Ocean, which means that other potential ligands of terrigenous origin (e.g., tannins) are important (Figure 3.8c). In the Amundsen, Makarov, and Nansen Basins, dFe exhibits also a very strong relationship with the marine humic component C₂₄₁₁, indicating that the autochthonous DOM plays an important role in iron distribution in the Arctic ocean.

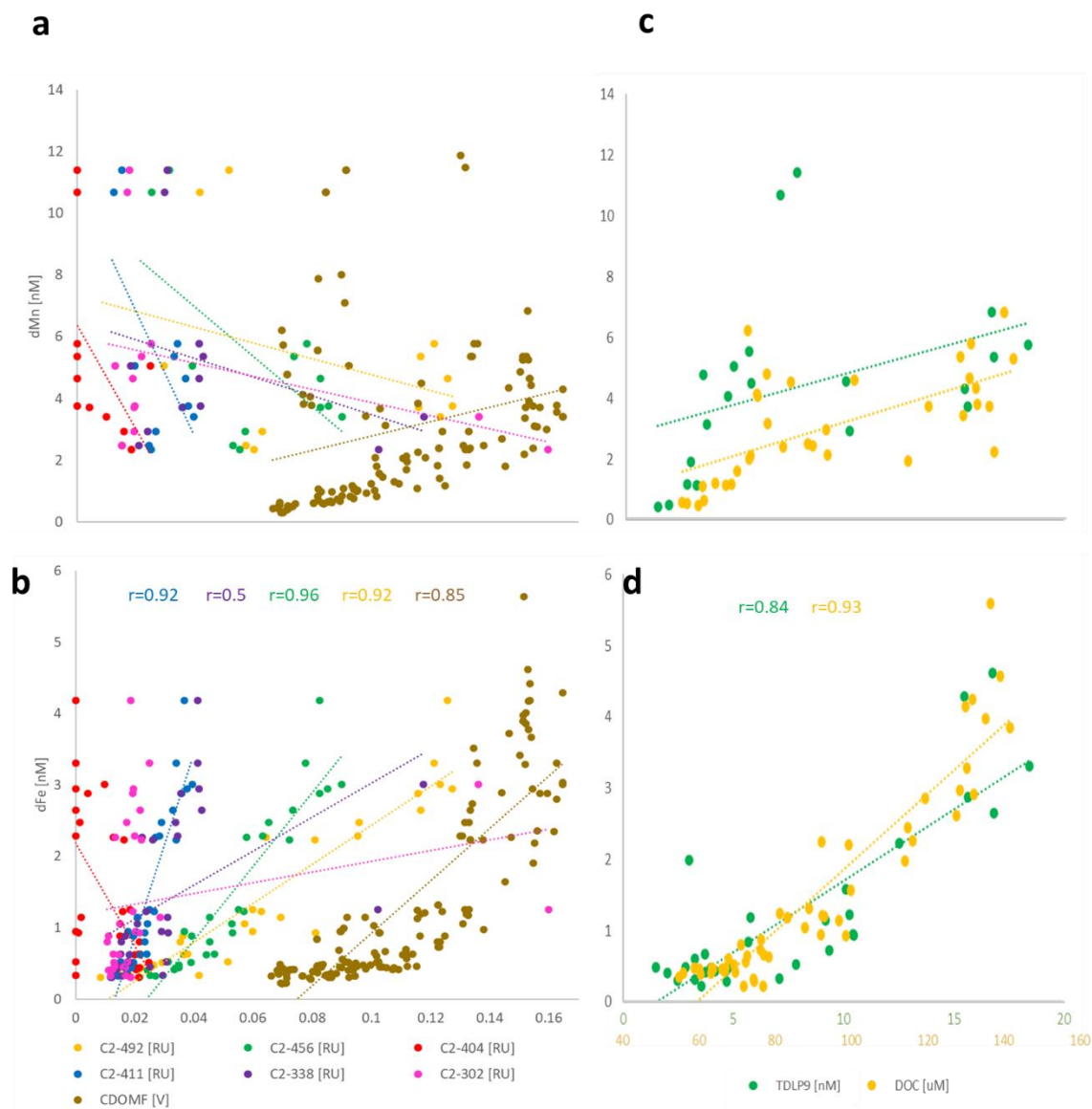


Figure 3.8. Scatterplots between the dMn (top panels), dFe (bottom panels) and C1 PARAFAC components and *in situ* CDOM fluorescence (CDOMF; a, b), lignin phenols (TDLP9) and dissolved organic carbon (DOC; b, d), in the top 300 meters of the Makarov and Amundsen Basins. Only significant correlations ($p < 0.001$) are shown.

Dissolved manganese shares common sources and sinks with dFe but has a different redox reactivity and speciation that causes differences in distribution in the Arctic Ocean (Middag et

al., 2011; Jensen et al. 2020). For example, the correlation between dFe and f_{Met} in the TPD was stronger than between dMn and f_{Met} in the TPD (Charette et al. 2020). The correlations between the dMn , in situ CDOM fluorescence, DOC and lignin phenols were positive, but statistically insignificant (Figure 3.8a, b). In contrast to the dFe , dMn is less dependent on organic complexation, most dMn in the seawater is considered to exist in the free form (Byrne, 2002). However, recent study in the Chesapeake Bay shows that in the presence of ligands, $Mn(III)$ can be stabilized in solution as stable $Mn(III)$ complexes (Oldham et al. 2015). Additionally, $Mn(III)$ has a strong affinity for ligands that also bind $Fe(III)$ (Duckworth et al., 2009). Within estuaries, dMn does not undergo significant salt-initiated coagulation or precipitation (Sholkovitz and Copland, 1981). Within the PML, the concentrations of dMn are maximum on the Chukchi shelf and they decrease offshore.

The other two dissolved metals that had strong TPD signals were dNi and dCu . The extrapolated riverine concentrations of dNi and dCu calculated from their TPD relationships with f_{Met} in the TPD are comparable to the Eurasian Arctic river averages (17nmol/L and 22nmol/L, respectively; Holmes et al., 2019), suggesting that these trace metals are organically complexed before leaving the river, thus escaping flocculation in estuarine waters. While divalent dCu is known to be organically complexed in natural waters (Semeniuk et al 2015, Shank et al. 2004), the organic chelation of dNi is less well understood (Vraspir & Butler, 2009) but at least partially complexed by strong organic ligands ($\log K=17-19$; Van den Berg and Nimmo, 1987; Morel et al. 2003). A prior study shows that terrestrial humic substances are the likely source of high-affinity, low abundance ligands for dCu (Muller and Batchelli, 2013). Another study reported that fluvial allochthonous organic matter dominated the strong

complexation capacity of dCu in the Cape Fear River estuary (Shank et al. 2004). However, the relative importance of such potential ligands in the central Arctic remains an open question.

Here, we report strong correlations within the TPD between dNi and dCu and all humic-like fluorophores (Figure 3.9a,b). The highest correlation, once again, was reported for the C2₄₉₂, and this correlation was higher than that with the lignin phenols (Figure 3.8c, d), indicating of presence of other terrigenous fluorophores that can serve as ligands. Interestingly, among the trace metals, dCu showed the strongest correlation with tDOM in the top 300 meters of the Arctic Ocean.

While we cannot know for sure that the correlations between the trace metals and the organic compounds mean organic complexation, their strong correlations certainly warrant further investigation of the organic ligand binding of these riverine-derived metals.

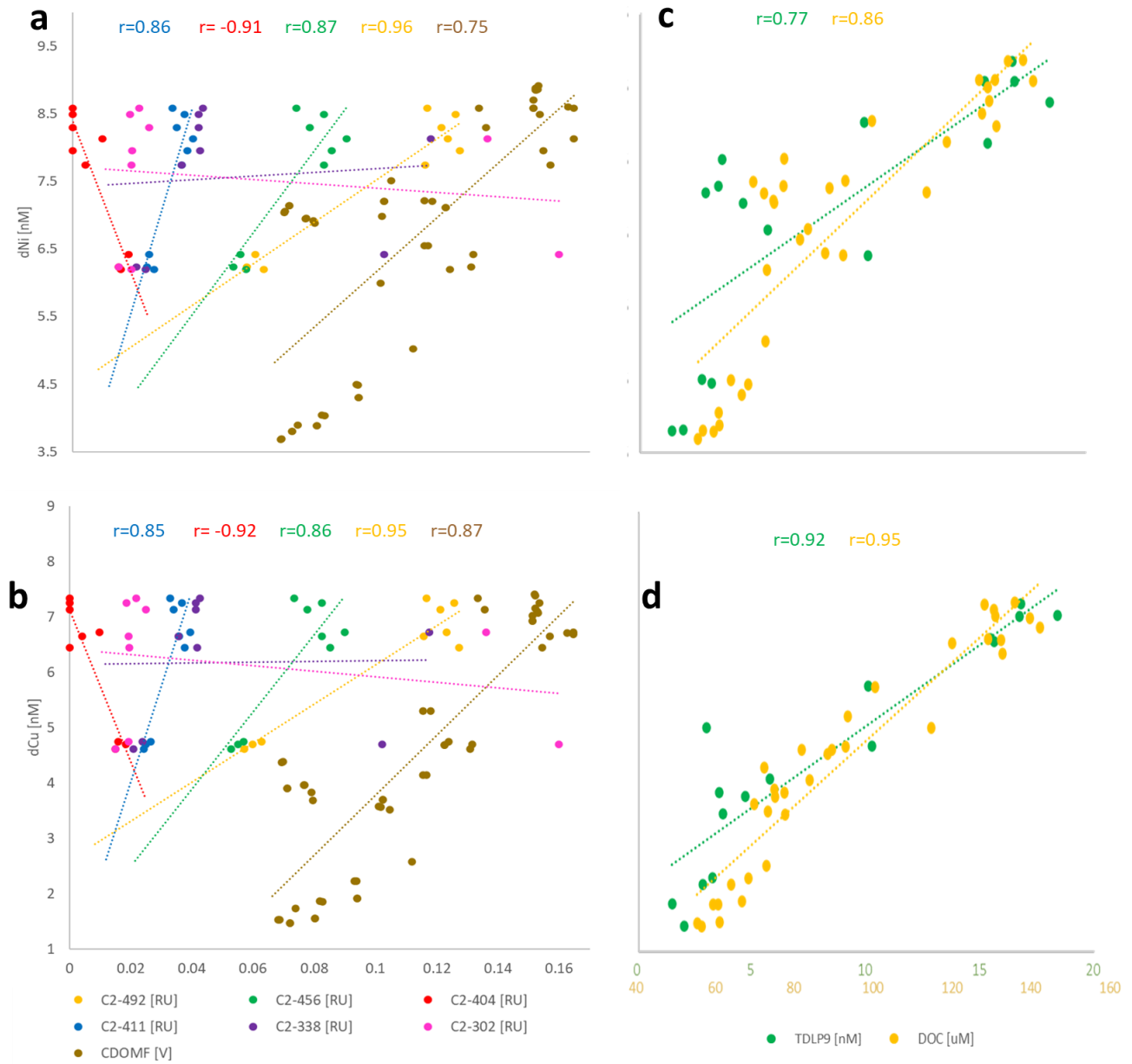


Figure 3.9. Scatterplots between the dNi (top panels), dCu (bottom panels) and C1 PARAFAC components and *in situ* CDOM fluorescence (CDOMF; a, b), lignin phenols (TDLP9) and dissolved organic carbon (DOC; b, d), in the top 300 meters of the Amundsen and Makarov basins. Only significant correlations ($p < 0.001$) are shown).

3.4.2.2. The haloclines

The shallow Chukchi Shelf is characterized by high seasonal primary productivity where sediments serve as a source of diagenetically altered DOM (Cooper et al. 2005). The remineralization process in these sediments enriches the bottom layer with organic ligands and all the trace metals examined in this study except for dCu (Jensen et al. 2019, 2020, 2021). Uniquely, due to brine rejection in these shelf waters, these metal- and organic-rich bottom waters became the source water for the UHC layer that extends far out into the Canada Basin, offering a rich opportunity to study the influence of shelf sediment-derived organic compounds on metal transport.

The border between the UHC and LHC is the most apparent from the water fractions (Fig. 3.7). The UHC contains up to 100% of f_{Pac} and the LHC contains up to 100% of f_{Atl} . The UHC exhibits a higher brine content (up to 5%), comparing to the LHC. The UHC had elevated DOC concentrations (~75uM, Figure 3.4a), second only to those in the TPD and PML. This DOC showed a pronounced CDOM signature (Figure 3.3) and high DIC concentrations (Figure 3.4b), which indicates the degradation process within the layer. The previous study report the apparent production of the fluorescent DOM in the Arctic sediments, associated with the organic matter degradation in the sediments as evidenced by the positive correlation with nutrients and by the inverse correlation with sulfates (Chen et al. 2016).

The levels of the *in situ* CDOM fluorescence and DOC concentration are lower in LHC than in UHC but are high comparing to the AW ranges. Elevated concentrations of the sediment-derived fluorophores C1₄₀₂ and C2₄₀₄ were observed in the UHC. The concentration of the marine component C2₄₁₁ was higher in the UHC comparing to the LHC, but the concentration of

the terrigenous component C₂₄₅₆ was higher in the LHC comparing to the UHC. Lignin phenols concentrations and *in situ* CDOM fluorescence peaked at the UHC/LHC border.

Several dissolved metals including dZn (Jensen et al. 2019), dCd (Zhang et al. 2019), dCu and dNi (Jensen et al. 2021) and dFe and dMn (Jensen et al. 2020) have been shown to have elevated concentrations throughout the UHC within the Canada Basin water column. The most important source of these metals is from the regeneration of metal-rich cells in sediment porewaters in the Chukchi Sea that are transported >1000 km offshore in the upper halocline (Jensen et al. 2019; Zhang et al. 2019; Kondo et al. 2016). The strong correlation between the dCd, dZn and dNi and C₁₄₀₂ in the Canada Basin (Figure 3.10f) points to not only the Chukchi shelf sediments being the most important source of trace metals, but also the source of the organic ligands that bind to them and carry them offshore within the UHC. In previous studies, dZn was shown to be strongly complexed (>95%) by organic ligands (Jakuba et al., 2012), especially sedimentary humic acids (Sohn and Hughes 1981; Raspor et al., 1984) and low-molecular-weight thiols (Dupont and Ahner 2005). Less is known about the potential organic ligands that bind to dCd, but prior studies have found about 70% of the dCd in surface waters was strongly complexed (Bruland 1992). The dNi had the weakest significant correlation with the C₁₄₀₂. The dZn, dCd and dNi also exhibit significant correlations to the terrigenous and marine humic-like fluorophores (Figure 3.10d,e)

Interestingly, the dCu was the only trace metal to exhibit significant correlation with the DOC concentration in the Canada Basin (Figure 3.10b), and the negative correlation with DIC (Figure 3.10c). This indicates that the trace metal is complexed to the marine DOM in the Canada Basin.

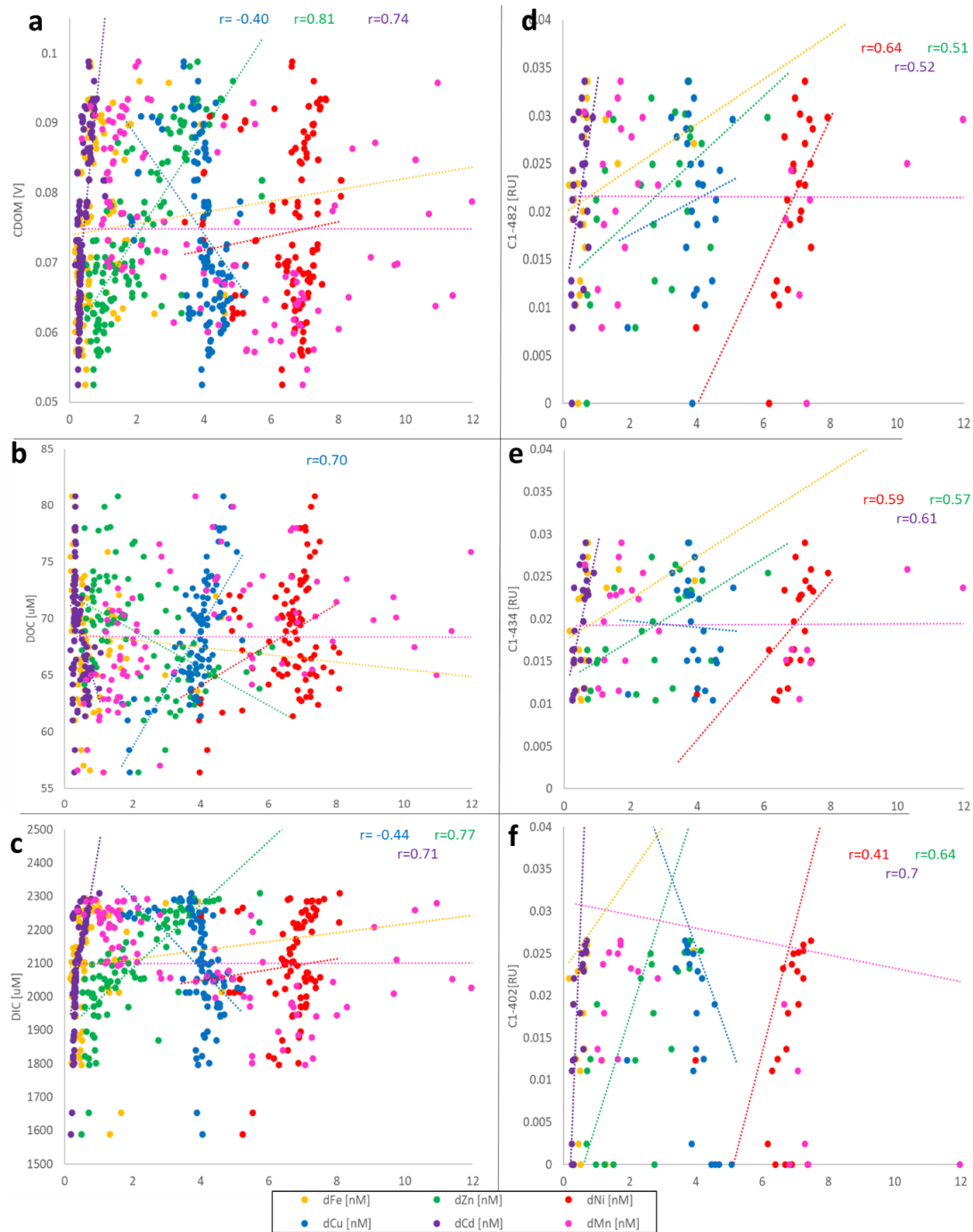


Figure 3.10. Scatterplots between the trace metals and *in situ* CDOM fluorescence (a), DIC (b), DOC (c), terrigenous humic-like C1₄₈₂ (d), marine humic-like C1₄₃₄ (e), marine humic-like with sediment signature C1₄₀₂ (f), in the top 300 meters of the Arctic Ocean. Only significant correlations ($p < 0.001$) are shown).

Scavenging-typed dFe and dMn might not be expected to persist for very long in the UHC layer, as they are scavenged away from their shelf source. Accordingly, the dFe and dMn had different transport timescales, and even different size fractions of Fe (soluble vs. colloidal) had different transport timescales (Jensen et al. 2020). The scavenging-prone dFe and dMn are rapidly lost moving away from the continental slope, demonstrating weak to absent complexation to the UHC DOM.

Finally, the Eurasian shelf derived LHC in the Amundsen, Nansen, and Makarov Basins exhibits relatively low concentrations of the trace metals (Gerringa et al. 2021) and similarly had low concentrations of DOM (Fig. 4). The Eurasian shelves are generally deeper and less biologically productive than the Chukchi Sea shelf which reduces the amount of remineralized and diagenetically altered organic matter released from sediments (Jones and Anderson, 1986; Sakshaug 2004). However, these shelves receive large amounts of terrigenous DOM which might mask the autochthonous DOM coming from the sediments.

3.4.2.3. The PML within the Beaufort Gyre

The Beaufort Gyre (GN01 Stations 48-60) alters the hydrography of the Canada Basin. The PML contains up to 5% of ice melt, but is dominated by the f_{Pac} (McLaughlin et al., 2004). According to our calculations, the Canada Basin PML also contained up to ~16% of f_{Met} . This is often explained by river discharge (Jensen et al. 2019; Proshutinsky et al. 2019). However, such a source is not supported by concentrations of lignin phenols and optical terrigenous proxies. The DOC concentrations were relatively high in the PML compared to halocline waters (Fig.4), but *in situ* CDOM fluorescence was very low (Fig.3) indicating the presence of non-fluorescent

substances such as carbohydrates in surface waters of the Canada Basin, which are mostly of marine origin (Wang et al. 2006; Shen et al. 2016).

The potential sources of DOM and trace metals to the surface layer of the Canada Basin are sea ice melt, fluvial discharge, and Pacific water inflow modified by interaction with the shallow Chukchi shelf sediments. Prior work shows that the concentrations of dNi, dCu, dCd, and dMn were elevated within this region, while the concentrations of the dFe and dZn were low. Jensen et al. (2019) described the dZn minima at the surface of the Canada Basins as diluted by sea-ice melt at the Marginal Ice Zone (MIZ) and Beaufort Gyre freshwater dilution. The dCu and dNi in the Arctic (Jensen et al., 2021) do not exhibit the typical hybrid-type and nutrient-type depths profiles, respectively, in the Canada Basin that was reported for these metals in previous studies of other ocean basins (Moffett and Brand, 1996; Bruland et al., 2014; Roshan and Wu, 2015; Böning et al., 2015; Middag et al., 2020).

The dCu signal was high at the surface and dissipated with depth. Compared to Fe and Ni, Cu is a softer acid (Zhengbin et al. 1982) and prefers sulfur-containing ligands of low molecular weight. For example, the thiol concentration decreased in response to increasing dCu concentrations, and the conditional stability constants of such complexes are high in the estuary of the river Scheldt in the Netherlands (12.3-14.1; Laglera and van den Berg 2003). Coccolithophorids were reported to release thiols in response to copper addition (Croot et al. 2000), and thiol-like levels were associated with the chlorophyll-a maximum in the Canadian Archipelago and Canada Basin (Gao and Guéguen, 2018; Nixon et al. 2019). Interestingly, rivers were shown to be the major source of dCu to the Arctic Ocean (Jensen et al. this issue), but our analysis suggests that marine DOM seems to be more important as a dCu ligand. The high correlation of the f_{Met} and dCu, but not with CDOM, is evidence that the river water went

through at least one freezing cycle before reaching the Beaufort Gyre (there was no correlation between the lignin phenols concentrations and the f_{Met} in the Canada Basin). Sea ice formation/melting in the Beaufort Gyre stripped out the tDOM signal, but the dCu content was conserved due to the production of ligands as indicated by high correlation with DOC (Figure 3.10b).

The Beaufort Gyre dNi and dCd concentrations exhibit moderate to strong correlations with the terrigenous and marine fluorophores (Figure 3.10 d,e), but dMn did not. The dNi correlates better with the terrigenous fluorophore, while the dCd correlated better with the marine one.

The distribution of C1₃₄₂, and the fact that its correlation with DIC is stronger than with DOC, implied that the protein-like fluorophore C1₃₄₂ is linked to microbial degradation; an example of this was reported in another study (Burdige et al. 2004). Alternatively, C1₃₄₂ could be related to tannins and lignins, known for their protein-binding capability and contribution to the fluorescence signature with an emission maximum near 315 nm (Maie et al. 2008). This fluorophore did not exhibit any significant correlations with any of the trace metals discussed in this study.

3.4.3. Processes affecting the distribution of DOM and trace metals in the Arctic Ocean

Interestingly, if you pool all water masses, the *in situ* CDOM fluorescence correlates better with f_{SIM} than with f_{Met} ($r=-0.6$, $r=0.5$, respectively, $p<0.0001$, Fig.3.8). The f_{SIM} predicts the distribution of CDOM better in all basins except for the Amundsen Basin. This correlation indicates that the ice melt/formation process plays a major role in the distribution of DOM in the Arctic Ocean, consistent with the study by Hölemann et al. (2021). Fluvial discharge is diluted by land fast ice melt during the spring freshet and undergoes at least one additional freeze-melt

cycle on the Arctic shelf seas. The mean residence time of the river-runoff on the shelves of the Siberian Seas is about 3.5 ± 2 years (Schlosser et al., 1994). During the shelf transition, the water is imprinted with the specific oxygen isotope and salinity signature that is later carried into the central basins of the Arctic Ocean, mostly in the TPD region.

The strongest correlation between f_{Met} and lignin phenol concentrations was observed in the TPD region of the Amundsen and Makarov Basins ($r=0.96$, $r=0.92$, respectively; $p < 0.0001$; Figure S3.5). A weaker correlation was found between lignin phenols and f_{Met} in the Nansen Basin ($r=0.76$, $p < 0.001$). No significant correlations were observed in the Chukchi Sea and the Canada Basin. The strong negative correlation between the f_{SIM} and lignin phenols in the central Arctic basins (Makarov and Amundsen) probably indicates that tDOM is frozen out and transported with the brine.

The high correlations between f_{SIM} and CDOM, tDOM, and trace metal distributions suggest that the freezing and thawing of sea ice is important for setting trace metal distributions. For example, *in situ* CDOM fluorescence exhibits a stronger correlation with f_{SIM} than with f_{Met} in this study (Fig. 3.8c), despite tDOM that enters the oceans from rivers being the most significant source of CDOM in the Arctic Ocean. We hypothesize the riverine contribution to f_{Met} is likely significantly overestimated in the PML of the Canada Basin because its riverine organic matter was low. We think that this can be explained by contributions of previously frozen river water (including fast ice) that is detected as " f_{Met} " based on $d^{18}O$ and salinity in the water but does not contain typical tDOM indicators, as the DOM is rejected from the crystal structure of ice during freezing (Amon 2004).

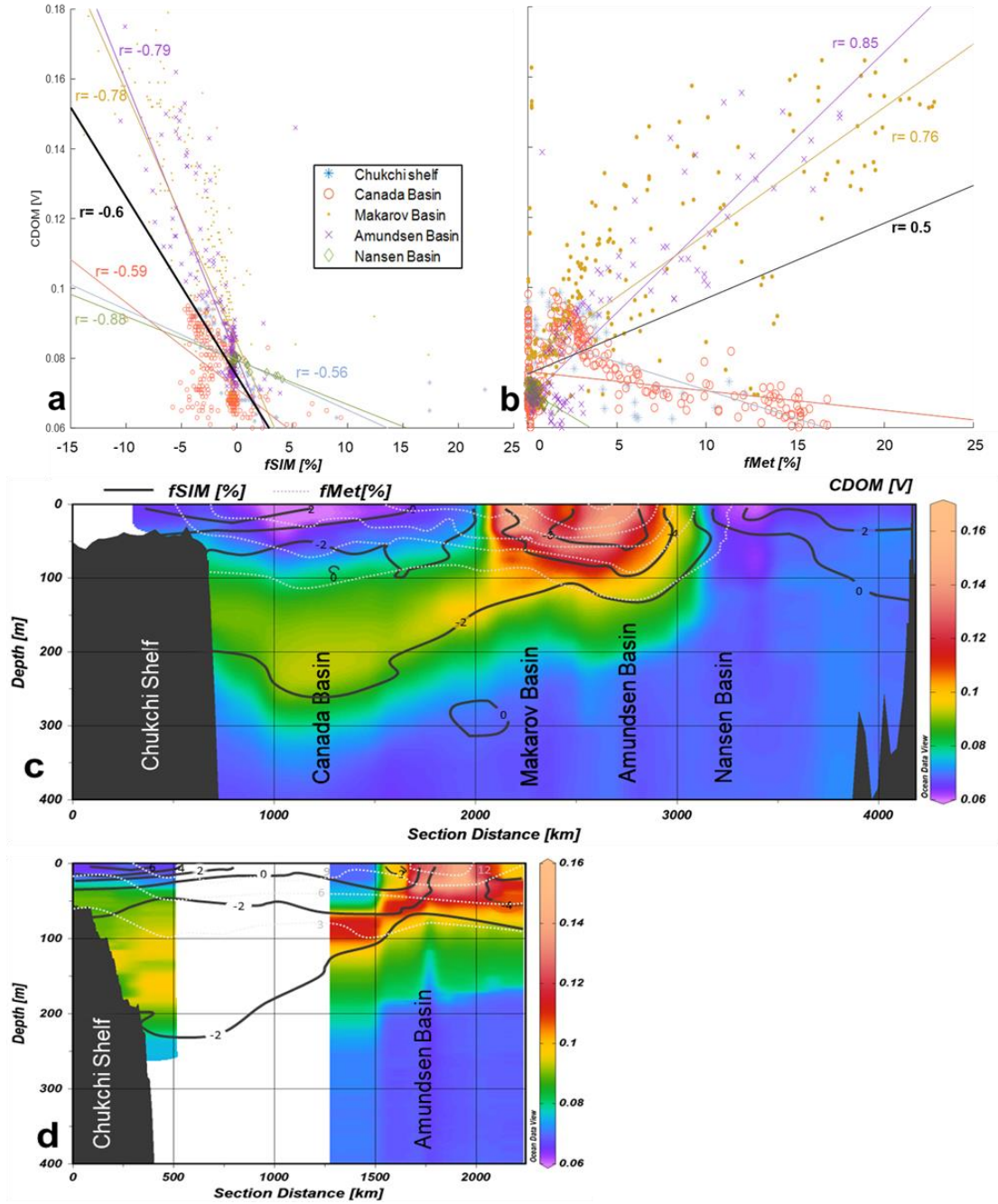


Figure 3.11. Relationship (Pearson correlation) of the CDOM *in situ* fluorescence, with f_{SIM} (a) and f_{Met} (b) in the Chukchi Sea, Canada, Makarov, Amundsen, and Nansen Basins. Only significant ($p < 0.001$) correlations are shown. The *in situ* CDOM fluorescence for sections A (c) and B (d) in the upper 400 m. The light gray dotted lines represent the f_{Met} isolines, and the solid black lines represent f_{SIM} isolines.

On the other hand, ice formation on the Eurasian shelves is imprinted into the shelf water and is reflected in elevated brine fractions (negative f_{SIM} values) along with high tDOM concentrations in the TPD (Hölemann et al. 2021). Due to the very low salinity of the PML over the shelves, the buoyancy change caused by brine formation is not enough to break through the pycnocline so the tDOM-enriched brine is advected offshore within the PML, as suggested by Hölemann et al. (2021), along with the trace metals that are complexed with the terrigenous organic ligands. This difference between the Eurasian and Chukchi Shelves calls for more detailed studies of the physical and biogeochemical processes in the Arctic Ocean as climate change brings significant and rapid changes to the region with potential implications for Arctic Ocean productivity and CO₂ sequestration/release.

Among all basins, surface waters of the Canada Basin had the lowest salinity, followed by the Makarov and Amundsen Basins. The Nansen Basin surface layer had the highest salinity. The current freshening of the Beaufort Gyre is a result of the moisture flux convergence above the high latitudes and by an increase in low-salinity anomalies entering from the Pacific Ocean (Carmack et al. 2015). With climate change, the increased runoff as well as increased inputs from glacial melt and permafrost will become more important sources of freshwater to the Arctic Ocean (Bring et al. 2016). The impacts of climate change include reduction of freshwater in the Eurasian basin (Wang et al. 2019), attributed to a freshened Beaufort Sea in response to a more positive AO mode (Givati and Rosenfeld, 2013; Morison et al. 2021). This change also affects the location of the front between the eastern and the western Arctic circulation systems. For some trace metals, like dMn, supplied into the surface layer of the Canada Basin from ice melt, the concentrations within the Beaufort Gyre might increase. For others, dilution will lower the concentrations at the surface.

Whether significant ice loss and more available light will cause an increase in the net Arctic Ocean primary production (and marine DOM) over this century, or the system will experience a decrease due to changes in nutrient supply and increased stratification, remains uncertain (Vancoppenolle et al. 2013). But over the last 14 years, a ~30% increase in net primary productivity throughout the Arctic Ocean has been reported (Arrigo and van Dijken, 2015; Frey et al. 2018). This changes the input of DOM to the shelf seas (Sakshaug, 2004), and in turn increases the mobilization of redox-sensitive metals like Fe and Mn, which will subsequently oxidize and may then enhance the scavenging of other metals throughout the water column (Jensen et al. 2020).

Over the past three and half decades, the export of alkalinity (Drake et al. 2018) and tDOM (Fichot et al. 2013; Ahmed et al. 2020) from the Arctic rivers increased. On the other hand, the projected climate change could decrease pH by more than 20% by 2070 ($\text{CO}_2 \approx 630$ ppm), mainly due to freshening and increased anthropogenic carbon uptake in response to sea ice decline (Steinacher et al. 2009; Ulfsbo et al. 2018; Woosley and Millero, 2020). Such changes affect the solubility of trace metals, resulting in changes in complexation, redox reactions, and scavenging (Millero et al. 2009). Arctic Ocean acidification and climate change in the wider Arctic region represent rapid regime shifts, triggering a series of complex, but poorly understood, feedbacks on physical and biogeochemical processes altering the distribution of hydrographic features, DOM, and trace metals.

3.5.Acknowledgments

We thank the captain and crew of the USCGC Healy and RV Polarstern, the chief scientists Ursula Schauer and David Kadko for leadership, and Martin Fleisher for sampling on the Healy. Funding came from the Office of Polar Programs (grant [1504469](#) to RMWA, RB, KK) and the Chemical Oceanography Program (https://www.nsf.gov/funding/pgm_summ.jsp?pims_id=11698) at the US National Science Foundation. Support for DAH came from US NSF award OCE- 1436748. We also acknowledge the international GEOTRACES Steering Committee, the U.S. GO-SHIP program, and all GEOTRACES colleagues who facilitated this extensive geochemical Arctic Ocean dataset. MAG was supported by the former Centre for Ice, Climate and Ecosystems at the Norwegian Polar Institute.

3.6.References

- Aagaard, K., A Synthesis of the Arctic Ocean Circulation, *Rapp. P.-V. Reun. Cons. Int. Explor. Mer.* 188, 11-22 (1989).
- Aguilar-Islas, A. M., Rember, R., Nishino, S., Kikuchi, T., & Itoh, M. (2013). Partitioning and lateral transport of iron to the Canada Basin. *Polar Science*, 7(2), 82-99.
- Amon, R. M. W., 2004. The role of dissolved organic matter for the Arctic Ocean carbon cycle, In “The Arctic Ocean Organic Carbon Cycle: Present and Past”, R. Stein, R.W. Macdonald, Eds., pp. 83-99. Springer.
- Amon, R. M. W., Rinehart, A. J., Duan, S., Louchouart, P., Prokushkin, A., Guggenberger, G., ... & McClelland, J. W. (2012). Dissolved organic matter sources in large Arctic rivers. *Geochimica et Cosmochimica Acta*, 94, 217-237.
- Amon, R. M., Budéus, G., & Meon, B. (2003). Dissolved organic carbon distribution and origin in the Nordic Seas: Exchanges with the Arctic Ocean and the North Atlantic. *Journal of Geophysical Research: Oceans*, 108(C7).

- Anderson L. G., Andersson P. S., Björk G., Peter Jones E., Jutterström S. and Waahlström I. (2013) Source and formation of the upper halocline of the Arctic Ocean. *J. Geophys. Res. Oceans* 118, 410–421.
- Anderson, L. G., & Amon, R. M. W., 2015. DOM in the Arctic Ocean. In *Biogeochemistry of marine dissolved organic matter*, pp. 609-633. Academic Press
- Anderson, L. G., Jutterström, S., Kaltin, S., Jones, E. P., & Björk, G. (2004). Variability in river runoff distribution in the Eurasian Basin of the Arctic Ocean. *Journal of Geophysical Research: Oceans*, 109(C1).
- Arrigo K. R. and van Dijken G. L. (2015) Continued increases in Arctic Ocean primary production. *Prog. Oceanogr.* 136, 60–70.
- Asbjørnsen, H., Årthun, M., Skagseth, Ø., & Eldevik, T. (2020). Mechanisms Underlying Recent Arctic Atlantification. *Geophysical Research Letters*, 47(15), e2020GL088036.
- Ballabio, D. (2015), A MATLAB toolbox for Principal Component Analysis and unsupervised exploration of data structure, *Chemometrics and Intelligent Laboratory Systems*, 149 Part B, 1-9 doi: 10.1016/j.chemolab.2015.10.003
- Bauch, D., van der Loeff, M. R., Andersen, N., Torres-Valdes, S., Bakker, K., & Abrahamsen, E. P. (2011). Origin of freshwater and polynya water in the Arctic Ocean halocline in summer 2007. *Progress in Oceanography*, 91(4), 482–495.
<https://doi.org/10.1016/J.POCEAN.2011.07.017>
- Benner, R., 2011. Loose ligands and available iron in the ocean. *Proceedings of the National Academy of Sciences*, 108, 3, 893-894.
- Benner, R., Louchouart, P., & Amon, R. M. (2005). Terrigenous dissolved organic matter in the Arctic Ocean and its transport to surface and deep waters of the North Atlantic. *Global Biogeochemical Cycles*, 19(2).
- Oldham, V. E., Owings, S. M., Jones, M. R., Tebo, B. M., & Luther III, G. W. (2015). Evidence for the presence of strong Mn (III)-binding ligands in the water column of the Chesapeake Bay. *Marine Chemistry*, 171, 58-66.
- Duckworth, O. W., Bargar, J. R., & Sposito, G. (2009). Coupled biogeochemical cycling of iron and manganese as mediated by microbial siderophores. *Biometals*, 22(4), 605-613.

- Berner, L. T., Massey, R., Jantz, P., Forbes, B. C., Macias-Fauria, M., Myers-Smith, I., ... & Goetz, S. J. (2020). Summer warming explains widespread but not uniform greening in the Arctic tundra biome. *Nature communications*, 11(1), 1-12.
- Bertosio, C., Provost, C., Sennéchaël, N., Artana, C., Athanase, M., Boles, E., ... & Garric, G. (2020). The Western Eurasian Basin halocline in 2017: insights from autonomous NO measurements and the Mercator physical system. *Journal of Geophysical Research: Oceans*, 125(7), e2020JC016204.
- Beszczynska-Moeller, A., Woodgate, R. A., Lee, C., Melling, H., & Karcher, M. (2011). A synthesis of exchanges through the main oceanic gateways to the Arctic Ocean. *Oceanography*, 24(3), 82-99
- Böning, P., T. Shaw, K. Pahnke, and H.-J. Brumsack (2015), Nickel as indicator of fresh organic matter in upwelling sediments, *Geochimica et Cosmochimica Acta*, 162, 99-108.
- Bring, A., Fedorova, I., Dibike, Y., Hinzman, L., Mård, J., Mernild, S. H., ... & Woo, M. K. (2016). Arctic terrestrial hydrology: A synthesis of processes, regional effects, and research challenges. *Journal of Geophysical Research: Biogeosciences*, 121(3), 621-649.
- Bruland, K. W. (1992). Complexation of cadmium by natural organic ligands in the central North Pacific. *Limnology and Oceanography*, 37(5), 1008-1017.
- Bruland, K. W., & Lohan, M. C. (2006). Controls of trace metals in seawater. *The oceans and marine geochemistry*, 6, 23-47.
- Bruland, K. W., R. Middag, and M. C. Lohan (2014), 8.2 - Controls of Trace Metals in Seawater, in *Treatise on Geochemistry (Second Edition)*, edited by H. D. Holland and K. K. Turekian, pp. 19-51, Elsevier, Oxford.
- Burdige, D. J., Kline, S. W., & Chen, W. (2004). Fluorescent dissolved organic matter in marine sediment pore waters. *Marine Chemistry*, 89(1-4), 289-311.
- Carmack, E. C., Yamamoto-Kawai, M., Haine, T. W., Bacon, S., Bluhm, B. A., Lique, C., ... & Williams, W. J. (2016). Freshwater and its role in the Arctic Marine System: Sources, disposition, storage, export, and physical and biogeochemical consequences in the Arctic and global oceans. *Journal of Geophysical Research: Biogeosciences*, 121(3), 675-717.
- Charette, M. A., Kipp, L. E., Jensen, L. T., Dabrowski, J. S., Whitmore, L. M., Fitzsimmons, J. N., et al., 2020. The Transpolar Drift as a source of riverine and shelf-derived trace elements

- to the central Arctic Ocean. *Journal of Geophysical Research: Oceans*, 125, e2019JC015920.
<https://doi.org/10.1029/2019JC015920>
- Chen, M., Jung, J., Lee, Y. K., & Hur, J. (2018). Surface accumulation of low molecular weight dissolved organic matter in surface waters and horizontal off-shelf spreading of nutrients and humic-like fluorescence in the Chukchi Sea of the Arctic Ocean. *Science of the Total Environment*, 639, 624-632.
- Chen, M., Kim, J. H., Nam, S. I., Niessen, F., Hong, W. L., Kang, M. H., & Hur, J. (2016). Production of fluorescent dissolved organic matter in Arctic Ocean sediments. *Scientific reports*, 6(1), 1-10.
- Conway, T. M., Rosenberg, A. D., Adkins, J. F., & John, S. G. (2013). A new method for precise determination of iron, zinc and cadmium stable isotope ratios in seawater by double-spike mass spectrometry. *Analytica Chimica Acta*, 793, 44–52.
<https://doi.org/10.1016/j.aca.2013.07.025>
- Cory, R. M., Miller, M. P., McKnight, D. M., Guerard, J. J., & Miller, P. L. (2010). Effect of instrument-specific response on the analysis of fulvic acid fluorescence spectra. *Limnology and Oceanography: Methods*, 8(2), 67-78.
- Croot PL, Moffett JW, Brand LE. Production of extracellular Cu complexing ligands by eucaryotic phytoplankton in response to Cu stress. *Limnol Oceanogr*. 2000;45:619–27.
- Cutter, G. A., Andersson, P. S., Codispoti, L., Croot, P. L., Francois, R., Lohan, M. C., et al. (2014). Sampling and Sample-handling Protocols for GEOTRACES Cruises. Retrieved from http://www.geotraces.org/images/stories/documents/intercalibration/Cookbook_v2.pdf
- Cutter, G., Andersson, P., Codispoti, L., Croot, P., Francois, R., Lohan, M. C., ... & Rutgers vd Loeff, M. (2010). Sampling and sample-handling protocols for GEOTRACES cruises.
- Dupont CL, Ahner BA. Effects of copper, cadmium, and zinc on the production and exudation of thiols by *Emiliana huxleyi*. *Limnol Oceanogr*. 2005;50:508–15. [Google Scholar]
- Dupont CL, Barbeau K, Palenik B. Ni uptake and limitation in marine *Synechococcus* strains. *Appl Environ Microbiol*. 2008;74:23–31
- Evans, G., Heath, A., & Lalljee, M. (1996). Measuring left-right and libertarian-authoritarian values in the British electorate. *British Journal of Sociology*, 93-112.

- Fichot, C. G., & Benner, R. (2012). The spectral slope coefficient of chromophoric dissolved organic matter (S_{275–295}) as a tracer of terrigenous dissolved organic carbon in river-influenced ocean margins. *Limnology and Oceanography*, 57(5), 1453-1466.
- Fichot, C. G., Kaiser, K., Hooker, S. B., Amon, R. M., Babin, M., Bélanger, S., ... & Benner, R. (2013). Pan-Arctic distributions of continental runoff in the Arctic Ocean. *Scientific reports*, 3(1), 1-6.
- Frey, K. E. (2018). Arctic Ocean Primary Productivity: The Response of Marine Algae to Climate Warming and Sea Ice Decline. Arctic Report Card 2018], <https://www.arctic.noaa.gov/Report-Card/Report-Card-2018/ArtMID/7878/ArticleID/778/Arctic-Ocean-Primary-Productivity-The-Response-of-Marine-Algae-to-Climate-Warming-and-Sea-Ice-Decline>.
- Fritz, M., Vonk, J. E., & Lantuit, H. (2017). Collapsing arctic coastlines. *Nature Climate Change*, 7(1), 6-7.
- Gao, Z., & Guéguen, C. (2018). Distribution of thiol, humic substances and colored dissolved organic matter during the 2015 Canadian Arctic GEOTRACES cruises. *Marine Chemistry*, 203, 1-9.
- Gerringa, L.J.A., Rijkenberg, M.J.A., Slagter, H.A., Laan, P., Paffrath, R., Bauch, D., Rutgers van der Loeff, M., Middag, R. Dissolved Cd, Co, Cu, Fe, Mn, Ni 1 and Zn in the Arctic Ocean Submitted to *Journal of Geophysical research Oceans*
- Gerringa, Loes J A; Rijkenberg, Micha J A; Slagter, Hans A (2018): Dissolved iron measured on board with Flow injection analysis and iron-binding dissolved organic ligands from Ultra Clean CTD collected depth profiles during GEOTRACES PS94 Arctic cruise on Polarstern. PANGAEA, <https://doi.org/10.1594/PANGAEA.890975>
- Givati, A., & Rosenfeld, D. (2013). The Arctic Oscillation, climate change and the effects on precipitation in Israel. *Atmospheric research*, 132, 114-124.
- Gonçalves-Araujo, R., Granskog, M. A., Bracher, A., Azetsu-Scott, K., Dodd, P. A., & Stedmon, C. A. (2016). Using fluorescent dissolved organic matter to trace and distinguish the origin of Arctic surface waters. *Scientific reports*, 6(1), 1-12.
- Gonçalves-Araujo, R., Granskog, M. A., Bracher, A., Azetsu-Scott, K., Dodd, P. A., & Stedmon, C. A. (2016). Using fluorescent dissolved organic matter to trace and distinguish the origin of Arctic surface waters. *Scientific Reports*, 6(1), 33978. <https://doi.org/10.1038/srep33978>

- Gonçalves-Araujo, R., Stedmon, C. A., de Steur, L., Osburn, C. L., & Granskog, M. A. (2020). A decade of annual Arctic DOC export with Polar Surface Water in the East Greenland Current. *Geophysical Research Letters*, 47(20), e2020GL089686.
- Gonçalves-Araujo, R., Stedmon, C. A., Heim, B., Dubinenkov, I., Kraberg, A., Moiseev, D., & Bracher, A. (2015). From fresh to marine waters: Characterization and fate of dissolved organic matter in the Lena River Delta Region, Siberia. *Frontiers in Marine Science*, 2, 108.
- Granskog, M. A. (2012). Changes in spectral slopes of colored dissolved organic matter absorption with mixing and removal in a terrestrially dominated marine system (Hudson Bay, Canada). *Marine Chemistry*, 134–135, 10–17.
<https://doi.org/10.1016/j.marchem.2012.02.008>
- Granskog, M. A., Stedmon, C. A., Dodd, P. A., Amon, R. M. W., Pavlov, A. K., de Steur, L., & Hansen, E. (2012). Characteristics of colored dissolved organic matter (CDOM) in the Arctic outflow in the Fram Strait: Assessing the changes and fate of terrigenous CDOM in the Arctic Ocean. *Journal of Geophysical Research*, 117, C12021.
<https://doi.org/10.1029/2012JC008075>
- Griffin, C. G. (2016). Dissolved organic matter in major rivers across the Pan-Arctic from remote sensing (Doctoral dissertation).
- Guéguen, C., Itoh, M., Kikuchi, T., Eert, J., and Williams, W. J. (2015). Variability in dissolved organic matter optical properties in surface waters in the Amerasian Basin. *Front. Mar. Sci.* 2:78. <https://doi.org/10.3389/fmars.2015.00078>
- Guieu, C., Huang, W. W., Martin, J. M., & Yong, Y. Y. (1996). Outflow of trace metals into the Laptev Sea by the Lena River. *Marine Chemistry*, 53(3-4), 255-267.
- Halewood, E., K. Opalk, L. Custals, M. Carey, D.A. Hansell, & C.A. Carlson. 2010. GO-SHIP Repeat Hydrography: Determination of dissolved organic carbon (DOC) and total dissolved nitrogen (TDN) in seawater using High Temperature Combustion Analysis. In *The GO-SHIP Repeat Hydrography Manual: A Collection of Expert Reports and Guidelines*. Hood, E.M., C.L. Sabine, and B.M. Sloyan, eds. IOCCP Report Number 14, ICPO Publication Series Number 134. <http://www.go-ship.org/HydroMan.html>.
- Hansell, D. A. (2005). Dissolved organic carbon reference material program. *Eos, Transactions American Geophysical Union*, 86(35), 318. <https://doi.org/10.1029/2005EO350003>

- Hansell, D.A. 2021. DOC data from Cruise 33HQ20150809, exchange version. Accessed from CCHDO <https://cchdo.ucsd.edu/cruise/33HQ20150809>. Access date 2021-03-27. CCHDO cruise DOI: 10.7942/C2MW25.
- Hansell, Dennis A (2017): Arctic dissolved organic carbon (DOC) and total dissolved nitrogen (TDN) collected during POLARSTERN cruise PS94 (GEOTRACES) in 2015. Rosenstiel School of Marine & Atmospheric Sciences, University of Miami, PANGAEA, <https://doi.org/10.1594/PANGAEA.884113>
- Hassler, C. S., Schoemann, V., Nichols, C. M., Butler, E. C., & Boyd, P. W., 2011. Saccharides enhance iron bioavailability to Southern Ocean phytoplankton. *Proceedings of the National Academy of Sciences*, 108, 3, 1076-1081.
- Hioki, N., Kuma, K., Morita, Y., Sasayama, R., Ooki, A., Kondo, Y., ... & Kikuchi, T. (2014). Laterally spreading iron, humic-like dissolved organic matter and nutrients in cold, dense subsurface water of the Arctic Ocean. *Scientific reports*, 4, 6775.
- Hoffmann, L. J., Breitbarth, E., Boyd, P. W., & Hunter, K. A. (2012). Influence of ocean warming and acidification on trace metal biogeochemistry. *Marine Ecology Progress Series*, 470, 191-205.
- Hölemann, J. A., Juhls, B., Bauch, D., Janout, M., Koch, B. P., & Heim, B. (2021). The impact of land-fast ice on the distribution of terrestrial dissolved organic matter in the Siberian Arctic shelf seas. *Biogeosciences Discussions*, 1-30.
- Holmes, R. M., McClelland, J. W., Tank, S. E., Spencer, R. G. M., & Shiklomanov, A. I. (2019). Arctic Great Rivers Observatory. Water Quality Dataset, Version 20190904. Retrieved from <https://arcticgreatrivers.org/data>
- Homoky, W. B., Severmann, S., McManus, J., Berelson, W. M., Riedel, T. E., Statham, P. J., & Mills, R. A. (2012). Dissolved oxygen and suspended particles regulate the benthic flux of iron from continental margins. *Marine Chemistry*, 134, 59-70.
- Horner-Devine, A. R., Hetland, R. D., & MacDonald, D. G. (2015). Mixing and transport in coastal river plumes. *Annual Review of Fluid Mechanics*, 47, 569-594.
- Hydes, D., Aoyama, M., Aminot, A., Bakker, K., Becker, S., Coverly, S., Daniel, A., Dickson, A., Grosso, O. and Kerouel, R. (2010) Determination of dissolved nutrients (N, P, Si) in seawater with high precision and inter-comparability using gas- segmented continuous flow analyzers.

- Jakuba, R. W., Saito, M. A., Moffett, J. W., & Xu, Y. (2012). Dissolved zinc in the subarctic North Pacific and Bering Sea: Its distribution, speciation, and importance to primary producers. *Global Biogeochemical Cycles*, 26, GB2015.
<https://doi.org/10.1029/2010GB004004>
- Jensen, L. T., Morton, P., Twining, B. S., Heller, M. I., Hatta, M., Measures, C. I., ... & Fitzsimmons, J. N. (2020). A comparison of marine Fe and Mn cycling: US GEOTRACES GN01 Western Arctic case study. *Geochimica et Cosmochimica Acta*.
- Jensen, L. T., Wyatt, N. J., Twining, B. S., Rauschenberg, S., Landing, W. M., Sherrell, R. M., & Fitzsimmons, J. N. (2019). Biogeochemical cycling of dissolved zinc in the Western Arctic (Arctic GEOTRACES GN01). *Global Biogeochemical Cycles*, 33(3), 343-369.
- Jones, E. P., & Anderson, L. G. (1986). On the origin of the chemical properties of the Arctic Ocean halocline. *Journal of Geophysical Research: Oceans*, 91(C9), 10759-10767.
- Kadko, D., & Landing, W. (2015). U.S. Arctic GEOTRACES USCGC Healy (HLY1502) cruise report. Retrieved from
https://www.bodc.ac.uk/resources/inventories/cruise_inventory/reports/healy1502.pdf
- Kaiser, K., Benner, R., & Amon, R. M. W. (2017). The fate of terrigenous dissolved organic carbon on the Eurasian shelves and export to the North Atlantic. *Journal of Geophysical Research, Oceans*, 122, 4–22. <https://doi.org/10.1002/2016JC012380>
- Karcher, M., Smith, J. N., Kauker, F., Gerdes, R., & Smethie, W. M. (2012). Recent changes in Arctic Ocean circulation revealed by iodine-129 observations and modeling. *Journal of Geophysical Research: Oceans*, 117(C8).
- Kikuchi, T., Fujii, M., Terao, K., Jiwei, R., Lee, Y. P., & Yoshimura, C. (2017). Correlations between aromaticity of dissolved organic matter and trace metal concentrations in natural and effluent waters: A case study in the Sagami River Basin, Japan. *Science of the Total Environment*, 576, 36-45.
- Klunder, M. B., Laan, P., Middag, R., De Baar, H. J. W., & Bakker, K. (2012). Dissolved iron in the Arctic Ocean: Important role of hydrothermal sources, shelf input and scavenging removal. *Journal of Geophysical Research: Oceans*, 117(C4).
- Kondo, Y., Obata, H., Hioki, N., Ooki, A., Nishino, S., Kikuchi, T., & Kuma, K. (2016). Transport of trace metals (Mn, Fe, Ni, Zn and Cd) in the western Arctic Ocean (Chukchi Sea

- and Canada Basin) in late summer 2012. *Deep Sea Research Part I: Oceanographic Research Papers*, 116, 236-252.
- Korhonen, M., Rudels, B., Marnela, M., Wisotzki, A., & Zhao, J. (2013). Time and space variability of freshwater content, heat content and seasonal ice melt in the Arctic Ocean from 1991 to 2011. *Ocean Science*, 9(6), 1015-1055.
- Kothawala, D. N., Stedmon, C. A., Müller, R. A., Weyhenmeyer, G. A., Köhler, S. J., & Tranvik, L. J. (2014). Controls of dissolved organic matter quality: Evidence from a large-scale boreal lake survey. *Global change biology*, 20(4), 1101-1114.
<https://doi.org/10.1111/gcb.12488>
- Krachler, R., Krachler, R. F., Wallner, G., Hann, S., Laux, M., Recalde, M. F. C., ... & Keppler, B. K., 2015. River-derived humic substances as iron chelators in seawater. *Marine chemistry*, 174, 85-93.
- Laglera LM, Van Den Berg CMG. Copper complexation by thiol compounds in estuarine waters. *Mar Chem.* 2003;82:71–89
- Laglera, L. M., & van den Berg, C. M. (2003). Copper complexation by thiol compounds in estuarine waters. *Marine Chemistry*, 82(1-2), 71-89.
- Laglera, L.M., Sukekava C., Slagter H.A., Downes J., Aparicio-Gonzalez A., Gerringa L.J.A., 2019. First direct evidence of humic substances controlling iron transport across the surface of the Arctic Ocean, *Env. Sci. & Techn.*, 53, 22, 13136-13145 DOI: 10.1021/acs.est.9b04240
- Laglera, L.M., Sukekava, C., Slagter, H.A., Downes, J., Aparicio-Gonzalez, A., Gerringa, L.J.A., 2019. First Quantification of the Controlling Role of Humic Substances in the Transport of Iron Across the Surface of the Arctic Ocean. *Environ. Sci. Technol.*
- Landing, W. M., Cutter, G., & Kadko, D. C. (2019a). Bottle data from the CTD-ODF carousel on the GEOTRACES Arctic section cruise(HLY1502) from August to October 2015 (U.S. GEOTRACES Arctic project). Biological and Chemical Oceanography Data Management Office (BCO-DMO). <https://doi.org/10.1575/1912/bco-dmo.646825.4>
- Landing, W. M., Cutter, G., & Kadko, D. C. (2019b). Bottle data from the GEOTRACES clean carousel sampling system (GTC) on the Arctic section cruise (HLY1502) from August to October 2015 (U.S. GEOTRACES Arctic project). Biological and Chemical Oceanography Data Management Office (BCO-DMO). <https://doi.org/10.1575/1912/bco-dmo.647259.4>

- Li, W. K., F. A. McLaughlin, C. Lovejoy, and E. C. Carmack (2009), Smallest algae thrive as the Arctic Ocean freshens, *Science*, 326, 539.
- Luoma, S. N., & Davis, J. A. (1983). Requirements for modeling trace metal partitioning in oxidized estuarine sediments. *Marine chemistry*, 12(2-3), 159-181.
- Maie, N., Pisani, O., & Jaffé, R., 2008. Mangrove tannins in aquatic ecosystems: their fate and possible influence on dissolved organic carbon and nitrogen cycling. *Limnology and Oceanography*, 53, 1, 160-171.
- Marsay, C. M., Aguilar-Islas, A., Fitzsimmons, J. N., Hatta, M., Jensen, L. T., John, S. G., ... & Pasqualini, A. (2018). Dissolved and particulate trace elements in late summer Arctic melt ponds. *Marine Chemistry*, 204, 70-85.
- Martin, J. M., Guan, D. M., Elbaz-Poulichet, F., Thomas, A. J., & Gordeev, V. V. (1993). Preliminary assessment of the distributions of some trace elements (As, Cd, Cu, Fe, Ni, Pb and Zn) in a pristine aquatic environment: the Lena River estuary (Russia). *Marine Chemistry*, 43(1-4), 185-199.
- McLaughlin, F. A., & Carmack, E. C. (2010). Deepening of the nutricline and chlorophyll maximum in the Canada Basin interior, 2003–2009. *Geophysical Research Letters*, 37(24).
- McLaughlin, F. A., Carmack, E. C., Williams, W. J., Zimmermann, S., Shimada, K., & Itoh, M. (2009). Joint effects of boundary currents and thermohaline intrusions on the warming of Atlantic water in the Canada Basin, 1993–2007. *Journal of Geophysical Research: Oceans*, 114(C1).
- McLaughlin, F. A., E. C. Carmack, R. W. Carmack, H. Macdonald, J. H. Melling, P. A. Swift, B. F. Wheeler, and E. B. Sherr (2004), The joint roles of Pacific and Atlantic-origin waters in the Canada Basin, 1997–1998, *Deep Sea Res., Part I*, 51, 107 – 128, doi:10.1016/j.dsr.2003.09.010.
- Middag, R., de Baar, H. J. W., Laan, P., and Klunder, M. B., 2011. Fluvial and hydrothermal input of manganese into the Arctic Ocean. *Geochim. Cosmochim. Acta* 75, 2393– 2408. doi:10.1016/j.gca.2011.02.011.
- Middag, R., H. J. de Baar, K. W. Bruland, and S. M. van Heuven (2020), The distribution of nickel in the west-Atlantic Ocean, its relationship with phosphate and a comparison to cadmium and zinc, *Frontiers in Marine Science*, 7, 105.

- Millero, F. J., Woosley, R., DiTrollo, B., & Waters, J. (2009). Effect of ocean acidification on the speciation of metals in seawater. *Oceanography*, 22(4), 72-85.
- Moffett, J. W., and L. E. Brand (1996), Production of strong, extracellular Cu chelators by marine cyanobacteria in response to Cu stress, *Limnology and Oceanography*, 41(3), 388-395.
- Morison, J., Kwok, R., Dickinson, S., Andersen, R., Peralta-Ferriz, C., Morison, D., ... & Guthrie, J. (2021). The Cyclonic Mode of Arctic Ocean Circulation. *Journal of Physical Oceanography*.
- Muller, F. L., & Batchelli, S. (2013). Copper binding by terrestrial versus marine organic ligands in the coastal plume of River Thurso, North Scotland. *Estuarine, Coastal and Shelf Science*, 133, 137-146.
- Murphy, K. R., Stedmon, C. A., Graeber, D., and Bro, R. (2013). Fluorescence spectroscopy and multi-way techniques. PARAFAC. *Anal. Methods* 5, 6557.
<https://doi.org/10.1039/c3ay41160e>
- Nakayama, Y., Fujita, S., Kuma, K., & Shimada, K. (2011). Iron and humic-type fluorescent dissolved organic matter in the Chukchi Sea and Canada Basin of the western Arctic Ocean. *Journal of Geophysical Research: Oceans*, 116(C7).
- Nguyen, A. T., Kwok, R., & Menemenlis, D. (2012). Source and pathway of the Western Arctic upper halocline in a data-constrained coupled ocean and sea ice model. *Journal of physical oceanography*, 42(5), 802-823.
- Nishimura, S., Kuma, K., Ishikawa, S., Omata, A., & Saitoh, S. I. (2012). Iron, nutrients, and humic-type fluorescent dissolved organic matter in the northern Bering Sea shelf, Bering Strait, and Chukchi Sea. *Journal of Geophysical Research: Oceans*, 117(C2).
- Nixon, R. L., Jackson, S. L., Cullen, J. T., & Ross, A. R. (2019). Distribution of copper-complexing ligands in Canadian Arctic waters as determined by immobilized copper (II)-ion affinity chromatography. *Marine Chemistry*, 215, 103673.
- Opsahl, S., & Benner, R., 1997. Distribution and cycling of terrigenous dissolved organic matter in the ocean. *Nature*, 386, 6624, 480.
- Opsahl, S., Benner, R., Amon, R. M. W., 1999: Major flux of terrigenous dissolved organic matter through the Arctic Ocean. *Limnology & Oceanography*: 44: 2017-2023

- Paffrath, R., Laukert, G., Bauch, D., van der Loeff, M. R., & Pahnke, K. (2021). Separating individual contributions of major Siberian rivers in the Transpolar Drift of the Arctic Ocean. *Scientific Reports*, 11(1), 1-11.
- Parker, C. E., Brown, M. T., & Bruland, K. W. (2016). Scandium in the open ocean: A comparison with other group 3 trivalent metals. *Geophysical Research Letters*, 43(6), 2758-2764.
- Pasqualini, A., Schlosser, P., Newton, R., & Koffman, T. N. (2017). U.S. GEOTRACES Arctic section ocean water hydrogen and oxygen stable isotope analyses (version 1.0) [dataset]. Interdisciplinary Earth Data Alliance (IEDA). <https://doi.org/10.1594/ieda/100633>
- Pearson, R. G. (1963). Hard and soft acids and bases. *Journal of the American Chemical society*, 85(22), 3533-3539.
- Pokrovsky, O. S., Viers, J., Dupre, B., Chabaux, F., Gaillardet, J., Audry, S., ... & Shevchenko, V. P. (2012). Biogeochemistry of carbon, major and trace elements in watersheds of northern Eurasia drained to the Arctic Ocean: the change of fluxes, sources and mechanisms under the climate warming prospective. *Comptes Rendus Geoscience*, 344(11-12), 663-677.
- Proshutinsky, A. Y., & Johnson, M. A. (1997). Two circulation regimes of the wind-driven Arctic Ocean. *Journal of Geophysical Research: Oceans*, 102(C6), 12493-12514.
- Proshutinsky, A., Krishfield, R., Toole, J. M., Timmermans, M. L., Williams, W., Zimmermann, S., ... & Zhao, J. (2019). Analysis of the Beaufort Gyre freshwater content in 2003–2018. *Journal of Geophysical Research: Oceans*, 124(12), 9658-9689.
- Rabe, Benjamin; Schauer, Ursula; Ober, Sven; Horn, Myriel; Hoppmann, Mario; Korhonen, Meri; Pisarev, Sergey; Hampe, Hendrik; Villaceros, Nicolas; Savy, Jean Philippe; Wisotzki, Andreas (2016): Physical oceanography during POLARSTERN cruise PS94 (ARK-XXIX/3). Alfred Wegener Institute, Helmholtz Centre for Polar and Marine Research, Bremerhaven, PANGAEA, <https://doi.org/10.1594/PANGAEA.859558>
- Raspor, B., Nürnberg, H. W., Valenta, P., & Branica, M. (1984). Studies in seawater and lake water on interactions of trace metals with humic substances isolated from marine and estuarine sediments: II. Voltammetric investigations on trace metal complex formation in the dissolved phase. *Marine Chemistry*, 15(3), 231-249.
- Rennermalm, A. K., Wood, E. F., Déry, S. J., Weaver, A. J., & Eby, M. (2006). Sensitivity of the thermohaline circulation to Arctic Ocean runoff. *Geophysical research letters*, 33(12).

- Richter-Menge, J., M. L. Druckenmiller, and M. Jeffries, Eds., 2019: Arctic Report Card 2019, <https://www.arctic.noaa.gov/Report-Card>
- Rijkenberg, Michiel J A; Slagter, Hans A; Rutgers van der Loeff, Michiel M; van Ooijen, Jan C; Gerringa, Loes J A (2018): Dissolved Fe in the Deep and Upper Arctic Ocean With a Focus on Fe Limitation in the Nansen Basin. *Frontiers in Marine Science*, 5, <https://doi.org/10.3389/fmars.2018.00088>
- Rogers, H. J., C. Synge, and V. E. Woods (1980), Antibacterial effect of scandium and indium complexes of enterochelin on *Klebsiella pneumoniae*, *Antimicrob. Agents Chemother.*, 18(1), 63–68, <https://doi.org/10.1128/AAC.18.1.63>
- Roshan, S., and J. Wu (2015), The distribution of dissolved copper in the tropical-subtropical north Atlantic across the GEOTRACES GA03 transect, *Marine Chemistry*, 176, 189-198.
- Roshan, S., DeVries, T., Wu, J., & Chen, G. (2018). The internal cycling of zinc in the ocean. *Global Biogeochemical Cycles*, 32(12), 1833-1849.
- Rudels, B. (2015). Arctic Ocean circulation, processes and water masses: A description of observations and ideas with focus on the period prior to the International Polar Year 2007–2009. *Progress in Oceanography*, 132, 22-67.
- Rudels, B., 2001. Ocean Current: Arctic Basin Circulation. In J. Steele, S. Thorpe, & K. Turekian, Eds., *Encyclopedia of Ocean Sciences*, pp. 177-187
- Rudels, B., Anderson, L. G., Jones, E. P., 1996. Formation and evolution of the surface mixed layer and halocline of the Arctic Ocean. *J. Geophys. Res.* 101, 8807-8821.
- Rudels, B., Friedrich, H. J., & Quadfasel, D. (1999). The Arctic circumpolar boundary current. *Deep Sea Research Part II: Topical Studies in Oceanography*, 46(6-7), 1023-1062.
- Rudels, B., Jones, E. P., Schauer, U., & Eriksson, P. (2004). Atlantic sources of the Arctic Ocean surface and halocline waters. *Polar Research*, 23(2), 181-208.
- Rudels, B., Korhonen, M., Schauer, U., Pisarev, S., Rabe, B., & Wisotzki, A. (2015). Circulation and transformation of Atlantic water in the Eurasian Basin and the contribution of the Fram Strait inflow branch to the Arctic Ocean heat budget. *Progress in Oceanography*, 132, 128-152.
- Sakshaug E. (2004) Primary and Secondary Production in the Arctic Seas, *The Organic Carbon Cycle in the Arctic Ocean*. Springer, pp. 57–81.

- Schauer, U. (2016). The Expedition PS94 of the research vessel POLARSTERN to the central Arctic Ocean in 2015, Bremerhaven, Alfred Wegener Institute for Polar and Marine Research. *Berichte zur Polar- und Meeresforschung = Reports on polar and marine research* 703 170 pp.
- Schlosser, P., Bauch, D., Fairbanks, R., & Bönisch, G. (1994). Arctic river-runoff: mean residence time on the shelves and in the halocline. *Deep Sea Research Part I: Oceanographic Research Papers*, 41(7), 1053-1068.
- Schlosser, P., Newton, R., Ekwurzel, B., Khatiwala, S., Mortlock, R., & Fairbanks, R. (2002). Decrease of river runoff in the upper waters of the Eurasian Basin, Arctic Ocean, between 1991 and 1996: Evidence from $\delta^{18}\text{O}$ data. *Geophysical Research Letters*, 29(9), 3-1.
- Semeniuk, D. M., Bundy, R. M., Payne, C. D., Barbeau, K. A., & Maldonado, M. T. (2015). Acquisition of organically complexed copper by marine phytoplankton and bacteria in the northeast subarctic Pacific Ocean. *Marine Chemistry*, 173, 222-233.
- Shank, G. C., Skrabal, S. A., Whitehead, R. F., & Kieber, R. J. (2004). Strong copper complexation in an organic-rich estuary: the importance of allochthonous dissolved organic matter. *Marine Chemistry*, 88(1-2), 21-39.
- Shen, Y., Benner, R., Robbins, L. L., & Wynn, J. G. (2016). Sources, distributions, and dynamics of dissolved organic matter in the Canada and Makarov Basins. *Frontiers in Marine Science*, 3, 198.
- Shimada, K., Carmack, E. C., Hatakeyama, K., & Takizawa, T. (2001). Varieties of shallow temperature maximum waters in the western Canadian Basin of the Arctic Ocean. *Geophysical Research Letters*, 28(18), 3441-3444.
- Newton, R., Schlosser, P., Mortlock, R., Swift, J., & MacDonald, R. (2013). Canadian Basin freshwater sources and changes: Results from the 2005 Arctic Ocean Section. *Journal of Geophysical Research: Oceans*, 118(4), 2133-2154.
- Sholkovitz, E. R., & Copland, D. (1981). The coagulation, solubility and adsorption properties of Fe, Mn, Cu, Ni, Cd, Co and humic acids in a river water. *Geochimica et Cosmochimica Acta*, 45(2), 181-189.
- Slagter, H. A., Reader, H. E., Rijkenberg, M. J. A., Van Der Loeff, M. R., de Baar, H. J. W., & Gerringa, L. J. A. (2017). Organic Fe speciation in the Eurasian Basins of the Arctic Ocean and its relation to terrestrial DOM. *Marine Chemistry*, 197, 11-25.

- Slagter, H.A., Laglera, L.M., Sukekava, C., Gerringa, L.J.A., 2019. Fe-Binding Organic Ligands in the Humic-Rich TransPolarDrift in the Surface Arctic Ocean Using Multiple Voltammetric Methods. *J. Geophys. Res. Ocean.* 1491–1508.
- Sohn, M. L., & Hughes, M. C. (1981). Metal ion complex formation constants of some sedimentary humic acids with Zn (II), Cu (II) and Cd (II). *Geochimica et Cosmochimica Acta*, 45(12), 2393-2399.
- Stedmon, C. A., Amon, R. M. W., Rinehart, A. J., & Walker, S. A. (2011a). The supply and characteristics of colored dissolved organic matter (CDOM) in the Arctic Ocean: Pan Arctic trends and differences. *Marine Chemistry*, 124(1–4), 108–118.
<https://doi.org/10.1016/J.MARCHEM.2010.12.007>
- Stedmon, C. A., Thomas, D. N., Papadimitriou, S., Granskog, M. A., & Dieckmann, G. S. (2011b). Using fluorescence to characterize dissolved organic matter in Antarctic sea ice brines. *Journal of Geophysical Research: Biogeosciences*, 116(G3).
- Stedmon, Colin A., Rainer M.W. Amon, Dorothea Bauch, Astrid Bracher, Rafael Gonçalves-Araujo, Mario Hoppmann, Richard Krishfield, Samuel Laney, Ben Rabe, Heather Reader, Mats A. Granskog. 2021. Insights into water mass circulation and origins in the central Arctic Ocean using in-situ fluorescence of colored dissolved organic matter as a tracer. *JGR*-this issue
- Steinacher, M., Joos, F., Frölicher, T. L., Plattner, G. K., & Doney, S. C. (2009). Imminent ocean acidification in the Arctic projected with the NCAR global coupled carbon cycle-climate model. *Biogeosciences*, 6(4), 515-533.
- Sukekava, C., Downes, J., Slagter, H.A., Gerringa, L.J.A., Laglera, L.M., 2018. Determination of the contribution of humic substances to iron complexation in seawater by catalytic cathodic stripping voltammetry. *Talanta* 189, 359-364.
- Talley, L. D. (2011). *Descriptive physical oceanography: an introduction*. Academic press. Chapter 12- Arctic Ocean and Nordic Seas.
- Thibodeau, B., & Bauch, D. (2015). River Water and Brine Inventory over the Laptev Sea Shelf: 2007 To 2011. In *AGU Fall Meeting Abstracts* (Vol. 2014, pp. OS51C-1005).
- Thibodeau, B., Bauch, D., Kassens, H., & Timokhov, L. A. (2014). Interannual variations in river water content and distribution over the Laptev Sea between 2007 and 2011: The Arctic Dipole connection. *Geophysical Research Letters*, 41(20), 7237-7244.

- Till, C. P., Shelley, R. U., Landing, W. M., & Bruland, K. W. (2017). Dissolved scandium, yttrium, and lanthanum in the surface waters of the North Atlantic: Potential use as an indicator of scavenging intensity. *Journal of Geophysical Research: Oceans*, 122(8), 6684-6697.
- Ulfssbo, A., Jones, E. M., Casacuberta, N., Korhonen, M., Rabe, B., Karcher, M., & Van Heuven, S. M. (2018). Rapid changes in anthropogenic carbon storage and ocean acidification in the intermediate layers of the Eurasian Arctic Ocean: 1996–2015. *Global Biogeochemical Cycles*, 32(9), 1254-1275.
- Van den Berg, C. M. G., & Nimmo, M. (1987). Determination of interactions of nickel with dissolved organic material in seawater using cathodic stripping voltammetry. *Science of the Total Environment*, 60, 185-195.
- Vancoppenolle, M., Bopp, L., Madec, G., Dunne, J., Ilyina, T., Halloran, P. R., & Steiner, N. (2013). Future Arctic Ocean primary productivity from CMIP5 simulations: Uncertain outcome, but consistent mechanisms. *Global Biogeochemical Cycles*, 27(3), 605-619.
- Vieira, L. H., Achterberg, E. P., Scholten, J., Beck, A. J., Liebetrau, V., Mills, M. M., & Arrigo, K. R. (2019). Benthic fluxes of trace metals in the Chukchi Sea and their transport into the Arctic Ocean. *Marine Chemistry*, 208, 43-55.
- Vihma, T., Screen, J., Tjernström, M., Newton, B., Zhang, X., Popova, V., ... & Prowse, T. (2016). The atmospheric role in the Arctic water cycle: A review on processes, past and future changes, and their impacts. *Journal of Geophysical Research: Biogeosciences*, 121(3), 586-620.
- Vraspir, J. M., and A. Butler (2009), Chemistry of marine ligands and siderophores.
- Walker, S. A., Amon, R. M. W., and Stedmon, C. A. (2013). Variations in high-latitude riverine fluorescent dissolved organic matter: a comparison of large Arctic rivers. *J. Geophys. Res. Biogeosci.* 118, 1689–1702. <https://doi.org/10.1002/2013jg002320>
- Walker, S.A., Amon, R. M. W., Stedmon, C., Duan, S.W. Louchouart, P., (2009). The use of PARAFAC modeling to trace terrestrial dissolved organic matter and fingerprint water masses in coastal Canadian Arctic surface waters. *J. Geophys. Res.* 114, <https://doi.org/10.1029/2009jg000990>

- Wang, D., Henrichs, S. M., & Guo, L. (2006). Distributions of nutrients, dissolved organic carbon and carbohydrates in the western Arctic Ocean. *Continental Shelf Research*, 26(14), 1654-1667.
- Wang, Q., Wekerle, C., Danilov, S., Koldunov, N., Sidorenko, D., Sein, D., ... & Jung, T. (2018). Arctic sea ice decline significantly contributed to the unprecedented liquid freshwater accumulation in the Beaufort Gyre of the Arctic Ocean. *Geophysical Research Letters*, 45(10), 4956-4964.
- Wang, Q., Wekerle, C., Danilov, S., Sidorenko, D., Koldunov, N., Sein, D., ... & Jung, T. (2019). Recent sea ice decline did not significantly increase the total liquid freshwater content of the Arctic Ocean. *Journal of Climate*, 32(1), 15-32.
- Watanabe, E. (2013). Linkages among halocline variability, shelf-basin interaction, and wind regimes in the Beaufort Sea demonstrated in pan-Arctic Ocean modeling framework. *Ocean Modelling*, 71, 43-53.
- Williford, T., Amon, R. M. W., Benner, R., Kaiser, K., Bauch, D., Stedmon, C., ... & Klunder, M. B. (2021). Insights into the origins, molecular characteristics and distribution of iron-binding ligands in the Arctic Ocean. *Marine Chemistry*, 103936.
- Woosley, R. J., & Millero, F. J. (2020). Freshening of the western Arctic negates anthropogenic carbon uptake potential. *Limnology and Oceanography*, 65(8), 1834-1846.
- Woosley, R. J., Millero, F. J., & Takahashi, T. (2017). Internal consistency of the inorganic carbon system in the Arctic Ocean. *Limnology and Oceanography: Methods*, 15(10), 887–896. <https://doi.org/10.1002/lom3.10208>
- Wünsch, U. J., Geuer, J. K., Lechtenfeld, O. J., Koch, B. P., Murphy, K. R., & Stedmon, C. A. (2018). Quantifying the impact of solid-phase extraction on chromophoric dissolved organic matter composition. *Marine Chemistry*, 207, 33-41.
- Yamashita, Y., Boyer, J. N., & Jaffé, R. (2013). Evaluating the distribution of terrestrial dissolved organic matter in a complex coastal ecosystem using fluorescence spectroscopy. *Continental shelf research*, 66, 136-144.
- Yan, G., & Kaiser, K., 2018. A rapid and sensitive method for the analysis of lignin phenols in environmental samples using ultra-high performance liquid chromatography-electrospray ionization-tandem mass spectrometry with multiple reaction monitoring. *Analytica chimica acta*, 1023, 74-80.

Yan, G., K. Kaiser., 2018. Ultra-low Sample Volume Cupric Sulfate Oxidation Method for the Analysis of Dissolved Lignin. *Anal. Chem.*, <https://DOI.org/10.1021/acs.analchem.8b01867>, 68, 1-2, 59-70

Zhang, R., Jensen, L. T., Fitzsimmons, J. N., Sherrell, R. M., & John, S. (2019). Dissolved cadmium and cadmium stable isotopes in the western Arctic Ocean. *Geochimica et Cosmochimica Acta*, 258, 258-273.

Supplemental

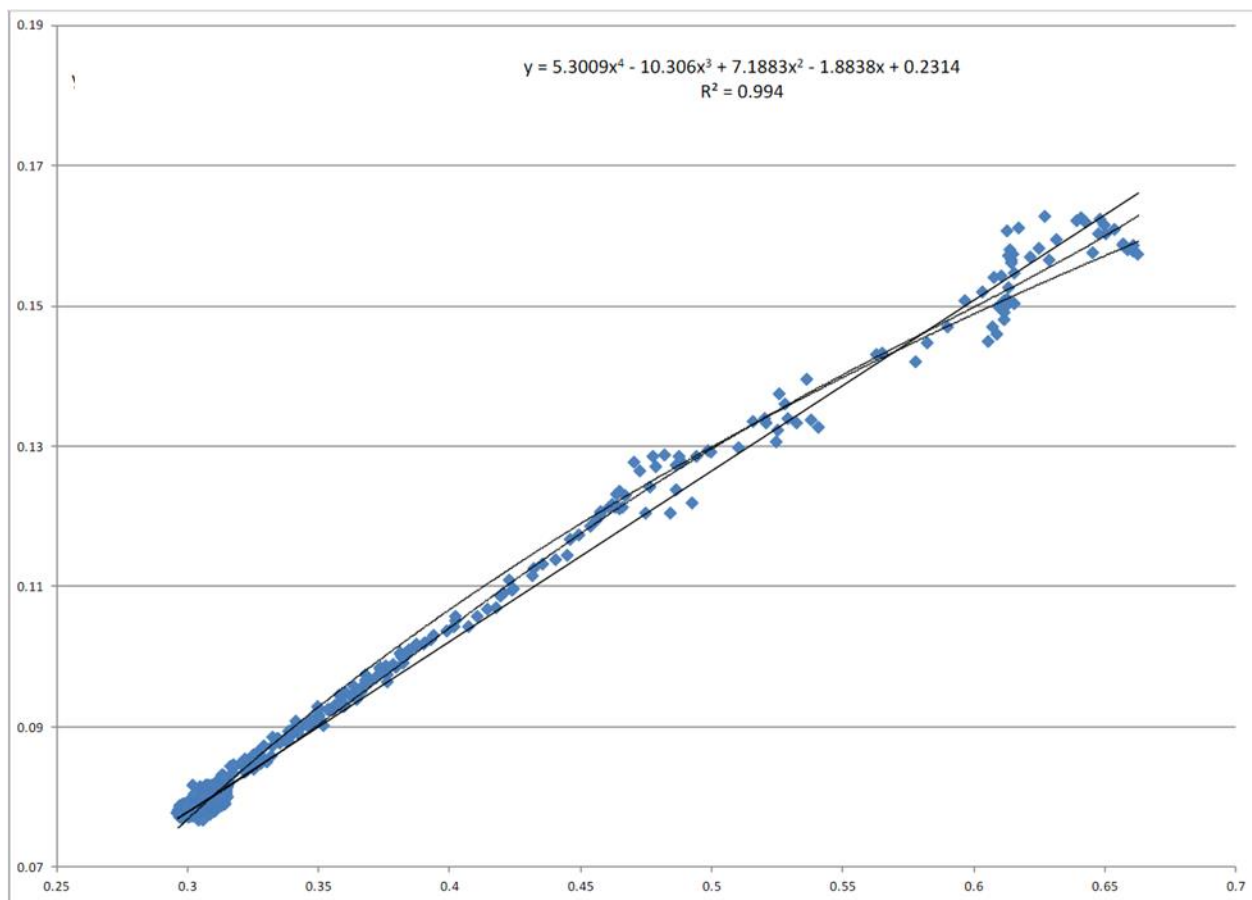


Figure S3.1. The calibration between the two fluorimeters with the deep water measurements (<1000 m).

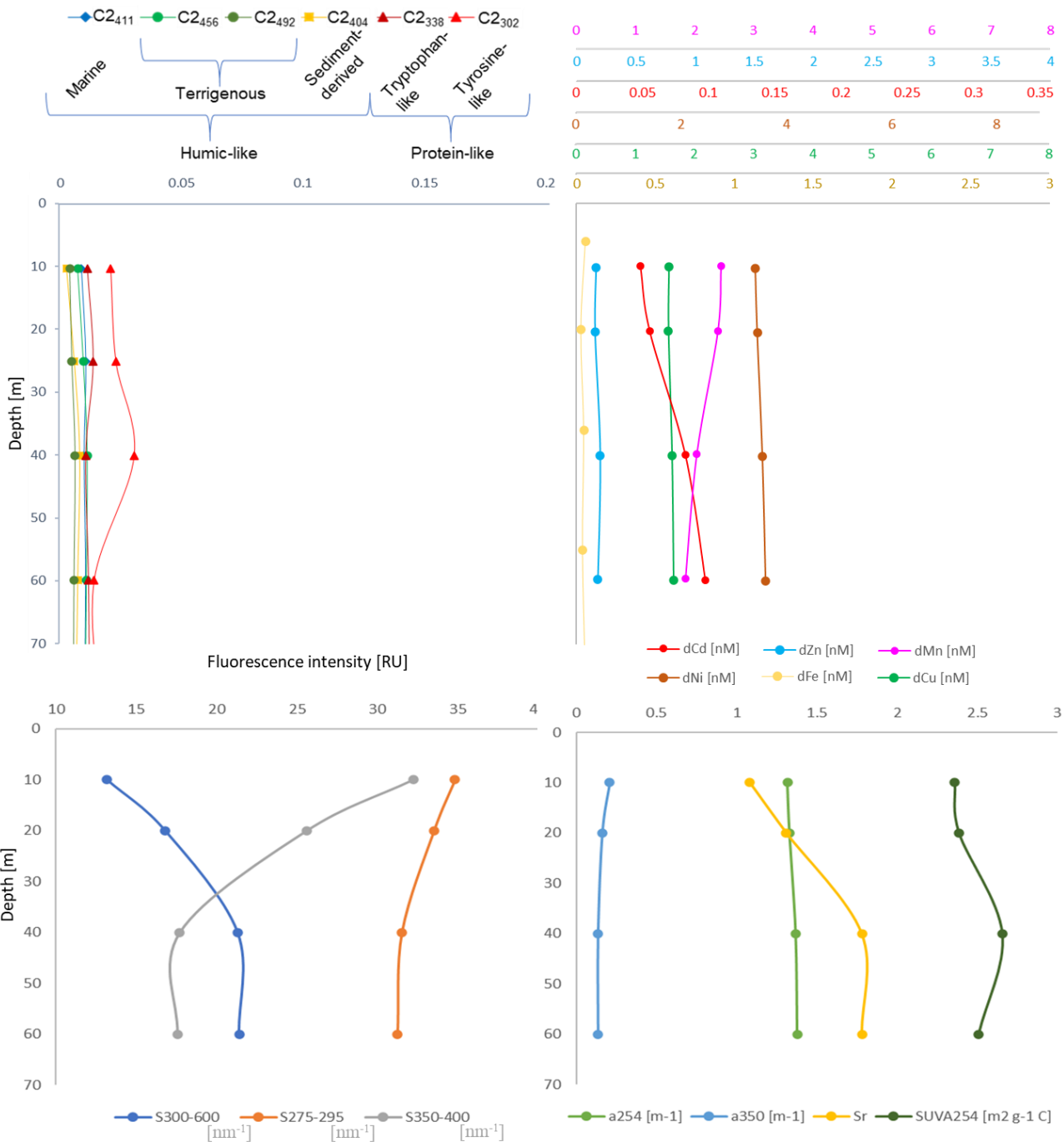


Figure S3.2. The Nansen Basin (PS94 station 58) top 70 m profile of C2 PARAFAC components' intensities (top left panel), absorbance-based optical properties (bottom panels) and trace metals concentrations (top right panel).

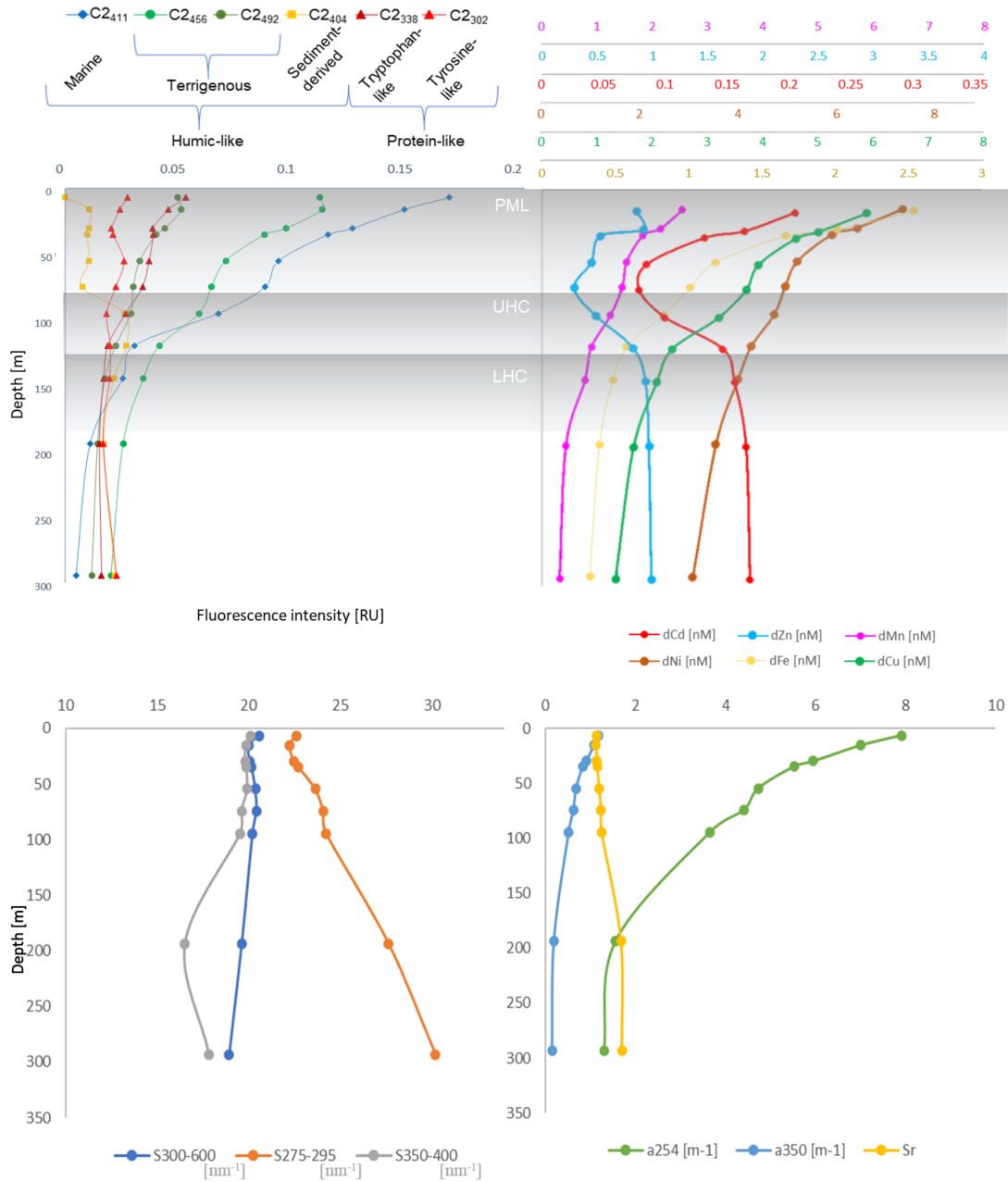


Figure S3.3. The Makarov Basin top 300 m. (PS94 station 87) profile of C2 PARAFAC components' intensities (top left panel), absorbance-based optical properties (bottom panels) and trace metals concentrations (top right panel). The grey shaded regions represent PML, the upper and the lower haloclines.

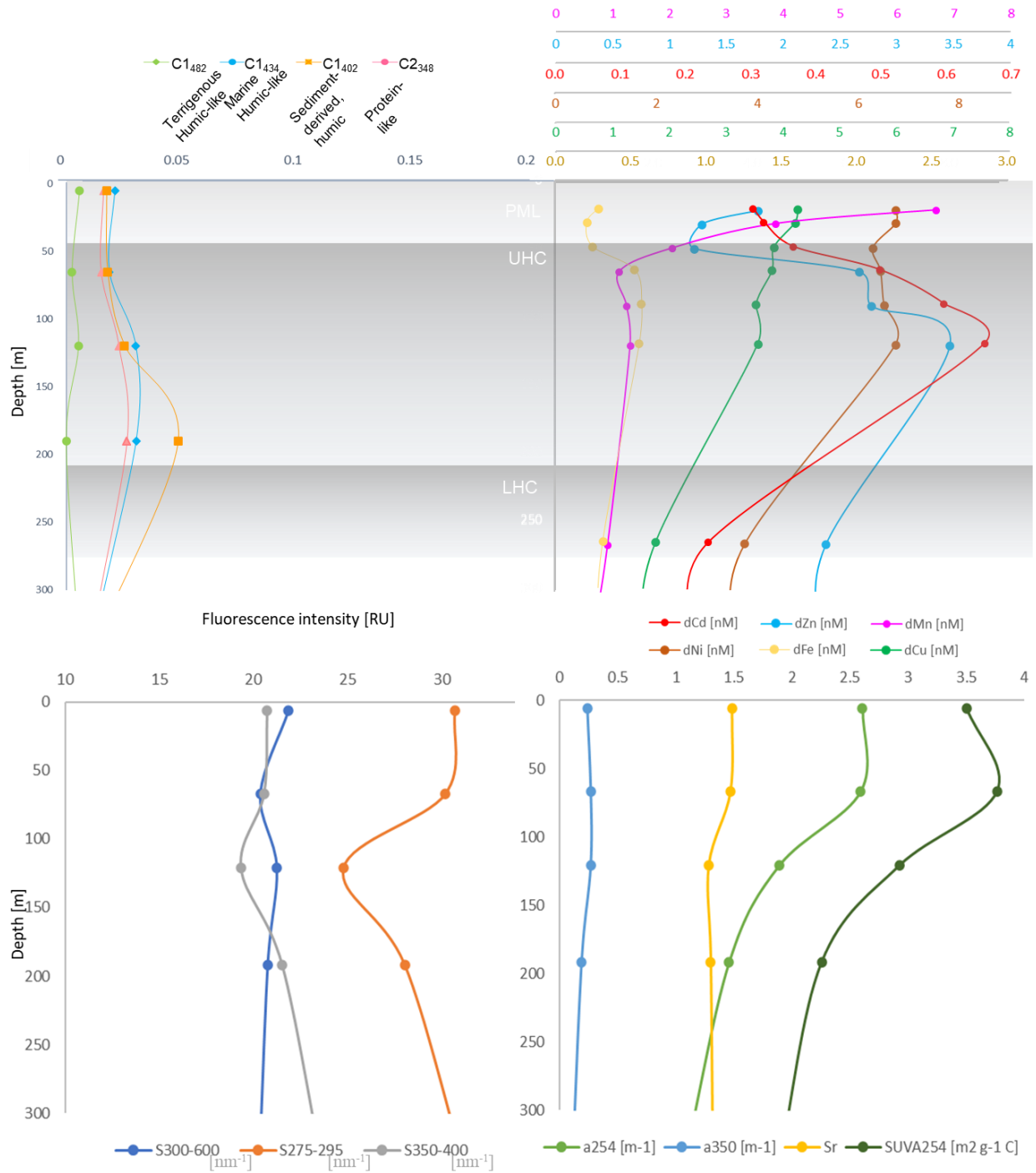


Figure S3.4. The Canada Basin (GN01 station 48) top 300 m profile of C1 PARAFAC components' intensities (top left panel), absorbance-based optical properties (bottom panels) and trace metals concentrations (top right panel). The grey shaded regions represent PML, the upper and the lower haloclines.

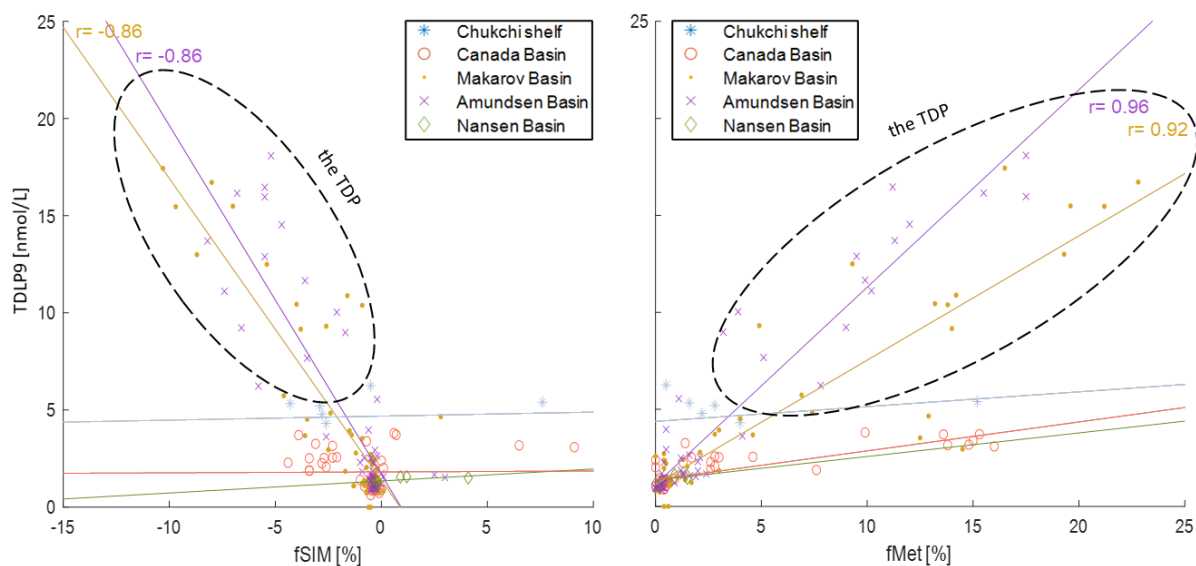


Figure S3.5. Relationship (Pearson correlation) of lignin phenol (TDLP9) concentrations, f_{SIM} and f_{Met} in the Chukchi Sea, Canada, Makarov, Amundsen and Nansen Basins. Only significant ($p < 0.001$) correlations are shown.

Table S3.1. Spectral characteristics of the six fluorescence components identified by PARAFAC in the Eurasian Basin and the TPD region and comparisons to previously identified components.

PS94	Description	Excitation max/ Emission max, nm	Similar components	References
C2 ₄₁₁	Humic-like	260,300/411	FloridaKeys C1	Yamashita et al. 2013
C2 ₄₅₆	Humic-like terrigenous	260,340/456	FloridaKeys C2, Lena2013 C2	Yamashita et al. 2013, Gonçalves-Araujo et al. 2015
C2 ₄₀₄	Humic-like	<260,309/404	Omdrev C2, Arctic Seawater C2	Kothawala et al. 2014, Chen et al. 2018

			C3	Williford et al. 2021
C2 ₄₉₂	Humic-like terrigenous	285/492	Omdrev C3	Kothawala et al. 2014
C2 ₃₃₈	Tryptophan- like	280/338	AntarcticIce C3	Stedmon et al. 2011
C2 ₃₀₂	Tyrosine-like	273/302	Arctic Seawater C3	Chen et al. 2018
			C5	Williford et al. 2021

Table S3.2. Spectral characteristics of the four components identified by PARAFAC in the Canada Basin and the Chukchi Sea and their comparison to previously identified components.

GN01	Description	Excitation max/ Emission max, nm	Similar components	References
C1 ₄₈₂	Humic-like, terrigenous	285,380/482	Omdrev C3, Beringia C3 C1	Kothawala et al. 2014, Walker et al. 2009 Williford et al. 2021
C1 ₄₃₄	Humic-like	260,340/434	Omdrev C4,	Kothawala et al. 2014,
C1 ₄₀₂	Humic-like	295,395/402	Arctic Seawater C2, Beringia C6	Chen et al. 2018, Walker et al. 2009
C1 ₃₄₈	Protein-like	275/348	ArcticFjords_PPL C4	Wünsch et al. 2018

4. TRACING ARCTIC OCEAN WATER MASSES WITH OPTICAL INDICES

4.1. Introduction

Shifts in circulation regimes (Proshutinsky and Johnson, 1997) and changes in the freshwater budget due to sea ice decline (Li et al. 2021) and increasing fluvial discharge (Fichot et al. 2013; Ahmed et al. 2020) in the Arctic Ocean are believed to be directly linked to the strength of the Atlantic Meridional Overturning Circulation (AMOC) and can have global impacts (Zhang et al. 2021; Jiang et al. 2021). The state-of-the-art climate models (e.g., Proshutinsky et al. 2020, Jiang et al. 2021), remote sensing (e.g., Fichot et al. 2013), and in situ studies (e.g., Yamamoto-Kawai et al. 2009, Guay et al. 2009) focus on the freshwater sources that feed the growing Beaufort Gyre- an anticyclonic system in the Canada Basin that maintains the largest oceanic freshwater reservoir in the Arctic Ocean (Proshutinsky et al. 2019). These sources are known and include the fluvial discharge, Pacific water, precipitation minus evaporation, and sea ice melt (Carmack et al., 2008); however, the relative contribution of the freshwater fractions of different origins have differed substantially between the studies. Secondly, how the freshwater from various sources reaches and leaves the Beaufort Gyre remains unknown. The subsequent pathways of the freshwaters from the Arctic Ocean are through the Davis Strait and the Fram Strait via Transpolar Drift (Zhang et al. 2021). The latter is another subject of lively investigations as the observed reduction of long-range transport due to the sea ice loss is anticipated to alter the freshwater, organic matter, and pollutant fluxes from the Arctic Ocean (Peeken et al. 2018; Krumpfen et al. 2019; Morison et al. 2021). The large-scale geochemical assessments of the Transpolar Drift, the Beaufort Gyre, and all the surrounding waters are needed to investigate the surface circulation of the region further.

Besides the importance of what occurs at the surface of the Arctic Ocean, the dominant external source of heat in the region is the Atlantic water, distributed throughout the Arctic basins at intermediate depths and containing enough heat to melt the Arctic sea ice 3–4 times over (Carmack et al. 2015). According to the study, the cold halocline that shields the surface layer from the underlying Atlantic heat has weakened substantially in recent years, which already affected the sea ice thickness and extent (Polyakov et al. 2020). Several mechanisms for the halocline formation have been described in the literature. These include the convective mechanisms of salination of cold and fresh surface water and melting of sea ice as Atlantic water enters the ice-covered Arctic shelves and the advective mechanism of cold and saline shelf water spreading into the deep Arctic basins (Metzner et al. 2020). These studies show that the cold halocline can be formed in the Barents, Laptev, and East Siberian Seas (Bauch et al. 2014; Itoh et al. 2007); additionally, the Chukchi Sea is thought to ventilate the halocline on the North American side (Woodgate et al. 2005). The importance of the halocline in the Arctic Ocean physical and biogeochemical processes emphasizes the pressing need for the pan-Arctic geochemical assessment of the water strata in order to constrain the sources and the pathways of the shelf water into the deep basins.

In this study, we compiled and seamlessly merged some of the existing regional datasets of the *in situ* measurements of the optical properties in an attempt to cover the "blind spots" in our knowledge of the Arctic water mass circulation on a pan-Arctic scale. The optical properties demonstrate a high potential for such application as the biogeochemical fingerprint of water masses is heavily influenced by river discharge, ice formation/melt processes, and interactions with the sediments on the extensive shelves. The different sources and transformations leave specific signatures on the chromophoric portion of dissolved organic matter (CDOM) detectable

by relatively simple optical measurements of light absorbance and fluorescence. Based on absorbance and fluorescence measurements, a number of indices have been developed by the scientific community (Helms et al., 2008; Fichot and Benner, 2012; Fichot et al. 2013; Helms et al. 2013; Murphy et al. 2013; Makarewicz et al. 2018), including a_{254} , a_{350} , $S_{275-295}$, $S_{350-400}$, $S_{300-600}$, S_R , and fluorophores deciphered by the Parallel Factor Analysis (PARAFAC). These indices were proven to be helpful in tracing specific processes or chemical signatures in the Arctic Ocean. Previously, on the regional level, the optical properties of DOM have been successfully employed, for example, to distinguish the origin of Arctic surface waters in the Fram and Davis Straits (Gonçalves-Araujo et al. 2016) or to fingerprint water masses in coastal Canadian Arctic surface waters (Walker et al. 2009). We hypothesize that the optical properties of CDOM can be applied for localization and constraining the geographical extent of major oceanographic features like the Beaufort Gyre, the Transpolar drift and the halocline layers. If the Beaufort Gyre is, at least partially, supplied by freshwater fluxes from fluvial discharge, it should be readily detectible in the CDOM fingerprint. If the cold halocline in the central Arctic Basins is at least partially fed by Eurasian shelves waters, using the optical properties, we should be able trace it to the region of their origin.

4.2. Methods and data

This study brings together the existing data on optical properties from 8 international research cruises carried out in the Arctic Ocean between 2005 and 2015.

4.2.1. Cruises and data sources

4.2.1.1. Beringia - Arctic Ocean Section (AOS 2005)

Hydrographic data, *in situ* fluorescence, and water samples were collected from August 21 through September 23, 2005, as part of the Beringia 2005 Expedition on board the icebreaker

Oden (Anders, 2005; Anderson et al. 2011). The Arctic Ocean Section (AOS-05) started north of Barrow, Alaska, crossed the Canada Basin and the Alpha Ridge along 150°W, passed through the Makarov Basin across the Lomonosov Ridge, through the Amundsen Basin, across the Gakkel Ridge, and through the Nansen Basin to Svalbard (Figure 1).

4.2.1.2. ARK-XXII/2 or PS70 (2007)

The research icebreaker *Polarstern* completed several oceanographic sections in the Eastern Arctic across the Nansen Basin, Amundsen Basin, and Makarov Basin (Figure 4.1) from July 29 to September 23, 2007. During the Ark-XXII/2 expedition, *in situ* CDOM fluorescence, water samples, and hydrographic data were collected (Schauer, 2008). The western sections of the cruise start on the Barents Sea shelf and in the St. Anna Trough, continuing offshore into the Nansen Basin. The eastern sections stretch from the Kara Sea shelf and the Laptev Sea shelf across the Nansen Basin, the Amundsen Basin, and the Lomonosov Ridge into the Makarov Basin and the northern Canada Basin.

4.2.1.3. NABOS (2008)

Samples were collected aboard the icebreaker *Kapitan Dranitsyn* in October 7-27, 2008, within the Nansen and Amundsen Basins Observational System (NABOS) framework. The cruise track consisted of 5 short shelf-slope sections (Figure 4.1), crossing the Eurasian continental slopes (from West to East) in the Barents Sea, the Nansen Basin, the Laptev, and the East Siberian Seas (Polyakov and Timokhov, 2008). The NABOS-08 campaign included CTD deployments, water sampling, hydrochemical and other observations available through the NABOS website (<http://nabos.iarc.uaf.edu>).

4.2.1.4. CFL (2008)

The Mackenzie Shelf and the Amundsen Gulf were sampled between 1 June and 7 August 2008 as a part of the Circumpolar Flaw Lead (CFL) study (Leitch, 2008). Several transects from open water into fast ice or mobile pack ice were conducted onboard the CCGS *Amundsen* (Figure 4.1). The main objective of the CFL field campaign was to collect a dataset that describes the physical controls of primary productivity within the flaw lead systems (Barber

et al. 2010). The dataset included the hydrographic and hydrochemical measurements. The *in situ* CDOM fluorescence was not measured during the fieldwork.

4.2.1.5. Malina (2009)

Onboard the same vessel, the CCGS *Amundsen*, oceanographic research on the Mackenzie shelf continued in July and August 2009. Several transects were conducted through the Mackenzie River plume into the southern Beaufort Sea (Figure 4.1) within the Malina Scientific Program (Malina Expedition Logbook, 2009). The focus of Malina missions was on primary production, bacterial activity, and organic matter photooxidation in the Arctic Ocean (Matsuoka et al., 2012; Massicotte et al., 2020). The hydrochemical and optical measurements of the water samples coupled with the hydrographic data from the field mission are used in this study.

4.2.1.6. ICESCAPE (2010)

The Impacts of Climate on the Eco-Systems and Chemistry of the Arctic Pacific Environment (ICESCAPE) program (https://espo.nasa.gov/icescape/content/ICESCAPE_0) was funded by NASA (National Aeronautics and Space Administration). The central objective of the program was to study the impact of climate change on the biogeochemistry and ecology of the Chukchi and Beaufort seas. The part of the data used in our study (hydrographic and hydrochemistry) was collected during the ICESCAPE field campaign onboard U.S. CGC *Healy* from 15 June to 22 July 2010 (Arrigo et al., 2010). The data is available in the Dryad Repository (<http://dx.doi.org/10.5061/dryad.4dn793t6>).

4.2.1.7. HLY1502 (2015)

Seawater samples along with CTD and other measurements were collected during the 2015 U.S. Arctic GEOTRACES (GN01) cruise aboard the USCGC *Healy* (HLY1502). The cruise track consisted of two legs. The vessel departed from Dutch Harbor, Alaska, on 9 August 2015, reached the North Pole ("Northbound leg"), and returned 12 October 2015 ("Southbound leg"). The "Northbound leg" began in the North Pacific, crossed the Bering Shelf, passed through the Bering Strait into the Chukchi Shelf, and continued northward along the 170°W to the North Pole. The "Southbound leg" stretched along the 150°W (Figure 4.1) and ended on the Chukchi

Sea shelf (Kadko and Landing, 2015). The data can be accessed through the British Oceanographic Data Centre (<http://www.bodc.ac.uk/geotraces>) and the Biological and Chemical Oceanography Data Management Office (Landing et al., 2019a, 2019b).

4.2.1.8. PS94 (2015)

The TransARC II cruise (PS94, GN02) onboard the German icebreaker RV Polarstern (Fig. 4.1; Rabe et al. 2016; Schauer, 2016) was a part of the 2015 Arctic GEOTRACES program. The PS94 cruise track (August 17th to October 15th) consisted of 2 transects extending from the Barents Sea and the Gakkel Ridge, respectively, into Makarov Basin (Schauer, 2016). The data can be found in Pangaea (<https://www.pangaea.de>, CTD data: <https://doi.org/10.1594/PANGAEA.859558>), the British Oceanographic Data Centre (<http://www.bodc.ac.uk/geotraces>), and Biological and Chemical Oceanography Data Management Office (Landing et al., 2019a, 2019b).

4.2.2. Hydrographic setting

Based on the differences in DOM and CDOM distribution we observed over the last 20 years (Amon et al. 2003; Amon 2004, Anderson and Amon 2015, Stedmon et al. 2011, Kaiser et al. 2017, Williford et al. 2021), and based on the prevailing water masses and ocean currents (Timmermans et al. 2020, Morison et al. 2021, Smith et al. 2021), we grouped the cruises into seven regions (Figure 4.1), as follows:

1. The Chukchi Sea shelf (CS) is a shallow inflow-type shelf (Wassmann et al. 2020) characterized by lower salinity and high primary productivity due to inflow of relatively fresh ($S < 33$) and nutrient-rich Pacific Water through the Bering Strait and exchanges with Canada Basin and the Arctic shelves via the East Siberian Current (Weingartner et al. 1999; Mathis et al. 2005).
2. The Beaufort Sea shelf (BS) is a narrow interior shelf (Wassmann et al. 2020) heavily influenced by the fluvial discharge from the Mackenzie River, which brings a large amount of nutrients, sediments, and tDOM (Holmes et al., 2002; Carmack et al., 2004; Matsuoka et al. 2012; Fichot et al. 2013). In addition, a narrow jet that intensifies in summer brings Pacific water into the region, although over the past

- decade, the flux has decreased by more than 80% due to the enhanced easterly winds along the Beaufort slope as a result of the intensification of the Beaufort High and deepening of the Aleutian Low (Brugler et al. 2014).
3. The Canada Basin (CB) water column is dominated by two water masses. The first one is relatively fresh ($S < 33$) Pacific water entering through Bering Strait and altered in the Chukchi Sea and Mackenzie River-influenced Beaufort Sea resides shallower than 150 m. The Beaufort Gyre, a large anticyclonic flow in the surface layer, is a prominent feature of the CB, marked by low salinity ($S < 31$) and low CDOM (Jones et al. 2008; Guéguen et al. 2015; Shen et al. 2016; Williford in prep). A recent study documented the strengthening of the trend for the Beaufort Gyre (Kaur et al., 2018). Secondly, there is saline ($S > 34.7$) and warm ($\theta > 0^\circ\text{C}$) Atlantic water, typically residing below 150 m that enters through the Fram Strait and the Barents Sea, partially modified on the extensive Eurasian shelves by mixing with fluvial discharge and freezing/thawing processes (Alkire et al. 2019).
 4. The Amundsen Gulf (AG) hydrography, in general, is similar to that described in the Canada Basin (Carmack et al. 1989). The notable unique feature of the gulf is the polynya, which is a part of the circum-Arctic system of flaw polynyas (Scheifele et al. 2020).
 5. The Nansen Basin (NB) is strongly influenced by the Atlantic water inflow, high in salinity and low in CDOM (Williford et al. 2021). It is divided into two branches: the Fram Strait branch that directly enters the NB and the Barents Sea branch that moves into the Barents Sea. The branches partially mix between the Franz Josef Land and Severnaya Zemlya and spread cyclonically in the Arctic Ocean (Rudels, 2015; Zhurbas & Kuzmina, 2020).
 6. The East Siberian and the Laptev Sea shelves (ESS and LS) are wide interior shelves heavily influenced by the Eurasian rivers discharge, which varies significantly between the seasons, peaking in May/June. The region is also characterized by ice melt/thaw processes, and polynyas are common (Bauch et al., 2011, 2016). The fluvial discharge brings suspended matter, tDOM, and nutrients into the system

(Hölemann et al. 2020; Williford et al. 2021). The Atlantic Ocean is the main source of marine water.

7. The Central Arctic (CA) consists of the Makarov and the Amundsen Basins, divided by the Lomonosov Ridge. The major surface feature of the CA is the Transpolar Drift (TPD), a current that transports shelf water with a strong tDOM signal from the ESS and LS toward the Fram Strait (Opsahl et al. 1999, Amon 2004, Charette et al. 2020, Williford et al. 2021). A recent study reports strengthening of the TPD (Kaur et al., 2018).

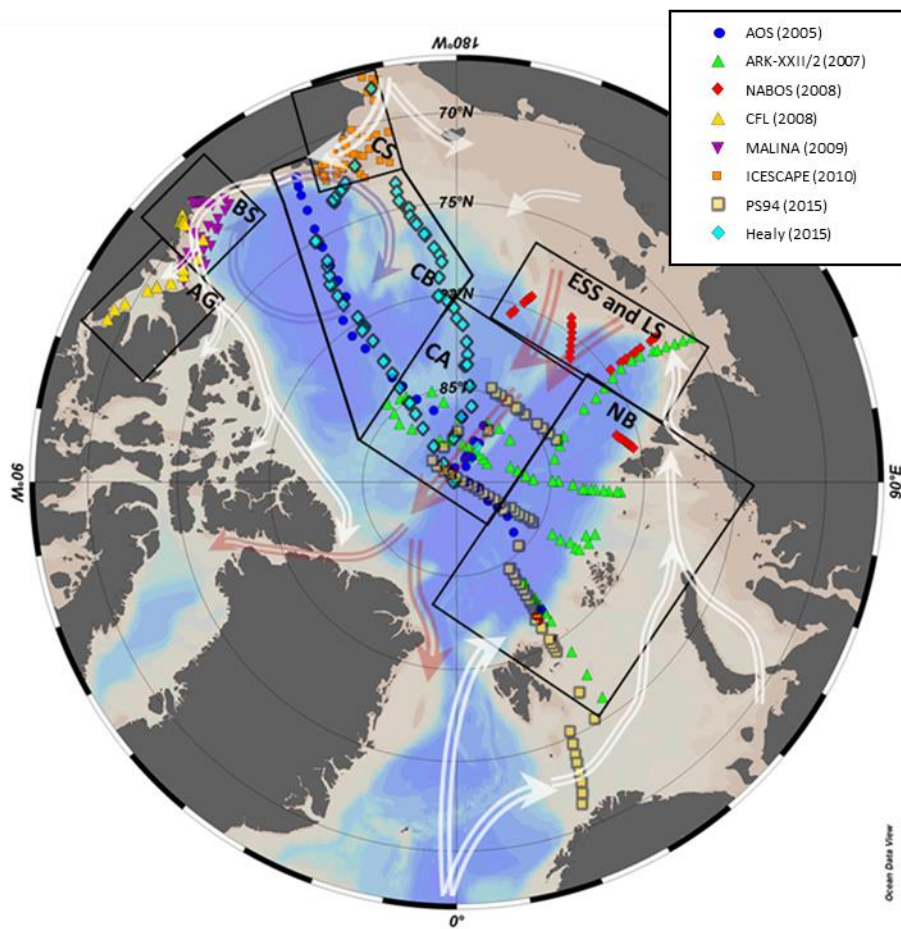


Figure 4.1. General map of the Arctic Ocean showing stations occupied during the 8 cruises: AOS 2005 (dark blue circles), ARK-XXII/2 (green triangles), NABOS-2008 (red diamonds), CFL-2008 (yellow triangle), Malina-2009 (purple reversed triangles), ICESCAPE-2010 (orange squares), PS94-2015 (semi-transparent yellow squares) and Healy-2015 (light blue diamonds); and study areas in black boxes: the Nansen Basin (NB), the East Siberian and the Laptev Seas

(ESS and LS), the Central Arctic (CA), the Amerasian Basin (AB), the Chukchi Sea (CS), the Beaufort Sea (BS) and the Amundsen Gulf (AG). The approximate locations of major upper ocean circulation features are shown with white, red (Transpolar Drift), and light purple (Beaufort Gyre).

4.2.3. The CDOM data

In total we compiled 1232 pairs of absorbance scans and emission matrices created for the 8 cruises in this pan-Arctic dataset. The absorbance spectra recorded between 200 and 1,000 nm. For the spectrofluorescence, emission scans from 300 to 550 nm (2 nm increment) and excitation scans ranging from 260 to 450 nm (5 nm increment) were used. Daily pure water (Milli-Q) blanks were obtained and subtracted to remove water scattering peaks. Measured data were spectrally corrected for instrument bias, and subsequently, Raman calibrated using the pure water blanks. The datasets were processed separately in MATLAB using the drEEM toolbox (version 0.6.3, Murphy et al., 2013). The five-component model was found optimal based on spectral loadings, residual examination, and split-half validation using a convergence criterion of $1e^{-8}$ (Figure 4.2). The components were labeled based on their emission maxima, sorted from overall highest fluorescence intensity to the lowest: C₄₈₄, C₃₃₆, C₄₁₈, C₃₀₃, C₄₀₄. The fDOM, a sum of all fluorescent components modeled by PARAFAC, was also computed.

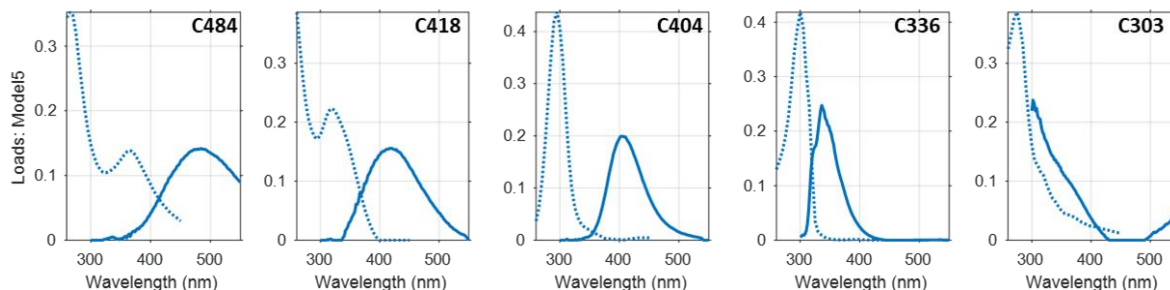


Figure 4.2. The fluorescence properties of the fluorescent components identified by PARAFAC modeling.

Several metrics based on the absorbance scans were used in this study. The raw absorbance was baseline corrected by subtracting an offset- exponential fit of the absorbance spectrum over the range from 300 nm to 650 nm (Stedmon et al. 2000). The corrected absorbance (A_λ) was converted to Napierian absorption coefficients (a_λ) for each wavelength, λ , with the following formula:

$$a_{\lambda} = \ln(10) \frac{A_{\lambda}}{L}, \quad (1)$$

Where L is the length of the cuvette in meters, here we use the absorption at 254 (a_{254}) and 350 nm. The a_{254} and a_{350} are used as proxies for CDOM concentration and terrigenous character (Walker et al., 2013; Griffin, 2016; Chen et al., 2018). The choice of the wavelengths for the absorption coefficients is explained in the other studies: the conjugated systems (e.g., aromatic rings) that are abundant in the tDOM have peak absorption near 254 nm (Weishaar et al., 2003), and the long-wavelength absorption tail of humics absorbs light at ~350 nm (Del Vecchio and Blough, 2002).

The spectral slopes ($S_{xxx-xxx}$, where subscripts denote wavelength range), for three absorbance spectra regions (275-295 nm, 350-400 nm, and 300-600 nm) and the Spectral Ratio (S_R ; $S_{275-295}/S_{350-400}$), were computed using a linear fit of the log-linearized a_{λ} (1) spectrum over their respective spectral range. If the absorption coefficients represent the specific chemical compounds, it is assumed that the spectral slopes reflect relative proportions of the chromophores within the CDOM pool. In general, degradation causes the shift of absorbance towards shorter wavelengths, and 275–295 nm and 350–400 nm are the most dynamic regions of the absorbance spectra. The studies suggested that the spectral slope values can be used as indicators of the history or origin of a water sample. For example, $S_{275-295}$ and $S_{350-400}$ served as indicators of photochemical alterations. $S_{275-295}$ was used as an effective tracer of tDOM in river-influenced ocean margins (Fichot and Benner, 2012). $S_{300-600}$ was shown to have potential as a dissolved organic carbon (DOC) concentration proxy (Makarewicz et al., 2018). S_R correlates well with CDOM molecular weight and increases exponentially with photobleaching (Helms et al., 2008).

A Principal Component Analysis (PCA) was performed with the normalized optical properties of CDOM using the Matlab package (Ballabio, 2015). PCA is a commonly used statistical technique for dimensionality reduction of the multivariate datasets. PCA is an unsupervised method of feature extraction, where original variables that might be redundant are combined and reduced to the most descriptive components.

The data used for this study are summarized in Table 1. Detailed descriptions of the methods of data collection (DOC, lignin phenols) and sample processing can be found in listed publications.

Table 4.1. Data compiled for this study

Cruise	Year	Parameters used in this study				Cruise report	Key publications
		Fluorescence/absorbance scans	<i>in situ</i> CDOM fluorescence	DOC	Lignin phenols		
AOS	2005	+	+	+	+	Anders, 2005 https://cchdo.ucsd.edu/data/8026/ODEN05do.pdf	Jones et al. 2008; Walker et al. 2009; Anderson et al. 2013; Ulfso et al. 2017; Bauch et al. 2011, 2016; Alkire et al. 2017; Williford et al. 2021
ARK-XXII/2	2007	+	+	+	+	Schauer, 2008	Fichot et al. 2013; Bauch et al. 2014, 2016; Rudels et al. 2015; Kaiser et al. 2017
NABOS	2008	+	+			Polyakov and Timokhov, 2008 https://uaf-iarc.org/wp-content/uploads/2018/10/NABOS-2008-report.pdf	Fichot et al. 2013; Bauch et al. 2014, 2016; Rudels et al. 2015; Kaiser et al. 2017
CFL	2008	+	+	+		Leitch, 2008. http://ipy.nwtresearch.com/Documents/Summaries/CFL_Summary.pdf	Barber et al. 2010; Shen et al. 2012; Fichot et al. 2013
Malina	2009	+	+	+		Malina Expedition Logbook, 2009. http://www.obs-uvfr.fr/malina/cruise_description.html?tab=1#TabbedPanels1	Matsuoka et al. 2012; Shen et al. 2012; Massicotte et al. 2020
ICESCAPE	2010	+	+			Arrigo, 2010. ICESCAPE 2010. http://ocean.stanford.edu/icescape/ICESCAPE_Cruise_Report_HLY1001_2010.doc	Fichot et al. 2013; Arrigo & Perovich 2010; Arrigo et al. 2012; Matsuoka et al. 2015
HLY1502	2015	+	+	+	+	Kadko and Landing, 2015).	Charette et al. 2020; Woosley and Millero, 2020; Williford et al. (in prep)
PS94	2015	+	+	+	+	Schauer, 2016	Charette et al. 2020; Williford et al. (in prep)

4.3 Results

4.3.1 PARAFAC components

The five fluorescence components identified by the PARAFAC model have been widely described in previous studies, including Arctic Ocean studies (Table 2). The PARAFAC component C₄₈₄ is a typical humic-like terrigenous component commonly found in the ocean (Walker et al., 2009; Kowalczyk et al., 2013; Gonçalves-Araujo et al. 2016; Osburn et al. 2016; Chen et al. 2018; Williford et al. 2021). The C₄₈₄ component had the strongest correlation with the lignin phenols concentrations. C₄₁₈ was characterized as humic-like of ambiguous marine and/or terrigenous origin (Walker et al., 2009; Chen et al., 2018; Amaral et al., 2016). The two protein-like components were identified by the study: C₃₃₆ and C₃₀₃ (Walker et al., 2009; Amaral et al., 2016; Osburn et al., 2016; Chen et al. 2018), resembling the fluorescence signatures of tryptophan and tyrosine, respectively. The autochthonous humic-like (Walker et al. 2009) component C₄₀₄ is similar to the previously described fluorophore, which had the lowest fluorescence signal among the other modeled compounds and was associated with a signal from degrading marine organic matter in sediment (Williford et al. 2021).

Table 4.2. Spectral characteristics of the five components identified by PARAFAC and their comparison to previously identified components, sorted by emission peak wavelength.

	Description	Excitation/ Emission max, nm	Similar components found in OpenFluor database	References
C ₄₈₄	Aromatic, high molecular weight, humic-like, terrigenous	265/484	Arctic Seawater C4 Arctic_Outflow C1 AMT20 C2 Osburn_OpticalTDOMproxies C1	Chen et al. 2018 Gonçalves-Araujo et al. 2016 Kowalczyk et al. 2013 Osburn et al. 2016
C ₄₁₈	Humic-like of mixed origin	260/418	Beringia C1 Arctic Seawater C2 vale3C C1	Walker et al. 2009 Chen et al. 2018 Amaral et al. 2016
C ₄₀₄	Marine humic-like component, likely linked to the sediment-derived DOM	295/404	Beringia C6 AMT20 C5	Walker et al. 2009 Kowalczyk et al. 2013
C ₃₃₆	Protein and tryptophan like	300/336	Arctic Seawater C1 vale3C C3	Chen et al. 2018 Amaral et al. 2016
C ₃₀₂	Amino acid-like, correlates with lignin	275/303	Osburn_OpticalTDOMproxies C4	Osburn et al. 2016

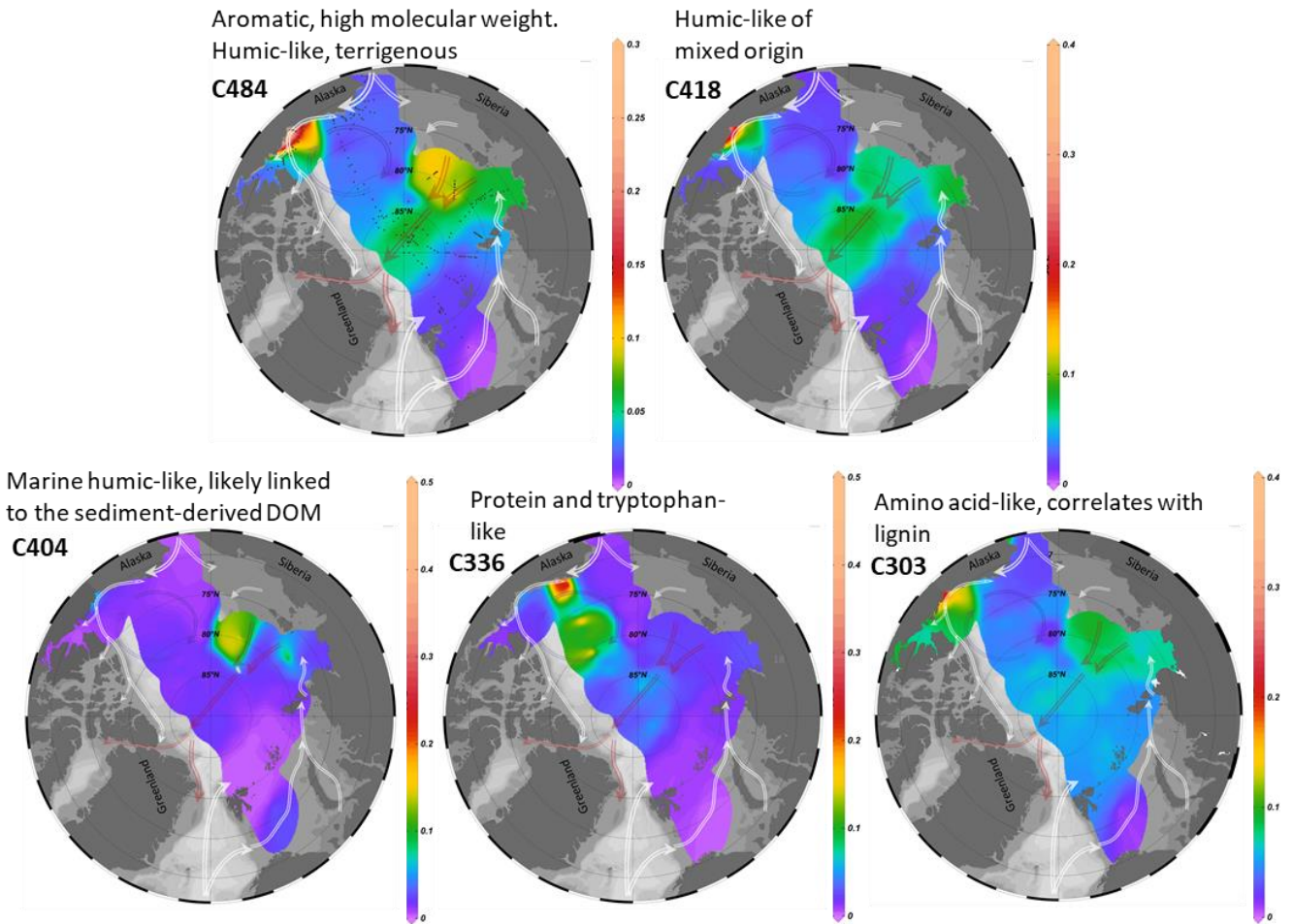


Figure 4.3. Surface distribution of five PARAFAC components identified in the study.

At the surface, the PARAFAC components showed various patterns related to the significant oceanographic features and topography. The humic-like fluorophores fluorescence (C_{484} , C_{418}) intensity distribution was accompanied by the C_{303} fluorescence. These three components exhibited very high fluorescence intensity by the Mackenzie river mouth and a moderate increase within the TPD system, constrained by the Mendeleev and Gakkel ridges. The terrigenous C_{484} and C_{404} were higher on the Mendeleev ridge side. The previous studies have identified the Mendeleev ridge as an upwelling place of the Atlantic-origin waters coming with the circumpolar current (Woodgate et al. 2005; Zhao et al. 2015). Besides, the Pacific influence at $S \sim 34$ was detected on the Canadian Basin side, but not on the Makarov Basin side (Woodgate et al. 2005). The protein-like component C_{303} was the only component enriched at the surface of the Amundsen Gulf. And is probably locally produced within the PML of the Dolphin and Union

Strait. The tryptophan-like C_{336} peaked at the surface of the Beaufort shelf-break on the Mackenzie mouth side of the Chukchi Plateau. It was also the only fluorophore with high fluorescence intensity within the Beaufort Gyre system.

4.3.2. Regional distributions of DOM

4.3.2.1. The Amundsen Gulf (CFL-2008, Malina-2009)

The AG water column has a structure resembling that of the Canada Basin (Carmack et al. 1989). The PML (top 80m, Shen et al. 2012) is influenced by the summer ice melt and is characterized by the high $S_{275-295}$ and C_{303} (Figure 4.4). The UHC ($32.0 \leq S \leq 33.9$; Shen et al. 2012) situated beneath the PML was characterized by the elevated C_{484} and C_{418} . The protein-like fluorophores C_{336} and C_{303} show an increase in the most eastern part of the gulf, within the PML and the UHC. The trend is accompanied by the rise in S_R towards the $115^\circ W$. Comparing to the UHC, the PML and the LHC ($S > 33.9$) have elevated levels of $S_{350-400}$. The $S_{350-400}$ peaks in the PML at $\sim 118^\circ W$.

4.3.2.2. The Beaufort Sea slope (CFL-2008, Malina-2009)

The vertical structure of the water column in the Beaufort Sea shelf is determined by Mackenzie river discharge, ice melt/brine formation, and lateral intrusion of Pacific and Atlantic waters (Figure 4.5). Matsuoka et al. (2013) has described six distinct water masses in the region. First, the surface layer was separated into the upper and lower PML (UPML and LPML, respectively). The UPML is heavily influenced by the Mackenzie river water and summer sea ice melt; therefore, is relatively fresh (salinity < 28). We would hypothesize the river-rich water mass to have high tDOM, and the data do support this with the high levels of CDOM (a_{254} , a_{350}), $S_{300-600}$, $S_{350-400}$, and all the PARAFAC components with the exception of tyrosine-like C_{303} , which showed low fluorescence intensity near the river mouth. Matsuoka et al. (2013) described the LPML as waters from the previous winter that do not penetrate the pycnocline and stay within the surface layer. In terms of the CDOM optical proxies, the LPML was the opposite of the UPML, with the highest levels of $S_{275-295}$ and S_R . The LPML is separated from the underlying layer by the salinity surface of $S=30.7$.

Below the PML is the Pacific summer water (PSW; $30.7 \leq S < 32.3$) brought by the circumpolar current from the Chukchi Sea during summer (Matsuoka et al. 2013). Comparing to

the adjacent waters above and below the PSW, the layer has slightly elevated fluorescence intensity levels of humic-like C_{418} , humic-like and sediment-derived C_{404} , and tryptophan-like C_{336} . Below the PSW, Pacific winter waters form the upper halocline waters (UHW; $32.3 \leq S < 33.9$) with apparent silicate concentrations signature of $>25 \mu\text{mol/L}$ (Matsuoka et al. 2013; Anderson et al. 2013). Among the optical properties of CDOM, only the $S_{350-400}$ was slightly elevated in this layer.

The lower halocline water (LHW; $33.9 \leq S < 34.7$) originates from the Barents Sea shelf during the ice formation (Carmack et al. 2004). The tyrosine-like C_{303} and $S_{275-295}$ are consistently high throughout the layer. $S_{350-400}$ peaks near the slope, while S_R and C_{336} levels are higher offshore. The more saline ($S > 34.7$) and warmer ($\theta > 0^\circ\text{C}$) AW is located below ~ 225 m (Matsuoka et al. 2012). Not enough data points were available for the layer to describe the associated optical properties trends.

4.3.2.3. The Chukchi Sea (ICESCAPE-2010)

The major water masses residing on the Chukchi shelf have been defined by their potential temperature and salinity, as described in Woodgate et al. (2005), Gong and Pickart (2015), and Yang and Bai (2020). Besides the PSW (defined in this region as $S < 33$, $\theta > 0^\circ\text{C}$), the Pacific Winter Water (PWW; $\theta < -1^\circ\text{C}$, $S > 31.5$) produced by winter cooling and brine formation is present on the shelf (Figure 4.7). The PWW is the source for the UHC (Timmermans and Marshall, 2020). The PWW is further separated into colder ($\theta < -1.6^\circ\text{C}$) newly-ventilated PSW and warmer ($\theta > -1.6^\circ\text{C}$) remnant PWW, that has been warmed by mixing with PSW and/or by solar radiation. The AW is defined by $S > 33.6$ and $\theta > -1^\circ\text{C}$.

The PSW occupying the top 15-30 m of the Chukchi shelf water column is heterogeneous in terms of the CDOM character and distribution due to the differences in the timing of sea ice melting and local circulations that are driven by the intricate local topography. During the early summer fieldwork within the ICESCAPE-2010 project, the Chukchi Sea was in the midst of its seasonal ice melt. In the central part of the chosen section, about 300 m offshore, the minimum surface salinity coincided with the highest values of $S_{350-400}$. The $S_{275-295}$ was monotonously high throughout the PSW, while the $S_{300-600}$ was low. The a_{254} peaked close to the coast, while the a_{350} had the highest values offshore. All PARAFAC components were low within this water mass.

The newly-ventilated PWW was characterized by the high humic-like fluorescence intensity, a_{254} , and a_{350} , $S_{350-400}$, and $S_{300-600}$. On the contrary, the remnant PWW was marked by the elevated protein-like fluorescence signal, specifically at the bottom of the shelf. The S_R was lower in the newly-ventilated PWW compared to the remnant PWW.

4.3.2.4. The East Siberian Sea and the Laptev Sea (ARK-XXII/2-2007; NABOS-2008)

The Eurasian shelves have, over most of the area, a water depth of only 20–50 m (Bauch et al. 2010). In this study, the hydrography of the region was represented in two major layers. The thin surface layer consisting of up to 6% of ice melt and up to 18% of river water occupied the top 20 meters ($S < 32$; Williford et al. 2021). The bottom layer marked by a strong brine signal and salinity of $32 < S < 33$ (Williford et al. 2021) occupied 20–45 meters. Both layers were characterized by elevated optical properties: a_{254} , a_{350} , $S_{350-400}$, C_{484} , and protein-like fluorophores C_{336} and C_{303} , as expected, considering a substantial supply of organics from the fluvial discharge, potential sediment resuspension, and local primary production. The surface layer had remarkably high fluorescence intensity at C_{303} and high values of $S_{300-600}$. The bottom layer was characterized by high fluorescence intensity of C_{484} , C_{418} , C_{404} , and C_{336} as well as a_{254} , a_{350} .

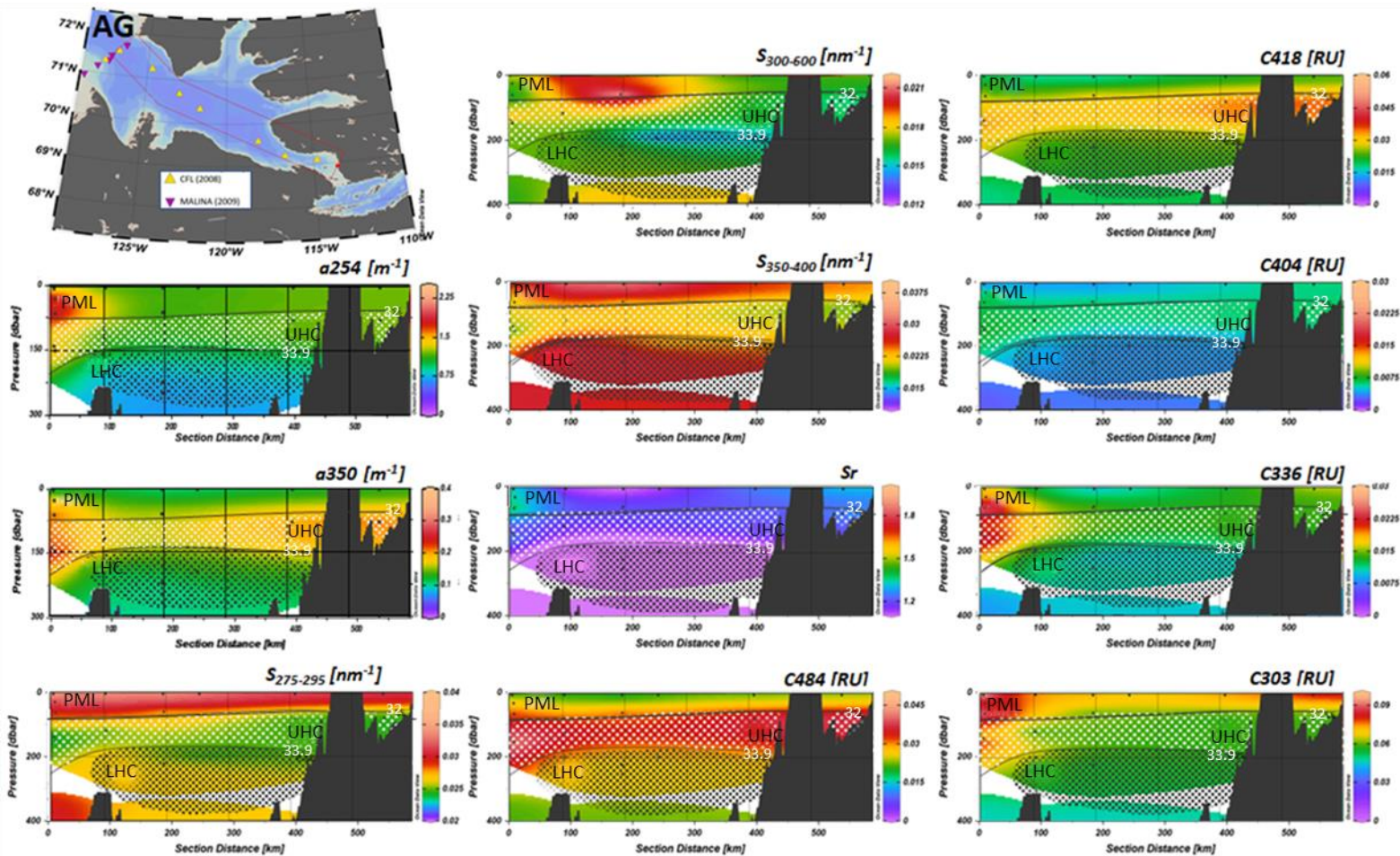


Figure 4.4. The representative section showing a_{254} , a_{350} , $S_{275-295}$, $S_{350-400}$, $S_{300-600}$, S_R , and PARAFAC components C_{484} , C_{336} , C_{418} , C_{303} , C_{404} in the upper 400 m in the Amundsen Gulf (AG). Black solid contour lines represent isohalines that bound water masses: PML ($S=32$), UHC ($S=32$, $S=33.9$), LHC ($S>33.9$). The LHC layer is overlaid by the black dot pattern and the UHC- by the light gray dot pattern.

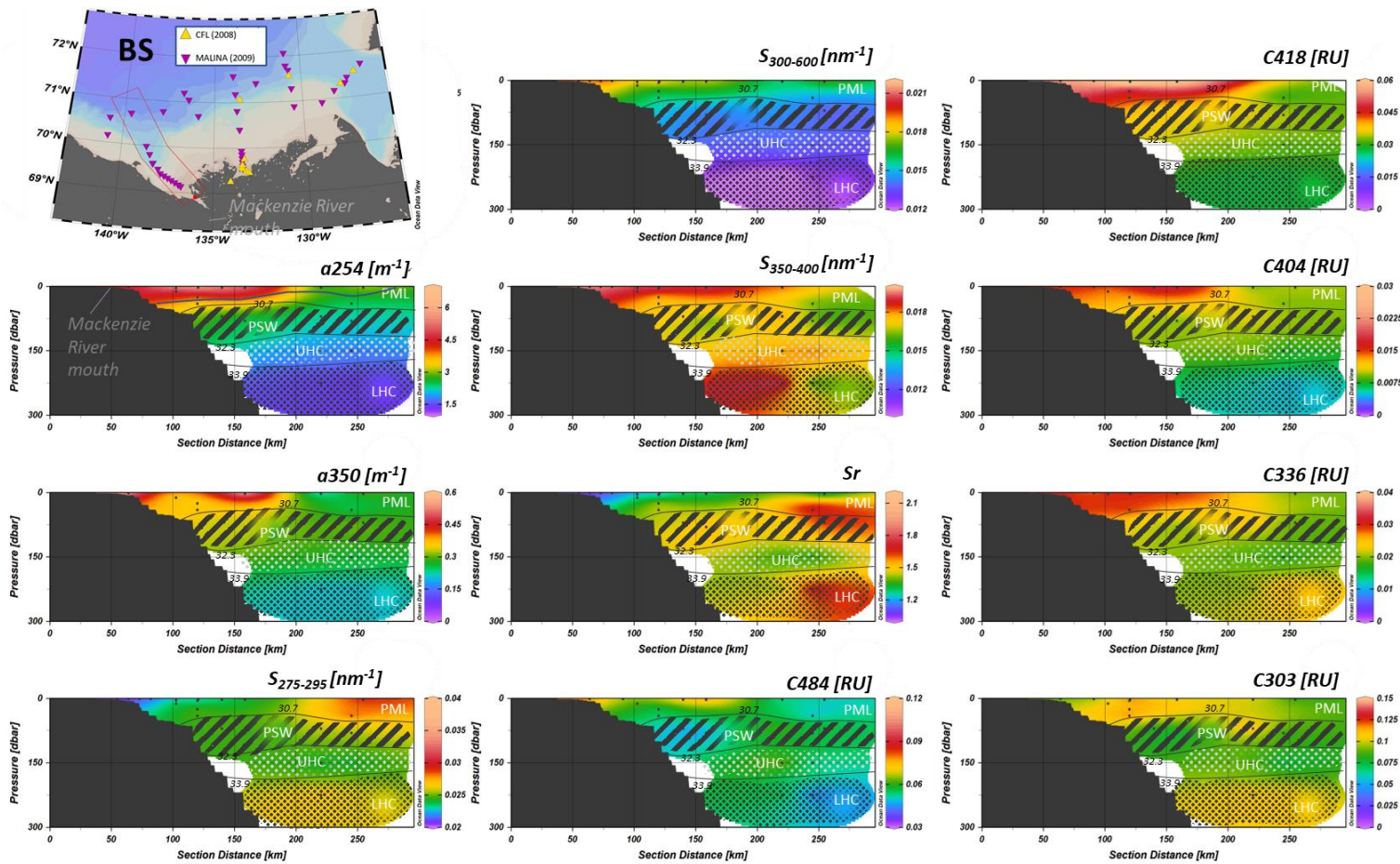


Figure 4.5. The representative section showing a_{254} , a_{350} , $S_{275-295}$, $S_{350-400}$, $S_{300-600}$, S_R , and PARAFAC components C_{484} , C_{336} , C_{418} , C_{303} , C_{404} in the upper 300 m in the Beaufort Sea slope regions (BS). Black solid contour lines represent isohalines that bound water masses: PML ($S=28$), LPML ($S=28$, $S=30.7$), PSW ($S=32.3$, $S=33.9$). The LHC layer is overlaid by the black dot pattern and the UHC- by the light gray dot pattern. The PSW is emphasized by the striped pattern.

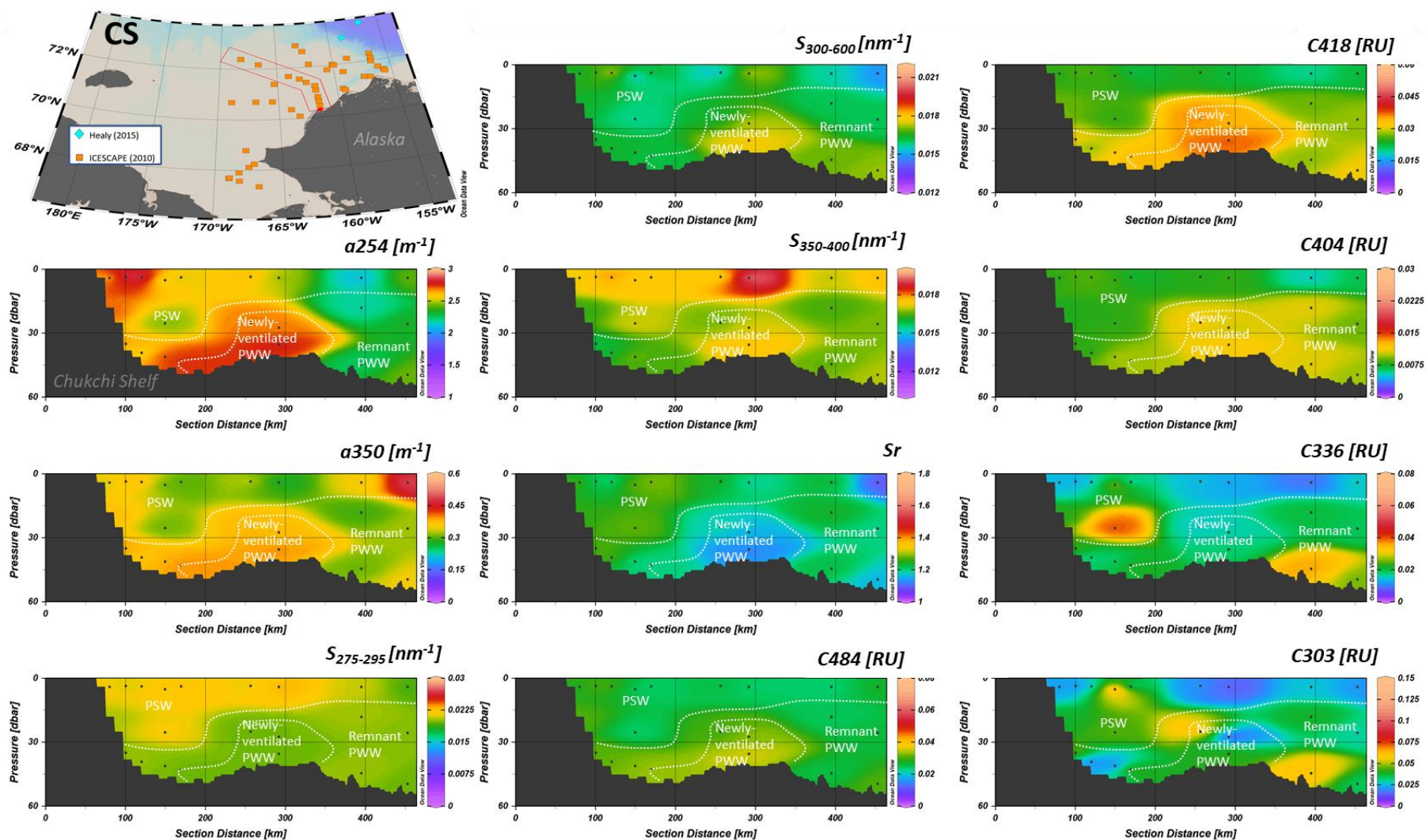


Figure 4.6. The representative section showing a_{254} , a_{350} , $S_{275-295}$, $S_{300-600}$, $S_{350-400}$, S_R , and PARAFAC components C_{484} , C_{336} , C_{418} , C_{303} , C_{404} in the upper 300 m in the Chuckchi Sea (CS). The following water masses are shown: PSW ($S < 33$, $\theta > 0^\circ\text{C}$), the PWW separated into colder ($\theta < -1.6^\circ\text{C}$) newly-ventilated PSW and warmer ($\theta > -1.6^\circ\text{C}$) remnant PWW.

4.3.2.5. The Canada Basin (AOS-2005, HLY1502)

The hydrography of the Canada Basin consists of water masses forming a unique pycnocline structure (Anderson et al., 2013; Timmermans and Marshall, 2020). The relatively fresh ($S < 31$) polar mixed layer occupies the top 50 meters (Figure 4.8). In 2005 and 2015, the PML within the Beaufort Gyre occupying the central Canada Basin was marked by low a_{254} , $S_{275-295}$, $S_{350-400}$, and slightly elevated C_{303} . Within the PML, the a_{254} peaks close to the Chukchi Shelf, while the spectral slopes are the highest in the northern part of the Canada Basin.

The UHC resides beneath the PML. Same as in the Chukchi Sea, we characterize the UHC as having a silica signature with a concentration of $>25 \mu\text{mol/L}$ (Anderson et al., 2013; Matsuoka et al., 2013), with the UHC core in the nutrient maximum. Comparing to the waters surrounding the UHC, the layer is characterized by the elevated a_{350} , $S_{350-400}$, $S_{300-600}$, C_{404} . The UHC in the region is characterized by the low $S_{275-295}$ and C_{303} . Beneath the UHC lays the thinner LHC. We observe the highest C_{484} , C_{418} at the UHC/LHC border. We consider the potential density surface of $\sigma = 27.4 \text{ kg/m}^3$ to be the lower boundary of the LHC (Timmermans and Marshall, 2020). The Atlantic water (AW) is found beneath the UHC ($\sigma > 27.4 \text{ kg/m}^3$).

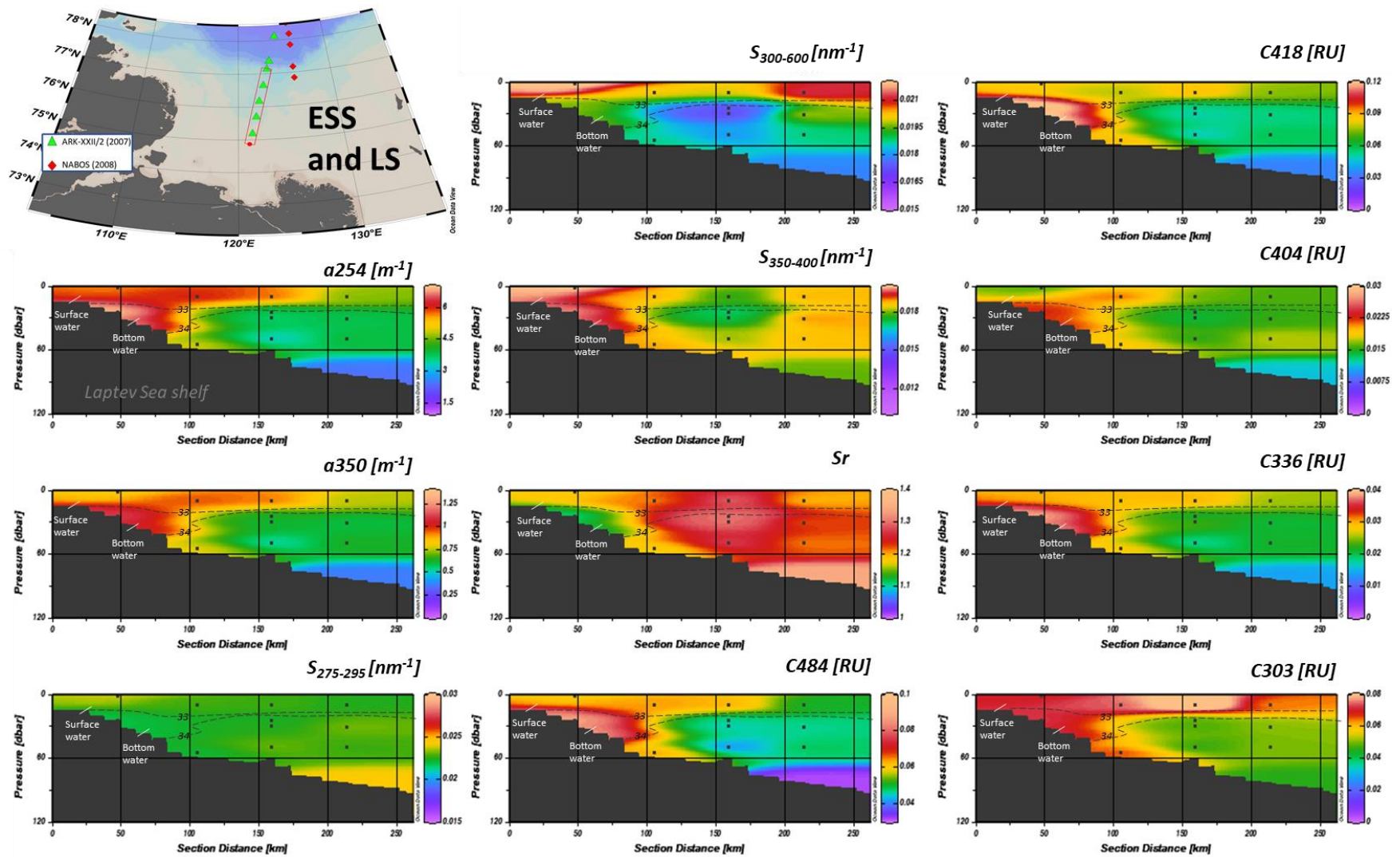


Figure 4.7. The representative section showing a_{254} , a_{350} , $S_{275-295}$, $S_{350-400}$, $S_{300-600}$, S_R and PARAFAC components C_{484} , C_{336} , C_{418} , C_{303} , C_{404} , and in situ CDOM fluorescence in the upper 120 m in the East Siberian and the Laptev Sea shelves. The black dashed contour line represents the isohalines of $S=33$ and $S=34$, marking the upper and the lower limit of the Laptev shelf bottom water.

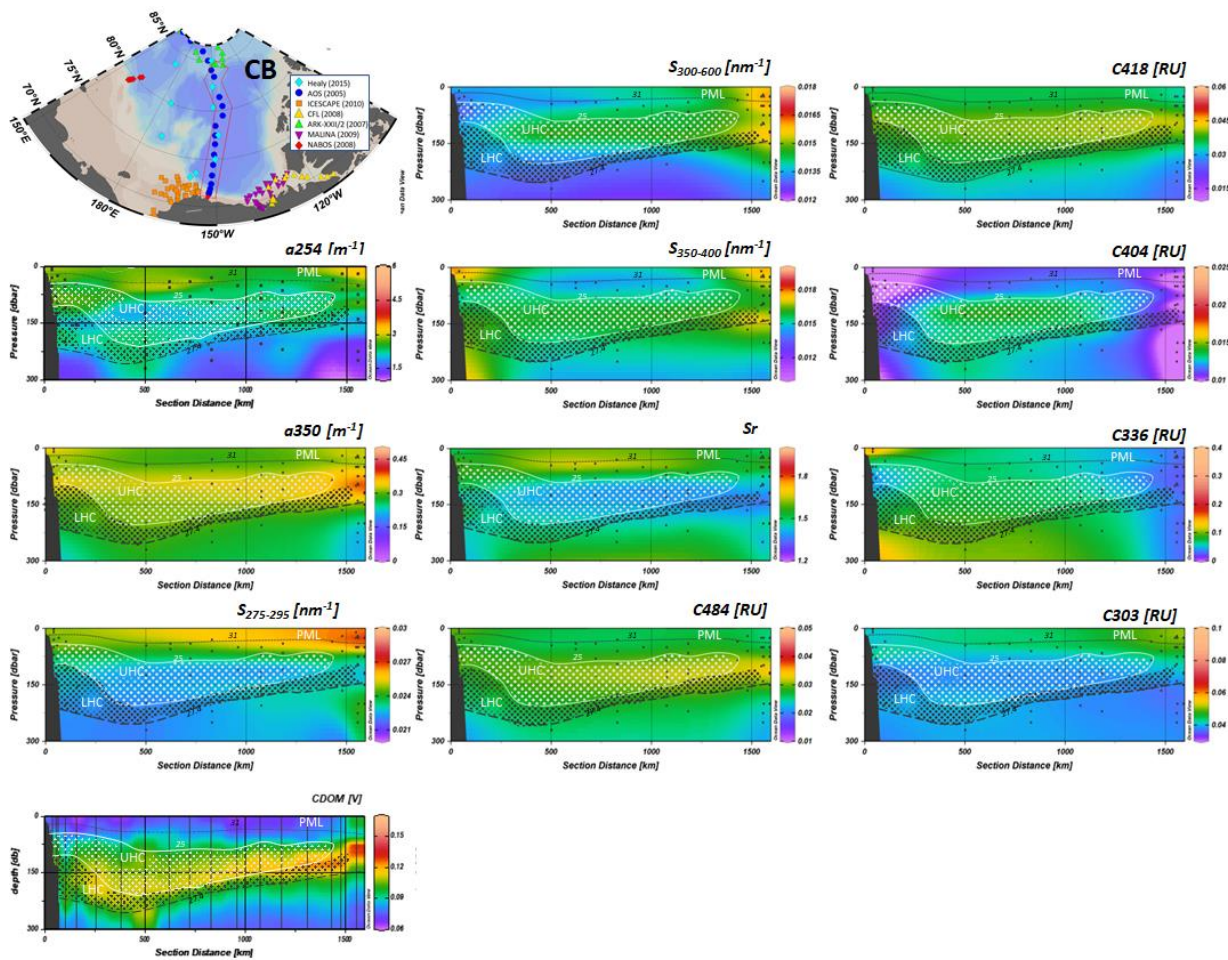


Figure 4.8. The representative section showing a_{254} , a_{350} , $S_{275-295}$, $S_{350-400}$, $S_{300-600}$, S_r and PARAFAC components C_{484} , C_{336} , C_{418} , C_{303} , C_{404} , and in situ CDOM fluorescence in the upper 300 m in the Canada Basin (CB). Only AOS 2005 data is used for the plot. The black dotted contour line represents the isohaline of $S=31$, which marks the base of the PML. The white solid contour line of $[Si] = 25 \mu\text{mol/L}$ represents the bounds of the UHC, overlaid by the white dot pattern. The LHC layer is overlaid by the black dot pattern, bordered at the bottom by the isopycnals (black dash line) of $\sigma = 27.4 \text{ kg/m}^3$.

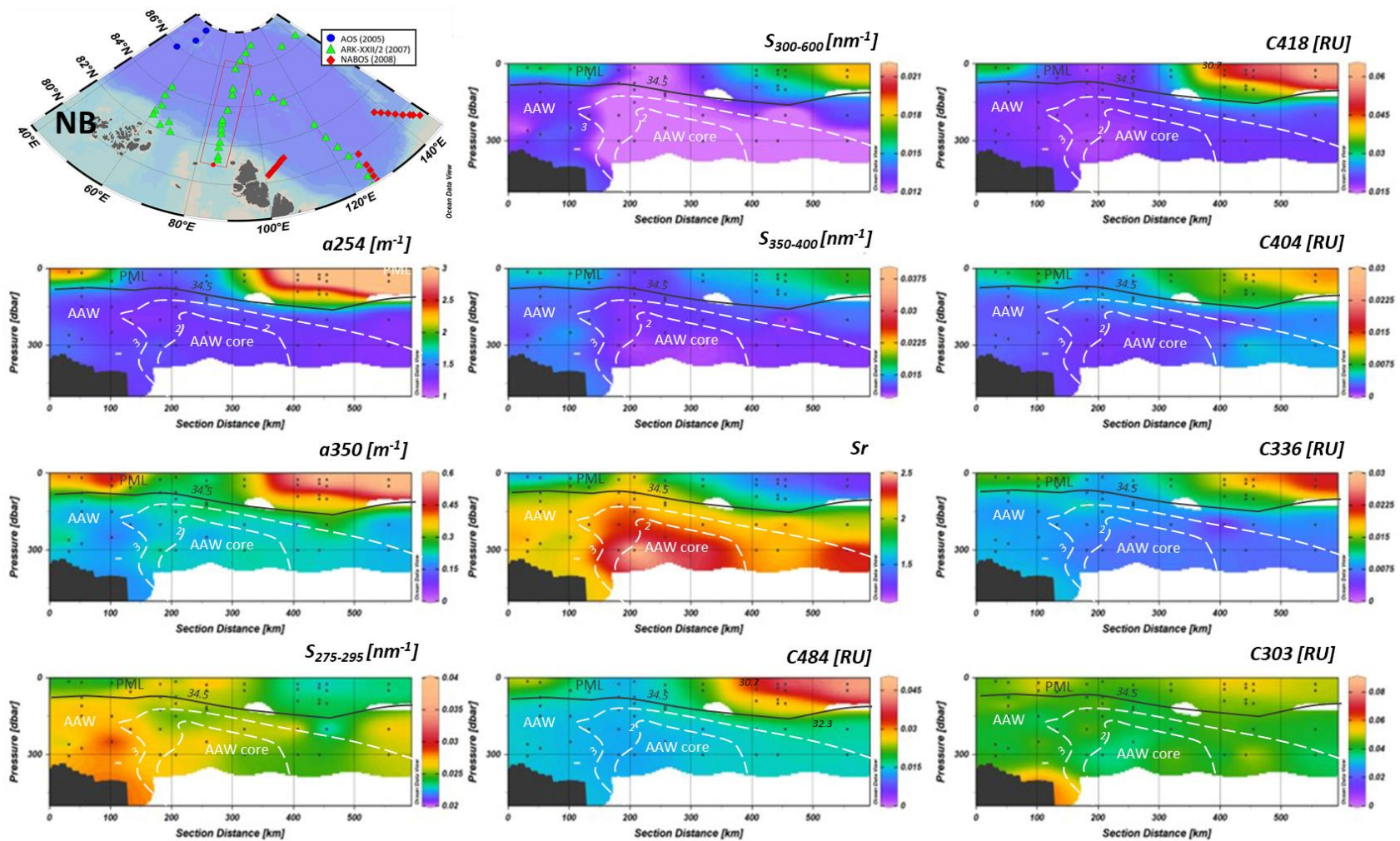


Figure 4.9. The representative section showing a_{254} , a_{350} , $S_{275-295}$, $S_{350-400}$, $S_{300-600}$, S_R , and PARAFAC components C_{484} , C_{336} , C_{418} , C_{303} , C_{404} in the upper 400 m in the Nansen Basin (NB). PML is characterized by $\theta < 0^\circ\text{C}$ and $S < 34.5$. AAW is marked by the $\theta > 0^\circ\text{C}$, with the layer core located around θ max.

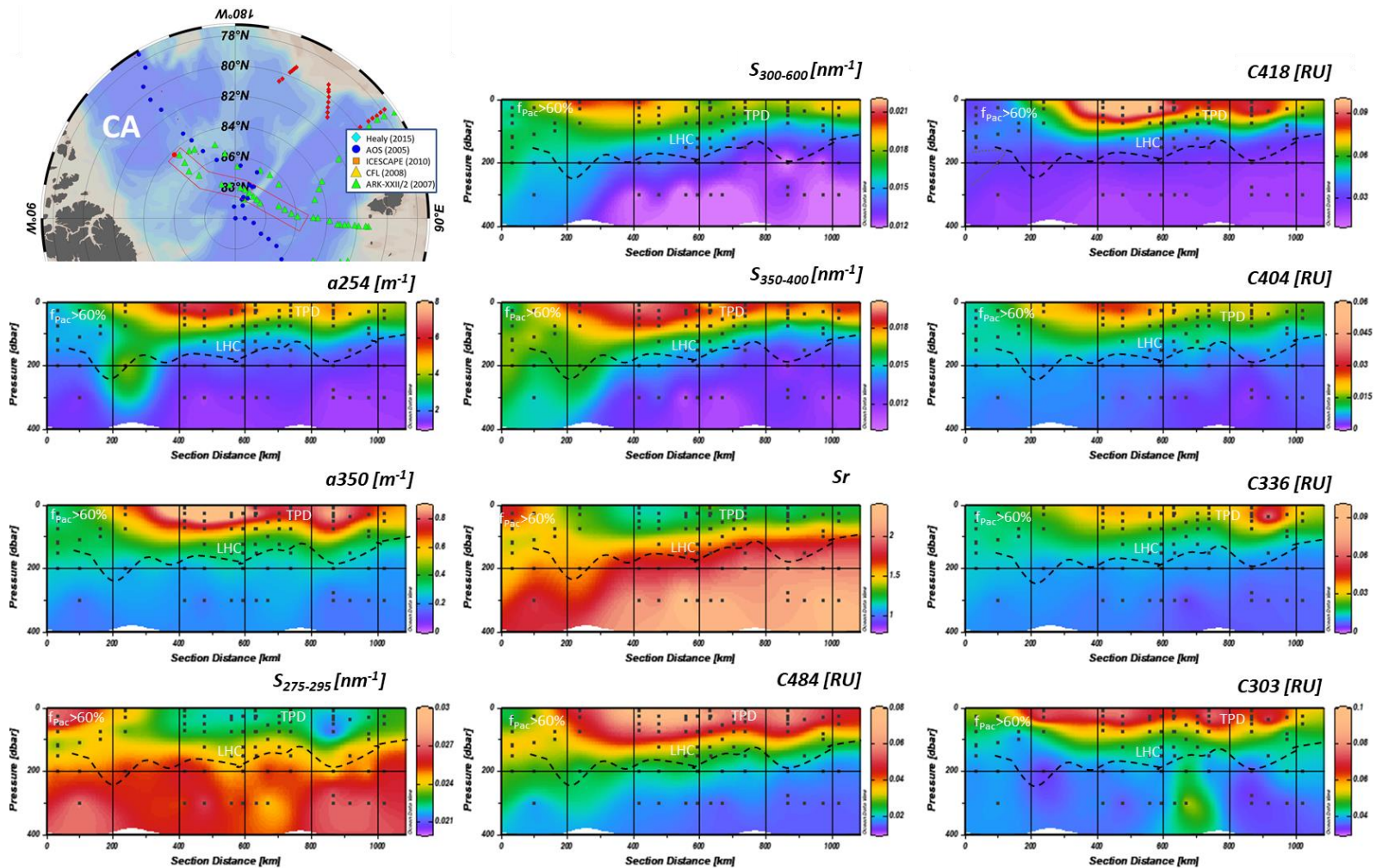


Figure 4.10. The representative section showing a_{254} , a_{350} , $S_{275-295}$, $S_{350-400}$, $S_{300-600}$, S_R , and PARAFAC components C_{484} , C_{336} , C_{418} , C_{303} , C_{404} in the upper 400 m in the Central Arctic region (CA). The top 100 m is occupied by the TPD in the Amundsen and the Northern Makarov Basins. The PML of the southern Makarov Basin contains up to 60% of f_{Pac} (Williford et al., 2021). The LHC is bordered at the bottom by the isopycnal of $\sigma = 27.4 \text{ kg/m}^3$. (black dashed line; Bertosio et al. 2020).

4.3.2.6. The Nansen Basin (ARK-XXII/2-2007; NABOS-2008)

The hydrography of the Nansen Basin is described by Rudels (2010, 2015). The Polar Surface Water (PSW) influenced by sea ice melt, and fluvial discharge is characterized by $\theta < 0^{\circ}\text{C}$ and $S < 34.5$ (Figure 4.9). The PML is highly heterogeneous in terms of the CDOM distribution. The a_{254} , a_{350} , $S_{350-400}$, $S_{300-600}$, and all the PARAFAC components show a noticeable increase towards the Amundsen Basin, are slightly elevated over the continental slope, and are low in the central Nansen Basin. By contrast, the $S_{275-295}$ and S_R are elevated in the PSW about 80 km from the shelf break.

The AW inflow via Fram Strait that is cooled and freshened on the Eurasian shelves is called Arctic Atlantic Water (AAW). This water mass is typically marked by the $\theta > 0^{\circ}\text{C}$, with the layer core located around θ max. The S_R peak coincides with the AAW core. $S_{275-295}$ and C_{303} were elevated around the shelf break.

4.3.2.7. The Central Arctic Ocean (ARK-XXII/2-2007; AOS-2005, HLY1502)

The PML ($S < 33$; Rudels 2001) contained two distinct water types. In the southern part of the Makarov Basin, the PML contained up to 60% of Pacific water (Williford et al. 2021), characterized by the elevated $S_{275-295}$, S_R (Figure 4.10). The PML in the northern part of the Makarov and the entire Amundsen Basin was occupied by the TPD, containing up to 20% of river water (Williford et al., 2021). We define the extent of the TPD based on the distributions of the optical properties. The a_{254} , a_{350} , $S_{350-400}$, $S_{300-600}$, and all the PARAFAC components peaked in this layer. The massive CDOM fluorescence signal in the TPD resulted in masking the LHC (bordered at the bottom by the isopycnal of $\sigma = 27.4 \text{ kg/m}^3$; Bertosio et al. 2020) footprint.

4.4. Discussion

4.4.1. Trends in DOM

The variation in the optical properties of CDOM showed distinct differences among the study regions and water masses. The highest fluorescence intensity was reported for the UPML in the BS region due to the direct influence of the Mackenzie river inflow (Figure 4.11). The fluorescence signal, including the terrigenous signature, was high at the surface of the ESSLS

region, closely followed by the TPD and then by the bottom water of ESSLS, that can indicate the dominance of the lateral transport of the CDOM from the source on the shelf into the central Arctic Ocean. The relative contribution of the C404 signal was the highest in the ESSLS region, probably due to the upwelling of the circumpolar current at Gakkel and Mendeleev ridges. In the Canada Basin, the fluorescence intensity was higher within the halocline layers than in the PML, occupied by the Beaufort Gyre system. In the CS region, the rPWW was characterized by fluorescence due to a higher degree of degradation. Overall, the NB region was marked by the lowest fluorescence intensity.

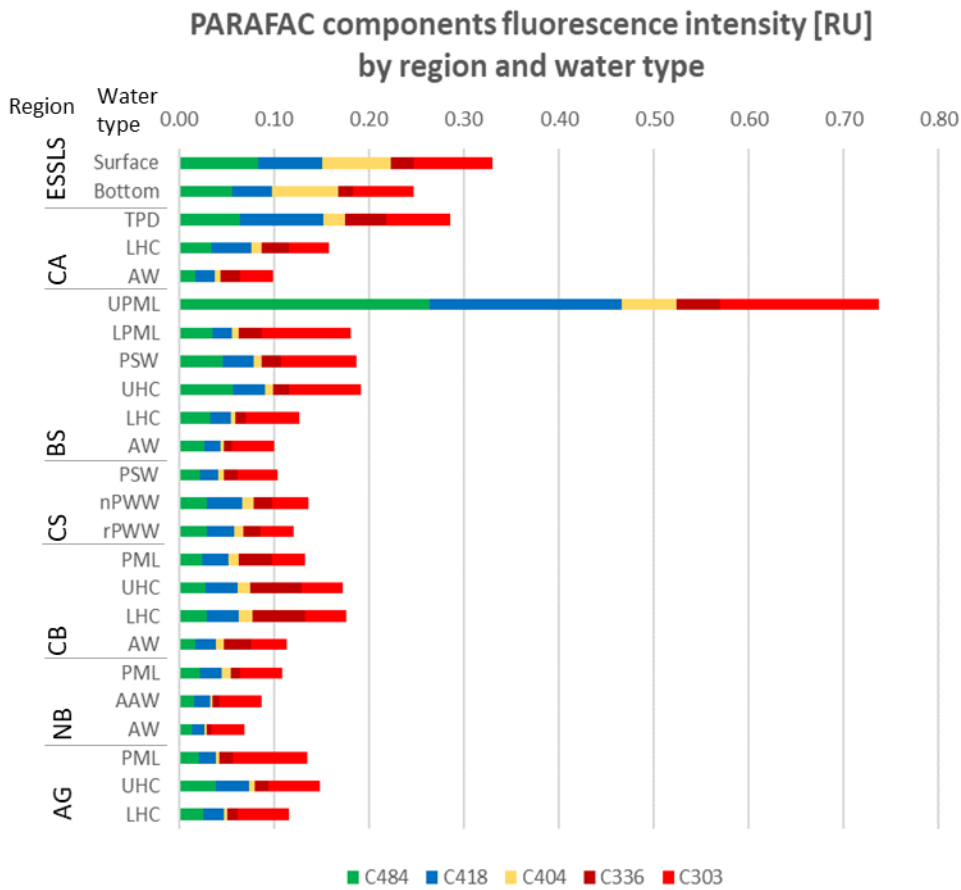


Figure 4.11. PARAFAC components fluorescence intensity by region and water mass

The absorbance also peaked in the UPML of the BS region and the lowest- within the LHC of the AG region (Figure 4.12). The lowest absorbance values were reported for the AG

region. Although the absorbance coefficients a_{254} and a_{350} are highly correlated ($R^2=0.98$, $p<0.0001$), a general trend was detected comparing the metrics within different water masses. The water masses located above ~ 70 meters exhibit higher a_{254} comparing to the underlying layers within the same region. The a_{350} is overall more elevated in the water masses below ~ 70 meters than the surface ones within the same region. This is related to the infrared shift in absorbance with depth.

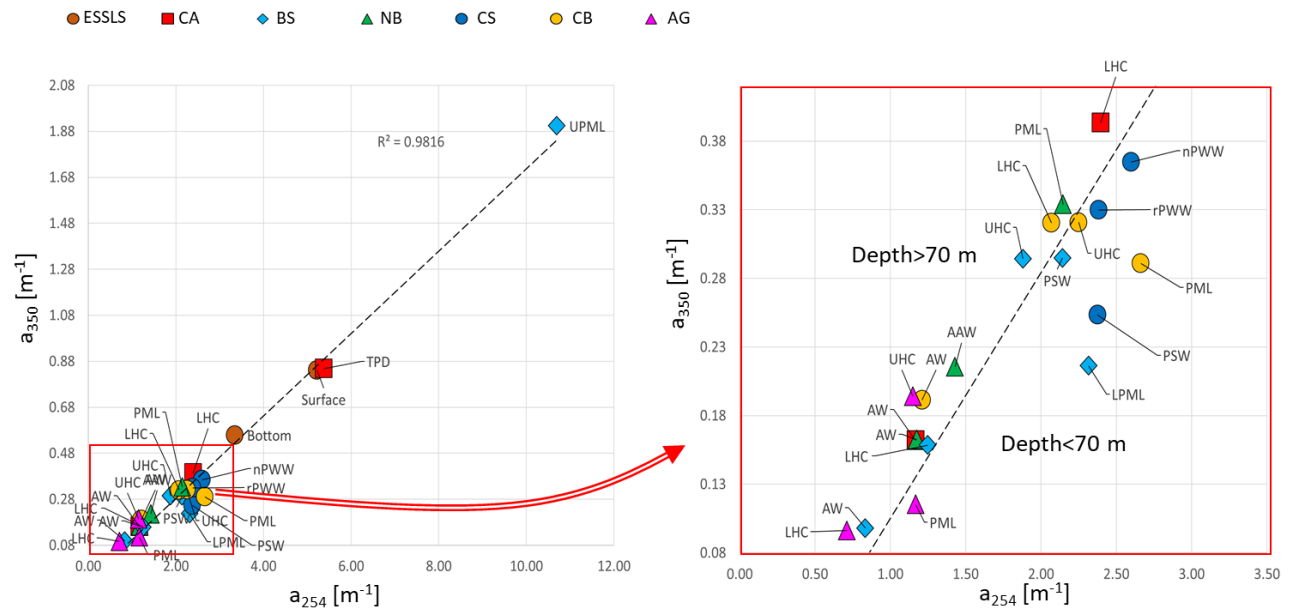


Figure 4.12. Scatter plot of a_{350} vs. a_{254} (left panel). Different regions are shown with different markers. The linear regression trend is shown as a dashed line. The lower absorbance region is zoomed in the right panel.

Previous studies suggested that $S_{275-295}$ can be used as an effective tracer of tDOM in river-influenced ocean margins (Fichot and Benner, 2012). This study, however, showed that the lowest values of $S_{275-295}$ (which should be indicative of tDOM presence) were reported in the PWW water masses (Figure 4.13). According to the previous study, $S_{300-600}$ exhibits potential as dissolved organic carbon (DOC) concentration proxy (Makarewicz et al. 2018). Nevertheless, $S_{300-600}$ did not exhibit a significant relationship with the available DOC data. $S_{300-600}$ was the lowest in the AW and the highest- in the UPML of the BS region and the PML of the CB. Overall, the $S_{350-400}$ was the highest in the AG, and the lowest values were reported for the AW.

The spectral slopes might indicate different degradation processes and require further research to constrain those processes.

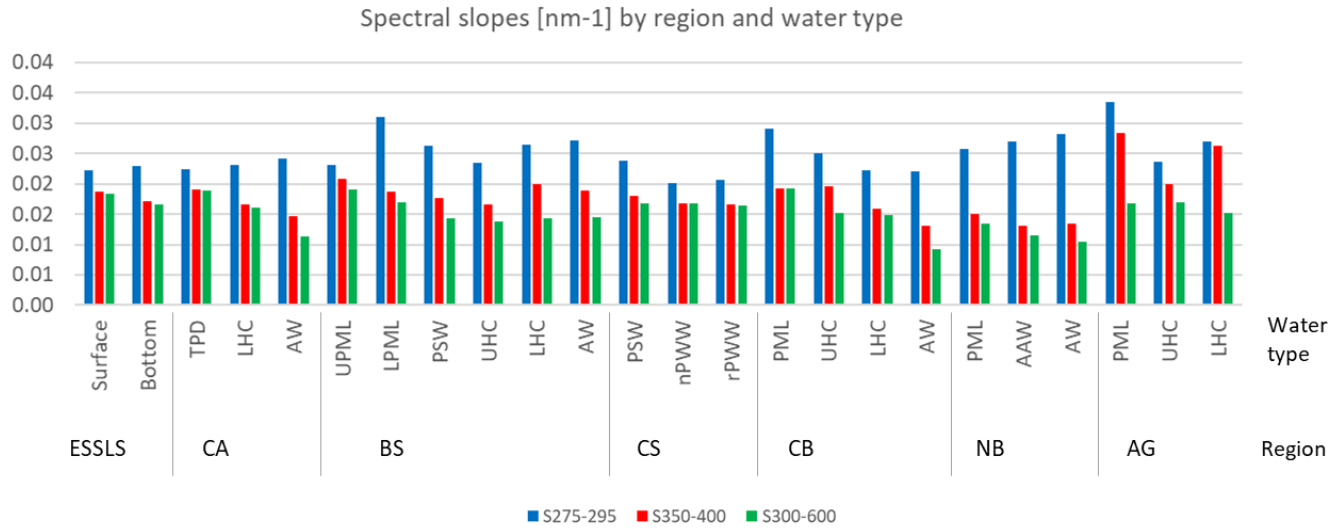


Figure 4.13. Spectral slopes by region and water mass

According to the previous studies, S_R correlates well with CDOM molecular weight (negative correlation) and increases exponentially with photobleaching (Helms et al., 2008). The highest S_r values were reported in the Atlantic-origin water masses in the Nansen Basin (Figure 4.14). The water masses of the AG and the UPML in the BS region had the lowest S_r values. The S_r remained unchanged between the surface water of the ESSLS and the TPD, and the AWW and AW in the Nansen Basin, indicating that the photobleaching process is not important in the water mass modification in these regions.

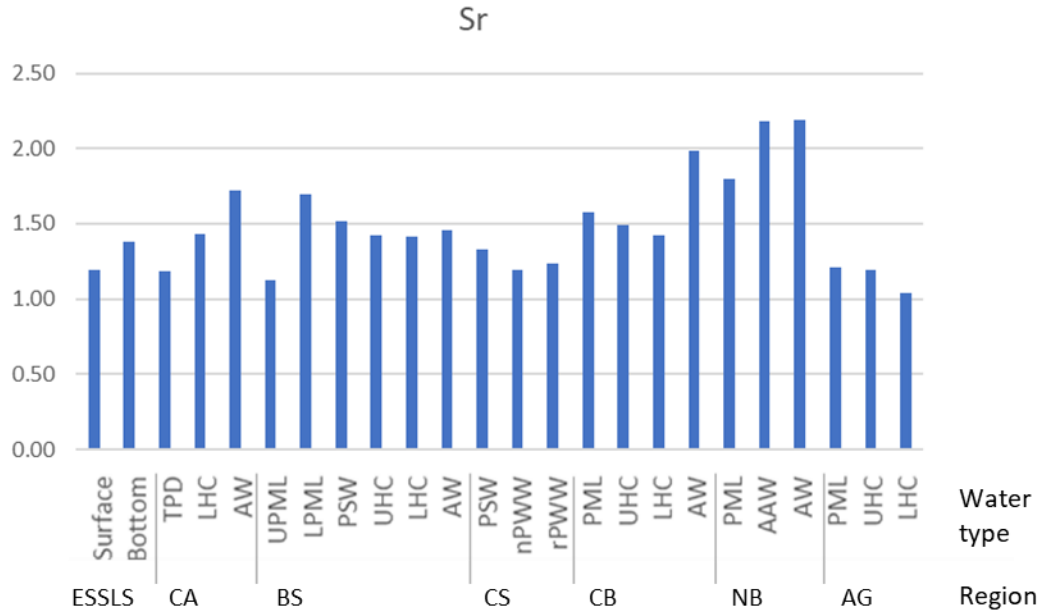


Figure 4.14. S_r by region and water mass

The total fluorescence (FDOM) calculated as a sum of PARAFAC components was compared to the *in situ* CDOM fluorescence (Figure 4.15). The parameters exhibited moderate correlation. The relationship was significantly improved when subtracting tryptophan-like C_{336} from the FDOM signal. A general trend was found comparing the metrics within different water masses (Figure 4.16). The halocline water masses exhibit higher *in situ* CDOM fluorescence comparing to the upper layers, but lower FDOM within the same region. This is because C_{336} is related to primary production above the halocline layers.

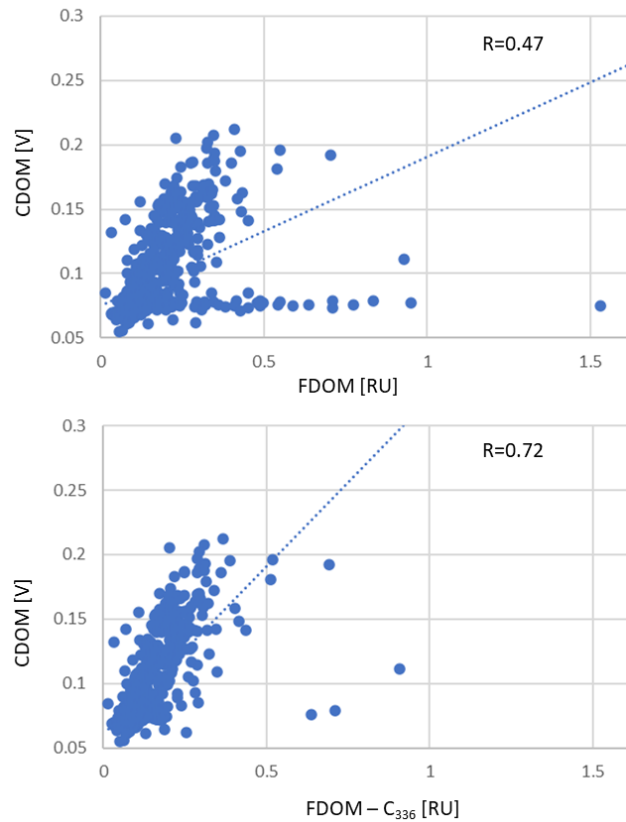


Figure 4.15. Scatter plot of FDOM (sum of all PARAFAC components) vs. *in situ* CDOM fluorescence (top panel). The linear regression trend is shown as a dashed line. The bottom panel shows the scatter plot of the sum of the PARAFAC components except for C₃₃₆ and *in situ* CDOM fluorescence.

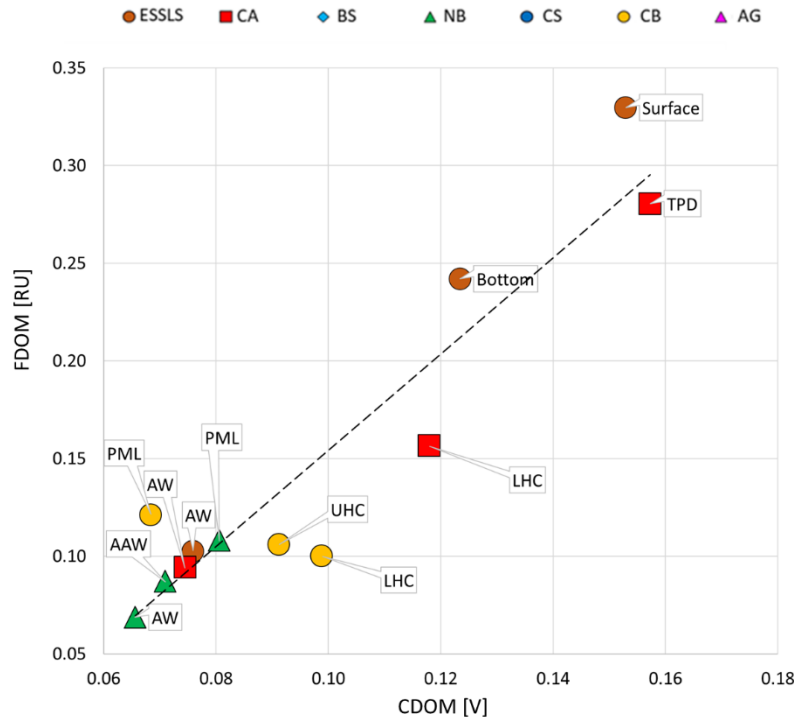


Figure 4.16. Scatter plot of FDOM vs. *in situ* CDOM fluorescence. Different regions are shown with different markers. The linear regression trend is shown as a dashed line.

4.4.2. The principal components based on the optical properties

The goal of PCA is to detect patterns in a dataset and to reduce the number of variables so that the data is simplified without losing important characteristics. The PCA is also useful for smoothing out the fluctuations of the individual co-varying variables to capture the major trends in the data. Of the PCA, the first principal component (PC1) accounted for 45% of the variability in optical properties of CDOM, the second principal component (PC2) accounted for 17% (Figure 4.17). The PC1 highly correlated with lignin phenols concentrations ($R=0.97$, $p<0.0001$; data from Walker et al. 2009; Massicotte et al. 2021; Williford et al. 2021), which are a distinctive biomarker for tDOM (Amon et al. 2012), with significant correlations to the terrigenous CDOM signal (Amon et al. 2003). The PC1 separated the optical proxies with S_R and $S_{275-295}$ having negative scores and the rest of the proxies having positive scores, with the highest scores for the CDOM absorptions (a_{254} , a_{350}), terrigenous-derived humic-like C_{484} , and mixed source humic-like C_{418} . Thus, PC1 was a terrigenous DOM component.

The PC2 split the optical proxies with the spectral slopes and C_{336} having negative scores and the a_{254} , a_{350} , C_{484} , C_{418} , C_{404} , C_{303} , S_R having positive scores. The highest positive score was computed for the S_R which is known to increase exponentially, while $S_{350-400}$ is known to decrease linearly with respect to photobleaching (Helms et al. 2008, 2013) and had the lowest score. Based on the distribution and the correlations, PC2 is linked to the Barents Sea branch, bringing modified AW further into the Arctic basins.

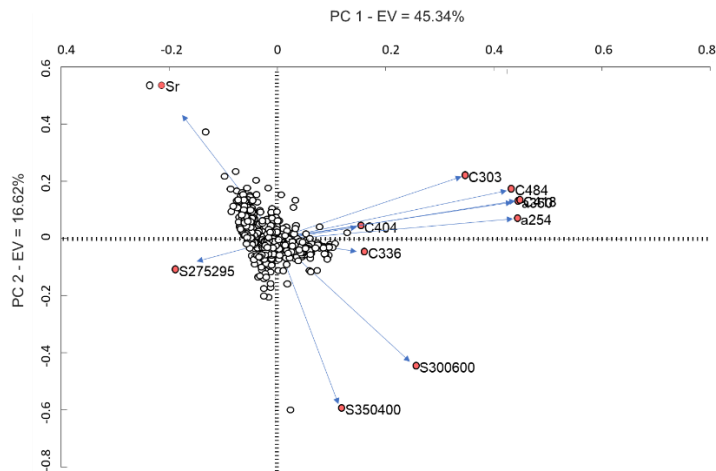


Figure 4.17. Loadings and scores for the PCA. The length of the vector associated with optical indices represents the overall strength of that variable on PC1, PC2.

The surface distribution of the PC1 score highlighted the Mackenzie and Lena rivers' input into the Arctic Ocean (Figure 14.18). According to the PC1 distribution, the Mendeleev ridge is an important feature, promoting the TPD curving at the Eurasian shelf towards the central Arctic basins. The surface layer of the Canada Basin did not exhibit an increase in PC1; therefore, the fluvial discharge can be excluded from the list of the potential freshwater sources feeding the growing Beaufort gyre. The distribution of the PC1 at the salinity surface of 34.7, though, showed that the cold halocline in the Canada Basin could be supplied from the East Siberian Sea shelf or the western part of the Chukchi Sea shelf.

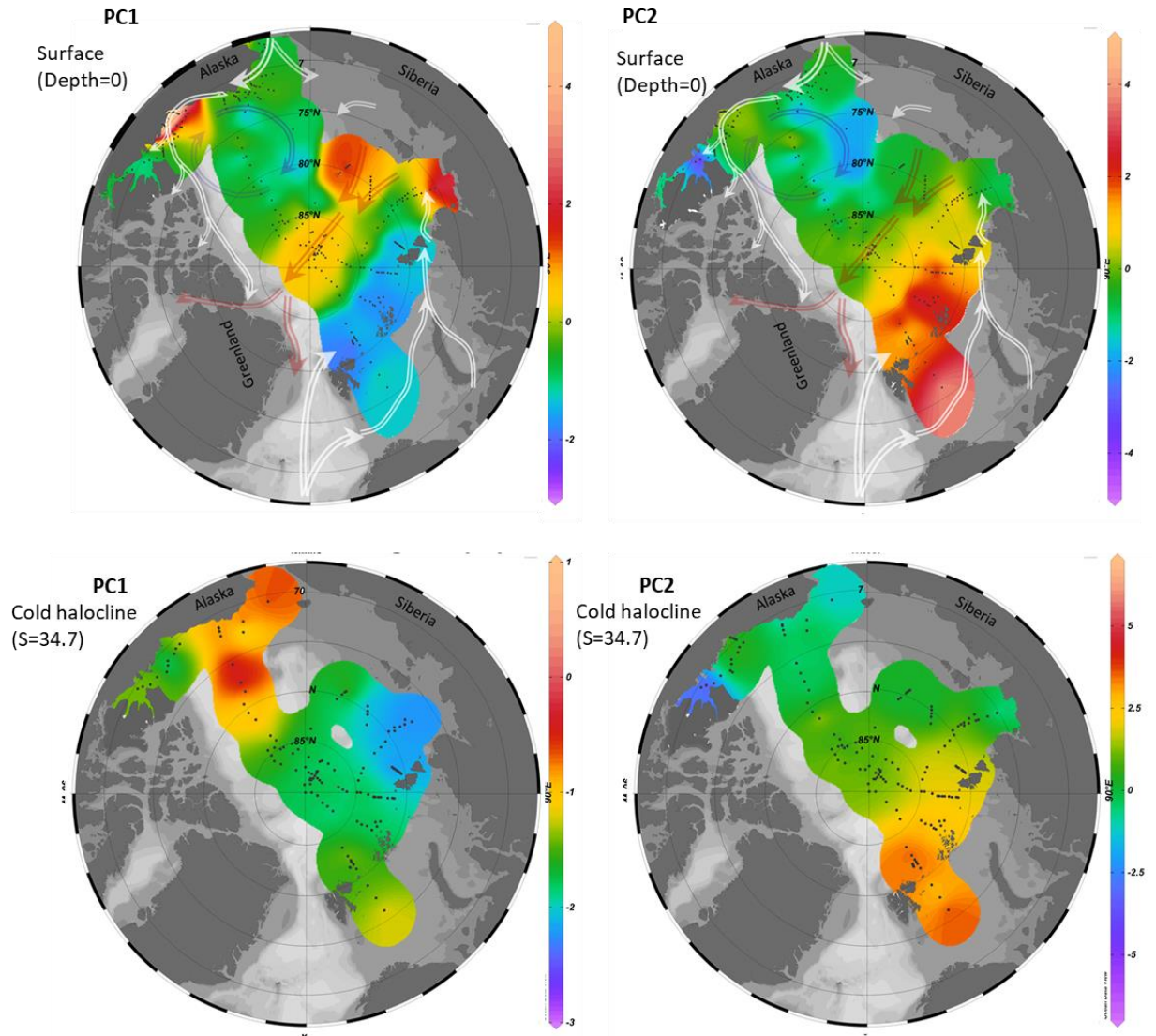


Figure 4.18 The surface distribution (top two panels) of the PC1 (left) and PC2 (right), overlaid by the main surface circulation patterns shown in arrows. The distribution of PC1 and PC2 at the salinity surface of $S=34.7$ is shown in the bottom panels.

The PC2, likely related to the Barents Sea branch of the AW inflow, is the highest in the Barents Sea and is elevated in the Nansen Basin (Figure 4.18). The convectional mechanism of cold halocline formation might occur on the Barents Sea shelf and in the Nansen Basin as indicated to the positive PC2 values at the salinity surface of 34.7 (which is located at the at ~ 100 meters depth in these regions), but likely this process does not feed the cold halocline beyond the Gakkel Ridge.

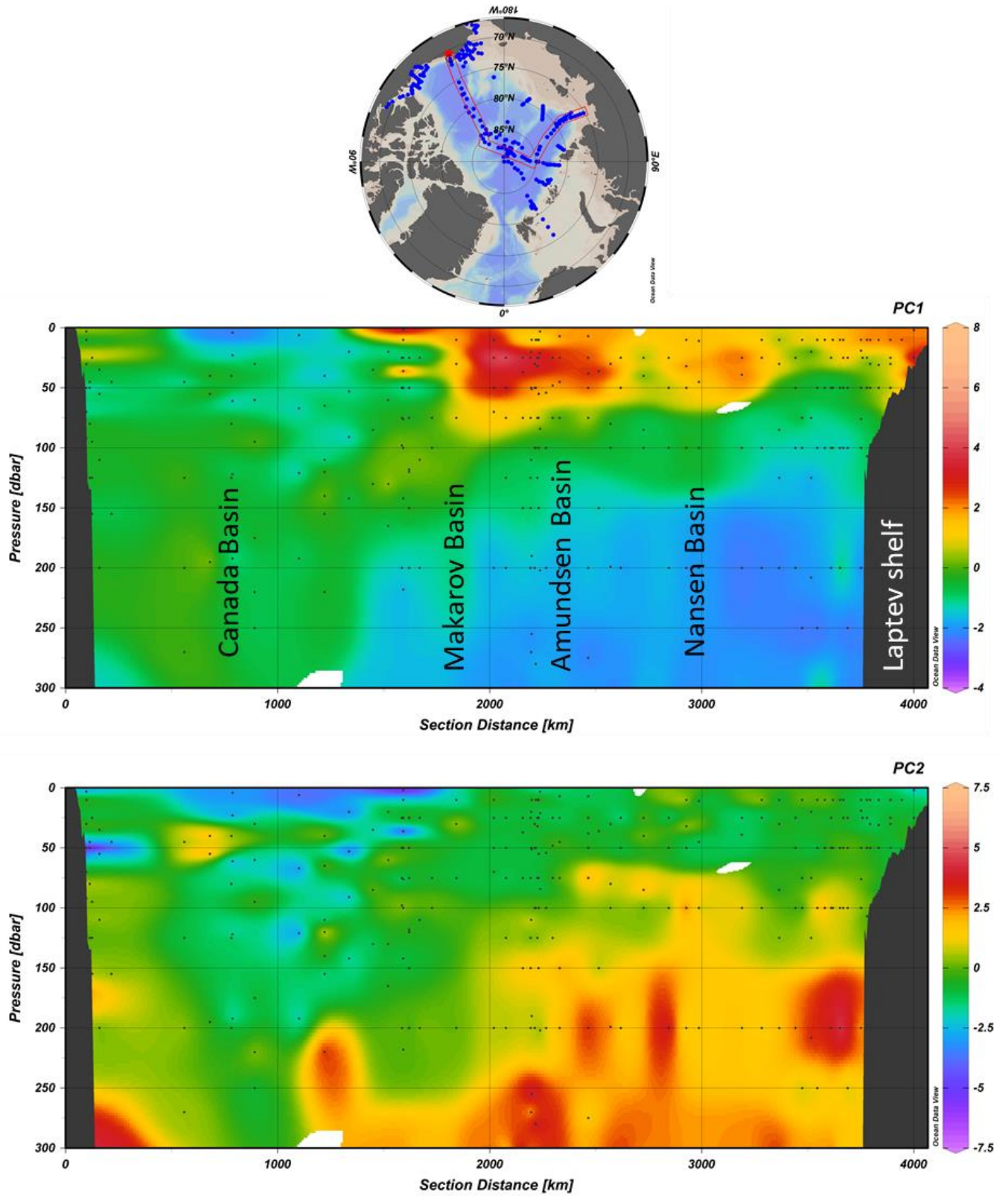


Figure 4.19. The PC1 (top) and PC2 (bottom) cross-section from the Beaufort Sea slope through the central Arctic into the Laptev Sea shelf.

The cross-sections through the Arctic Ocean of the two PC components show clear patterns in relation to the Arctic Ocean hydrography (Figure 4.19). The terrigenous PC1 peaks at the surface of the Laptev Sea shelf and in the TPD region, spreading trace of the component into the Canada Basin halocline. The distribution of the PC2 mimics the AW distribution in the Arctic Ocean, with the characteristic shoaling pattern beneath the Beaufort Gyre. This approach shows great potential to visualize major circulation patterns in the Arctic Ocean and will be further developed with data sets from additional studies over the last 25 years.

4.5. References

- Alkire, M. B., Polyakov, I., Rember, R., Pnyushkov, A., Ivanov, V., & Ashik, I. (2017). Combining physical and geochemical methods to investigate lower halocline water formation and modification along the Siberian continental slope. *Ocean Science*, 13(6), 983-995.
- Alkire, M. B., Rember, R., & Polyakov, I. (2019). Discrepancy in the identification of the Atlantic/Pacific front in the central Arctic Ocean: NO versus nutrient relationships. *Geophysical Research Letters*, 46, 3843–3852. <https://doi.org/10.1029/2018GL081837>
- Amon, R. M. W., Rinehart, A. J., Duan, S., Louchouart, P., Prokushkin, A., Guggenberger, G., ... & Zhulidov, A. V. (2012). Dissolved organic matter sources in large Arctic rivers. *Geochimica et Cosmochimica Acta*, 94, 217-237.
- Anders (2005) Cruise report. <https://cchdo.ucsd.edu/data/8026/ODEN05do.pdf>
- Anderson, L. G., Andersson, P. S., Björk, G., Peter Jones, E., Jutterström, S., & Wählström, I. (2013). Source and formation of the upper halocline of the Arctic Ocean. *Journal of Geophysical Research: Oceans*, 118(1), 410-421.
- Anderson, L. G., Tanhua, T., Jones, E. P., & Karlqvist, A. (2011). Hydrographic, chemical and carbon dioxide data from R/V Oden cruise 77DN20050819, August 19–September 25, 2005.

Oak Ridge, TN: Carbon Dioxide Information Analysis Center, Oak Ridge National Laboratory, US Department of Energy. https://doi.org/10.3334/CDIAC/otg.CLIVAR_77DN20050819

Arrigo, K. (2010). ICESCAPE 2010.

http://ocean.stanford.edu/icescape/ICESCAPE_Cruise_Report_HLY1001_2010.doc

Arrigo, K. R., Perovich, D. K., Pickart, R. S., Brown, Z. W., Van Dijken, G. L., Lowry, K. E., ... & Swift, J. H. (2012). Massive phytoplankton blooms under Arctic sea ice. *Science*, 336(6087), 1408-1408.

Arrigo, K. R., Perovich, D. K., Pickart, R. S., Brown, Z. W., Van Dijken, G. L., Lowry, K. E., ... & Swift, J. H. (2012). Massive phytoplankton blooms under Arctic sea ice. *Science*, 336(6087), 1408-1408.

Ballabio, D. (2015), A MATLAB toolbox for Principal Component Analysis and unsupervised exploration of data structure, *Chemometrics and Intelligent Laboratory Systems*, 149 Part B, 1-9 (doi: 10.1016/j.chemolab.2015.10.003)

Barber, D. G., Asplin, M. G., Gratton, Y., Lukovich, J. V., Galley, R. J., Raddatz, R. L., & Leitch, D. (2010). The International Polar Year (IPY) Circumpolar Flaw Lead (CFL) system study: overview and the physical system. *Atmosphere-ocean*, 48(4), 225-243.

Bauch, D., Cherniavskaia, E., & Timokhov, L. (2016). Shelf basin exchange along the Siberian continental margin: Modification of Atlantic Water and Lower Halocline Water. *Deep Sea Research Part I: Oceanographic Research Papers*, 115, 188-198.

Bauch, D., Hölemann, J., Andersen, N., Dobrotina, E., Nikulina, A., & Kassens, H. (2011). The Arctic shelf regions as a source of freshwater and brine-enriched waters as revealed from stable oxygen isotopes. *Polarforschung*, 80(3), 127-140.

Bauch, D., Hölemann, J., Willmes, S., Gröger, M., Novikhin, A., Nikulina, A., ... & Timokhov, L. (2010). Changes in distribution of brine waters on the Laptev Sea shelf in 2007. *Journal of Geophysical Research: Oceans*, 115(C11).

Bertosio, C., Provost, C., Sennéchaël, N., Artana, C., Athanase, M., Boles, E., ... & Garric, G. (2020). The western Eurasian Basin halocline in 2017: Insights from autonomous NO measurements and the Mercator physical system. *Journal of Geophysical Research: Oceans*, 125(7), e2020JC016204.

Brugler, E. T., Pickart, R. S., Moore, G. W. K., Roberts, S., Weingartner, T. J., & Statscewich, H. (2014). Seasonal to interannual variability of the Pacific water boundary current in the Beaufort Sea. *Progress in Oceanography*, 127, 1-20.

Carmack, E. C., Macdonald, R. W., & Papadakis, J. E. (1989). Water mass structure and boundaries in the Mackenzie shelf estuary. *Journal of Geophysical Research: Oceans*, 94(C12), 18043-18055.

Carmack, E., Macdonald, R. W., and Jasper, S.: Phytoplankton productivity on the Canadian Shelf of the Beaufort Sea, *Mar. Ecol. Prog. Ser.*, 277, 37–50, 2004.

Chen, H., Zheng, B., Song, Y., & Qin, Y. (2011). Correlation between molecular absorption spectral slope ratios and fluorescence humification indices in characterizing CDOM. *Aquatic Sciences*, 73(1), 103-112.

Chen, M., Jung, J., Lee, Y. K., & Hur, J., 2018. Surface accumulation of low molecular weight dissolved organic matter in surface waters and horizontal off-shelf spreading of nutrients and humic-like fluorescence in the Chukchi Sea of the Arct

- Chen, M., Kim, J. H., Hong, S., Lee, Y. K., Kang, M. H., Jin, Y. K., & Hur, J. (2021). Spectral Characterization of Dissolved Organic Matter in Seawater and Sediment Pore Water from the Arctic Fjords (West Svalbard) in Summer. *Water*, 13(2), 202.
- Del Vecchio, R., & Blough, N. V. (2002). Photobleaching of chromophoric dissolved organic matter in natural waters: kinetics and modeling. *Marine Chemistry*, 78(4), 231-253.
- Fichot, C. G. (2013). Transformations and Fates of Terrigenous Dissolved Organic Matter in River-Influenced Ocean Margins.
- Gong, D., & Pickart, R. S. (2015). Summertime circulation in the eastern Chukchi Sea. *Deep Sea Research Part II: Topical Studies in Oceanography*, 118, 18-31.
- Griffin, C. G. (2016). Dissolved organic matter in major rivers across the Pan-Arctic from remote sensing (Doctoral dissertation).
- Guéguen, C., Itoh, M., Kikuchi, T., Eert, J., & Williams, W. J. (2015). Variability in dissolved organic matter optical properties in surface waters in the Amerasian Basin. *Frontiers in Marine Science*, 2, 78.
- Helms, J. R., Stubbins, A., Perdue, E. M., Green, N. W., Chen, H., & Mopper, K. (2013). Photochemical bleaching of oceanic dissolved organic matter and its effect on absorption spectral slope and fluorescence. *Marine Chemistry*, 155, 81-91.
- Helms, J. R., Stubbins, A., Ritchie, J. D., Minor, E. C., Kieber, D. J., & Mopper, K. (2008). Absorption spectral slopes and slope ratios as indicators of molecular weight, source, and photobleaching of chromophoric dissolved organic matter. *Limnology and oceanography*, 53(3), 955-969.
- Hintze, J. L., & Nelson, R. D. (1998). Violin plots: a box plot-density trace synergism. *The American Statistician*, 52(2), 181-184.

Hölemann, J. A., Juhls, B., Bauch, D., Janout, M., Koch, B. P., & Heim, B. (2021). The impact of land-fast ice on the distribution of terrestrial dissolved organic matter in the Siberian Arctic shelf seas. *Biogeosciences Discussions*, 1-30.

Holmes, R. M., McClelland, J. W., Peterson, B. J., Shiklomanov, I. A., Shiklomanov, A. I., Zhulidov, A. V., Gordeev, V. V., and Bobrovitskaya, N. N.: A circumpolar perspective on fluvial sediment flux to the Arctic Ocean, *Global Biogeochem. Cycles*, 16(4), doi:10.1029/2001GB001849, 2002
<https://github.com/bastibe/Violinplot-Matlab>, DOI: 10.5281/zenodo.4559847

Jones E. P., Anderson L. G., Jutterstrom S., Mintrop L. and Swift J. H. (2008) Pacific freshwater, river water and sea ice meltwater across Arctic Ocean basins: results from the 2005 Beringia Expedition. *J. Geophys. Res. Oceans* 113. <http://dx.doi.org/10.1029/2007jc004124>.

Kadko, D., & Landing, W. (2015). U.S. Arctic GEOTRACES USCGC Healy (HLY1502) cruise report. Retrieved from
https://www.bodc.ac.uk/resources/inventories/cruise_inventory/reports/healy1502.pdf

Kaiser, K., Benner, R., & Amon, R. M. W. (2017). The fate of terrigenous dissolved organic carbon on the Eurasian shelves and export to the North Atlantic. *Journal of Geophysical Research: Oceans*, 122(1), 4-22.

Kaur, S., Ehn, J. K., & Barber, D. G. (2018). Pan-arctic winter drift speeds and changing patterns of sea ice motion: 1979–2015. *The Polar Record*, 54(5-6), 303-311.

Landing, W. M., Cutter, G., & Kadko, D. C. (2019a). Bottle data from the CTD-ODF carousel on the GEOTRACES Arctic section cruise (HLY1502) from August to October 2015 (U.S. GEOTRACES Arctic project). Biological and Chemical Oceanography Data Management Office (BCO-DMO). <https://doi.org/10.1575/1912/bco-dmo.646825.4>

Landing, W. M., Cutter, G., & Kadko, D. C. (2019b). Bottle data from the GEOTRACES clean carousel sampling system (GTC) on the Arctic section cruise (HLY1502) from August to October 2015 (U.S. GEOTRACES Arctic project). Biological and Chemical Oceanography Data Management Office (BCO-DMO). <https://doi.org/10.1575/1912/bco-dmo.647259.4>

Leitch (2008). Project summary
http://ipy.nwtresearch.com/Documents/Summaries/CFL_Summary.pdf

Makarewicz, A., Kowalczyk, P., Sagan, S., Granskog, M. A., Pavlov, A. K., Zdun, A., ... & Zabłocka, M. (2018). Characteristics of chromophoric and fluorescent dissolved organic matter in the Nordic Seas. *Ocean Science*, 14(3), 543-562.

Malina cruise report (2009). http://www.obs-vlfr.fr/malina/cruise_description.html?tab=1#TabbedPanels1

Malina Expedition Logbook (2009). Retrieved April 2021. http://www.obs-vlfr.fr/malina/cruise_description.html?tab=1#TabbedPanels1

Massicotte, P., Amon, R., Antoine, D., Archambault, P., Balzano, S., Bélanger, S., ... & Babin, M. (2020). The Malina oceanographic expedition: How do changes in ice cover, permafrost and UV radiation impact biodiversity and biogeochemical fluxes in the Arctic Ocean?. *Earth System Science Data Discussions*, 1-43.

Mathis, J. T., Hansell, D. A., & Bates, N. R. (2005). Strong hydrographic controls on spatial and seasonal variability of dissolved organic carbon in the Chukchi Sea. *Deep Sea Research Part II: Topical Studies in Oceanography*, 52(24-26), 3245-3258.

Matsuoka, A., Bricaud, A., Benner, R., Para, J., Sempéré, R., Prieur, L., ... & Babin, M. (2012). Tracing the transport of colored dissolved organic matter in water masses of the Southern Beaufort Sea: relationship with hydrographic characteristics. *Biogeosciences*, 9(3), 925-940.

Matsuoka, A., Ortega-Retuerta, E., Bricaud, A., Arrigo, K. R., & Babin, M. (2015). Characteristics of colored dissolved organic matter (CDOM) in the Western Arctic Ocean: Relationships with microbial activities. *Deep Sea Research Part II: Topical Studies in Oceanography*, 118, 44-52.

Murphy, K. R., Stedmon, C. A., Graeber, D., and Bro, R. (2013). Fluorescence spectroscopy and multi-way techniques. PARAFAC. *Anal. Methods* 5, 6557. <https://doi.org/10.1039/c3ay41160e>

Polyakov and Timokhov (2008). Cruise report. <https://uaf-iarc.org/wp-content/uploads/2018/10/NABOS-2008-report.pdf>

Rudels, B. (2010). "Arctic Ocean circulation," in *Ocean Currents, A Derivative of the Encyclopedia of Ocean Sciences*, eds J. Steele, S. Thorpe, and K. Turekian (Cambridge: Academic Press), 647.

Rudels, B. (2015). Arctic Ocean circulation, processes and water masses: a description of observations and ideas with focus on the period prior to the international polar year 2007–2009. *Prog. Oceanogr.* 132, 22–67. doi: 10.1016/j.pocean.2013.11.006

Rudels, B.: Arctic Ocean circulation, processes and water masses: A description of observations and ideas with focus on the period prior to the International Polar Year 2007–2009, *Prog. Oceanogr.*, 132, 22–67, <https://doi.org/10.1016/j.pocean.2013.11.006>, 2015.

Schauer, U. (2008). The expedition ARKTIS-XXII/2 of the Research Vessel “Polarstern” in 2007. *Berichte zur Polar- und Meeresforschung – Reports on Polar and Marine Research*, vol. 579, 271pp

Scheifele, B., Waterman, S., & Carpenter, J. R. (2021). Turbulence and Mixing in the Arctic Ocean's Amundsen Gulf. *Journal of Physical Oceanography*, 51(1), 169-186.

- Shen, Y., Benner, R., Robbins, L. L., & Wynn, J. G. (2016). Sources, distributions, and dynamics of dissolved organic matter in the Canada and Makarov Basins. *Frontiers in Marine Science*, 3, 198.
- Stedmon, C. A., Markager, S., & Kaas, H., 2000. Optical properties and signatures of chromophoric dissolved organic matter, CDOM in Danish coastal waters. *Estuarine, Coastal and Shelf Science*, 51, 2, 267-278.
- Timmermans, M. L., & Marshall, J. (2020). Understanding Arctic Ocean Circulation: A Review of Ocean Dynamics in a Changing Climate. *Journal of Geophysical Research: Oceans*, 125(4).
- Tipping, M. E., & Bishop, C. M. (1999). Probabilistic principal component analysis. *Journal of the Royal Statistical Society: Series B (Statistical Methodology)*, 61(3), 611-622.
- Walker, S. A., Amon, R. M. W., and Stedmon, C. A. (2013). Variations in high-latitude riverine fluorescent dissolved organic matter: a comparison of large Arctic rivers. *J. Geophys. Res. Biogeosci.* 118, 1689–1702. <https://doi.org/10.1002/2013jg002320>
- Walker, S. A., Amon, R. M., Stedmon, C., Duan, S., & Louchouart, P. (2009). The use of PARAFAC modeling to trace terrestrial dissolved organic matter and fingerprint water masses in coastal Canadian Arctic surface waters. *Journal of Geophysical Research: Biogeosciences*, 114(G4).
- Wassmann, P., Carmack, E. C., Bluhm, B. A., Duarte, C. M., Berge, J., Brown, K., ... & Huntington, H. P. (2020). Towards a unifying pan-arctic perspective: A conceptual modelling toolkit. *Progress in Oceanography*, 102455.
- Weingartner, T. J., Danielson, S., Sasaki, Y., Pavlov, V., & Kulakov, M. (1999). The Siberian Coastal Current: A wind-and buoyancy-forced Arctic coastal current. *Journal of Geophysical Research: Oceans*, 104(C12), 29697-29713.

Weishaar, J. L., Aiken, G. R., Bergamaschi, B. A., Fram, M. S., Fujii, R., & Mopper, K. (2003). Evaluation of specific ultraviolet absorbance as an indicator of the chemical composition and reactivity of dissolved organic carbon. *Environmental science & technology*, 37(20), 4702-4708.

Woodgate, R. A., Aagaard, K., Swift, J. H., Falkner, K. K., & Smethie Jr, W. M. (2005). Pacific ventilation of the Arctic Ocean's lower halocline by upwelling and diapycnal mixing over the continental margin. *Geophysical Research Letters*, 32(18).

Woodgate, R.A.; Aagaard, K.; Weingartner, T.J. Monthly temperature, salinity, and transport variability of the Bering Strait through inflow. *Geophys. Res. Lett.* 2005, 32, L04601

Woosley, R. J., & Millero, F. J. (2020). Freshening of the western Arctic negates anthropogenic carbon uptake potential. *Limnology and Oceanography*, 65(8), 1834-1846.

Zhao, J., Wang, W., Kang, S. H., Yang, E. J., & Kim, T. W. (2015). Optical properties in waters around the Mendeleev Ridge related to the physical features of water masses. *Deep Sea Research Part II: Topical Studies in Oceanography*, 120, 43-51.

Zhurbas, N., & Kuzmina, N. (2020). Variability of the thermohaline structure and transport of Atlantic water in the Arctic Ocean based on NABOS (Nansen and Amundsen Basins Observing System) hydrography data. *Ocean Science*, 16(2), 405-421.

5. SUMMARY

The goals of this dissertation were to expand the existing quantitative and qualitative assessments of DOM distribution in the Arctic Ocean, link it to environmental processes and decrease the large uncertainty of its role in trace metal circulation. The first chapter examined the distribution of optical properties of DOM, lignin phenols concentrations in the water masses of the eastern Arctic, specifically, the Laptev sea shelf, the Nansen, Amundsen and Makarov basins. The terrigenous biomarker concentration and CDOM peaked on the Laptev Sea shelf and within the Transpolar drift system, illuminating a significant DOM flux from the Eurasian shelf into the central Arctic. The Nansen basin was characterized by low levels of CDOM fluorescence and lignin phenols due to influence of the Atlantic water. The study also allowed elucidating the sources, molecular characteristics, and distributions of iron-binding ligands in the Arctic Ocean in the water masses of the Nansen, Makarov, Amundsen Basin, and the Laptev Sea. The primary sources of iron-binding ligands appear to be the riverine discharge of terrigenous DOM, marine organic matter produced on the shelves, and degradation products of plankton-derived organic matter in the shelf sediments. Overall, the freshly discharged terrigenous DOM was the most important source of iron-binding ligands. Besides lignin phenols, the presence of other terrigenous ligands, such as aromatic tannins, is likely. In general, iron-binding functional groups appear to occur in diverse molecules of multiple sources. The observed dFe distributions in the Arctic Ocean were not explained by the presence of a single ligand type, but rather by a mixture of ligand molecules of varying concentrations and binding strengths. This molecular diversity of ligands and associated binding strengths ultimately controls the distribution and transport of dFe in the Arctic Ocean.

The third chapter focuses on tracing DOM from various sources in the different water masses of the Nansen, Makarov, Amundsen, and Canada Basin, and the Chukchi Sea. The composition of the eastern Arctic Ocean organic matter pool was similar to that described in the second chapter. Each water mass of the Canada Basin was unique in terms of the organics signature. The PML was characterized by the elevated DOC, indicating high primary productivity, but low CDOM and lignin phenols concentration. It is related to the fact that the ice melt feeding the surface of the Canada Basin has been stripped off the organic matter during the freezing process. The upper halocline was characterized by the lower DOC values, comparing to the surface layer, but higher in situ CDOM fluorescence. The sediment-derived humic-like fluorophore was abundant within this layer. The lower halocline was characterized by the low DOC concentration. The in situ CDOM fluorescence and lignin phenols concentrations exhibited a peak in the UHC/LHC border. Additionally, we identified the organic ligands and their binding potential for a multitude of TE including Fe, Mn, Ni, Cu, Zn, Sc.

The fourth chapter contains a large pan-Arctic dataset of the optical properties, compiled from 8 international cruises. The usefulness of the commonly used optical indices in tracing water mass transformation in the Arctic Ocean has been demonstrated in the existing regional studies, but never on this geographical scale, covering the Beaufort sea slope, the Amundsen gulf, the Chukchi sea, the Canada, Makarov, Amundsen and Nansen basins. In summary, this dissertation presented the conclusions based on the comprehensive biochemical analyses of an extensive and exceptional dataset, which reduces the uncertainties about the unique Arctic trace metal profiles, water masses circulation, and freshwater balance in the Arctic Ocean. There is no doubt that the implementation of new observing systems like the autonomous platforms with CDOM sensors, development of new sensors, and analytical tools will allow further advances in

the analysis and interpretation of DOM properties, and though that enhance our understanding of the biochemistry of the ocean.